Probabilistic Design of Wind Turbine Structures: Design Studies and Sensitivities to Model Parameters

NJOMO WANDJI, Wilfried

Link to article, DOI:
10.11581/DTU:00000026

Publication date:
2017

Document Version
Publisher's PDF, also known as Version of record

Probabilistic Design of Wind Turbine Structures

⋆ Design Studies and Sensitivities to Model Parameters ⋆

Department of Wind Energy
PhD Report 2018

NJOMO WANDJI Wilfried

DTU Wind Energy PhD-0083(EN)
DOI Number: 10.11581/DTU:00000026

November 2017

DTU Wind Energy
Department of Wind Energy

Authors: NJOMO WANDJI Wilfried

Title: Probabilistic Design of Wind Turbine Structures - Design Studies and Sensitivities to Model Parameters

Department: Wind Energy

2017

Project Period:

15/11-2014 – 14/11-2017

Education:

PhD

Sponsorships:

The research leading to these results has partially received funding from:

- the European Community's 7th Framework Programme FP7-ENERGY-2012-1-2 STAGE project INNWIND.EU under grant agreement No. 308974; and
- the European Union Seventh Framework Programme project IRPWIND under the grant agreement No. 609795.

Main Supervisor:

Anand Natarajan, DTU Wind Energy

Co-Supervisors:

Nikolay K. Dimitrov, DTU Wind Energy

Thomas Buhl, Suzlon Blade Science Center

Thesis Examiners:

Henrik Bredmose, DTU Wind Energy

Michael Muskulus, NTNU

Subhamoy Bhattacharya, University of Surrey

DTU Wind Energy is a department of the Technical University of Denmark with a unique integration of research, education, innovation and public/private sector consulting in the field of wind energy. Our activities develop new opportunities and technology for the global and Danish exploitation of wind energy. Research focuses on key technical-scientific fields, which are central for the development, innovation and use of wind energy and provides the basis for advanced education.

DTU Wind Energy has a staff of approximately 240 and a further 35 PhD-students, spread across 38 different nationalities. The variety of research, education, innovation, testing and consultancy is reflected in the employment profile which includes faculty with research and teaching responsibilities, researchers and technical academic staff, highly skilled technicians and administrative staff.

Our facilities are situated at DTU Risø Campus and at DTU Lyngby Campus. Furthermore the department is running the national test stations in Høvsøre and Østerild.

Technical University of Denmark
Department of Wind Energy
Frederiksborgvej 399
Building 118
4000 Roskilde
Denmark

www.vindenergi.dtu.dk

Summary

Several societies have envisaged renewables as sources of energy for ecological and geo-strategical considerations. Amongst others, wind energy has gained considerable interest in the past decades due to its high potential to fulfil the aspirations of the societies that opted for it. However, harnessing offshore wind energy poses challenges such as cost of energy reduction, handling of very large structures, randomness pertaining to the metocean environment, and need for better understanding of the mechanical behavior of the structures.

Three means are employed in this thesis for cost reduction: decrease of conservatism level, improvement of design procedures, and development of innovative structural systems that suit well for large wind turbines. The increasing size of the structure introduces new problems that were not present for small structures. These problems include: (i) the preparation of models with sufficient adequacy in replacement of models whose validity ranges were restricted for small size structure; (ii) the upscaling of supplementary structures like mass dampers whose volume or mass become prohibitive; (iii) the satisfaction of fatigue lifetime requirements for jacket substructures.

In addition to being aggressive, conditions for offshore environments and the associated models are highly uncertain. Appropriate statistical methodologies should be used in order to design robust structures, which are structures whose engineering performance is not significantly affected by reasonably small changes of the environmental conditions. Recent inspections of some installed wind turbines on monopiles have unveiled serious damage to the grouted joints. The subsequent investigations revealed a misunderstanding of phenomena related to the mechanical behaviour of the grouted joints. Explanations have been proposed by previous studies and the present thesis investigates one of the derived solutions.

This study addresses these challenges sorted in three research areas: (i) *Area 1*: reduction of conservatism; (ii) *Area 2*: Lifetime improvement; and (iii) *Area 3*: Innovative systems. These research areas are differentially implemented through tasks on various wind turbine structures (shaft, jacket, semi-floater, monopile, and grouted joint). In particular the following research questions are answered:

- How are extreme and fatigue loads on a given structure influenced by the design of other structures on the same wind turbine? How can loads be prepared in order to be exchanged between the designers / manufacturers of different wind turbine components with better accuracy and lower conservatism level?
- How can fatigue lifetime of large substructures at deep waters be extended? What techniques are suitable? To which extent do they act on the structures? What are their efficiencies?
- How can innovative structures be developed/adapted which allow installations in deeper waters while maintaining low fatigue load levels and being economically competitive to floating structures? Why is the innovative concept efficient?
- How do the design parameters individually impact the design of monopiles and their engineering performance? What could be the effect of the interaction of these parameters?
- How do the design parameters influence the long term survival of the grouted joint under normal conditions? Given the computational cost of the finite element simulation, how can

the grouted joint be assessed under extreme loading taken into account the uncertainties in the variables?

Respectively, the principal contributions and findings of the present work are:

Format for load exchange. A preparative method of loads to be exchanged between the different stakeholders of a complex design process is introduced. The development of this method is buttressed on the stress calculation algorithm. For the extreme loads, the promoted method is in line with the standards' recommendations relative to determination of the extreme loads as the highest of the peak averages of each mean wind speed. Comparison between this method and the conventional load format seen in literature shows that additional structure capacity is revealed by the proposed method and that material saving is possible.

Improvement of fatigue lifetime. Three methods for fatigue lifetime improvement have been developed for jacket substructures. The first focuses on the joint design methodology. Clear guideline rules have been established to help designers to reduce stress concentration factors at joints. The second intends to reduce the vibration of braces based on the application of magneto-rheological dampers. Modelling methods and effectiveness are presented together with installation steps. The third employs an aero-elastically tailored rotor to alleviate fatigue loads on the support structure. Whereas the rotor optimization process was not done within the present study, its effect on the substructure is shown in this work.

Semi-floater: An innovative substructure. The semi-floater concept has been introduced by previous studies. In this work, the detailed design of the universal joint has been proposed together with the installation process of the substructure. A design process of such substructure type has been presented along side with an algorithm to design mooring line at the preliminary phase.

Monopile: Influence of model parameters. The individual influences of some key model parameters (damping, construction errors, soil properties) and their interactions have been quantified in a comparative manner. It has been established for example that the soil-structure interaction can interact with the construction errors to amplify the fatigue demand at some hotspots of the monopile.

Grouted joint: Mechanical behavior and determinant parameters. A probabilistic design approach based on a detailed finite element model has been developed. In order to reduce the computationally expensive analysis of the joint, a method based on load criteria is proposed and the adapted probabilistic analysis process is explained. The influences of the steel wall thickness, of the conical angle, and of the grout length have been respectively identified. Recommendations are given to improve the design process.

Resumé

Mange samfund introducerer bæredygtige energi kilder ud fra økologiske og geo-strategiske overvejelser. Vind energi er blandt de energi teknologier, som har opnået betydelig interesse over de seneste årtier, fordi den kan opfylde de behov som flere samfund har brug for. Der er dog en række udfordringer forbundet med at udnytte havvindkraft, så som reduktion af prisen på energien, håndtering af store strukturer, uforudsigeligheden af havbetingelserne og en bedre forståelse af de mekaniske egenskaber af strukturerne.

Tre tiltag er anvendt til at reducere kosten af energien fra havvind i denne afhandling: Reduktion af konservatismen i design, forbedrede design procedurer og udvikling af innovative strukturelle systemer som passer til store havvindmøller. Opskaleringen af strukturerne medfører nye udfordringer, som ikke er tilstede for små strukturer. Disse inkluderer: forberedelse af brugbare modeller, som kan erstatte modeller verificeret på mindre strukturer, opskalering af substrukturer så som masse dæmpere (hvis volumen bliver for store) og forlængelse af udmattelses levetid for jacket substrukturer.

Udover at være aggressive, så er miljø betingelserne og de tilsvarende modeller for havmiljøer meget usikre. Passende statistiske metoder skal derfor bruges for at opnå robuste design af strukturer, hvis ydeevne ikke påvirkes betydeligt af små ændringer i havmiljøet. Nylige inspektioner af havvindmøller installeret på monopæle har vist seriøse skader på støbte sammenføjninger. Den efterfølgende undersøgelse viste at de mekaniske fænomener for støbte sammenføjninger var blevet misforstået. Forklaringer på dette er blevet foreslået i tidligere studier og denne afhandling undersøger en af de foreslåede løsninger.

Dette studie adresserer ovenstående udfordringer gennem tre aktiviteter: (i) *Aktivitet 1*: reduktion af konservatisme, (ii) *Aktivitet 2*: Levetidsforlængelse og (iii) *Aktivitet 3*: Innovative systemer. Disse aktiviteter er implementeret forskelligt gennem opgaver på forskellige vindmøllestrukturer (aksel, jacket, semi-flyder, monopæl og støbte sammenføjninger). Nedenstående forskningsspørgsmål er specielt besvaret:

- Hvordan bliver ekstrem og udmattelseslaster på en given struktur påvirket af designet af andre strukturer på den samme vindmølle? Hvordan kan belastningerne forberedes, så de bedre kan udveksles mellem designere og fabrikanter af forskellige vindmølle komponenter og med højere nøjagtighed og med mindre konservatisme?

- Hvordan kan levetiden for store strukturer på dybt vand forlænges? Hvilke teknikker er brugbare? Hvor stort er omfanget af disse teknikker? Hvilken effektivitet har de?

- Hvordan kan innovative strukturer, som tillader installation på dybt vand, bibeholder en lav udmattelsesbelastning og er konkurrencedygtige med flydende strukturer udvikles/tilpasses? Hvorfor er de innovative koncepter effektive?

- Hvordan påvirker de individuelle design parametre designet af en monopæl og dens ydelse? Hvad er effekten af vekselvirkninger mellem parametrene?

- Hvordan influerer designparametrene langtidsoverlevelsen af støbte sammenføjninger under normale forhold? Givet regnekraftbehovet for finite element-simuleringer, hvordan kan støbte sammenføjninger evalueres under ekstrembelastning, hvor der samtidig tages højde for unøjagtigheder i variable?

De primære bidrag og resultater af denne afhandling er:

Format for udveksling af belastninger. En forberedende metode til udveksling af belastninger mellem interessenter i en kompleks design proces er blevet introduceret. Udviklingen af denne metode er baseret på spændingsberegningsalgoritmen. For ekstrem belastninger er den foreslåede metode i overensstemmelse med standard anbefalingerne for bestemmelse af disse som den højeste af maksimalgennemsnit af hver gennemsnitsvind hastigheden. Sammenligning mellem denne og den konventionelle belastningerbestemmelse fra litteraturen viser, at yderligere strukturel kapacitet er tilstede ved den foreslåede metode og at materiale besparelse er mulig.

Forlængelse af udmattelseslevetid. Tre metoder for udmattelseslevetidsforlængelse er blevet udviklet for jacket substrukturer. Den første fokuserer på metoder til design af sammenføjninger. Klare retningslinjer regler er blevet etableret for at hjælpe designere til at reducere spændingskoncentrationsfaktorer for sammenføjninger. Den anden har til formål at reducere vibrationer i tværforbindelser i substrukturer ved at anvende magneto-rheologiske-dæmpere. Modellerings metoder og effektivitet er præsenteret sammen med installationstrin. Den tredje anvender en skræddersyet aero-elastisk rotor til at reducere udmattelseslasterne på supportstrukturen. Rotor optimeringsprocessen blev ikke udført i dette arbejde, men effekten på substrukturen er blevet vist.

Semi-flyder: En innovativ sub-struktur. Semi-flyder konceptet blev introduceret i tidligere studier. I dette arbejde er det detaljerede design af en universal sammenkobling blevet foreslået sammen med installations processen af sub-strukturen. En design proces af sådanne sub-strukturer er blevet præsenteret sammen med en algoritme til indledende design af ankerlinjer.

Monopæl: Indflydelse af modelparametre. Den individuelle indflydelse af nogle af nøgleparametrene (dæmpning, konstruktions fejl og bundegenskaber) og deres vekselvirkning er blevet kvantificeret i et sammenlignende studie. Det er blevet eftervist, at vekselvirkningen mellem bund or struktur kan vekselvirke med konstruktionsfejl og øge udmattelse i visse positioner på monopæle.

Støbte sammenføjninger: Mekaniske egenskaber og afgørende parametre. En sandsynlighedsdesign tilgang baseret på finite element modellering er blevet udviklet. For at reducere den beregningstunge analyse af sammenføjninger, er en metode baseret på et belastningskriterie blevet foreslået og den tilpassede sandsynlighedsanalyseproces er forklaret. Indflydelsen af ståls vægtykkelse, af den koniske vinkel og længden af samlingen er blevet identificeret. Anbefalinger er givet for at forbedre design processen.

Publications

Publications included in this thesis:

- Njomo Wandji *et al.* [2016] *Development and design of a semi-floater substructure for multi-megawatt wind turbines at 50+ m water depths.* / Njomo Wandji, Wilfried; Natarajan, Anand; Dimitrov, Nikolay Krasimirov. **Published in: Ocean Engineering 125(2016) 226 – 237**

- Njomo Wandji *et al.* [2017] *Influence of model parameters on the design of large diameter monopiles for multi-megawatt offshore wind turbines at 50 m water depths.* / Njomo Wandji, Wilfried; Natarajan, Anand; Dimitrov, Nikolay Krasimirov. **Submitted to: Wind Energy.**

- Njomo Wandji *et al.* [2017] *Structural probabilistic assessment of conical grouted joint using numerical modelling.* / Njomo Wandji, Wilfried; Natarajan, Anand; Dimitrov, Nikolay Krasimirov. **To be submitted to: Ocean Engineering.**

Publications not included in this thesis:

- Njomo Wandji *et al.* [2015] *Design of monopiles for multi-megawatt wind turbines at 50 m water depth .* / Njomo Wandji, Wilfried; Natarajan, Anand; Dimitrov, Nikolay Krasimirov; Buhl, Thomas. **Part of: Scientific Proceedings. EWEA Annual Conference and Exhibition 2015, 8 – 12, European Wind Energy Association (EWEA) (ISBN: 9782930670003). Presented at: EWEA Annual Conference and Exhibition 2015, Paris**

- Njomo Wandji *et al.* [2016] *Reduction of fatigue loads on jacket substructure through blade design optimization for multimegawatt wind turbines at 50 m water depths.* / Njomo Wandji, Wilfried; Pavese, Christian; Natarajan, Anand; Zahle, Frederik. **Published in: Journal of Physics: Conference Series (Online) 753(2016) (ISSN: 1742-6596) (DOI: http://dx.doi.org/10.1088/1742-6596/753/4/042022). Presented at: The Science of Making Torque from Wind, 2016, Munich.**

- Njomo Wandji *et al.* [2017] *Application of magneto-rheological dampers to alleviate fatigue damage of jacket substructures for 20 MW wind turbines.* / Njomo Wandji, Wilfried; Natarajan, Anand. **Presented at: Wind Energy Science Conference, 2017, Lyngby.**

Acknowledgements

I would like to express my gratitude to all who contributed to this PhD Program.
In particular, I warmly thank:

- Anand Natarajan
- Nikolay Dimitrov
- Thomas Buhl
- Christian Pavese
- Frederic Zahle
- Mathias Stolpe

A special acknowledgement goes to Anders Melchiors Hansen, also known as ***The Hero***, whose constant help is greatly appreciated.

Contents

List of Figures

List of Tables

Reading Path

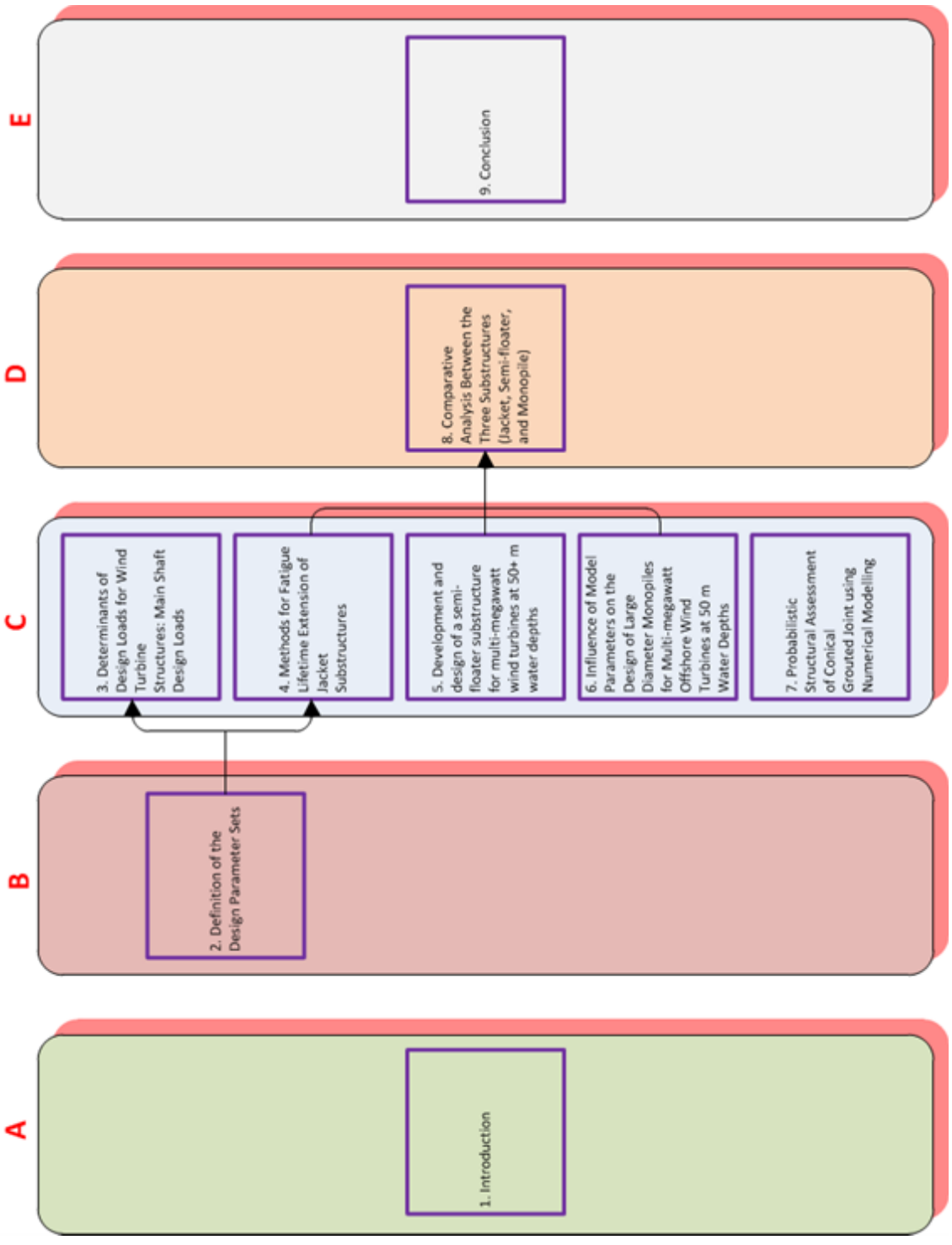

1 Introduction

I love dishes that feature the various shades of a single colour, making you stop to check what's in there.

Yotam Ottolenghi

1.1 Generalities

Several energy sources are competing to fuel the human-made machines, equipment, and devices used in the sectors of heating, electricty, manufacturing, transportation, and light. The primary energy sources are listed in Table 1.1 as given by Ref [1].

Table 1.1: Primary energy sources [1]

Type	Sources	Usage
Non-renewable	Petroleum	Transportation, manufacturing
	Natural gas	Heating, manufacturing, electricity
	Coal	Electricity, manufacturing
	Uranium	Electricity
Renewable	Biomass	Heating, electricity, transportation
	Hydropower	Electricity
	Geothermal	Heating, electricity
	Wind	Electricity
	Solar and Other	Light, heating, electricity

For many societies, ecological and geo-strategical considerations have favoured renewable energy sources, which should be cost-efficient in order to be economically viable. One energy type that has attracted attention and gained interest is wind energy. While onshore based wind energy stands as a strong competitor, its offshore based counterpart is still relatively expensive. For example, the projected detailed cost of electricity in the Nordic countries by 2040 for different sources of energy is illustrated by Figure 1.1. It shows that, although the levelized cost of electricity (LCOE)

of the offshore wind energy will be relatively low, its capital cost will still be higher compared to the alternatives.

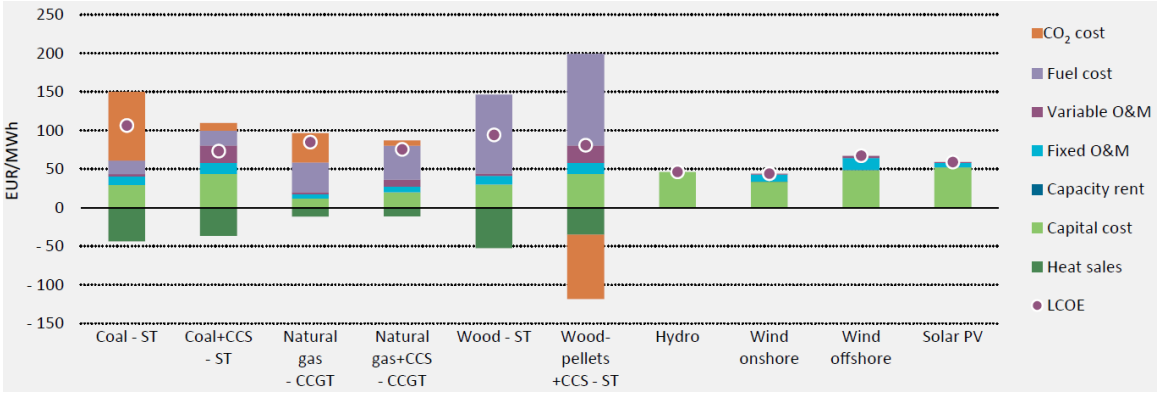

Figure 1.1: Projected cost of electricity in the Nordic countries by 2040 as of 2016 by energy sources [2]. LCOE = levelized cost of electricity; ST = steam turbine; O & M = operation and maintenance; CCGT = combined-cycle gas turbine; CCS = carbon capture and storage.

The observed LCOE of the offshore wind energy is due to its higher capital cost required for the latter option. However, being at the beginning of its commercial deployment, the offshore wind industry shows a considerable potential. Offshore wind energy can benefit from several advantages compared to onshore wind energy:

1. **Higher tower and longer blades.** For wind turbines of same rated power, hubs are placed higher on land than above seas. As the rated power increases, larger rotors are required and thereby higher towers. On land, safety regulations impose a minimal distance between wind turbines and human-made exploitations (such as habitations, schools, industrial facilities) in function of the wind turbine height. Hence, many wind turbines are limited in height. Off the coast, wind turbines can be built with larger rotor diameters, whose swept areas are approximatively proportional to the maximum energy that can be extracted from the wind. Producing more energy with one wind turbine contributes to the reduction of capital/maintenance cost. The continuous exploitation of this potential is illustrated in Figure 1.2, where diameters of up to 250 m are expected in a foreseen future.

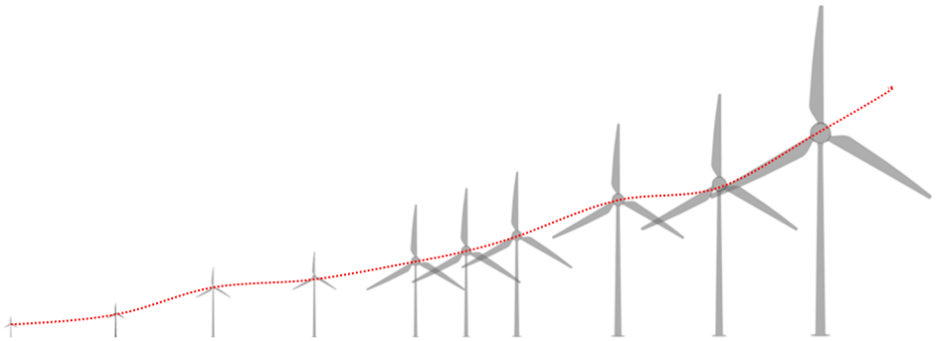

Years	1980	1985	1990	1995	2000		2005	2010	2015	2020
Rotor diameter [m]	15	20	40	50	112	124	126	150	178	252
Rated Power [MPa]	0.01	0.10	0.50	0.60		5.0		7.5	10.0	20.0

Figure 1.2: Size growth of wind turbines from 1980 till nowadays (Data are extracted from [3]).

2. **Higher average wind speeds but low turbulence.** Wind turbulence is created by the shear friction of the air flow with the ground roughness (topography, vegetation, or constructions). Above the sea waters, the roughness and the obstacles are minimal, which reduces the ambient turbulence while allowing high average wind speeds. As available energy grows cubically with the wind speed, this contributes to the production of more energy with wind systems exposed to lower ambient turbulence.

3. **Larger wind farms.** In the sea, more area is available compared to on land where constraints (e.g. protected areas) can be dissuasive for the commissioning of large wind farms.

If all these potentials are fully exploited, it is expected that the LCOE from offshore wind will considerably decrease due to scale effect as more energy could be produced. However, on contrary to the land environment, seas offer a much harsher environment, which requires more complex and expensive support structure systems to ensure the structural integrity of wind turbines. In contrast to the relatively simple (reinforced concrete) bases used as foundations for onshore wind turbines, more advanced substructure + foundation systems are needed for offshore ones.

For up to 50+ m water depths where fixed bottom substructures apply, Kallehave *et al.* [4] have listed common concepts and their occurrences in commercial wind farms: monopile (74 %), gravity based foundation (16 %), and spatial truss (10 %). Each of these substructures shows advantages that can be the disadvantages of the others, and all raise design problems, which can be specific or common. Besides the inherent complexity of these structural systems, the randomness of the metocean environment, the diverseness of the seabed properties (topographically and geologically), and the difficulty to model such media with high fidelity confront designers to exciting challenges.

In addition to these engineering challenges, the offshore substructure + foundation systems are substantially costly. Figure 1.3 breaks downs the capital cost for typical onshore and offshore wind systems. It can be seen that they consume more than a quarter of the total cost for offshore wind turbines, which is necessary to reduce in order to increase the competitiveness of the offshore wind. Specifically for 10 MW wind turbines, the capital expenditure (CAPEX) share of the substructure + foundation systems can reach up to 32 % at 50 m water depth [5].

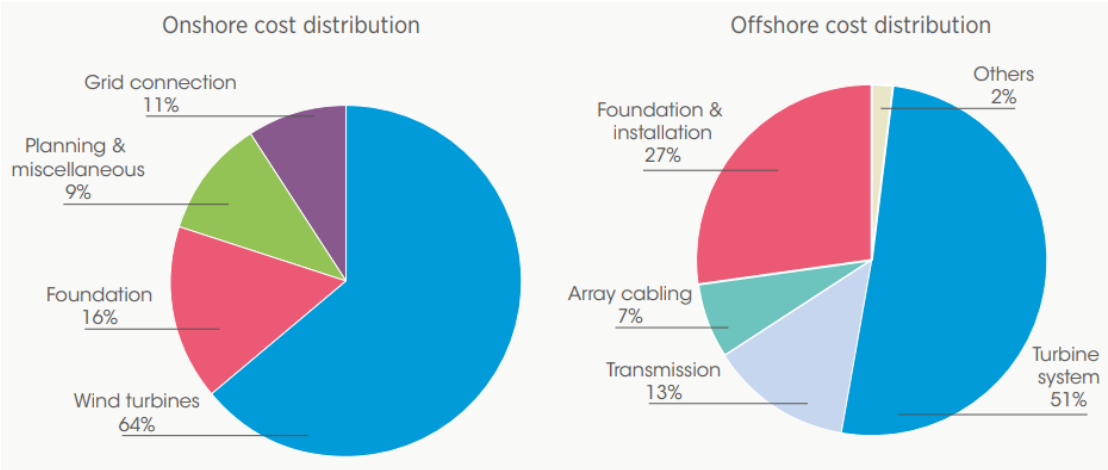

Figure 1.3: Capital cost breakdowns for typical onshore and offshore wind systems [6].

This thesis addresses the probabilistic design of offshore multi-megawatt wind turbine structures placed at medium to deep waters with an emphasis on substructure + foundation. Considering various uncertainties, it focusses on the structural design of the components to ensure structural integrity at minimal cost.

1.2 Challenges in Offshore Wind Industry

The ultimate goal of this thesis is to provide methods for the design of ***robust*** wind turbines structures that are ***structurally safe*** and ***cost-efficient***. In order to achieve this goal, some challenges posed by the contemporary offshore wind industry have been selected: cost reduction, large structure size, uncertainty pertaining to the metocean environment, and better understanding of the structural mechanisms of offshore turbine components.

The cost of the substructures represents a considerable CAPEX portion for offshore wind turbines and needs to be reduced. Three means are employed in this thesis for cost reduction: decrease of the level of conservatism, improvement of design procedures, and development of innovative structural systems that suit well to large wind turbines. The increasing size of the structure introduces new problems that were not present for small structures. These problems include: (i) the preparation of models with sufficient adequacy in replacement of models whose validity ranges were restricted for small size structure; (ii) the upscaling of supplementary structures like mass dampers whose volume or mass become prohibitive; (iii) the satisfaction of fatigue lifetime requirements for jacket substructures, as it will be discussed later.

In addition to the aggressive offshore environments, the models describing them are highly uncertain. Therefore, appropriate statistical methodologies should be used in order to design robust structures, which are structures whose engineering performance is not significantly affected by reasonable changes of the environmental conditions. Recent inspections of some installed wind turbines on monopiles have unveiled failures of the grouted joints [7]. The subsequent investigations revealed a misunderstanding of some phenomena related to the mechanical behaviour of the grouted joints. Explanations have been proposed and the derived solutions need to be investigated [8], [9], [10].

This study will address these challenges sorted in three research areas: (i) *Area 1*: Reduction of conservatism; (ii) *Area 2*: Lifetime improvement; and (iii) *Area 3*: Innovative systems. These research areas are incrementally implemented through tasks on various wind turbine structures: shaft, jacket, an innovative concept referred to as 'semi-floater', monopile, and grouted joints. These structures have been chosen as the representatives of the components mainly concerned by the challenges. The motivation of their selection are presented in detail in subsequent sections.

1.3 Objectives of the Thesis

Several objectives contribute to the achievement of the goal of the present thesis. In particular the following research questions will be answered:

- How are extreme and fatigue loads on a given structure influenced by the design of other structures on the same wind turbine? How can loads be prepared in order to be exchanged between the designers / manufacturers of different wind turbine components with better accuracy and lower conservatism level?
- How can fatigue lifetime of large substructures at deep waters be improved? What techniques are suitable? To which extent do they act on the structures? What are their efficiencies?
- How can innovative structures be developed/adapted which allow installations in deeper waters while maintaining low fatigue load levels and being economically competitive to floating structures? Why is the innovative concept efficient?
- How do the design parameters individually impact the design of monopiles and their engineering performance? What could be the effect of the interaction of these parameters?
- How do the design parameters influence the long term survival of the grouted joint under normal conditions? Given the computational cost of the finite element simulation, how can

the grouted joint be assessed under extreme loading taken into account the uncertainties in the variables?

1.4 Scope of the Thesis

During the design processes, a great effort has been devoted to ensure that the recommendations and guidelines given by the standards or the certification bodies are respected. The designs are checked against the general and fundamental constructability techniques and the installation procedures. Limited number of design load cases are simulated, restricting the design load basis to the cases relevant to demonstrate the methods. In fact, the goal is not to propose ready-to-be-built structures, but to demonstrate design methods. For this reason, advanced details on manufacturing processes are not considered in this thesis.

1.5 Wind Turbines Structures: Motivation of their Selection

1.5.1 Shaft: Extreme and Fatigue Loads

The shaft is typically a cylindrical/frustoconical bar (see Figure 1.4) that transmits the rotary motion of the rotor to the generator possibly through other components such as gearbox. Notwithstanding its simplicity, it is an example of wind turbine components whose design involves many stakeholders. The communication between the different parts requires the exchange of information such as loads, material properties, and geometry. For an efficient design, the loads should be exchanged such that the design can be pursued along the recommended practices with less conservatism. In fact, the largest of the maxima extreme load values are generally shared, which is not in conformity with the design practices that require considering the highest average of the peaks. They are generally presented under a format not appropriate for stress calculations, which is the design criterion. In this study, a load preparation technique is introduced that reduces the level of conservatism and is in conformity with the design guidelines.

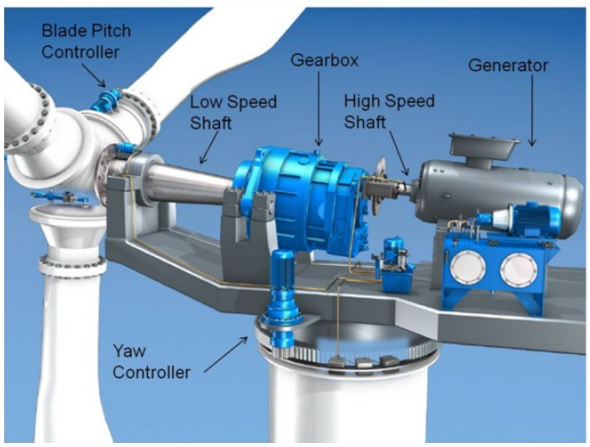

Figure 1.4: View of typical nacelle components [11].

The shaft is used as a representative nacelle component to investigate the effect of a rotor change on the structural integrity of the nacelle structures. A reference rotor is replaced by an optimized rotor developed in [12] for the purpose of minimizing the tower-bottom fore-aft damage equivalent moments while limiting the amplitude of the side-side moments. Fatigue and extreme loads are computed on the shaft for both rotors under various design load cases to assess the influence of surrounding structures on the structural integrity of a given structure.

1.5.2 Jacket Substructure: Fatigue Lifetime Improvement

The design of jacket substructure for 10 MW wind turbine has given challenges ensuring sufficient fatigue lifetime when employing the traditional design procedure [13]. Figure 1.5 depicts a typical jacket substructure. As wind turbines gain larger capacity, their larger rotors exhibit lower rotational speeds, whose multiples may coincide with the natural frequencies of the stiff jacket structures during operations and result in resonance phenomenon. Attempts for satisfactory designs under traditional design procedures have therefore generally resulted in massive substructures [13].

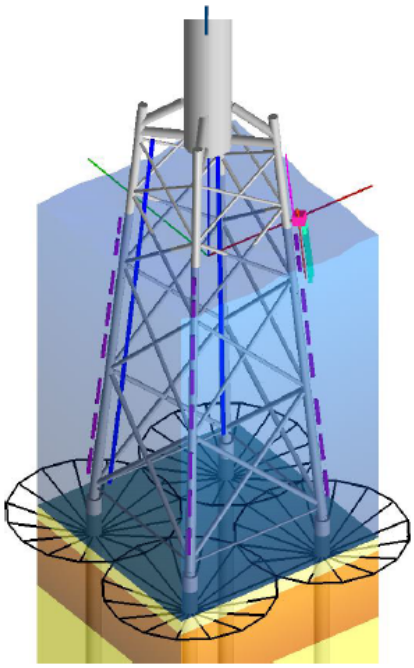

Figure 1.5: View of a typical jacket [13].

Several authors aspired for cost-efficient jacket substructures. For example, Sandal [14] and Oest *et al.* [15] proposed methodologies based on optimization with fatigue constraints. Due to the computational cost, the multiple calls of the main design function requires an uncoupled load approach, which leads to conservative substructures [16]. An alternative proposed by Natarajan *et al.* [17] consists of an optimization strategy that sets the natural frequencies of the jacket substructures away from the rotor harmonics. This solution results in lighter jacket substructures that require some welded joint re-design. Henceforth, a good insight of the welded joint design space is needed so as for the designer to propose adequate joint design. Guidance rules are established to reduce stress concentration factors (SCFs) at the joints so that relatively close-to-optimal joint design can be easily proposed at the preliminary phase, during the design procedure if done manually, or at the design update phase after an optimization process for example.

Since hotspot stresses are obtained as the product of the SCFs and the nominal stresses, their reduction can also be achieved by the dimunition of the nominal stresses. For example, passive tuned vibration absorbers (TVAs) and passive tuned mass dampers (TMDs) have been studied as load mitigation techniques for a 10 MW wind turbine in [18]. It has been shown that the TVAs are able to reduce the tower top displacement by nearly 36 % whereas TMDs succeed to reduce the sideways bending moment at the tower base by up to 25 %. However, as the turbines become larger higher mass and thereby volume is required for the TMDs and the available volume in the tower top can be found insufficient. TMDs and TVAs require integrated designs of the whole wind systems to capture the actual interaction between the components. Decoupled analyses can exhibit very low fidelity. It has been noted that these load mitigation techniques, which operate on the support structure as a whole,

affect only a narrow frequency range, which is non-optimal for a system with multiple excitation frequencies. As the wind turbine becomes larger, disturbances and changes in natural frequencies can lead to the de-tuning of the damper system: whence passive devices become non-optimal.

Semi-active magneto-rheological (MR) dampers have been proposed as an alternative to the passive systems. MR dampers can have a local effect and can be used in multiple units to accommodate various exciting frequencies. They are moderate in size and may not require extra-space. They can be put in place at the brace level, eliminating the necessity of integrated design of the couple made of the support structure and the rotor-and-nacelle assembly. These devices cannot only relatively easily be upscaled, but they can also work under various operational conditions: passive, semi-active, and active. Next sections will show the feasibility of this concept for jacket substructures as a fatigue mitigation technique.

In general, fatigue loads on a jacket result from the contributions of sea, wake turbulence, and rotor induced loadings. It is expected that the first contribution can be mitigated to some extent by the MR dampers whereas the latter two contributions can be alleviated by selecting appropriate load mitigating control algorithms and/or appropriate blade aerodynamic designs. Using the optimised rotor, this study investigates its impact on the fatigue lifetime of jacket substructures.

1.5.3 Semi-floater Substructure: Innovative Substructure System

The design of the jacket substructure, which is a typical fixed-bottom concept, has been proven to be a challenge for multi-megawatt wind turbines in 50+ m water depth. The floating substructures as categorized by Wang *et al.* [19] are attractive for deeper waters (100+ m) and may prove to be highly capital intensive at water depths near 50 m. As a merger of different current design practices, this study presents a semi-floater concept developed as a hybrid between the fixed support types and the floating ones. The objective is to achieve a cost effective solution with low fatigue damage and maintain targeted displacements at mean water level. This concept has been introduced in the oil and gas industry by Sedillot and Stevenson [20] and was conceptually adapted to large wind turbines (5 MW and 10 MW) at deep water depths (100 m and 50 m) in [21] and in [22], where a conceptual model has been used to assess loads. Herein the detailed structural design of the components of a semi-floater are developed and verified to required reliability levels as used in the wind turbine industry. The performance of the resulting design is assessed following an iterative design scheme with structural analysis of resulting stresses on the foundation and ensuring reliability and fatigue endurance. Figure 1.6 illustrates the semi-floater concept developed in this thesis.

1.5.4 Monopile Substructure: Influences of Modelling Parameters

The traditional monopile substructure (see Figure 1.7) is the most used substructure for offshore wind systems [4]. However, few investigations have been made on monopile foundations for multi-megawatt wind turbines at greater water depths (about 40 m). Sharff and Siems [23] proposed a monopile design based on parameter study for a 6 MW wind turbine at water depths between 20 m and 40 m. In this study, the buckling state of the pile shell was not explicitly discussed. Later, Sharff and Siems [24] presented a new design methodology where the buckling limit state was studied using a 3D numerical shell model.

Arany *et al.* [25] have mentioned the necessity to assess the soil limit states in case of large diameter monopiles, as the soil can fail before the structure. However, the soil models or their parameters used in these abovementionned studies are generally derived and appropriate for small diameter monopiles and may not be optimal for large ones. The recommended nonlinear soil stiffness values based on the Murchison and O'Neil's work [26] and firstly incorporated in API-RP2A-WSD [27] were developed for monopile diameters smaller than 1.00 m. It has been since shown that this method, although widely used, was improper for large diameter monopiles, see e.g. [28]. Thieken *et*

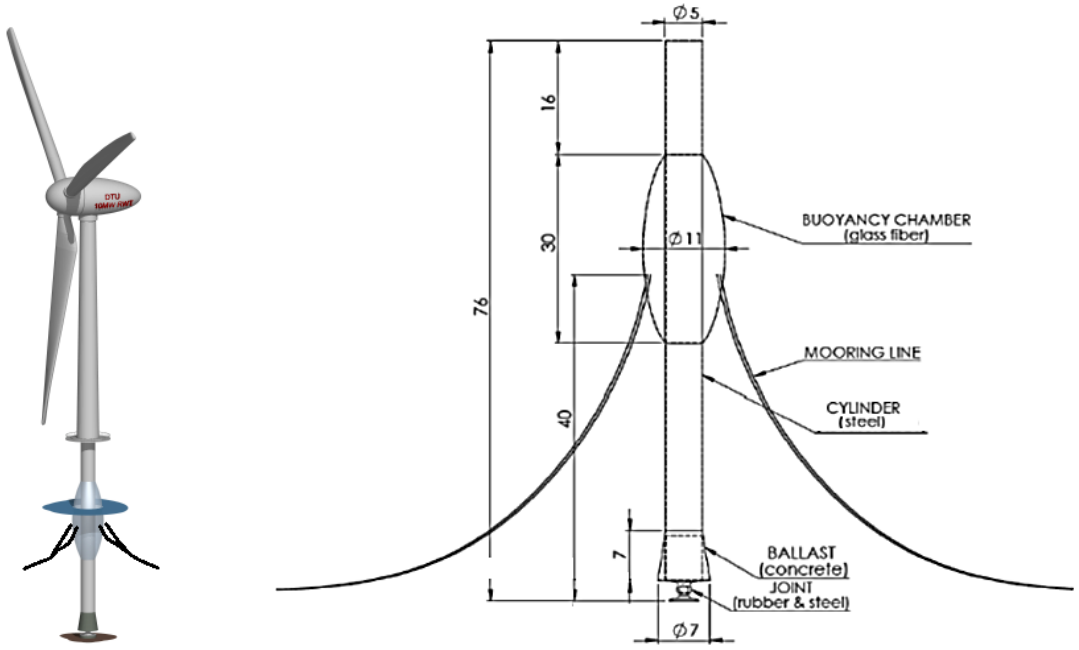

Figure 1.6: View of semi-floater. Left: full elevation view. Right: semi-floater substructure.

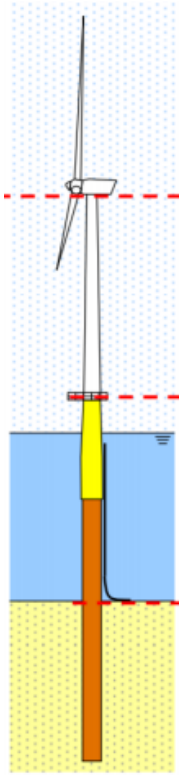

Figure 1.7: View of a typical monopile [14].

al. [28] have underlined that the standard method tends to underestimate the soil stiffness for small displacements, which is the operational domain of large monopiles, and overestimate the soil capacity. In addition, the method does not account for the soil medium continuity and proposes similar

behavior at the pile head, partway, or tip, which leads to erroneous pile deflection shapes. Therefore, an adequate soil-structure interaction model, developed by Thieken *et al.* [28], is employed for the design process in this study.

Typical design values for overall structural logarithmic decrement damping are about 6.70 % [4]. Koukoura *et al.* [29] measured a stand-still support-structure damping of approximately 12.00 % for a multi-megawatt wind turbine supported by a monopile substructure. The study concludes that significant savings could be achieved if an appropriate damping value was used in the design phase for stress calculations. These stresses are usually amplified at the welded connections mainly due to geometric imperfections as suggested by standards [30]. However, it is challenging to estimate the level of imperfections that will be actually present once the structure will be commissioned. The selection of a given geometric imperfection level with respect to the fabrication tolerance significantly impacts the result and may affect the design integrity if the construction does not ensure that the hypothesised level is respected.

Subsequent sections investigate the impact of the primary modelling choices on the design of the reference large diameter monopile. They explore models and model parameters related to soil-structure interaction, construction errors, and damping. Based on fully coupled load simulations of a conceptual 10 MW wind turbine located at 50 m water depth, several limit states are analysed - fatigue, ultimate (strength, stability, and soil capacity), and serviceability - and the effects of modelling choices are discussed.

1.5.5 Conical Grouted joint: Insight of Mechanical Behavior

Owing to the Petroleum and Gas industry experience, the connections between the transition piece and the monopile for wind turbine support structures are made by the means of grouted joints. Classically, the grouted joints for monopile substructures are built from the overlap of two cylindrical tubes: the transition piece and the pile, whose resulting annulus is filled with a high strength concrete. The grouted joints are efficient as they are easily constructible and they serve to correct the pile misalignment due to driving errors [9] as presented in Figure 1.8.

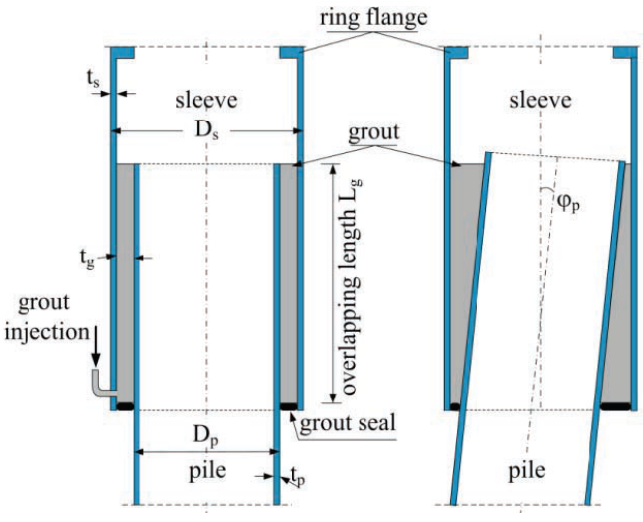

Figure 1.8: Grouted joint with plain cylindrical tubes [9].

Recent inspections of some offshore wind farms have unveiled that many grouted joints showed inadequate performance [7] due to misunderstanding of the structural mechanisms of grouted joints for wind systems. Subsequent investigations have proposed novel design methodologies [31] which do not cover large monopile diameters. Given the randomness of the metocean conditions and the

criticality of grouted joints which offer no redundancy, the mechanical behavior of grouted joints for large monopiles should be better understood. Their behavior under various limit states should be investigated in detail based on finite element model in order to identify the influence of the main design parameters.

1.5.6 Distribution of the tasks to the wind turbine structures

Each of the three research areas presented above comprises a number of tasks. which are applied to the selected wind turbine structures. Table 1.2 presents the tasks that compose each research area and links them to the structures. It can be seen that every structure is used for the implementation of several tasks.

Table 1.2: Distribution of the tasks to the wind turbine structures

Areas	Tasks	Shaft	Jacket	Semi-floater	Monopile	Grouted joint
Reduction of conservatism	Load exchange	✓				
	Coupled analysis	✓	✓	✓	✓	
	Suitable models				✓	✓
Lifetime improvement	Efficient design		✓		✓	✓
	MR Damper		✓			
	Tailored rotor	✓	✓			
	Suitable models				✓	
	Risk reduction			✓		✓
Innovative systems	Semi-floater			✓		
	MR Damper		✓			

Figure 1.9 depicts the research map used in the present thesis. Each structure is used to implement several tasks in order to carry out the corresponding areas, which in turn resolve some of the challenges contributing thereby to the achievement of the ultimate goal.

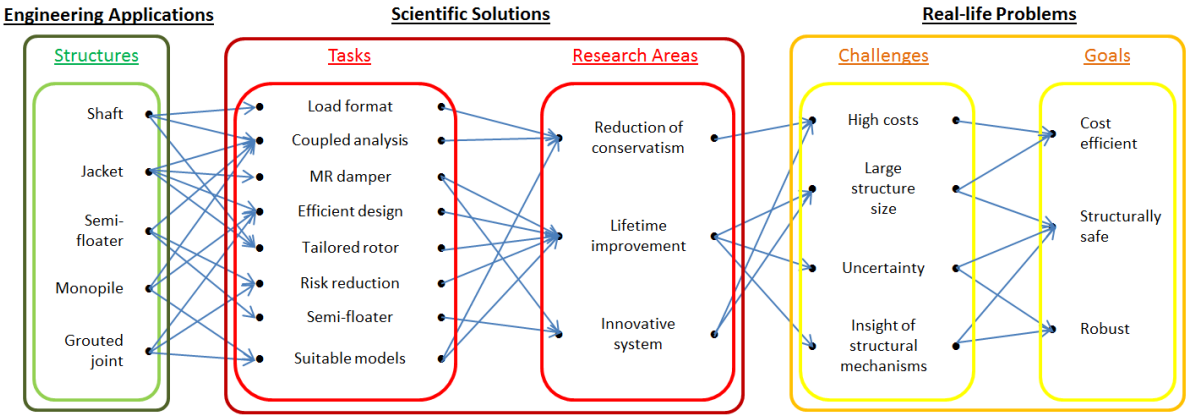

Figure 1.9: Research Map: achievement of the research goal using engineering applications.

1.6 Outline of the Thesis

The present thesis is organised in different chapters contributing to the ultimate goal.

In Chapter 2, the principal ingredients required for the design processes are presented. They encompass the environmental conditions, the reference structures, the design load cases and the dynamic analysis methods. In particular, the reference structures include two rotor designs

whose effects will be investigated in Chapters 3 and 4 on the shaft and on the support structures, respectively.

In Chapter 3, a method to evaluate the extreme loads is formulated based on the shaft study. The effect of the rotors on the shaft are studied with respect to the ultimate and fatigue limit states. The positive effect of the optimized rotor with respect to fatigue limit state will be used later as a fatigue lifetime improvement method.

In Chapter 4, three techniques for fatigue lifetime improvement are developed for jacket substructures. The fatigue lifetime improvement is achieved by actions on various levels: efficient design for joints, innovative dampers for brace, and optimized rotor for the support structure. The innovative damper is of magneto-rheological type as used in civil and automotive industries.

In Chapter 5, a second adaptation from another industry is made: the semi-floater substructure is adapted from the Oil and Gas industry and applied for wind turbines in deep waters. It is made of a monopile connecting the tower bottom to an articulated joint attached at the seabed.

In Chapter 6, an XL monopile substructure is studied. The influence of model parameters on the design of large diameter monopiles is investigated based on perturbation analyses. Attention is given to the effect of construction tolerances, damping, and soil models on a monopile design assumed to be rigidly connected to the transition piece.

In Chapter 7, a detailed probabilistic design is developed using the grouted joint for large diameter monopiles, as the actual connection between the monopile and the transition piece. Probabilistic study is carried out under extreme loading and the long term behaviour of the joint under normal conditions is investigated based on finite element analysis.

In Chapter 8, a comparative analysis examines the similarities and dissimilarities of the jacket, semi-floater, and monopile substructures. Guidance rules are provided to help designers to select the substructure which suits best to their projects.

Finally, conclusions and recommendations on probabilistic design of multi-megawatt wind turbine structures at deep waters are given.

2

Definition of the Design Parameter Sets

A well-made salad must have a
certain uniformity;
it should make perfect sense for
those ingredients to share a bowl.

Yotam Ottolenghi

2.1 Environmental Conditions

2.1.1 Wind Conditions

Throughout this study, structures are considered to be located in the Dutch North Sea at 53°13’04.0" N; 3°13’13.0" E [32], as depicted in Figure 2.1.

Figure 2.1: Site location (Source: Google Maps). The North direction points downwards.

The atmospheric conditions are adapted from Ref [13]. The operational wind speeds range from 4 m/s to 25 m/s and are subdivided into 11 wind speed bins of 2 m/s width each. Each wind speed

bin is associated to turbulence intensities that prevail during either normal or extreme conditions (see Table 2.1). Storm case is modelled with mean wind speed of 42.73 m/s and turbulence intensity of 11.00 %.

The wind speed parameter follows a Rayleigh distribution with 9.25 scale parameter as shown in Figure 2.2 [13]. The wind rose shown in Figure 2.3 represents the distribution of the wind direction at the selected site [32].

Table 2.1: Atmospheric conditions [13]

Mean wind speed [m/s]	Normal turbulence intensity [%]	Extreme turbulence intensity [%]
5	18.95	43.85
7	16.75	33.30
9	15.60	27.43
11	14.90	23.70
13	14.40	21.12
15	14.05	19.23
17	13.75	17.78
19	13.50	16.63
21	13.35	15.71
23	13.20	14.94
25	13.00	14.30

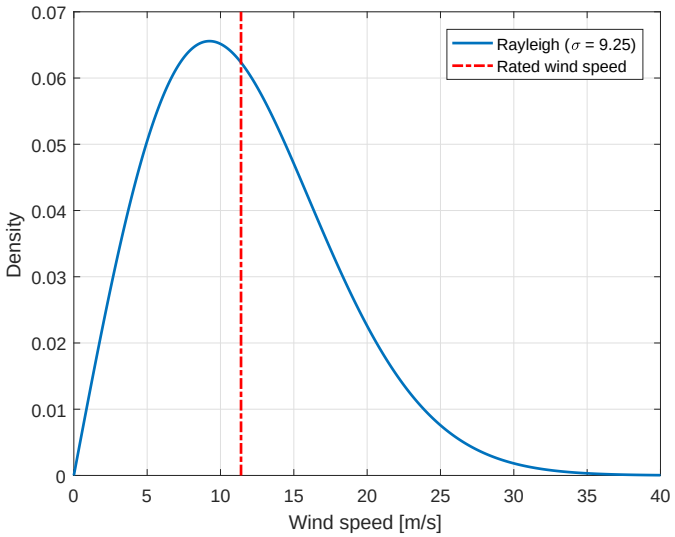

Figure 2.2: Rayleigh distribution modelling the wind speed distribution at the site [13]. The red line indicates he rated wind speed of the turbines used in this thesis.

2.1.2 Sea Data

The sea states are given in dependence on the atmospheric conditions. The significant wave height and the peak period are conditional on the mean wind speed, as tabulated in Table 2.2 [13]. The wave height is modelled based on either the JONSWAP spectrum [33] (under extreme turbulence conditions or extreme wind conditions) or the Pierson-Moskowitz spectrum [33] (under normal turbulence) at the expected value of the sea state characteristics conditional on the mean wind speed.

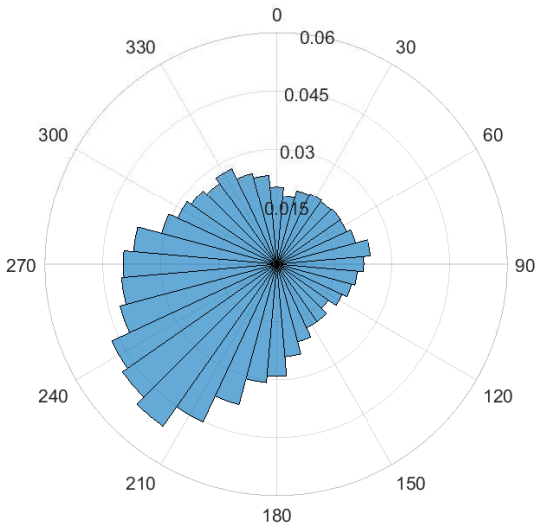

Figure 2.3: Wind direction on the site [32]. The North direction is aligned to 0°

The Pierson-Moskowitz type is used for fatigue load case simulations because of its wide-band energy distribution. The JONSWAP type is suitable for ultimate load cases due to its peaked shape which can promote resonance if the peak coincides with the natural frequencies of the structure.

The water depth is typically 50 m for all case studies except for the study of the grouted joint where it is 26 m. The normal sea current is 0.6 m/s and the extreme sea current is 1.2 m/s, all of parabolic type. Marine growth is present from the mean sea level to the seabed with a thickness of 100 mm in accordance with API RP 2A-WSD [27]. The submerged density of the marine growth is taken as 373 kg/m^3.

Table 2.2: Sea states conditional to mean wind speed [13]

Mean wind speed [m/s]	Significant wave height, Hs [m]	Peak period, Tp [s]
5	1.140	5.820
7	1.245	5.715
9	1.395	5.705
11	1.590	5.810
13	1.805	5.975
15	2.050	6.220
17	2.330	6.540
19	2.615	6.850
21	2.925	7.195
23	3.255	7.600
25	3.600	7.950
42.73	9.400	13.700

2.1.3 Soil Parameters

As in the case of the meteocean data, the soil parameters are also adapted from Ref [13]. The soil is composed of superimposed sandy layers with submerged density varying between 9.00 kN/m^3 and 11.00 kN/m^3, as shown in Table 2.3.

Table 2.3: Soil properties

Depth range [m]	0.0 – 15.0	15.0 – 20.0	20.0 – 22.5	22.5 – 90.0
Angle of internal friction [°]	35.0	37.5	40.0	40.0
Poisson's ratio [-]	0.250	0.225	0.200	0.200
Void ratio [-]	0.69	0.65	0.60	0.57
Submerged unit weight [kN/m^3]	9.76	10.00	10.50	11.00

2.2 Wind Turbines

In this section, two wind turbines are introduced. They have rated powers of 10 MW and 20 MW, respectively. For the wind turbine of 10 MW, two rotor designs are presented.

2.2.1 DTU 10 MW RWT

The reference turbine used in this study is the generic 10 MW reference wind turbine developed by the Department of Wind Energy of the Technical University of Denmark (DTU 10 MW RWT) [34]. The turbine is a variable-speed, pitch-controlled, direct drive machine. Its key design parameters are presented in Table 2.4. The details of the native rotor associated to the DTU 10 MW RWT are presented in [34]. This rotor is denoted 'reference rotor'.

Table 2.4: Key parameters of the DTU 10 MW RWT [34]

Parameters	Values
Wind regime	(See Table 2.1)
Rotor type, orientation	3 bladed - Clockwise rotation - Upwind
Control	Variable speed - Collective pitch
Cut-in, rated, cut-out wind speeds	4 m/s, 11.4 m/s, 25 m/s
Rated power	10 MW
Rotor, hub diameters	178.3 m, 5.6 m
Hub height	119.0 m
Drive train	Medium speed, Multiple-stage gearbox
Minimum, maximum rotor speeds	6.0 rpm, 9.6 rpm
Maximum generator speed	480.0 rpm
Gearbox ratio	50
Maximum tip speed	90.0 m/s
Hub overhang	7.1 m
Shaft tilt, coning angle	5.0°, -2.5°
Blade prebend	3.3 m
Rotor mass including hub	227,962 kg
Nacelle mass	446,036 kg
Tower mass	628,442 kg

2.2.2 Aero-Elastically Tailored Rotor for the DTU 10 MW RWT

An aero-elastically tailored rotor [12], called 'optimized rotor', has been designed with the aim of reducing the fatigue loads at the tower bottom. For the optimization problem, the objective function combines the tower bottom fore-aft damage equivalent load and the blade first mass moment with respect to its root:

$$f(\{\mathbf{x_p},\mathbf{x_s}\},\mathbf{p},w) = (1-w)\frac{M_m(\{\mathbf{x_p},\mathbf{x_s}\},\mathbf{p})}{M_m(\{\mathbf{0},\mathbf{0}\},\mathbf{p})} + w\frac{DEL(\{\mathbf{x_p},\mathbf{x_s}\},\mathbf{p})}{DEL(\{\mathbf{0},\mathbf{0}\},\mathbf{p})} \tag{2.1}$$

where

f	:	is the objective function
$\mathbf{x_p}$	:	is the set planform variables
$\mathbf{x_s}$	:	is the set of structural variables
$\mathbf{p}$	:	is the set of constant parameters describing the DTU 10 MW RWT
w	:	is a weight factor defining toward which addend the objective is biased
$M_m(\{\mathbf{0},\mathbf{0}\},\mathbf{p})$	:	is the reference blade mass moment
$DEL(\{\mathbf{0},\mathbf{0}\},\mathbf{p})$	:	is the reference tower bottom fore-aft damage equivalent load

The constraints include criteria related to the planform, to the geometry, to the material strength, and to the aero-elasticity. Reference is made to [12] for further details. As a result, both rotors share the same profile coefficients, thickness-chord ratios, and radius. The optimized rotor is 4 % heavier than the reference one. They also differ with the layups (Figure 2.4), structural components (Figure 2.5), and planform (Figures 2.6 and 2.7).

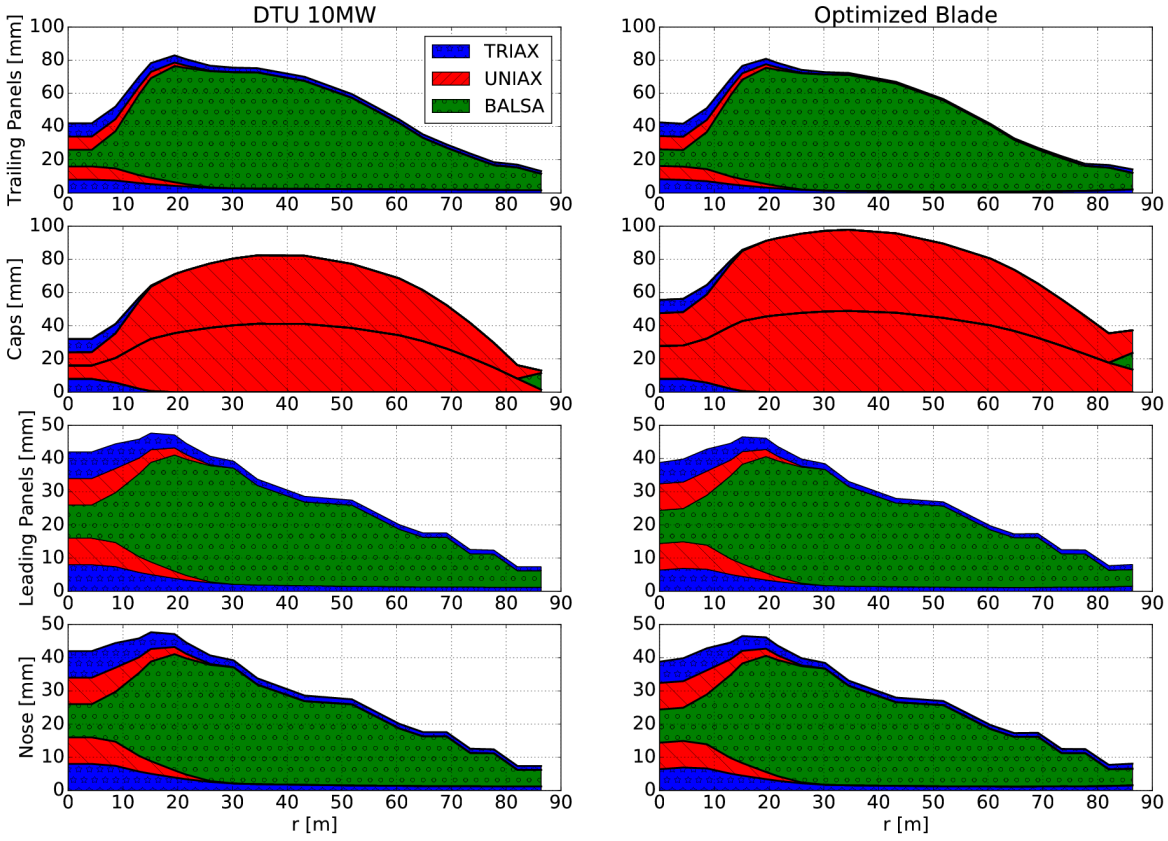

Figure 2.4: Comparison between the baseline blade layups (left) and optimized blade layups (right). [12]

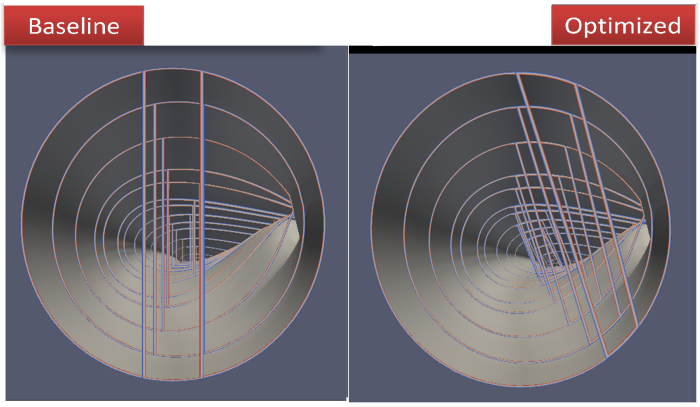

Figure 2.5: Close up to highlight the location of the caps. [12]

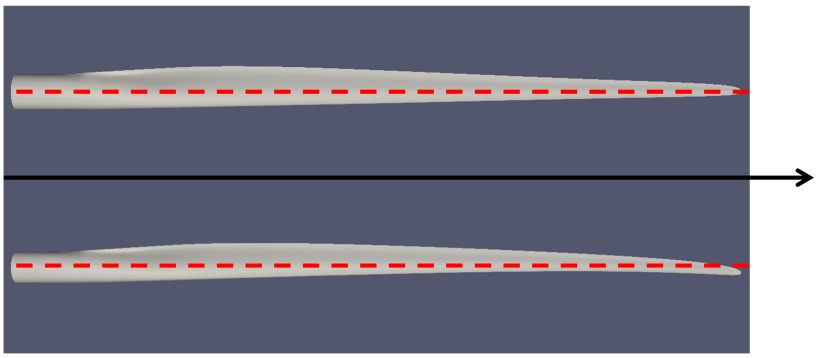

Figure 2.6: Comparison between the blade longitudinal shapes. The top sketch corresponds to the reference blade and the bottom sketch to the optimized one. Red dashed lines represent the pitch axis) [12].

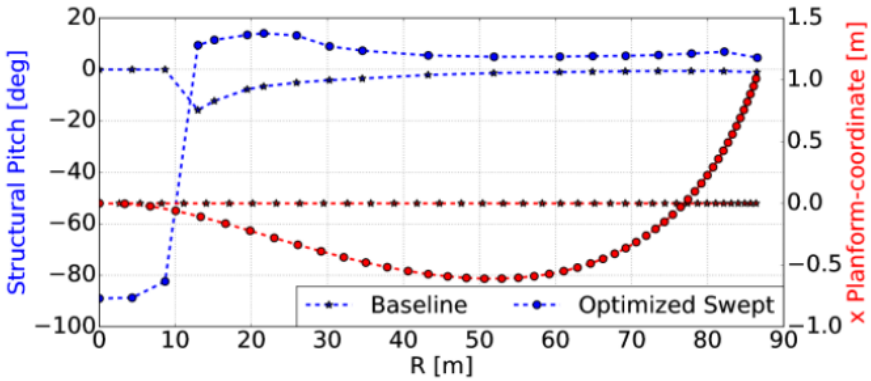

Figure 2.7: Comparison between the blade longitudinal geometries. Blue dashed lines represent the structural pitch axis, while the red ones is the x-coordinate of the centreline. [12]

2.2.3 INNWIND 20 MW RWT

The DTU 10 MW RWT has been upscaled to obtain a version of 20 MW rated power, denoted INNWIND 20 MW RWT, within the European project INNWIND.EU [35]. The up-scaling factor has been determined to be 1.414. Controller parameters of the upscaled model have been tuned to guarantee suitable performance. The key parameters of the INNWIND 20 MW RWT are given in Table 2.5.

Table 2.5: Key parameters of the INNWIND 20 MW RWT [35]

Parameters	Values
Wind regime	(See Table 2.1)
Rotor type, orientation	3 bladed - Clockwise rotation - Upwind
Control	Variable speed - Collective pitch
Cut-in, rated, cut-out wind speeds	4 m/s, 11.4 m/s, 25 m/s
Rated power	20 MW
Rotor, hub diameters	252.2 m, 7.9 m
Hub height	167.9 m
Drive train	Medium speed, Multiple-stage gearbox
Minimum, maximum rotor speeds	4.45 rpm, 7.13 rpm
Maximum generator speed	339.4 rpm
Gearbox ratio	47.6
Maximum tip speed	90.0 m/s
Hub overhang	10.0 m
Shaft tilt, coning angle	5.0°, -2.5°
Blade prebend	4.7 m
Rotor mass including hub	632,016 kg
Nacelle mass	1,098,270 kg
Tower mass	1,141,067 kg

2.3 Jacket Substructures

2.3.1 INNWIND Jacket Substructure for 10 MW Turbine

Designed as a substructure for the DTU 10 MW RWT with the native rotor, a jacket substructure, denoted INNWIND 10 MW Jacket, has been developed within the INNWIND project [13]. The jacket is prepared for 50 m water depth and is made of four legs and four X-brace levels. Figure 2.8 depicts the primary layout of the INNWIND 10 MW Jacket. Its main characteristics are tabulated in Table 2.6.

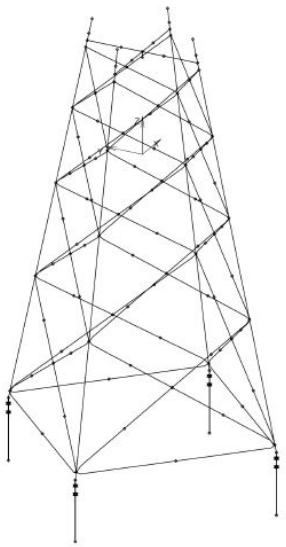

Figure 2.8: INNWIND 10 MW Jacket substructure topology [13]

When it is necessary, the INNWIND 10 MW Jacket has been modelled as a superelement at the tower bottom located at 26 m above the mean sea level. The superelement matrices (stiffness, mass, and damping) have been determined by Ref [13] and given in Appendix A.

Table 2.6: Main Characteristics of the INNWIND 10 MW Jacket [13]

Parameters	Values
Jacket general	
Base width	34.0 m
Top width	14.0 m
Interface elevation	26 m above mean sea level
Transition piece height	9.00 m
Number of horizontal braces	4 mudbraces
Legs	
Number of legs	4 legs
Batter angle	12.2°
Outer diameter	1400 mm
Maximum wall thickness	120 mm
Minimum wall thickness	42 mm
X-braces	
Maximum upper x-brace outer diameter	900 mm
Maximum upper x-brace wall thickness	50 mm
Maximum middle-upper x-brace outer diameter	876 mm
Maximum middle-upper x-brace wall thickness	38 mm
Maximum middle-lower x-brace outer diameter	968 mm
Maximum middle-lower x-brace wall thickness	34 mm
Maximum lower x-brace outer diameter	1088 mm
Maximum lower x-brace wall thickness	44 mm
Natural frequency	
1^{st} eigenfrequency (1^{st} bending mode)	0.287 Hz

2.3.2 DTU Jacket Substructure for 10 MW Turbine

Another jacket substructure has been designed by DTU to support the DTU 10 MW RWT [36] with the reference rotor and is called 'DTU 10 MW Jacket'. This innovative jacket results from an optimization process whose objective is the minimization of the first natural frequencies of the support structure in order to avoid the rotor harmonics. The general topology of the DTU 10 MW Jacket is similar to that of the INNWIND 10 MW Jacket. However, they differ by the respective sizes of their members. The main characteristics of the DTU 10 MW Jacket is given in Table 2.7.

2.3.3 DTU Jacket Substructure for 20 MW Turbine

In order to support the INNWIND 20 MW RWT, a corresponding jacket substructure named 'DTU 20 MW Jacket' has been prepared as resulting from the upscaling of the DTU 10 MW Jacket. The member sizes and the planar node coordinates have been multiplied by a typical scaling factor. The node altitudes have been kept unchanged since the water depth is the same. Starting with the value 1.414 as for the turbine, the scaling factor has been iteratively sought to ensure the integrity at strength limit state. Iterations have resulted in the sufficient scaling factor of about 1.32, which is not optimal but appropriate to satisfy the strength limit state. The resulting main characteristics are given in Table 2.8.

Table 2.7: Main Characteristics of the DTU 10 MW Jacket [36]

Parameters	Values
Jacket general	
Base width	16.97 m
Top width	10.25 m
Interface elevation	26 m above mean sea level
Transition piece height	10.00 m
Number of horizontal braces	4 mudbraces
Legs	
Number of legs	4 legs
Outer diameter (upper/lower leg)	700.0/742.5 mm
Maximum wall thickness	74.0 mm
Minimum wall thickness	49.3 mm
X-braces	
Maximum upper x-brace outer diameter	690.0 mm
Maximum upper x-brace wall thickness	80.0 mm
Maximum middle-upper x-brace outer diameter	699.6 mm
Maximum middle-upper x-brace wall thickness	99.8 mm
Maximum middle-lower x-brace outer diameter	541.2 mm
Maximum middle-lower x-brace wall thickness	20.6 mm
Maximum lower x-brace outer diameter	567.0 mm
Maximum lower x-brace wall thickness	22.0 mm
Natural frequency	
1^{st} eigenfrequency (1^{st} bending mode)	0.2267 Hz

2.4 Design Load Cases

The verification of the structural integrity of the wind turbines components is carried out under various design load cases (DLCs) as recommended by standards such as IEC 61400-1 Ed. 3 [37], DNV-OS-J101 [38], or Germanischer Lloyd [39]. Relevant DLCs are selected in this study depending on the case study, which include:

DLC 1.1 *(Ultimate limit state)* is a load case primary used for the prediction of extreme loads on the rotor and nacelle assembly (RNA) with return period of 50 years. The extreme loads are generally obtained from statistical extrapolation of normal operational loads or determined as the multiples of their extreme values;

DLC 1.2 *(Fatigue limit state)* is a load case associated with wind speeds in the operational range with normal turbulence model and normal sea states. For this design load case, the 11 mean wind speeds are considered with several (generally six) wind turbulence seeds each, directed with 0° or ±10° yaw error, and misaligned to the Pierson-Moskowitz type waves by 0° or ±10°. This metocean condition occurs 7806 hours each year [13];

DLC 1.3 *(Ultimate limit state)* is a load case considering normal operations with extreme turbulence but normal sea states. Six wind seeds for each of the 11 wind speed bins are simulated, all assuming zero yaw error. The waves of JONSWAP type are aligned along the wind direction;

DLC 1.4 *(Ultimate limit state)* is associated to extreme coherent gust with wind direction change. Three scenarios related to 9 m/s, 11 m/s, and 13 m/s, respectively are simulated;

Table 2.8: Main Characteristics of the DTU 20 MW Jacket

Parameters	Values
Jacket general	
Base width	22.39 m
Top width	13.53 m
Interface elevation	26 m above mean sea level
Transition piece height	10.00 m
Number of horizontal braces	4 mudbraces
Legs	
Number of legs	4 legs
Outer diameter (upper/lower leg)	905.8/979.6 mm
Maximum wall thickness	97.6 mm
Minimum wall thickness	60.7 mm
X-braces	
Maximum upper x-brace outer diameter	712.4 mm
Maximum upper x-brace wall thickness	26.4 mm
Maximum middle-upper x-brace outer diameter	923.1 mm
Maximum middle-upper x-brace wall thickness	131.7 mm
Maximum middle-lower x-brace outer diameter	714.0 mm
Maximum middle-lower x-brace wall thickness	27.2 mm
Maximum lower x-brace outer diameter	712.4 mm
Maximum lower x-brace wall thickness	26.4 mm
Natural frequency	
1^{st} eigenfrequency (1^{st} bending mode)	0.1841 Hz

DLC 1.5 *(Ultimate limit state)* is associated to extreme wind shear situation in conjunction of the 11 mean wind speeds;

DLC 2.3 *(Ultimate limit state)* is associated to extreme operating gust coupled with external or internal electrical fault including loss of electrical network connection;

DLC 3.1 *(Fatigue limit state)* represents the start-up of the turbine. Three mean wind speeds are considered with no yaw error during 250 s: 4 m/s, 11 m/s, and 25 m/s. The Germanischer Lloyd guidelines [39] recommends considering for each year 1500, 50, and 50 start-up procedures at cut-in, rated, and cut-out wind speeds, respectively;

DLC 4.1 *(Fatigue limit state)* simulates the normal shut-down. It is modelled for 100 s with the mean wind speeds 4 m/s, 11 m/s, and 25 m/s. The Germanischer Lloyd guidelines [39] recommends considering for each year 1500, 50, and 50 normal shut-down procedures at cut-in, rated, and cut-out wind speeds, respectively;

DLC 5.1 *(Ultimate limit state)* is a load case arising from emergency shut down. The mean wind speeds 9 m/s, 11 m/s, 13 m/s, and 25 m/s are simulated during 100 s each with no yaw error;

DLC 6.2a *(Ultimate limit state)* is a load case resulting from turbulent extreme wind under storm conditions with extreme sea states, coupled with loss of electrical power. The storm wind is applied along 24 directions: from 0° to 345° in 15° steps. An irregular JONSWAP wave type is directed along the wind direction with 0° or $\pm$30° yaw error. With no active controller, the structure is also loaded with an extreme sea current (1.2 m/s) of parabolic type at 0°. The blades are pitched to an angle of about 90° with no dynamic induction;

DLC 6.4 *(Fatigue limit state)* is a load case corresponding to parked rotor situation with mean wind speeds up to 0.7 times the reference wind speed coupled with yaw errors. It is assumed that this load case occurs 913.57 hours per year;

DLC 7.2 *(Fatigue limit state)* simulates the situation of parked turbine with locked rotor and mean wind speed of 21 m/s for 11.0 % turbulence intensity. The sea state matches the corresponding entries in Table 2.2. The applied mean wind speed is considered with six wind turbulence seeds each, directed along 24 directions: from 0° to 345° in 15° steps, and is misaligned to the Pierson-Moskowitz type waves by 0° or ±10°. DLC 7.2 is only employed in Chapter 6 is assumed to occur 250 hours per year.

2.5 Dynamic Analysis

The dynamic analyses for load assessment are carried out in the aero-servo-hydro-elastic tool HAWC2 (Horizontal Axis Wind turbine simulation Code 2nd generation) [40] with defined boundary conditions. HAWC2 utilizes a multibody formulation which couples different elastic bodies together. Bodies are composed of Timoshenko beam [41] finite elements whereby their stiffness, mass, and damping are assembled into the governing equations of motion, whose solution is obtained using the Newmark-β method [42] in time domain. The damping coefficients are adjusted using Rayleigh coefficients to obtain desired damping levels for the global structure.

The unsteady aerodynamics between the rotor and the wind is described with the blade element momentum theory supplemented with Beddoes-Leishman type dynamic stall model and dynamic inflow [43]. The wind is modelled as a turbulent wind field defined for each mean wind speed and a turbulence intensity using the Mann model [44].

The hydrodynamic loads resulting from the interactions between the sea water and the structure are computed using the Morison's equation [45]. For a unit length of cylinder, the hydrodynamic force normal to its axis is calculated as:

$$F = \frac{1}{2}\rho_w D\, C_D\, (u_w + u_c - u_s)\, |u_w + u_c - u_s| + \rho_w C_a \frac{\pi D^2}{4}\, (\dot{u}_w - \dot{u}_s) + \rho_w \frac{\pi D^2}{4} \dot{u}_w \qquad (2.2)$$

where

$D\ [m]$	:	cylinder's outer diameter
$u_c\ [m/s]$	:	current speed
$u_w\ [m/s]$	:	wave particle speed normal to the cylinder's axis
$u_s\ [m/s]$	:	moving cylinder velocity
$\dot{u}_w\ [m/s^2]$	:	wave particle acceleration normal to the cylinder's axis
$\dot{u}_s\ [m/s^2]$	:	moving cylinder acceleration
$\rho_w = 1025\ kg/m^3$	:	water mass density
$C_D\ [-]$	:	equivalent drag coefficient
$C_a\ [-]$	:	added mass coefficient

The soil-structure interactions are modelled in dependence on the foundation type. For jacket substructures, the leg are assumed fully restrained at the seabed. Details will be given for other cases in appropriate sections. Amongst other possible results, the structural responses, which includes time series of translations and rotations, internal forces and moments, are determined at several locations where requested for.

3

Determinants of Design Loads for Wind Turbine Structures: Main Shaft Design Loads

I like to talk about food, ingredients, and how to adapt recipes.

Yotam Ottolenghi

3.1 Introduction

The shaft is typically a cylindrical/frustoconical bar that transmits the rotary motion of the rotor to the generator possibly through other components such as gearbox (see Figure 3.1). It is a part of the main load carrying structure, and failure will lead to loss of structural integrity with potential loss of the turbine - so failure is very undesirable. Also repairs are difficult as dismounting most probably requires taking the rotor down, which should be avoided. Moreover, its simplicity does not expect any significant technology improvement over the turbine lifetime so it is very unlikely to be replaced more frequently than other components.

On contrary, surrounding components are more subjected to replacement due to several possible causes. The causes can be (i) component deterioration; (ii) improved technology for better efficiency; and (iii) necessity to adapt to a change of design parameter sets. For example, after damages had occurred on the reference rotor, the optimized rotor can be used as substitute. With this replacement, the turbine owner ensures the continuation of the operations and benefits from the improved technology that offers the optimized rotor.

As the shaft fabrication is often done by a third-party company, its design requires communication between the different parties, namely for the exchange of design loads. The objectives of this chapter are (1) to introduce a method of preparation for design loads suitable for exchange that is in line with the standard and reduces the conservatism level; and (2) to investigate how the interaction between structures in the same turbines can affect their safety by assessing the structural integrity of the shaft in case of rotor replacement.

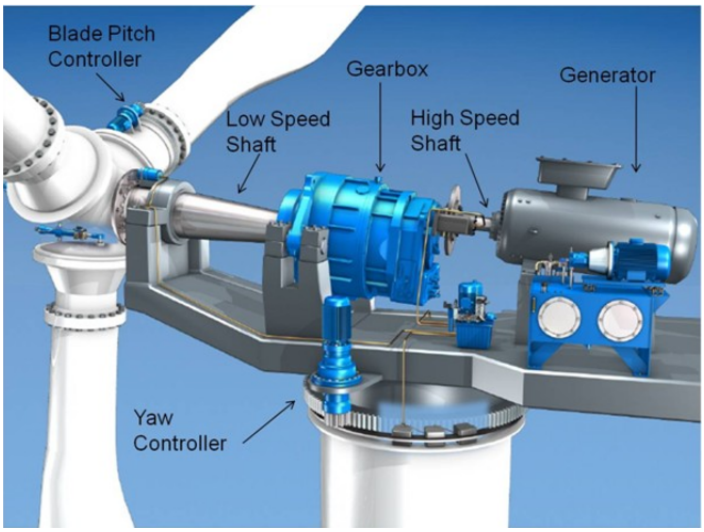

Figure 3.1: Nacelle components. [11]

3.2 Equivalent loads: Resulting and Corresponding Loads

A coordinate system can be associated to a given circular cross-section as depicted in Figure 3.2. The load Cartesian components, which include axial force, N, shear forces, Q_1 and Q_2, bending moments, M_1 and M_2, and torsional moment, T, as typically obtained from dynamic analysis, are represented in this figure.

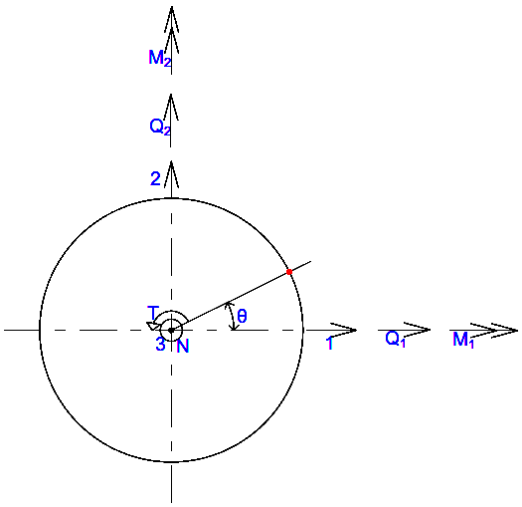

Figure 3.2: Coordinate system associated to circular cross-section.

For the fatigue limit state, fatigue-damage-equivalent zero-mean load ranges (DELs) are generally computed from the time series of each load components. For the time series of a generic non-zero-mean load component L, the dependence of the fatigue load amplitude L_A on the mean load L_m is approximated by: $L_A(L_m) = L_A(0) - M\ L_m$ [33], with the mean load sensitivity M calibrated for each metallic material. It can be shown that the resulting DEL, $\overline{\Delta L}_{eq}$ can be written [33]:

$$\overline{\Delta L}_{eq} = \left(\frac{1}{N_{eq}} \sum_{V=V_{in}}^{V_{out}} \frac{p(V)}{T_{sim}} \sum_{i=1}^{n} \left(\Delta L_i(V) + 2\ M\ L_{mi}(V) \right)^m \right)^{(1/m)} \tag{3.1}$$

where

V	:	mean wind speed
$p(V)$	:	number of occurrence hours for each time series of the mean wind speed V
T_{sim}	:	simulation duration of the time series
ΔL_i	:	range of load cycle i obtained from rainflow counting
L_{mi}	:	mean of load cycle i obtained from rainflow counting
M	:	fatigue strength mean stress (or load) sensitivity
m	:	Wöhler exponent
n	:	total number of load cycles in the given time series
V_{in}, V_{out}	:	mean wind speed bounds
N_{eq}	:	equivalent number of cycles. When N_{eq} equals the component's lifetime in seconds, the computed damage equivalent load range has 1 Hz frequency.

The computation of the DELs of individual components misses the superposition of loads or their effects that actually exists in the structure. A possible alternative is to compute the DEL of resultant loads. Instead of computing $\Delta M_{1,eq}$ and $\Delta M_{2,eq}$ separately, one can compute $\Delta M_{res,eq}$, where $M_{res} = \sqrt{M_1^2 + M_2^2}$. With the direction of the resultant constantly changing, the hotspot or structural point of interest is not always the same. These observations call for a methodology that holds a fixed hotspot and accounts for the load superposition.

Similarly, the extreme loads are generally presented in a table like the one depicted by Figure 3.3. Although this method combines loads, it takes the *maximum maximorum* value of this combination, which is too conservative with regard to the design guidelines. The design guidelines recommend employing the highest value of the averages of the maxima obtained for various seeds of the same mean wind speed.

		Load case	γ_F [–]	F_x [MN]	F_y [MN]	F_z [MN]	F_{res} [MN]	M_x [MNm]	M_y [MNm]	M_z [MNm]	M_{res} [Nm]
F_x	max	dlc1.3	1.35	0.9155	0.8241	1.7060	1.2318	-19.4659	26.0434	0.2850	32.5143
	min	dlc1.3	1.35	-0.8371	0.0019	1.7420	0.8371	1.9130	-27.2759	-0.6774	27.3429
F_y	max	dlc1.3	1.35	0.7025	1.6879	1.3008	1.8282	-61.9121	18.6724	0.1983	64.6666
	min	dlc6.2	1.1	0.0646	-1.4296	0.2524	1.4311	48.9713	5.2403	0.6872	49.2509
F_z	max	dlc2.1	1.35	-0.1241	-0.0987	2.8841	0.1586	8.3027	-1.1409	-0.2991	8.3807
	min	dlc6.2	1.1	-0.0294	-0.5627	-0.8436	0.5635	30.8746	-1.2720	0.2912	30.9008
F_{res}	max	dlc1.3	1.35	0.8374	1.6646	1.6515	1.8633	-50.4330	23.9342	0.2973	55.8241
M_x	max	dlc6.2	1.1	0.0646	-1.4296	0.2524	1.4311	48.9713	5.2403	0.6872	49.2509
	min	dlc1.3	1.35	0.1689	1.4054	1.0211	1.4155	-65.6709	8.4290	0.4223	66.2096
M_y	max	dlc2.1	1.35	0.8556	0.0672	1.6054	0.8582	12.8450	29.6236	0.6948	32.2886
	min	dlc1.3	1.35	-0.8371	0.0019	1.7420	0.8371	1.9130	-27.2759	-0.6774	27.3429
M_z	max	dlc2.3	1.1	0.7082	-0.4000	1.7072	0.8133	28.2533	25.3360	1.0627	37.9495
	min	dlc2.1	1.35	-0.2554	-0.0295	0.5137	0.2571	-0.0104	-10.2805	-1.2084	10.2805
M_{res}	max	dlc1.3	1.35	0.1689	1.4054	1.0211	1.4155	-65.6709	8.4290	0.4223	66.2096

Figure 3.3: Example of table presenting the extreme loads [40].

Contemporary design formats are based on stress: the corresponding design loads should therefore be established under stress basis. The nominal stresses engendered in a typical circular section due to forces and moments are given by:

$$\sigma(\theta) = \frac{N}{A} + \frac{M_1}{I/R}\sin\theta - \frac{M_2}{I/R}\cos\theta \tag{3.2}$$

$$\tau(\theta) = \begin{cases} \left| \frac{T}{2\pi t R^2} - \frac{2Q_1}{A}\sin\theta + \frac{2Q_2}{A}\cos\theta \right| & \text{If thin-wall circular tube} \\ \left| \frac{2T}{\pi R^3} - \frac{4Q_1}{3\pi R^2}\cos^2\theta + \frac{4Q_2}{3\pi R^2}\sin^2\theta \right| & \text{If solid circular section} \end{cases} \tag{3.3}$$

where

N	:	axial force
M_1, M_2	:	bending moments about axes 1 and 2, respectively
T	:	torsional moment
Q_1, Q_2	:	shear forces along axes 1 and 2, respectively
A	:	section's area
I	:	section's second moment of area
R	:	outer radius
t	:	wall thickness
θ	:	circumferential coordinate, measured from axis 1
σ	:	axial stress
τ	:	shear stress

From Equations 3.2 and 3.3, the corresponding nominal loads are defined as per Equations 3.4 – 3.7. The corresponding nominal loads are determined for circumferential coordinates around the shaft. So, they fulfill the requirements stated above: combining load components at a given circumferential coordinate taken as hotspot. They are utilized for DEL calculation and for the extreme load determination. The combination of N_{Corr} and M_{Corr} on the one hand and of T_{Corr} and Q_{Corr} on the other hand can be done if cross section geometry is known, but it will result in stresses no longer in loads.

$$\text{Axial force} \quad N_{Corr}(\theta) = N \tag{3.4}$$

$$\text{Shear force} \quad Q_{Corr}(\theta) = \begin{cases} -Q_1\sin\theta + Q_2\cos\theta & \text{If thin-wall circular tube} \\ -Q_1\cos^2\theta + Q_2\sin^2\theta & \text{If solid circular section} \end{cases} \tag{3.5}$$

$$\text{Bending moment} \quad M_{Corr}(\theta) = M_1\sin\theta - M_2\cos\theta \tag{3.6}$$

$$\text{Torsional moment} \quad T_{Corr}(\theta) = T \tag{3.7}$$

3.3 Loads for Fatigue Limit State

Examples of individual component fatigue loads and their transformation to corresponding loads are given in Figure 3.4. The left column of this figure shows a 50 s excerpt of the 10 min time series of all six individual loads produced at 11 m/s mean wind speed for the reference rotor case. The corresponding loads of these time series are presented in the right hand side of the figure for various circumferential coordinates.

The main shaft is assumed to be solid-circular-section type made of hardened and tempered alloy steels and is stress-relieved after treatment [46]. Veldkamp [33] reported that for such materials, the fatigue strength mean load sensitivity, M, is between 0.33 and 0.40. The value of 0.35 is taken in this study. From test results, Rafsanjani and Sørensen [47] obtained an expected value of about 10 for Wöhler exponent of cast steel. With these values, Markov matrices and load duration diagram (LDD) are prepared using rainflow counting analysis for each corresponding component (see Equations 3.4 – 3.7), which are illustrated by Figures 3.5 – 3.8 for DLC 1.2. Similar results are prepared for all selected DLCs related to fatigue limit state, but not presented here for brevity.

The spectra present significant variation with mean and amplitude. Although the spectra look alike within each pair, a numerical index, which accounts for the means and amplitudes, should

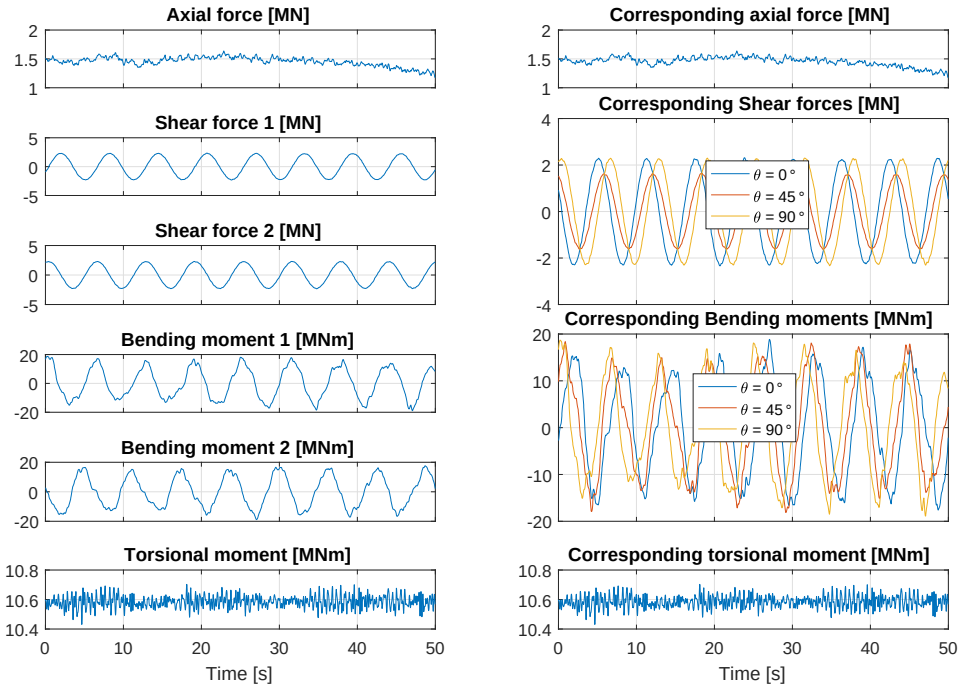

Figure 3.4: Fatigue load time series generated at 11 m/s mean wind speed under normal turbulence conditions (DLC 1.2) for the reference rotor case. An excerpt of 50 s out of 600 s is shown to illustrated the details. Raw component loads (left) and corresponding nominal loads (right).

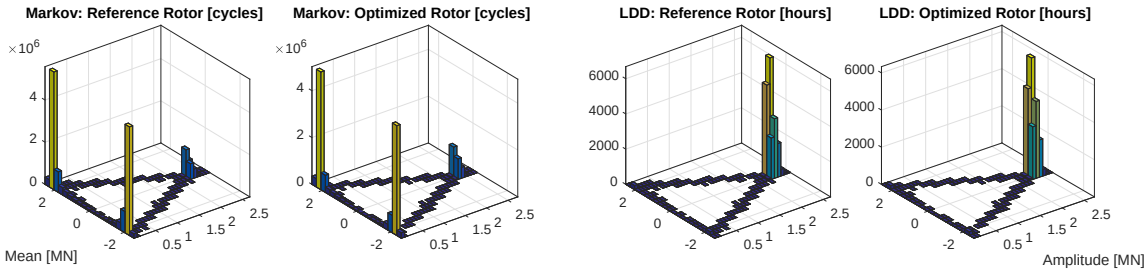

Figure 3.5: Illustration of Markov matrices and LDDs of shear force for both rotors for DLC 1.2.

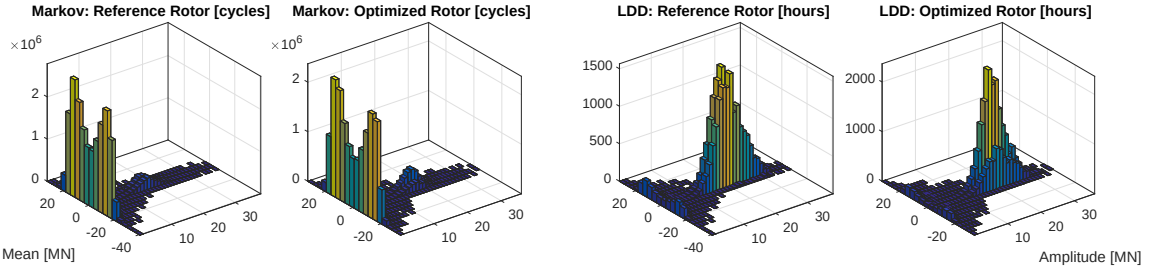

Figure 3.6: Illustration of Markov matrices and LDDs of bending moment for both rotors for DLC 1.2.

be able to reveal the effect of each rotor. That is why the 1 Hz fatigue-damage-equivalent zero-mean load ranges (1Hz-DEL), $\overline{\Delta L_{eq}}$, related to each corresponding load component is calculated.

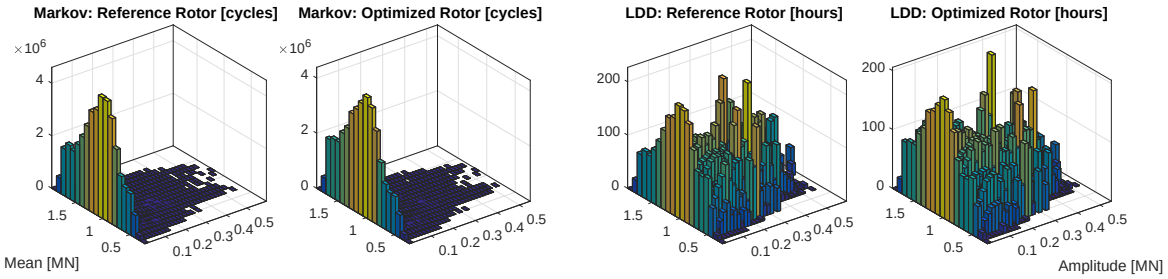

Figure 3.7: Illustration of Markov matrices and LDDs of axial force for both rotors for DLC 1.2.

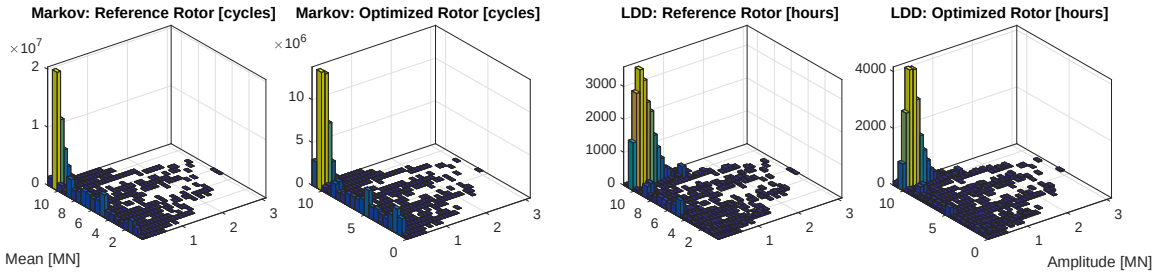

Figure 3.8: Illustration of Markov matrices and LDDs of torsional moment for both rotors for DLC 1.2.

For each DLC, the variations of $\overline{\Delta L_{eq}}$ with the circumferential coordinates and with the wind speed are investigated. DNV-RP-C203 [48] recommends considering at least height points equally spaced around the circumference.

On the one hand, Figure 3.9 depicts the variation of the 1Hz-DEL resulting from DLC 1.2 at 11 m/s mean wind speed with respect to the circumferential coordinates. On this figure, the results from the reference rotor case are compared to those with the optimized rotor. It can be readily noticed that the axial force 1Hz-DEL and the torsion 1Hz-DEL are independent of the circumferential coordinates. Similar results are prepared for all mean wind speeds pertaining to this DLC, but not presented here for brevity.

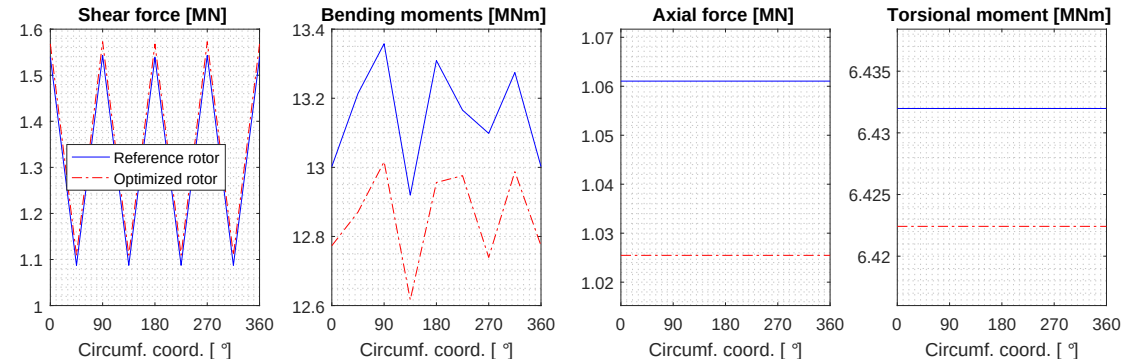

Figure 3.9: Variation of the 1 Hz fatigue damage equivalent zero-mean load ranges resulting from DLC 1.2 at 11 m/s mean wind speed with respect to circumferential coordinates.

On the other hand, Figure 3.10 presents the 1Hz-DEL resulting from DLC 1.2 at $\theta = 0°$ in function of wind speeds including their respective occurrence frequency. Similarly, the results from both rotor cases are compared. In all cases, high 1Hz-DELs are observed around the rated wind speed. Similar results are prepared for the seven other circumferential points, but not presented here

for brevity.

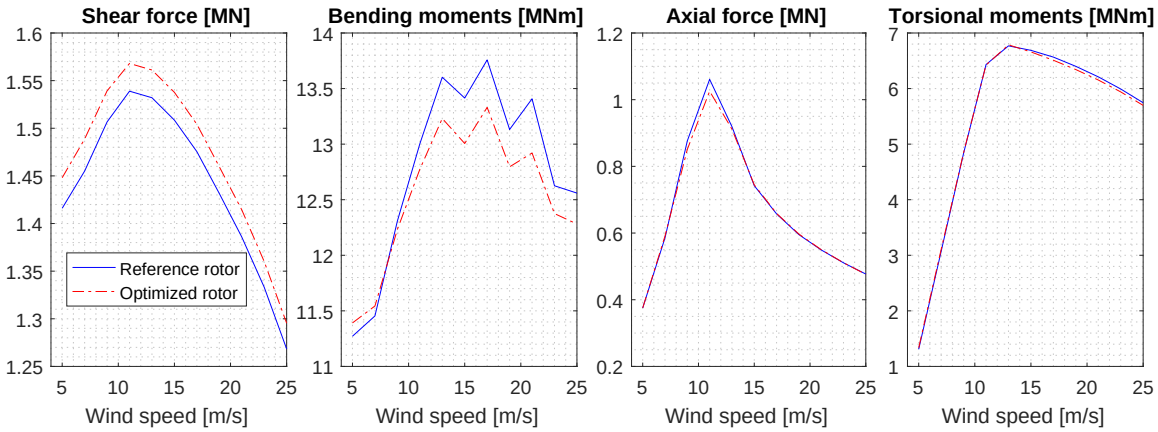

Figure 3.10: Variation of the 1 Hz fatigue-damage-equivalent zero-mean load ranges resulting from DLC 1.2 at $\theta = 0°$ with respect to wind speed.

For each corresponding load component, the 1Hz-DELs are aggregated across the whole wind range for each DLC. Figure 3.11 presents the aggregated 1Hz-DELs for all selected DLCs related to fatigue limit state. Results for half of the circumferential hotspots are presented taking advantage from the structure symmetry.

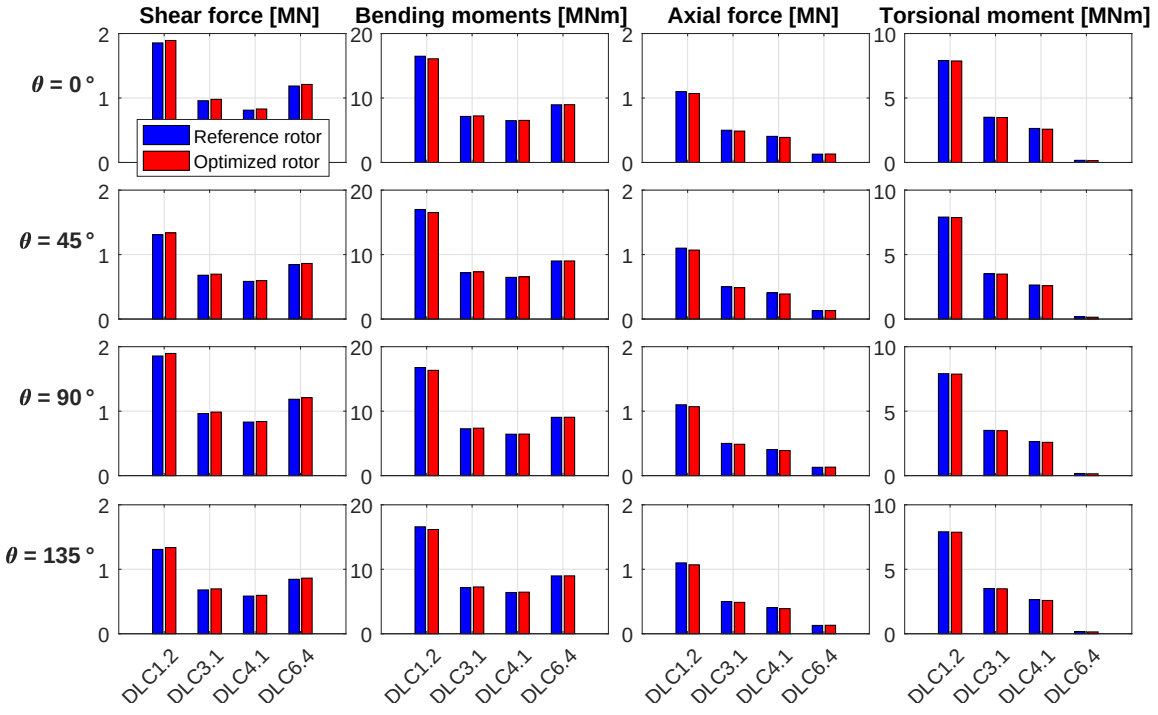

Figure 3.11: 1 Hz fatigue load contributions from each DLC for both rotors at $\theta = 0°, 45°, 90°$, and 135°.

It is noticeable that DLC 1.2 contributes the most to the fatigue damage of the shaft whichever corresponding load component is considered. Axial force and torsional moment 1Hz-DELs resulting from DLC 6.4 cause an insignificant amount of fatigue damage. This was expected as during the parked rotor situations (DLC 6.4), no torsional moment is transmitted to the shaft and the thrust force is minimal. 1Hz-DELs from DLC 3.1 are consistently higher than those from DLC 4.1 for all

load components. This means that the shaft undergoes more fatigue loads during the start-ups than during the normal shut-downs.

The total 1Hz-DELs for each rotor and their respective relative differences are tabulated in Table 3.1. It is evident to have the axial force and the torsional moment 1Hz-DELs constant around the circumference as the related spectra are not dependent on the circumferential coordinates. The bending moment 1Hz-DEL insignificantly changes with the circumferential coordinates whereas a greater variation is observed for shear force 1Hz-DEL.

Except for the shear force where the change from reference to optimized rotor induces an increase of the 1Hz-DEL of about +2 %, it results in a decrease for the other component 1Hz-DEL. Whereas the moment 1Hz-DELs undergo changes less than 1 %, a decrease of -2.67 % is observed with the axial force 1Hz-DEL.

Table 3.1: Variation of the 1 Hz fatigue-damage-equivalent zero-mean load ranges between rotor cases and circumferential coordinates

	Shear force			Bending moments		
	Ref. Rot.	Opt. Rot.	Rel. Diff	Ref. Rot.	Opt. Rot.	Rel. Diff
$\theta = 0°$	4.81 MN	4.91 MN	+2.10 %	39.08 MNm	38.81 MNm	-0.69 %
$\theta = 45°$	3.42 MN	3.49 MN	+2.17 %	39.65 MNm	39.39 MNm	-0.66 %
$\theta = 90°$	4.84 MN	4.93 MN	+1.96 %	39.52 MNm	39.20 MNm	-0.81 %
$\theta = 135°$	3.42 MN	3.49 MN	+2.17 %	39.12 MNm	38.86 MNm	-0.64 %
	Axial force			Torsional moments		
	Ref. Rot.	Opt. Rot.	Rel. Diff	Ref. Rot.	Opt. Rot.	Rel. Diff
$\forall\theta \in [0°, 360°]$	2.13 MN	2.08 MN	-2.67 %	14.22 MNm	14.09 MNm	-0.95 %

3.4 Loads for Ultimate Limit State

In accordance to DNVGL-ST-0437 [49], extreme loads resulting from DLC 1.1 have been computed by multiplying by 1.35 the extreme loads resulting from normal design situations. Consequently, DLC 1.3 should be obtained with increased values of turbulence intensity until the resulting extreme design values of the blade root moments get greater or equal to those resulting from DLC 1.1, if it was not already the case. Despite of that, in this study DLC 1.3 loads are presented as they are obtained before the increase of the turbulence intensity. It is expected that the loads from the modified DLC 1.3 are similar to those from DLC 1.1 when equality is met after the turbulence intensity tuning.

For all DLCs, loads computed with both rotors are compared. Extreme loads are obtained in two different ways: (i) based on resultant load time series ($L_{res} = \sqrt{L_1^2 + L_2^2}$) as classically done (see Figure 3.3) and (ii) based on corresponding load time series (see Equations 3.4 – 3.7). The latter being dependent on the circumferential coordinates, the extreme design loads are calculated in function of this variable as depicted in Figure 3.12 for the DLC 1.1.

Obviously, extreme design axial forces and torsional moments do not vary in function of the circumferential coordinates, neither do the extreme resultant loads. Yet, the extreme values of the corresponding shear forces and bending moments vary and are consistently lower than the resultant loads. This was expected as the extreme resultant value corresponds to the *maximum maximorum* values of the time series, while the corresponding loads is the highest of peak averages.

Figure 3.13 presents the variation of the extreme values of design loads with respect to wind speed for DLC 1.1 at the circumferential coordinate $\theta = 0°$. The curves pertaining to the axial force and to the torsional moment are respectively shaped as those of the thrust force and the rotor rotational speed curve, whereas the curves related to the shear force and to the bending moment monotonically

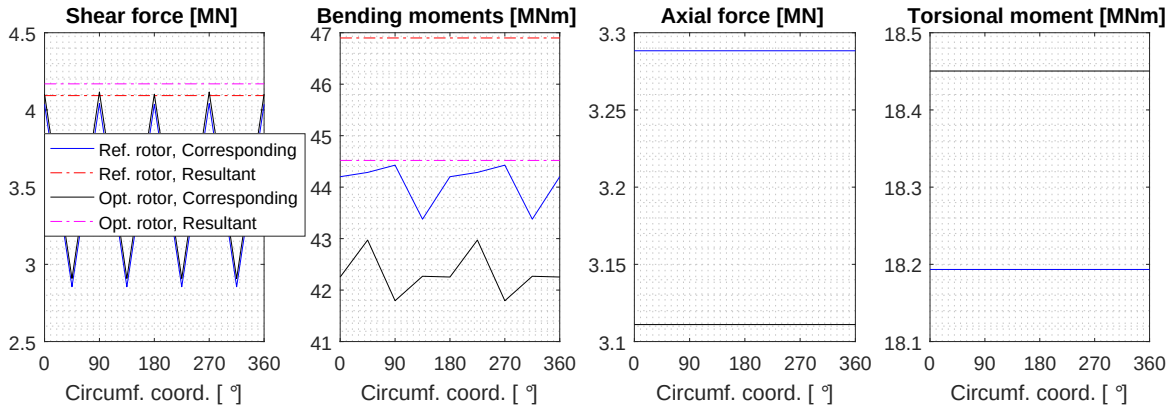

Figure 3.12: Variation of the extreme design loads resulting from DLC 1.1 at 11 m/s mean wind speed with respect to circumferential coordinates.

increase with the wind speed.

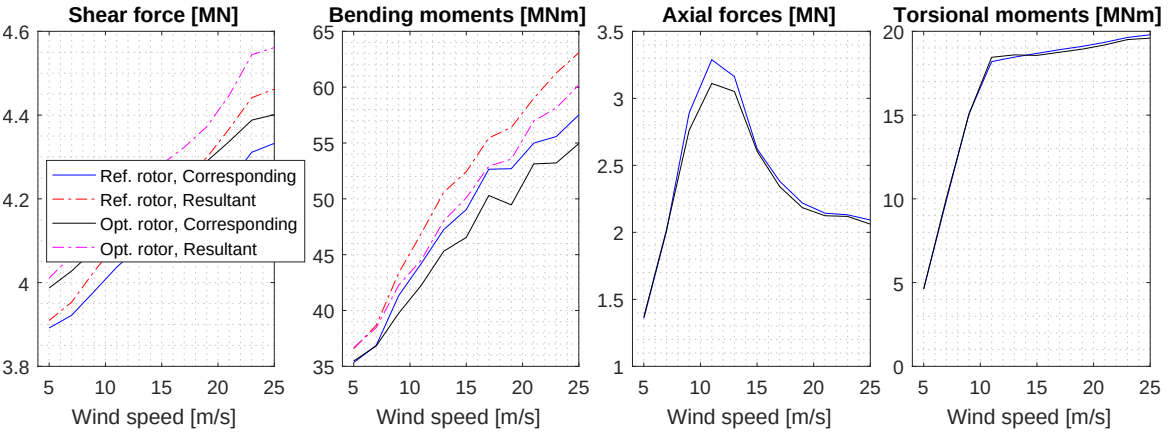

Figure 3.13: Variation of the extreme design loads resulting from DLC 1.1 at $\theta = 0°$ with respect to wind speed.

Similar results are prepared for all selected ULS related DLCs, and are summarized in Figure 3.14 for the circumferential coordinates $\theta = 0°, 45°, 90°$, and $135°$.

The extreme design values of all load components resulting from DLC 1.1 are the highest: DLC 1.1 could be the design driver. For the torsional moment, the extreme value does not significantly vary (-0.96 %) from the reference rotor (19.79 MNm) to the optimized rotor (19.60 MNm). The change from the reference rotor case (3.29 MN) to the optimized rotor case (3.11 MN) attains -5.47 % for the axial force.

The shear force is mainly due to the rotor weight and the integration of the aerodynamic forces coplanar to the rotor. Table 3.2 details the load extreme design value changes at the hotspots $\theta = 0°$ and 45° between the two rotor cases and between the equivalent load strategy. The shear force extreme design values from the optimized rotor case is about 2 % higher than that from the reference rotor case: this reflects the higher weight of the optimized rotor. The extreme design values from the corresponding shear force differ by about 3 % from those from the resultant shear force at the critical hotspot.

The bending moment is mainly generated by the effects of the shear force and of the distributed forces normal to the rotor plane. The load extreme design value changes are presented in Table 3.3. About 4 % relative difference is spared when changing from the reference rotor to the optimized one.

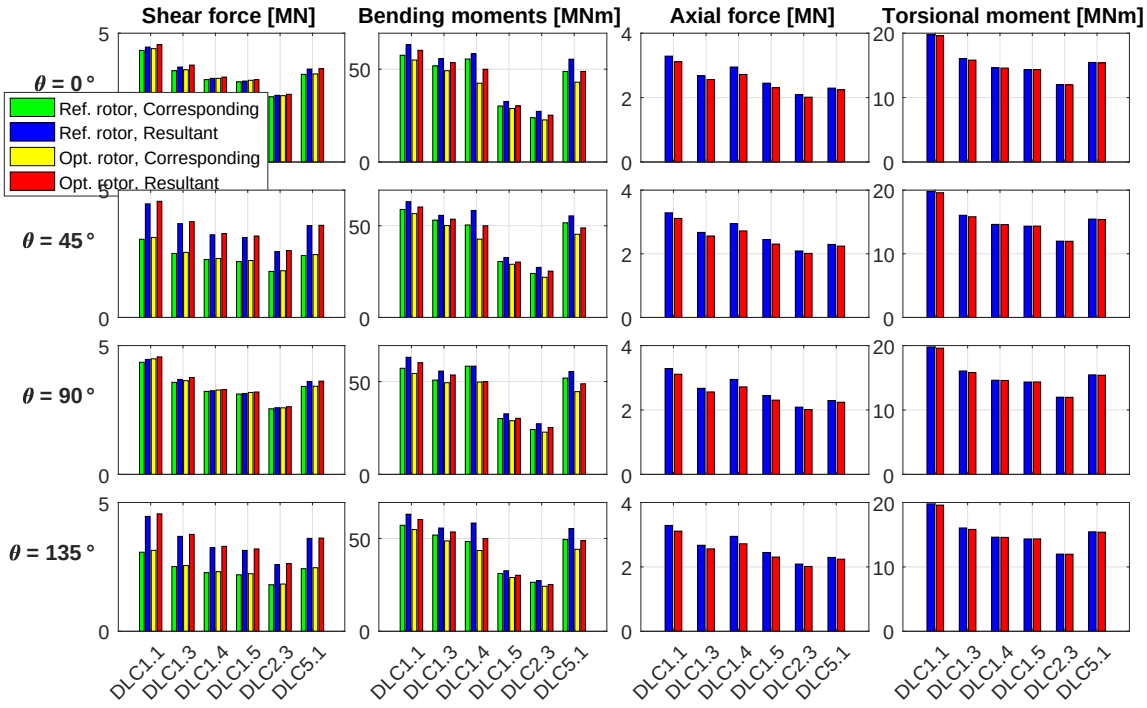

Figure 3.14: Extreme design values for load components from each DLC for both rotors at $\theta = 0°, 45°, 90°$, and $135°$.

Table 3.2: Changes of the extreme design values of the shear force within rotor cases and load equivalence strategies at hotspots $\theta = 0°$ and $45°$

	Hotspot $\theta = 0°$			Hotspot $\theta = 45°$		
	Ref. Rotor	Opt. Rotor	Rel. Diff	Ref. Rotor	Opt. Rotor	Rel. Diff
Q_{Corr}	4.33 MN	4.40 MN	+1.62 %	3.07 MN	3.14 MN	+2.28 %
Q_{Res}	4.46 MN	4.56 MN	+2.24 %	4.46 MN	4.56 MN	+2.24 %
Rel. Diff.	-2.91 %	-3.51 %		-31.17 %	-31.14 %	

The extreme design value of the resultant bending moment is approximatively 6 % higher than that of the corresponding counterpart. Up to 13 % change of the bending moment can be revealed by selecting the optimized rotor and the load stress-based equivalence strategy rather than the reference rotor and the load resultant equivalence strategy.

Table 3.3: Changes of the extreme design values of the bending moment within rotor cases and load equivalence strategies at hotspots $\theta = 0°$ and $45°$

	Hotspot $\theta = 0°$			Hotspot $\theta = 45°$		
	Ref. Rotor	Opt. Rotor	Rel. Diff	Ref. Rotor	Opt. Rotor	Rel. Diff
M_{Corr}	57.52 MN	54.95 MN	-4.47 %	58.87 MN	56.59 MN	-3.87 %
M_{Res}	63.09 MN	60.20 MN	-4.58 %	63.09 MN	60.20 MN	-4.58 %
Rel. Diff.	-8.83 %	-8.72 %		-6.69 %	-6.00 %	

3.5 Concluding Remarks

The present chapter computes for various load components the 1 Hz fatigue-damage-equivalent zero-mean load ranges and the extreme design value of the loads applied on the shaft of the DTU 10 MW RWT successively with the reference rotor and the optimized one. The time series of the load Cartesian components have been combined based on the stress-based design format as opposed to the canonical resultant strategy. The former strategy is in line with the modern standard design format and therefore yields results more suitable for interpretation, usage, or exchange.

It is found that DLC 1.2 loads contribute the most to the fatigue damage but an actual stress assessment is required to validate this preliminary conclusion as the equivalent stress time series resulting from the combination of individual stresses can lead to a different conclusion. Yet, the other DLCs altogether also contribute with a significant proportion to the overall fatigue damage.

The DLC 1.1, which is specific for the rotor and nacelle components, stands as the critical DLC. However, DLC 1.3 can be more severe if the extreme turbulence intensity is tuned according to the standard [49]. This indicates that it is more likely to have failure during normal operations than in other situations. Used to assess the extreme design values of the forces and moments, the equivalence load strategy based on stress reveals extra-capacity of the shaft compared to the resultant counterpart. This means that material saving can be realized in the design phase by considering the former strategy. Rather than the classical extreme load table, the adoption of this strategy for information sharing between various stakeholders (designers, manufacturers, testing firms) is encouraged for both accuracy and conservatism reduction.

Whichever limit state is considered, the optimized rotor in general yields smaller loads that the reference rotor. It is concluded that the optimized rotor is not detrimental to the shaft and such rotor replacement can serve as a method for fatigue lifetime improvement for nacelle components, towers, substructures, or foundations.

4

Methods for Fatigue Lifetime Improvement of Jacket Substructures

> Good asparagus needs minimal treatment and is best eaten with few other ingredients.
>
> *Yotam Ottolenghi*

The design process of jacket substructures for 10 MW wind turbine at 50 m water depth has given challenges to ensuring sufficient fatigue lifetime when employing the traditional design procedure [13]. Indeed, as wind turbines get higher power ratings, their larger rotors exhibit lower rotational speeds, whose multiples coincide with the natural frequencies of the stiff jacket structures during operations and may result in resonance phenomenon. Therefore, attempts for satisfactory designs under traditional design procedures have generally resulted in massive substructures.

On the one hand, various studies proposed solutions to reduce fatigue loads by alleviating the support-structure vibrations [18]. These methods include the use of dampers at the tower top or better design of the rotor and nacelle assembly. They act on the global structural level and lead to some successful results, but become less adequate for multi-megawatt turbines. Indeed, as wind turbines become larger, the dampers need to be upscaled conveniently, then require more space in the nacelle whose volume is quite constant. Moreover, they affect only a narrow frequency range, which is non-optimal for a system with multiple excitation frequencies [18]. An appropriate solution should involve dampers that can accommodate various exciting frequencies and are moderate in size. Magneto-rheological (MR) dampers fulfill these criteria but does not act on the whole jacket. An alternative with global level effect can be the aero-elastic tailoring of the rotor with the purpose of minimizing the fatigue loads due to aero-dynamics.

On the other hand, several authors focused on the local level and also intended for cost-efficient jacket substructures. For example, Sandal [14] and Oest *et al.* [15] proposed methodologies based on optimization with fatigue constraints. Due to the computational cost, the multiple calls of the main design function requires an uncoupled load approach, which leads to conservative substructures [16]. An alternative proposed by Natarajan *et al.* [17] consists of an optimization strategy that sets the natural frequencies of the jacket substructures away from the rotor harmonics. This solution results in lighter jacket substructures that require some welded joint re-design. Henceforth, a good insight of the welded joint design space is needed so as for the designer to propose adequate joint design.

The objectives of this chapter is to develop methods for fatigue lifetime improvement based on jacket supporting multi-megawatt wind turbines at deep waters. For the sake of cost-efficiency, the methods should be compatible with the optimization procedures presented. Moreover, they should be applicable with the current state of technology. The next sections address three methods for fatigue lifetime improvement of jacket substructures, which pertain to three structural levels: (i) joint level; (ii) member level; and (iii) support structure level. The first method explores the joint design space and offer guidance for joint design so as to satisfy the fatigue limit state requirements. The second method employs magneto-rheological dampers at brace level to relieve fatigue at the most critical joints. The last method alleviates the support structure vibrations based on the optimized rotor.

4.1 Lifetime Estimation Procedure

4.1.1 Stress and Stress Concentration Factors

Traditionally, jacket substructures are spatial frames whose members are of circular hollow section type. Aero-servo-hydro-elastic simulations result in loads evaluated at different sections of the members, including axial force, N, in-plane bending moment, M_{IP}, and out-of-plane bending moment, M_{OP}, as depicted in Figure 4.1.

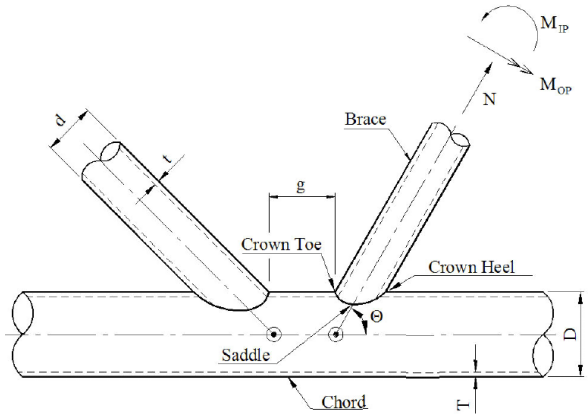

Figure 4.1: General definitions for tubular joints (Adapted from [48]).

The maximum nominal axial stresses (evaluated at a member current section) associated to each load are, respectively:

$$\sigma_x = \frac{N}{A} \tag{4.1}$$

$$\sigma_{IP} = \frac{M_{IP}}{I/R} \tag{4.2}$$

$$\sigma_{OP} = \frac{M_{OP}}{I/R} \tag{4.3}$$

$$\tag{4.4}$$

where

N	:	axial force
M_{IP}, M_{OP}	:	in-plane and out-of-plane bending moments, respectively
A	:	section's area
I	:	section's second moment of area
R	:	outer radius
σ_x	:	axial stress due to axial force
σ_{IP}, σ_{OP}	:	axial stresses due to in-plane and to out-of-plane bending moments, respectively.

At the joints, stresses are amplified due to stress concentration. The stress concentration factors (SCFs) - ratios between the amplified stresses and the nominal ones - are evaluated at the crowns and saddles for each side of the weld (brace side and chord side). Based on the Efthymiou's equations [50], DNVGL-RP-C203 [48] recommends the SCF expressions reported in Appendix C. The hotspot stresses are then computed around the weld circumference as:

$$\sigma_k(\theta) = \left(\hat{\theta}\ SCF_{AC} + (1-\hat{\theta})\ SCF_{AS}\right)\ \sigma_x + SCF_{IP}\ \sigma_{IP}\ \sin\theta - SCF_{OP}\ \sigma_{OP}\ \cos\theta \tag{4.5}$$

where θ is the circumferential coordinates around the weld measured from the saddle-saddle line and $\hat{\theta} = \frac{2}{\pi}\arcsin\left(\sin\left(\arccos(\cos\theta)\right)\right)$, in which the ranges of the trigonometric functions $\arcsin(\cdot)$ and $\arccos(\cdot)$ are restricted to the usual principal angle values in radians. The indices *AS*, *AC*, *IP*, and *OP* respectively denotes 'axial at the saddle points', 'axial at the crown points', 'in-plane', and 'out-of-plane'. DNVGL-RP-C203 [48] recommends to assess at least eight equally distributed hotspots around the circumference as shown in Figure 4.2.

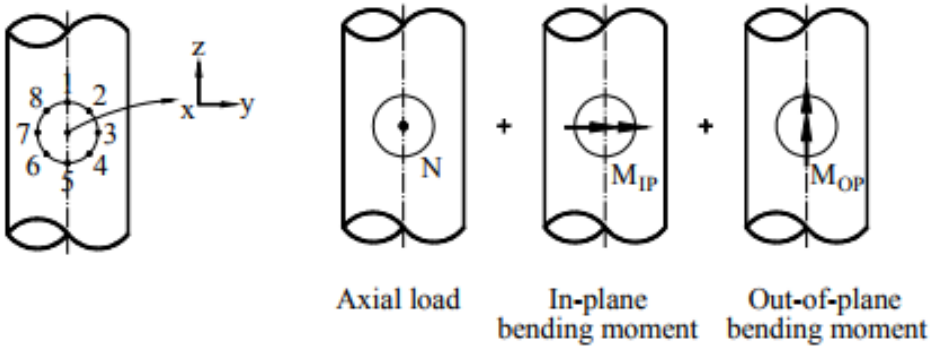

Figure 4.2: Superposition of hotspot stresses at points around the weld circumference (Adapted from [48]).

4.1.2 Rainflow counting and S-N Curve

For each hotspot, the Rainflow stress range counting method is applied on the hotspot stress time series. The details of this method are given by Ref [51]. For each time series, it results in a set of stress cycles each characterised by its range or its amplitude, its mean, and its number of occurrences. In order to evaluate the maximum number of occurrences for each stress cycle that a hotspot sitting around a tubular welded structural details can bear before failure, DNVGL-RP-C203 [48] proposes design S-N curves of T-type suitable for various environmental conditions. The S-N curves map a given stress range $\Delta\sigma$ to its corresponding number of cycles to failure N depending on whether the structural details is (i) in the air; (ii) in seawater with cathodic protection; or (iii) in seawater let to free corrosion. In either case, the stress range should be corrected to account for the effect of the thickness through which the crack will most likely grow. The general shape of the S-N curve is given by:

$$\log N = \log \bar{a} - m \log \left(\Delta\sigma \left(\frac{t}{t_{ref}} \right)^{k} \right) \tag{4.6}$$

where

m	:	negative inverse slope of the S-N curve as given in Table 4.1
$\log \bar{a}$	:	intercept of $\log N$ axis as given in Table 4.1
t_{ref}	:	reference thickness equal to 32 mm for tubular joints
t	:	thickness through which the crack will most likely grow, $t = \max(t,\ t_{ref})$
k	:	thickness exponent as given in Table 4.1

Table 4.1 gives the S-N curve parameters as recommended by DNV-RP-C203 (2011). The three curves thus defined are illustrated by Figure 4.3 for each environment.

Table 4.1: Parameters of S-N curves for tubular joints in various environments as per DNV-RP-C203 (2011).

Environment	m [-]	$\log \bar{a}$ [-]	k [-]
Air	$\begin{cases} 3.0 & \text{if } N \le 10^7 \\ 5.0 & \text{if } N > 10^7 \end{cases}$	$\begin{cases} 12.164 & \text{if } N \le 10^7 \\ 15.606 & \text{if } N > 10^7 \end{cases}$	$\begin{cases} 0.25 & \text{if } SCF \le 10.0 \\ 0.30 & \text{if } SCF > 10.0 \end{cases}$
Seawater (cathodic protection)	$\begin{cases} 3.0 & \text{if } N \le 10^6 \\ 5.0 & \text{if } N > 10^6 \end{cases}$	$\begin{cases} 11.764 & \text{if } N \le 10^6 \\ 15.606 & \text{if } N > 10^6 \end{cases}$	$\begin{cases} 0.25 & \text{if } SCF \le 10.0 \\ 0.30 & \text{if } SCF > 10.0 \end{cases}$
Seawater (free corrosion)	3.0	11.687	$\begin{cases} 0.25 & \text{if } SCF \le 10.0 \\ 0.30 & \text{if } SCF > 10.0 \end{cases}$

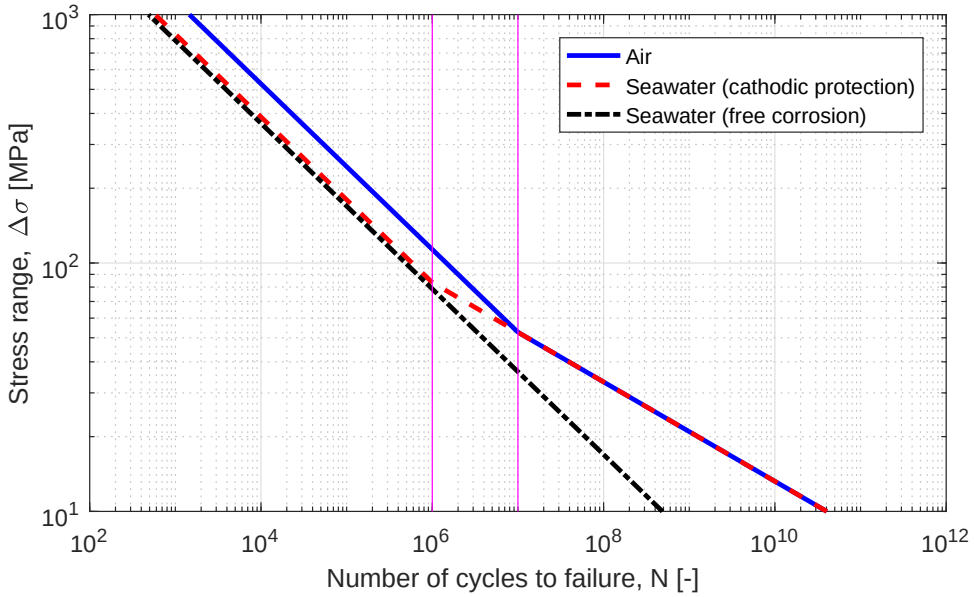

Figure 4.3: Design S-N curves for tubular welded joints of thickness less than t_{ref} as per DNV-RP-C203 (2011).

4.1.3 Influence of the Mean Stress on Fatigue Demand

Under some circumstances, DNVGL-RP-C203 [48] allows the reduction of the stress ranges before entering the S-N curve depending on the stress range regime (tensile or compressive). These circumstances include post-weld heat treatment or documentation of low residual stresses for welded structural details. The reduction factor is obtained by:

$$f_m = \frac{\sigma_t + 0.8|\sigma_c|}{\sigma_t + |\sigma_c|} \tag{4.7}$$

where σ_t and σ_c stand for the extremum tensile stress (defined as positive) and for the extremum compressive stress, respectively. Figure 4.7 illustrates the variation of the reduction factor in function of the mean stress. It shows that, when the specified circumstances are fulfilled, the reduction factor can be up to 0.8 for a cycle entirely under compression. However, as the application of this recommendation is subjected to conditions, it will not be accounted for in the following design processes.

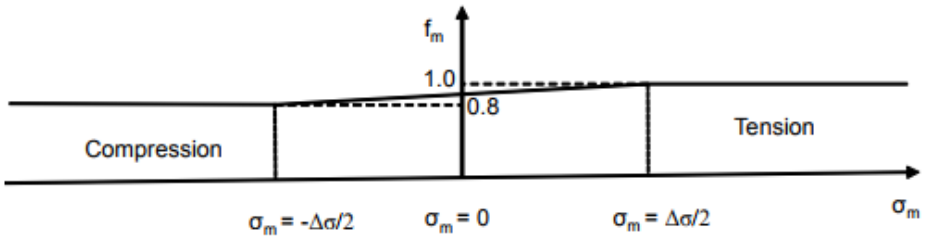

Figure 4.4: Variation of the stress range reduction factor, f_m in function of the mean stress, σ_m [48]. $\Delta\sigma$ is the stress range.

4.1.4 Palmgren-Miner's Rule and Fatigue Damage

During a given period of time, each stress cycle expectedly occurs a number of times equal to the number of occurrences of the time series it has been extracted from, which is obtained in relation to the wind speed distribution (see Figure 2.2). The generated fatigue damage pertaining to the given stress cycle is computed as the ratio of the number of times it occurs over the number of times it will lead to failure, given by Equation 4.6. Palmgren Miner's rule [52] allows the linear summation of the individual damage due to each stress cycle over a period of time. During one year, the aggregated fatigue damage is given by:

$$D_1 = \gamma_{DFF} \frac{T_1}{T} \int_{V_{in}}^{V_{out}} \int_{\Delta\sigma_A}^{\Delta\sigma_B} \frac{n(\Delta\sigma|V,T)}{N(\Delta\sigma)}\, p(V)\, \mathrm{d}\Delta\sigma\, \mathrm{d}V \tag{4.8}$$

where:

γ_{DFF}	:	the design fatigue factor associated to the accessibility of the structures.
V	:	mean wind speed;
V_{in}, V_{out}	:	cut-in and cut-out wind speeds;
$p(V)$	:	probability of occurrence of the mean wind speed V;
T	:	simulation duration. $T = 600\ s$;
T_1	:	number of seconds in one year; and
$n(\Delta\sigma\|V,T)$	:	number of stress cycles $\Delta\sigma$, given V and T, obtained after rainflow counting.

According to DNVGL-OS-C101 [53], $\gamma_{DFF} = 3$ for non-accessible structures or structures whose accessibility for inspection and repair during operation are not planned; and $\gamma_{DFF} = 2$ for external structures not accessible for inspection and repair in dry and clean conditions.

Based on the one-year fatigue damage, the damage accumulated during the lifetime, i.e. 25 years, is $D_{25} = 25 \cdot D_1$ and the fatigue lifetime in years is obtained as $L = D_1^{-1}$.

4.2 Efficient Joint Design: Reduction of Stress Concentration Factor

4.2.1 Parametrization of Welded Joints

As each fatigue stress componenet in Equation 4.5 is directly proportional to the SCFs' values, an efficient joint design ought to have lower SCF levels. Each SCF' expression recommended by DNV-RP-C203 [48] mainly depends on the proportions between the dimensions of the members. So, properly choosing these ratios will improve at some extent the design of the different types of joints.

Joint dimensions can be non-dimensionalized so as to have geometrical joint parameters as given in Figures 4.5 and 4.6. The parameters describe (i) the ratio between the diameters of the connected members, β; (ii) the ratio between their wall thicknesses, τ; (iii) a measure of the leg's slenderness, α; (iv) a measure of its shell rigidity, γ; and (v) a measure of the gap's slenderness, ζ, if it exists. When assessing the weld connection between a given brace and the leg at a K-joint, this brace is labelled A and the other brace B.

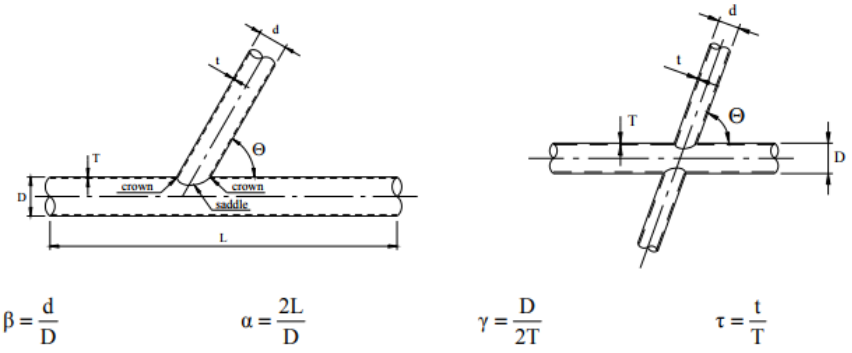

Figure 4.5: Definition of geometrical parameters for Y- and X-joints [48].

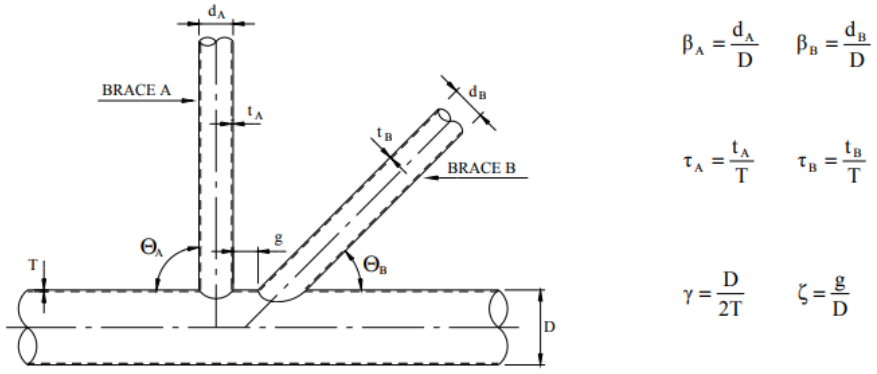

Figure 4.6: Definition of geometrical parameters for K-joints [48].

In order to evaluate the influence of the non-dimensional geometrical parameters on the SCF values, a design of experiments of orthogonal-factorial type has been carried out over the whole validity range (Appendix C). From the SCF's expressions, two subspaces within which continuity is ensured can be distinguished: the short-chord subspace ($\alpha < 12$) and the long-chord subspace ($\alpha > 12$). Each geometrical parameter has been chosen with several equally-spaced levels over each

sub-space. Six levels are chosen for the K-joints in each subspace and 10 levels for Y- and X-joints. The sensitivity of a given parameter is assessed by the means of correlation coefficients between the said parameter and the SCF taken as dependent variable. Three types of correlation coefficients are computed: Pearson's, Spearman's, and Kendall's types [54]. They all convey similar information needed for this study. Therefore, only the Spearman's type correlation coefficients are presented here for each type of joints.

4.2.2 Y-Joint Type

For the Y-joint type, Figure 4.7 depicts the correlation coefficients between the geometrical parameters and the SCFs of each load component for each subspace. Where they are both significant, the correlation coefficients for each subspace have the same sign.

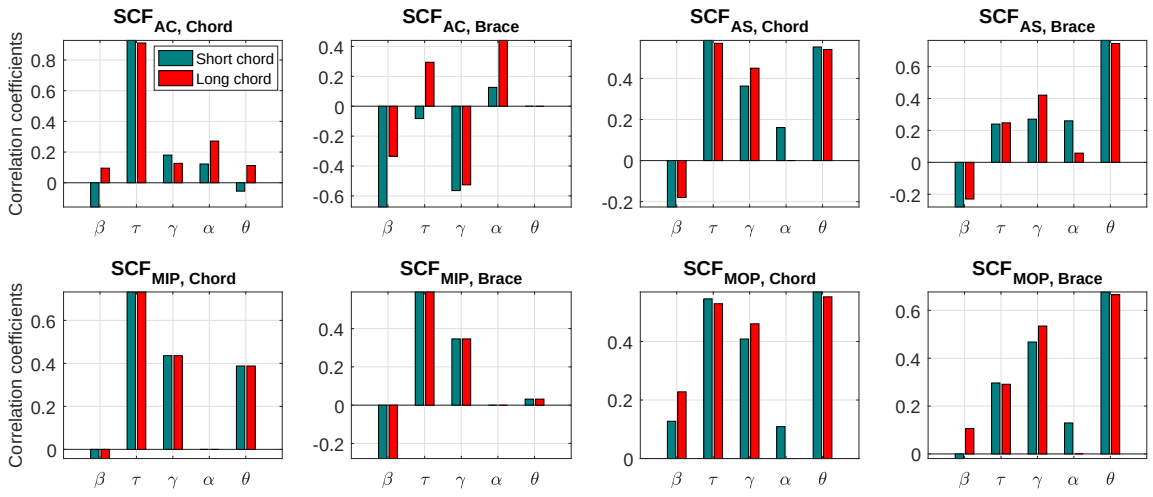

Figure 4.7: Correlation coefficients between geometrical parameters and SCFs for Y-joint types.

The coefficient associated to β is either null or negative for all load components except for the out-of-plane bending moment. This indicates that for Y-joints a small difference between the member diameters is in general desirable but attention should be given to the increase of the SCF associated the out-of-plane bending moment. However, the positive coefficient related to τ invite to have as dissimilar wall thicknesses as possible. A greater incidence angle between the members will lead to higher SCF values. Even if the slenderness of the leg does not have the most significant influence on the SCF values, it is preferable to keep it as small as possible. In general it is better to have less rigid shell but this will increase the SCF for the axial force at the brace side of the crown. As a result, Table 4.2 summarizes the guidance rules useful to reduce the SCF values for Y-joints.

Table 4.2: Guidance rules for efficient Y-joint design.

Geometric Parameters	Indications
Diameter	***Competitive effect***: brace's and chord's diameters should be as similar as possible, in general!
Wall thickness	***Dissimilar***: brace's and chord's wall thicknesses should be as different as possible
Chord's shell rigidity	***Competitive effect***: chord's shell should be as flexible as possible, in general!
Chord's slenderness	***Short***: the chord's diameter should be relatively large compared to the chord's length
Incidence angle	***Acute***: the angle between the brace and the chord should be as small as possible

4.2.3 X-Joint Type

Similar to the case of Y-joint, the correlation coefficients between the geometrical parameters and the SCFs of each load component have the same sign for each subspace where they are both significant. Similar diameters but dissimilar wall thicknesses of the overlap braces are beneficial for the design as β-coefficients are negative or null and τ-coefficients are positive or null (see Figure 4.8).

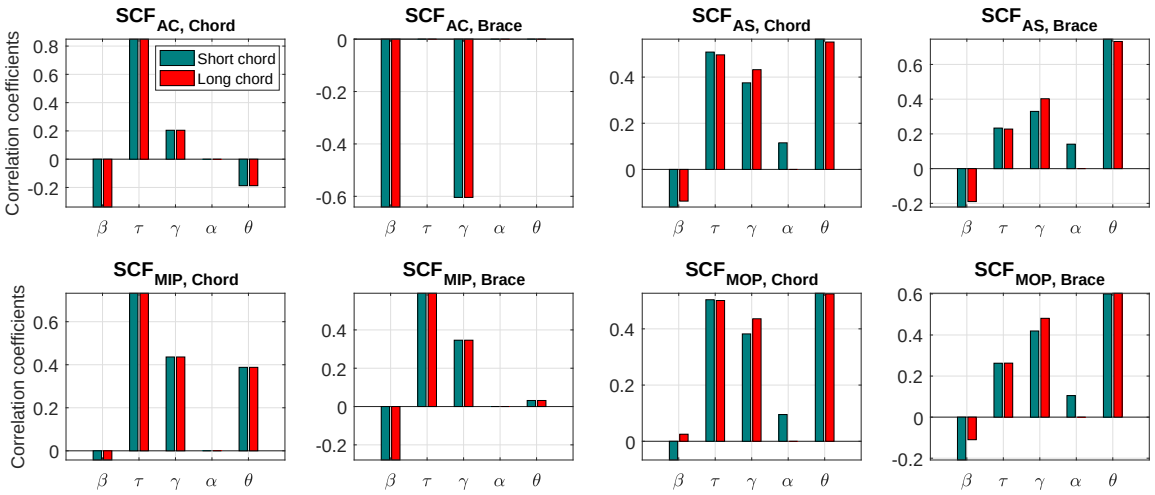

Figure 4.8: Correlation coefficients between geometrical parameters and SCFs for X-joint types.

Also, the more acute is the angle between the braces, the lower the SCF values are. As for the Y-joint, the shell rigidity of the chord poses a dilemma as changing its value can modify some SCF values in a favourable manner but can be detrimental to the SCF associated to the axial force at the brace side of the crown. The slenderness of the chord does not show any significant monotonic relationship with the SCF values as the α-coefficients are close to zero. Table 4.3 tabulates the derived guidance rules.

Table 4.3: Guidance rules for efficient X-joint design.

Geometric Parameters	Indications
Diameter	***Similar***: brace's and chord's diameters should be as similar as possible
Wall thickness	***Dissimilar***: brace's and chord's wall thicknesses should be as different as possible
Chord's shell rigidity	***Competitive effect***: chord's shell should be as flexible as possible, in general!
Chord's slenderness	***Short***: the chord's diameter should be relatively large compared to the chord's length
Incidence angle	***Acute***: the angle between the brace and the chord should be as small as possible

4.2.4 K-Joint Types

In a K-joint design, braces can have a gap between them or they can overlap each other as illustrated in Figure 4.9. For an overlap K-joint, the through brace is the most intact brace while the overlapping brace is the cropped one.

Figures 4.10, 4.12, and 4.11 present the correlation coefficients for the gap K-joint, the through brace in a overlap K-joint, and for the overlapping brace in an overlap K-joint, respectively. The SCF sensitivities are generally correspondingly similar for either K-joint situation. It is advantageous to provide smaller brace wall thickness than the leg wall thickness, while keeping low leg shell rigidity. Whereas the correlation coefficients of the leg slenderness are null for the SCFs associated to the other load components, a slender leg tends to amplify the SCFs associated to the out-of-plane

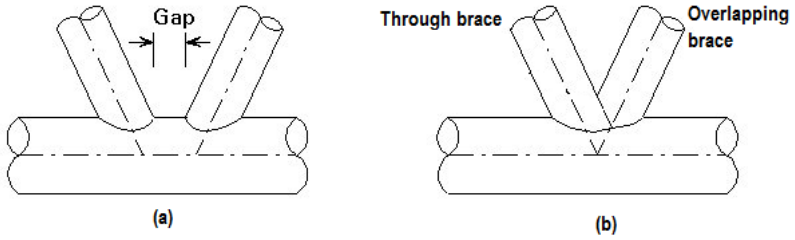

Figure 4.9: Gap and overlap between braces of K-joints [55]. (a) Gap K-joint. (b) Overlap K-joint.

moments for short-chord designs: less slender legs are desirable. Furthermore, small incidence angles are advisable as seen for the other joint types.

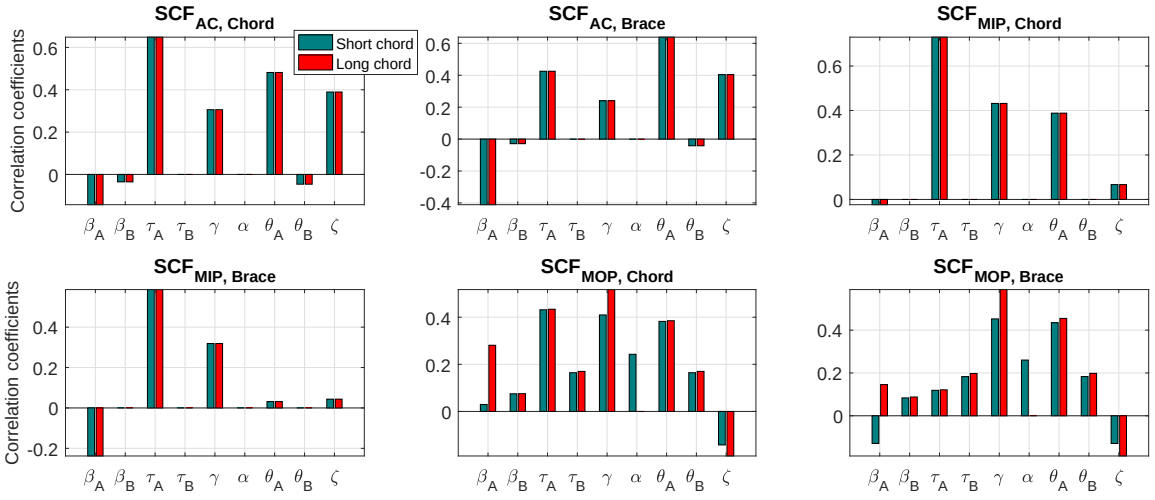

Figure 4.10: Correlation coefficients between geometrical parameters and SCFs for gap K-joint types.

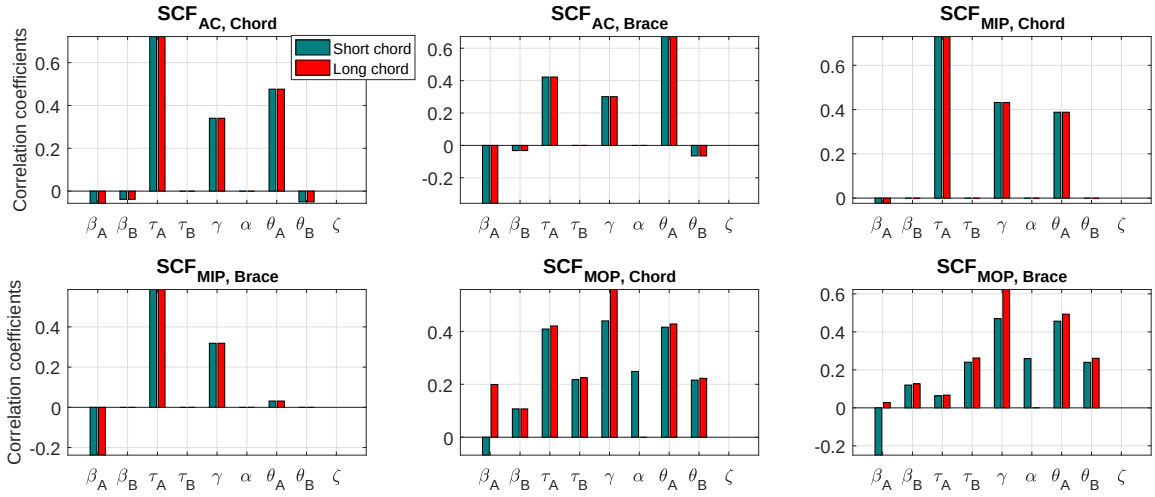

Figure 4.11: Correlation coefficients between geometrical parameters and SCFs for the through brace at K-joint types.

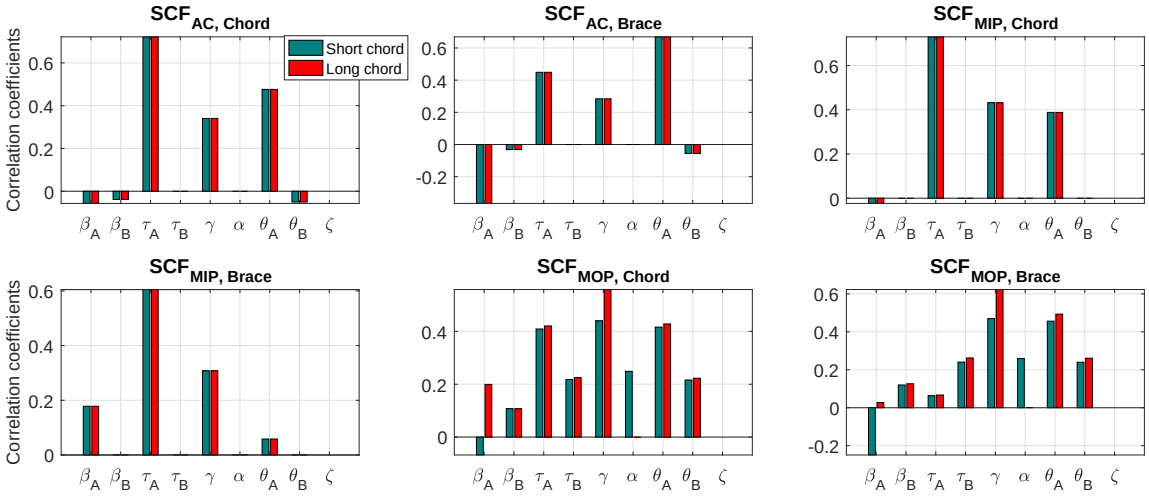

Figure 4.12: Correlation coefficients between geometrical parameters and SCFs for the overlapping brace at K-joint types.

Specially for gap K-joints, the gap slenderness should be dealt with carefully. Its reduction lowers the axial force related SCF levels but slightly increases the out-of-plane moment ones. Another particularity is risen by the diameter ratio β. In general, its influence is similar for either K-joint situations: similar diameters lessen SCF levels. However, for SCFs relative to the out-of-plane bending moment at the chord of all K-joint types and for SCF relative to the in-plane bending moment at the brace of the overlapping brace, it is preferable to have smaller brace's diameter than the leg's one in other to reduce the SCF level. This raises a conflicting design problem when defining the diameters of the K-joint members.

In general, the effect of brace *B* in K-joints is not the dominant. The associated sensitivities are most of the time negligible except for the out-of-plane bending moment. For this case, the rules governing the brace *A* still hold except for the diameter ratio. In clear, whereas large brace *A* diameter is preferable for almost all the cases, it is gainful to decrease the brace *B* diameter. In any case and for both braces, smaller incidence angles and wall thicknesses comparable to the leg's one are favourable.

Whether gap or overlap K-joints have been chosen, design guidance rules are given in Table 4.4 for their efficient design.

Table 4.4: Guidance rules for efficient K-joint design.

Brace	Parameters	Gap K-joints	Overlap K-joints	
			Through brace	Overlapping brace
A	Diameter	***Dilemma***: brace's and chord's diameters should be as similar as possible, in general!		
	Wall Thickness	***Dissimilar***: brace's and chord's wall thicknesses should be as different as possible		
	Chord's shell rigidity	***Flexible***: the chord's wall should be thin relatively to its diameter		
	Chord's slenderness	***Short***: the chord's diameter should be relatively large compared to its length		
	Incidence angle	***Acute***: the angle between the brace and the chord should be as small as possible		
	Gap's slenderness	***Dilemma***: see description above	- *NA* -	- *NA* -
B	Diameter	***Dissimilar***: brace *B*'s and chord's diameters should be as different as possible		
	Wall Thickness	***Dissimilar***: brace *B*'s and chord's wall thicknesses should be as different as possible		
	Incidence angle	***Acute***: the angle between brace *B* and the chord should be as small as possible		

4.2.5 A case study: the Re-design of a K-joint

A lowest K-joint in the DTU 10 MW Jacket is used as a case study. It is an overlap K-joint connecting two braces of outer diameter $d = 540$ mm and wall thickness $t = 20$ mm each to a leg of outer diameter $D = 684$ mm and wall thickness $T = 45$ mm. Fatigue lifetime calculations are carried out for the through brace based on fatigue loads assessed under DLC 1.2. The SCFs of the selected welds are given in Table 4.5 and the minimum fatigue lifetime are 23 years for the chord side and 21 years for the brace side, which are insufficient and require a design update.

Table 4.5: SCFs for the initial design.

Side	Axial (AC)	In-plane (MIP)	Out-of-plane (MOP)	fatigue lifetime [years]
Chord	1.70	1.27	3.04	23
Brace	1.91	2.15	2.76	21

A design update strategy can consist of changing the leg dimensions in order to keep unchanged the nominal stresses. (Changing the leg dimensions modifies the structure and new simulations will yield a new set of internal loads. The changes of internal loads are assumed insignificant as far as the support structure natural frequencies are not significantly altered.) As per the guidance rules tabulated in Table 4.4, the SCFs can be reduced by decreasing the leg diameter or by increasing its wall thickness. The new diameter is obtained by multiplying the initial diameter by 0.95 and the new wall thickness is obtained by multiplying the initial wall thickness by 1.05. Table 4.6 shows that both strategies effectively increase the fatigue lifetime of the joint by reducing the SCFs. The combination of these strategies further enhances the joint performance.

Table 4.6: Design improvement by changing the leg dimensions.

SCFs and lifetime ...	... at the Chord				... at the Brace			
Re-design strategy	AC	MIP	MOP	Life [yrs]	AC	MIP	MOP	Life [yrs]
Initial design	1.70	1.27	3.04	23	1.91	2.15	2.76	21
$0.95D$	1.62	1.23	2.84	31	1.85	2.12	2.54	27
$1.05T$	1.59	1.19	2.76	35	1.87	2.11	2.58	25
$(0.95D) + (1.05T)$	1.52	1.16	2.59	47	1.81	2.08	2.38	33

Another design update strategy can involve the change of the brace dimensions. According to the guidance rules, the brace diameter should be increased or its wall thickness should be decreased. Table 4.7 presents the results for various re-design strategies. By increasing the brace diameter, the minimum fatigue lifetime of the joint increases due to the reduction of the SCFs and the decrease of the nominal stresses. However, if decreasing the brace wall thickness actually lowers the SCFs, the nominal stresses are increased and it results in a decrease of the joint performance. Yet, combining the reduction of the brace wall thickness to the increase of brace diameter reduces the conservatism created by just enlarging the diameter.

In general, priority will be given to the modifications that are less likely to affect the other modes. For example, increasing the brace diameter is preferred to decreasing the brace thickness as the shell buckling limit state can be violated in the latter case. Similarly, increasing the leg wall thickness is preferred to decreasing its diameter to prevent column buckling for example.

4.2.6 Other Techniques to Improve the Performance of Welded Joints

Notwithstanding the effort brought to reduce the SCFs, the stress levels can sometimes be so high that the fatigue requirements are still not satisfied. In these cases, other techniques could be applied

Table 4.7: Design improvement by changing the brace dimensions.

SCFs and lifetime ...	... at the Chord				... at the Brace			
Re-design strategy	AC	MIP	MOP	Life [yrs]	AC	MIP	MOP	Life [yrs]
Initial design	1.70	1.27	3.04	23	1.91	2.15	2.76	21
$1.10d$	1.68	1.25	2.96	55	1.85	2.12	2.60	51
$1.05d$	1.69	1.26	3.02	35	1.88	2.13	2.69	33
$0.95t$	1.62	1.21	2.94	22	1.89	2.13	2.74	17
$(1.05d)+(0.95t)$	1.62	1.20	2.92	34	1.86	2.12	2.67	27

without altering the whole jacket geometry. For example, one can provide post-weld heat treatment or ensure low residual stresses so as to validly account for the influence of the mean stress as presented above. Considerations of the overstress phenomenon can also reveal more fatigue resistance [56]. Other techniques consists of improvement by fabrication, which include grinding, TIG dressing, hammer peening [48], and ultrasonic peening [57]. Further details of these techniques are out of the scope of the present study.

Furthermore, if these techniques are not sufficient to increase the fatigue resistance, a more global strategy moving from the joint level to the member level can be envisaged. Indeed, braces can be supplemented by dampers of magneto-rheological type, for example.

4.3 Magneto-rheological Damper

4.3.1 Magneto-rheological Damper Device: Anatomy and Phenomenology

Magneto-rheological (MR) dampers are schematically made of a piston which translates in a magneto-rheological fluid. Rheological fluids are materials that combines both plastic solid and non-Newtonian fluid properties. As plastic, they permanently deform under sufficiently high stresses and as non-Newtonian, the strain rates are not proportional to the shear stress. In this application, specific oils are utilized for their rheological properties. They are enriched with metallic suspension of micrometer scale. As shown in Figure 4.13, when subjected to a magnetic field, the particles align to increase the apparent viscosity of the solution, thus the designation of *magneto-rheological fluid*. The magnetic field is generated by an electric current along a coil surrounding the chamber.

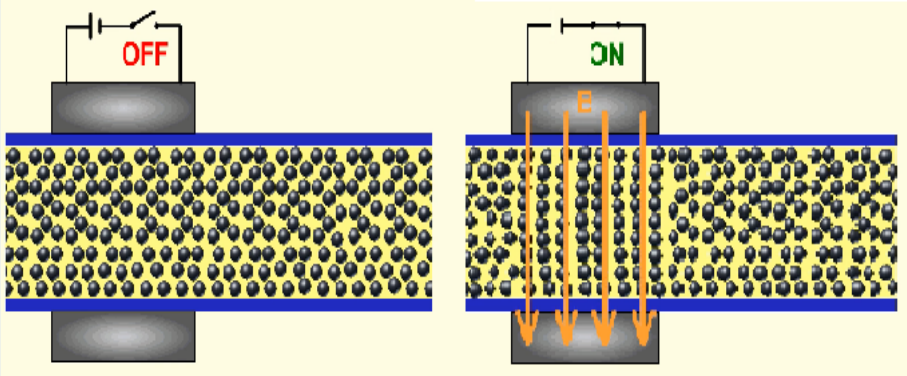

Figure 4.13: Magneto-rheological fluid effect [58]. On the left, in the absence of electric current, and thus the absence of magnetic field, the flow of fluid and the particles is continuous. On the right, the electric current creates a magnetic field, which aligns the particles and stops the flow, increasing thereby the apparent viscosity of the fluid. Double-clicking on the figure launches a video if the document is read in its digital form.

External actions that tend to move the piston exert strains on the fluid and the generated stresses develop a force that resists to the external displacement. Other contributions to the force include the fluid inertial effect and the elastic contribution of the accumulator. Reference is made to [59] for a schematic representation of a typical magneto-rheological damper device.

The relationship between the exciting external actions on the piston (displacement, velocity, and acceleration) and the reaction force developed by the damper system is extremely nonlinear and presents a hysteretic loop. In order to accurately represent the physics of MR dampers, various phenomena, such as fluid inertia and shear thinning effects, should be considered [60]. Yang *et al.* [60] proposed a phenomenological model based on Bouc-Wen hysteresis model [61] as shown in Figure 4.14. The specificity of this model rests on the variable damping coefficient. In addition to the ability to estimate the MR damper behaviour, this model has the advantage to use few parameters and state variables compared to the other state-of-the-art models [60].

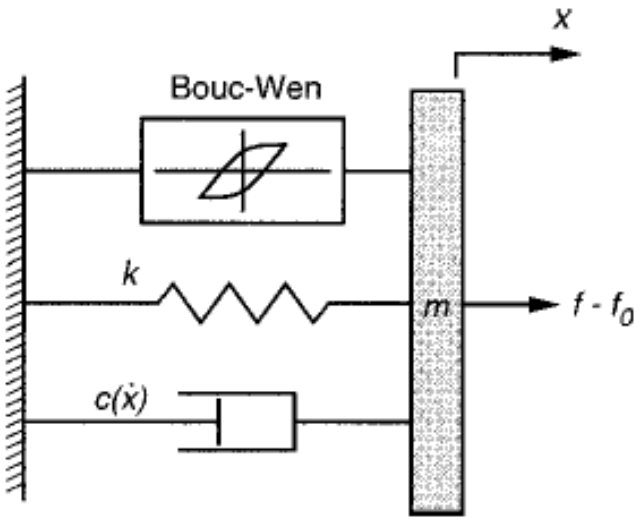

Figure 4.14: Phenomenological model of MR damper proposed by Yang *et al.* [60].

The dynamic equilibrium along the x-axis gives the damper force:

$$f = m\ddot{x} + c(\dot{x})\dot{x} + kx + \alpha z + f_0$$

with the evolutionary variable z of the Bouc-Wen model [61] is obtained by:

$$\dot{z} = -\gamma|\dot{x}| \cdot z \cdot |z|^{n-1} - \beta\dot{x}|z|^n + A\dot{x}$$

and the variable damping coefficient:

$$c(\dot{x}) = a_1 e^{-(a_2|\dot{x}|)^p}$$

where the variables are described in Table 4.8 for a constant current $I_{max} = 2.0\,A$ and for a rated capacity of 200 kN. In fact, while the others are constant, the parameters α, a_1, a_2, m, n, and f_0 vary with the current as presented in Table 4.9.

The dynamics of the system when the MR fluid reaches the rheological equilibrium needs to be accommodated by a first order filter:

$$H(s) = \frac{31.4}{s + 31.4}$$

The selected device is 1.00 m long and about 300 mm wide with 203 mm inside diameter. It is composed of 5.0 litres of MR fluid and 1.5 km of coil wire for a total mass of 250 kg. The coil has an induction of 6.6 H and a resistance of 21.9 Ω. With a stroke of ± 80 mm, about 90 cm^3 of fluid is energized by the magnetic field at any given instant.

Table 4.8: Parameters describing the magneto-rheological damper model [60].

Symbols	Units	Description	Values
γ	1/m	Bouc-Wen constant	25179.04
β	1/m	Bouc-Wen constant	27.1603
A	1/m	Bouc-Wen constant	1377.9788
k	N/m	Accumulator stiffness and MR fluid compressibility	20.1595
p	-	Positive constant	0.2442
α	N	Positive constant	$2.30 \cdot 10^5$
a_1	Ns/m	Positive constant	$35.00 \cdot 10^6$
a_2	s/m	Positive constant	4335.00
m	kg	Mass equivalent to stiction phenomenon and inertia effect	22000.00
n	-	Bouc-Wen constant	6.73
f_0	N	Damper friction force due to seals and measurement bias	5126.00

Table 4.9: Variation of some parameters with the current [60].

Current (A)	α (10^5N)	a_1 (Ns/m)	a_2 (10^6Ns/m)	m (t)	n (-)	f_0 (N)
0.0237	1.3612	4.349	862.03	3.00	1.0000	1465.82
0.2588	2.2245	24.698	3677.01	11.00	2.0679	2708.36
0.5124	2.3270	28.500	3713.88	16.00	3.5387	4533.98
0.7625	2.1633	32.488	3849.91	18.00	5.2533	4433.08
1.0132	2.2347	24.172	2327.49	19.50	5.6683	2594.41
1.5198	2.2200	38.095	4713.21	21.00	6.7673	5804.24
2.0247	2.3002	35.030	4335.08	22.00	6.7374	5126.79

4.3.2 Operational Conditions and Control Strategy

The electricity that flows in the coil can be commanded either by controlling the current parameter or by controlling the voltage parameter. The test carried out by Yang *et al.* [60] showed that the current-based control leads to much more responsive damper than the voltage-based control. Indeed, 1 s is needed for the voltage power supply to achieve 95 % of the final value, which is too slow compared to the high-frequency harmonics contained in the vibrations of wind turbine systems. With the current driven system, the final value is attained in 0.06 s. Therefore, the latter strategy is utilised for this application.

The observation of the mathematical model indicates that even with zero current, MR dampers will still react to external actions. This property allows a minimum service even if a failure occurs or the input energy is null. The other extreme occurs at 2.0 A and above, where the MR effect saturates. The input energy is then maximal but not necessarily needed by the damper if the excitation requirements are not considerable for example. Between the two extreme cases, a control strategy can help to efficiently use the input energy. The idea is to input a current in proportion to the exciting actions. Several studies have shown the appropriateness of the fuzzy logic as a control methodology for this type of problems ([62], [63]). These three operational strategies respectively correspond to passive, active, and semi-active case. As the power (78 W) needed by the damper devices are relatively small, the active strategy is opted in the present study with constant current of 2.0 A.

4.3.3 Application on Jacket and Installation Procedure

The vibrations of the jacket braces engender the motions of the brace ends and inversely. Exerting an action that counteracts the relative motions of brace ends will reduce brace vibrations. If a force was

set to inhibit brace node motions, braces would vibrate less, and less fatigue would be engendered. MR damper devices are suitable for this purpose as the piston basically resists to the exterior actions. Inserted inside a brace with its base attached to one brace end and its piston to the second brace end, the relative motion of the brace nodes is hindered by the damper force, which should translate into reduction of the global fatigue damage.

The system formed by MR damper and brace described above can be built up during the jacket manufacturing in four main steps, Figure 4.15.

Step (a): a can with flattened sides that firmly fits the leg interior is inserted into the leg; if necessary, an extra fixative point like bolt can be added. The MR damper base is hooked to the can.

Step (b): the X-brace is put in place with the relevant brace set around the MR damper, which is possible due to the transversal size of the damper (less than 600 mm).

Step (c): the piston is pulled off and hooked to the second can, which is already set inside the other leg.

Step (d): the second leg is put in place as the piston is brought to its neutral position. The welding of the K-joints are done.

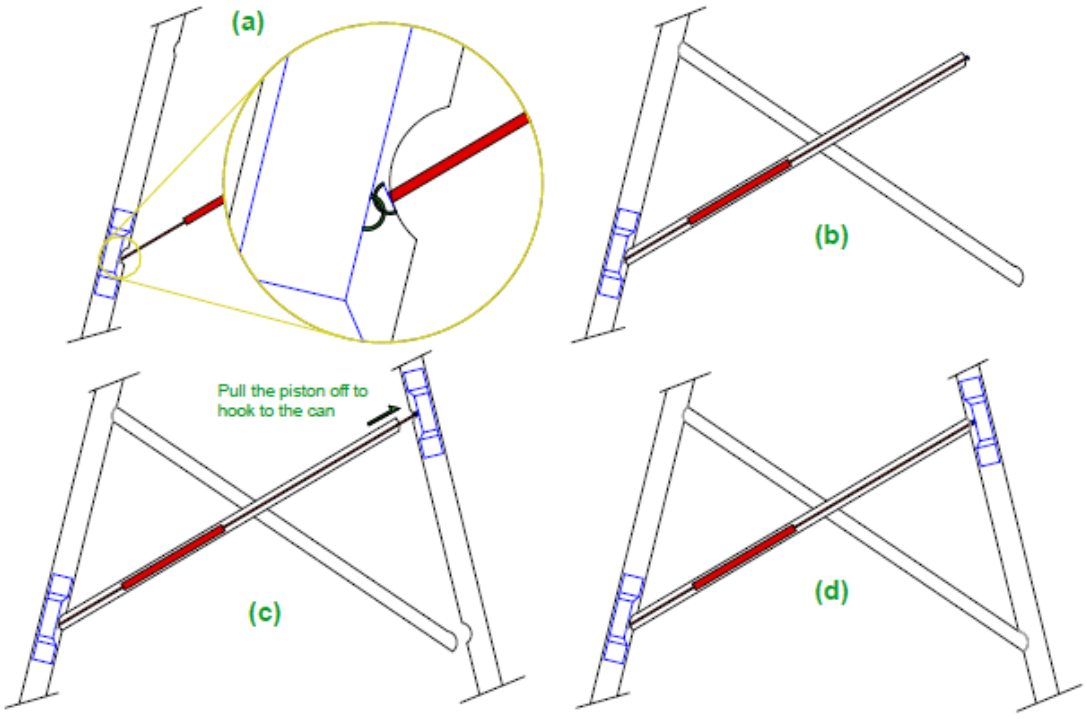

Figure 4.15: Installation steps of the MR damper into the jacket brace. (a) Hooking of the first MR damper end on the inserted can. (b) The X-brace is put in place around the MR damper. (c) Hooking of the second MR damper end. (d) Welding of the legs to the X-brace.

4.3.4 Impact on Fatigue Damage

The efficiency of the MR damper is investigated using a structure setup made of the INNWIND 20 MW RWT supported by the DTU 20 MW Jacket. The hotspots are selected at the first X-brace level. The hotspot nomenclature is illustrated by Figure 4.16: P, Q, R, and S designate the sides and 1,

2, 3, and 4 the positions of welded joints on the same side. Joint names are the formed from the combination of the two labels. For example, joints can be named P1, P2, or Q3.

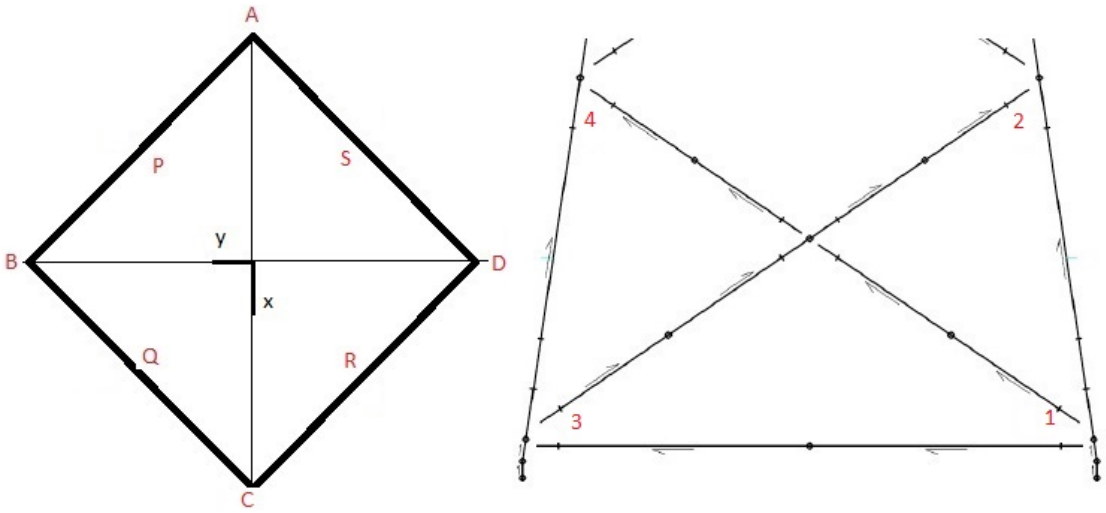

Figure 4.16: Selected hotspots for the DTU 20 MW Jacket substructure. (Left) plan view with side label. (Right) position of the selected hotspots on a given jacket side. A joint name is made of the side label name (P, Q, R, or S) and the joint position (1, 2, 3, or 4). For example, joint names can be P1, P2 etc. Sides are looked at from the inside of the jacket.

Fatigue loads are evaluated under DLC 1.2. One brace of the DTU 20 MW Jacket is equipped with an active 200 kN MR damper device as shown in the bold line in Figure 4.20. Results (as shown in Figure 4.22) show unsatisfactory fatigue lifetime change. This can be explained by the fact that the nominal capacity of the device is not sufficient to counteract the loads in presence. Indeed, this device has been developed for civil engineering purposes. Though very large compared to the models used in automotive industry, it is still of small capacity for multi-megawatt wind turbine structures. In order to obtain large capacity systems, a pair of devices is assembled in parallel such that the resulting capacity becomes 400 kN. The brace Q2 – Q3 is equipped with the damper assemblage and the fatigue loads are evaluated. Figure 4.17 compares the time series of the fatigue axial load at the joint Q2 from the non-equipped structure, taken as reference, versus that from the structure equipped with a double dampers. It can be noticed that the fatigue load amplitudes have significantly reduced; suggesting a reduction of the fatigue damage.

In another form, the comparison of the respective frequency spectra of the presented time series shows a significant reduction of the energy with the case of the damper assemblage (see Figure 4.18).

The dampers mainly impact the fatigue axial force. Indeed, the damper systems counteract the axial deformation of the equipped brace, which reduces the axial strain amplitude and ultimately the axial force amplitude. However, the damper's effect on bending moments is not satisfactory enough. Figure 4.19 shows the time series and the spectra for the out-of-plane bending moments at node Q2. A relatively small increase of the fatigue damage can be noted from the spectra. This is due to the fact that the connection between the K-joint and the brace gets a limited displacement and behaves more like a rigid joint, thus attracts more loads in terms of amplitude.

Combining the effects of the axial force and bending moments, the maximum fatigue damages at all four hotspots of side Q are estimated for the reference structure and for the equipped structure, respectively. The relative change of the maximum fatigue damages $\Delta(D) = -1 + D_{equipped}/D_{reference}$ is calculated and presented in Figure 4.20. Computations show a damage reduction of 33 % at node Q2 and 83 % at node Q3. At nodes Q1 and Q4, the reductions are 19 % and 0 %, respectively. At node

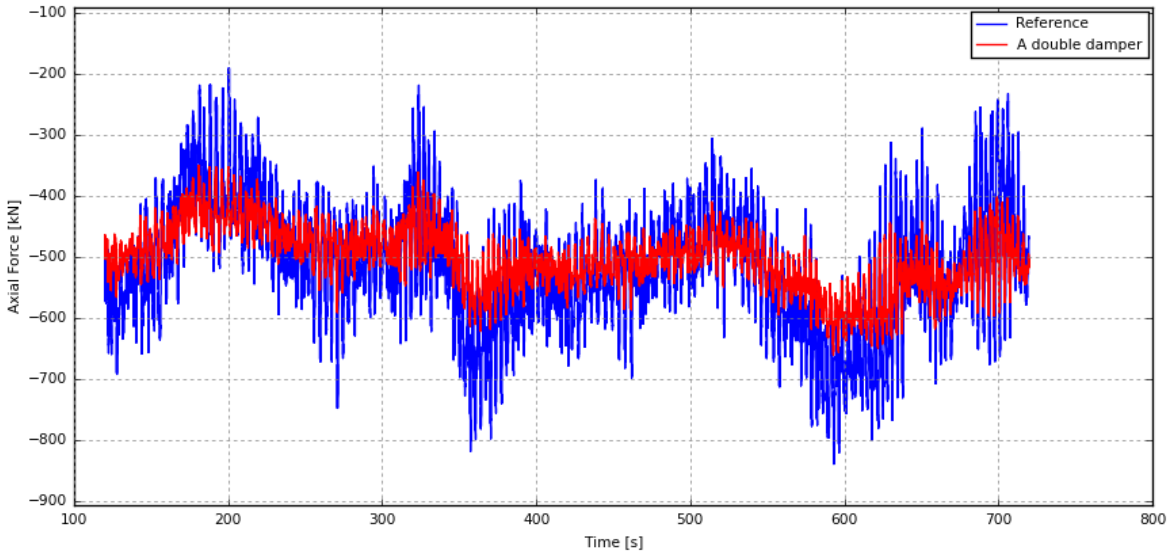

Figure 4.17: Times series of the fatigue axial forces at node Q2. The reference fatigue axial force (in blue) shows higher amplitude than that of the fatigue axial force with a double damper (in red).

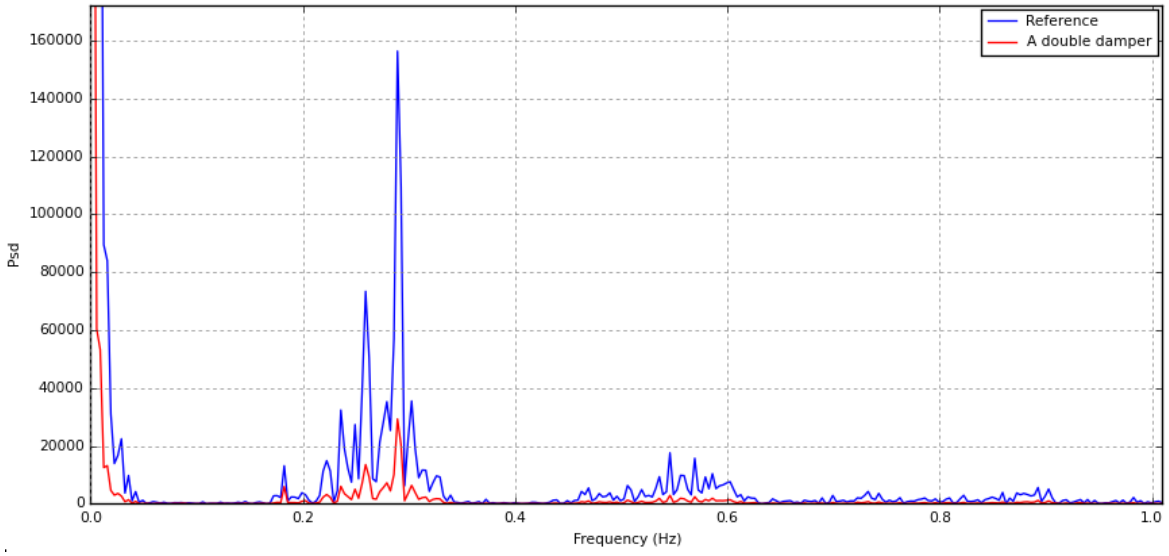

Figure 4.18: Spectra of the axial forces at node Q2. The reference axial force (in blue) shows higher energy than that of the axial force with a double damper (in red).

Q1, the fatigue damage reduction is caused by the vibration reduction of leg Q1-Q2. However, there is no noticeable change at node Q4 as the damper system does not significantly affect leg Q3-Q4.

Despite the overall satisfactory results obtained on side Q, negative effects are observed in the other sides, where the fatigue damages increase by 2 % to 102 %. This can be due to the increased share of vibrations by the other sides as side Q has been rigidified. In particular, joints S4 and Q2 are adjacent to side P at legs A and B, respectively. The vibration reduction at joint Q2, which leads to a damage reduction of 33 %, contributes to an increase of vibratory motion at joint S4, which leads to an increase of fatigue damage of 102 %. This compensatory effect suggests a design strategy of multiple MR damper setups that conjointly impact at different joints.

Therefore, one pair of MR dampers is inserted in one brace in each side. Two others configurations are investigated as illustrated in Figure 4.21.

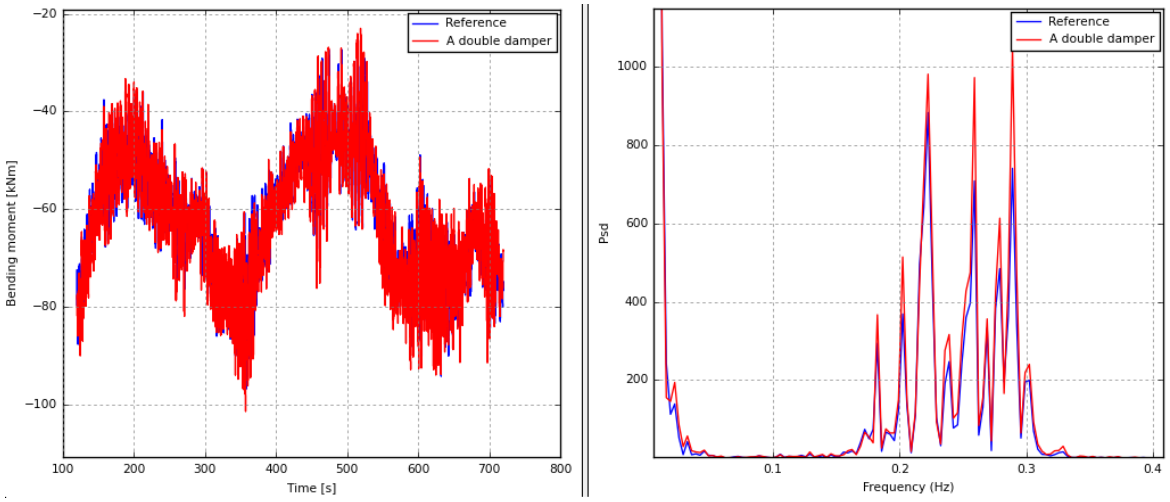

Figure 4.19: Time series and spectra of the out-of-plane bending moment at node Q2. The reference load (in blue) shows relatively smaller amplitude than the load with a double damper (in red).

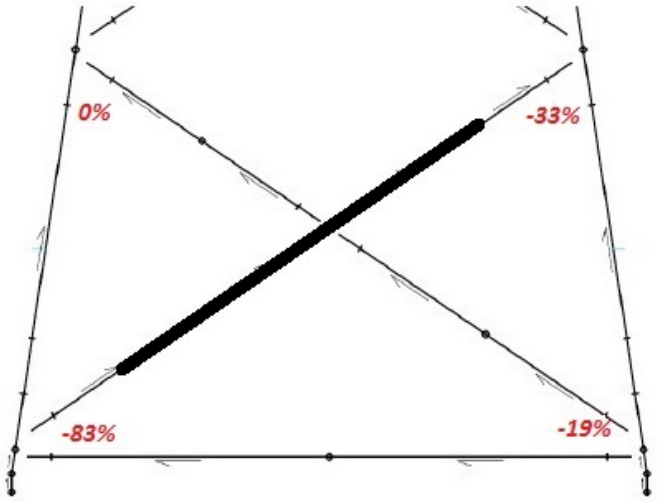

Figure 4.20: Damage change on side Q after setting-up a pair of dampers.

Configuration *Boat*: pairs of MR dampers are ascending in one side and descending in the adjacent side. In other words, damper assemblages are alternatively put in place in a left-down-and-right-up manner (ascending) in one side and in a left-up-and-right-down manner (descending) in the next side.

Configuration *Rain*: pairs of MR dampers are consistently set either ascending or descending in all sides.

Figure 4.22 depicts the fatigue damage change for each node between the reference case and each MR damper setup case. The results for the four aforementioned cases (unique damper, pair of dampers, Configuration *Boat*, and Configuration *Rain*) are shown. With the unique damper, insignificant improvement is partially obtained in side Q but nowhere else. The double damper positively affects the whole side Q, but shows some negative effects on the other sides as said above. Configuration *Boat* shows a consistent reduction of fatigue damage varying from 4 % to 79 % except at node Q4 and at node S4 where slight increases are observed. With Configuration *Rain*, a similar behaviour

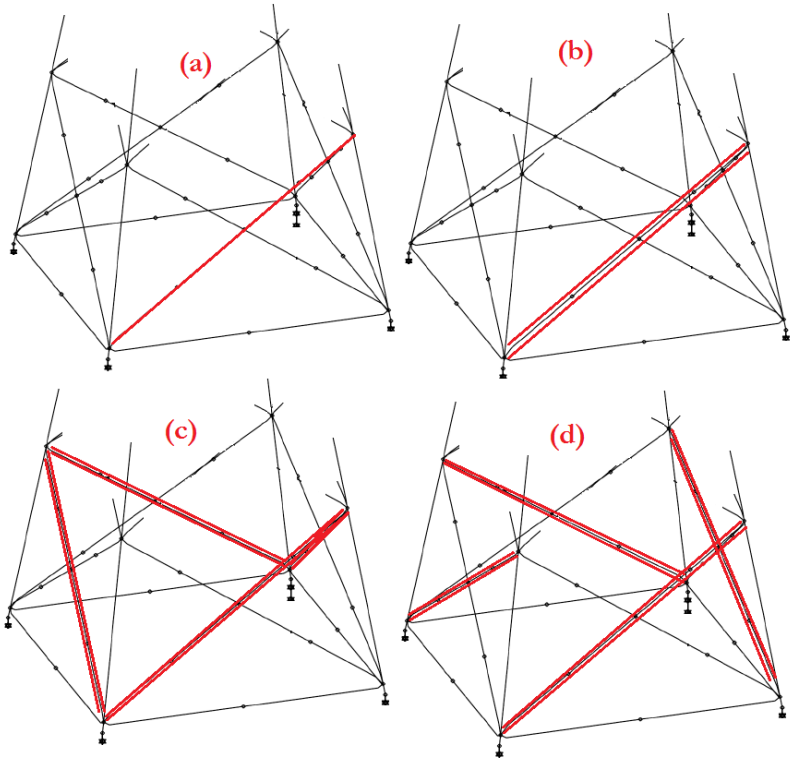

Figure 4.21: Four different configurations. (a) one damper. (b) double damper. (c) Configuration *Boat*. (d) Configuration *Rain*. Red lines represent MR device units.

is observed: fatigue damage reduction is general except for the nodes P1 and S4. This shows that an appropriate distribution of the MR dampers around the jacket can contribute to the mitigation of fatigue damage at every point of interest depending on the design objectives.

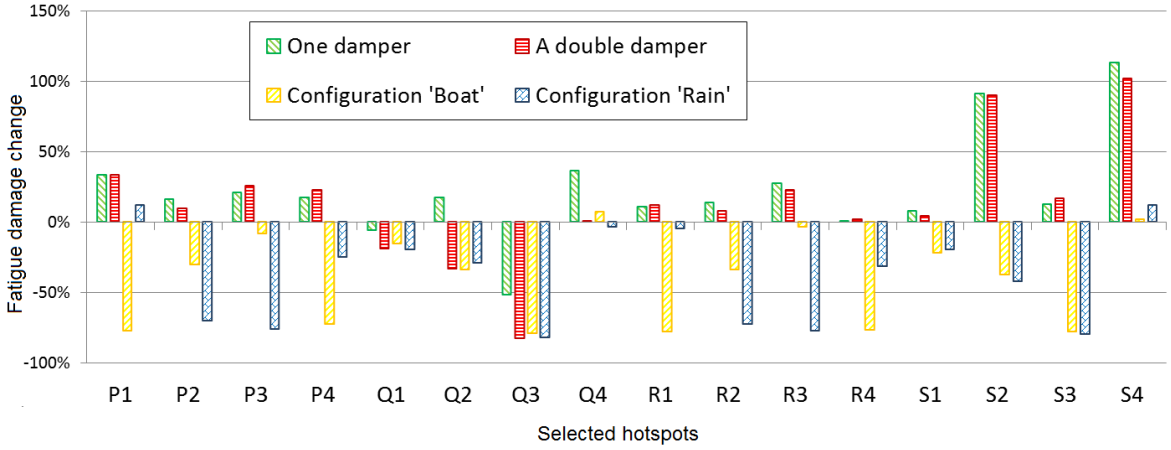

Figure 4.22: Fatigue damage change at the selected hotspots for the four configurations.

Either in replacement of the distribution of MR damper devices around the structure or as a supplement, a global-level fatigue alleviation strategy based on purposefully tailored rotor can be envisioned in order to make up for some of the scantiness of the MR dampers.

4.4 Impact of Optimized Rotor Blades on the Fatigue Demand

The minimum fatigue lifetime of the INNWIND 10 MW Jacket has been estimated to four years [13], which is clearly lower than the intended lifetime of typical offshore wind turbine that is 25 years. In order to extend its fatigue lifetime, the optimized rotor is employed. Three setups are considered for the investigation of the rotor change effect on the fatigue:

- The DTU 10 MW RWT, with the reference rotor placed on land;
- The DTU 10 MW RWT, with the reference rotor supported by the INNWIND 10 MW Jacket placed at 50 m water depth; and
- The DTU 10 MW RWT, with the optimized rotor supported by the INNWIND 10 MW Jacket placed at 50 m water depth.

4.4.1 Global Performance of the Whole Structure

The global performance of the structures is evaluated in terms of natural frequencies, power curves, and aerodynamic rotor thrust. Table 4.10 presents the first natural frequencies for the three setups, respectively. It can be seen that, whereas the jacket substructure has stiffened the support structure compared to that of the on-land setup, the effect of the rotor is insignificant on the support structure's frequencies. Therefore, the controller used for the reference rotor setup can be utilised for the optimized rotor setup without further change.

Table 4.10: Respective natural frequencies [Hz] of the three setups

Mode	On-land setup	Offshore, Reference rotor setup	Offshore, Optimized rotor setup
Mode 1	0.251	0.288	0.287
Mode 2	0.256	0.295	0.294
Mode 3	0.547	0.550	0.551
Mode 4	0.589	0.592	0.588
Mode 5	0.630	0.632	0.618

The power curve and the aerodynamic rotor thrust as depicted in Figure 4.23 compare the performance of the three setups. The power productions on the left side are similar with either setup, notwithstanding the insignificant reduction observed around the rated wind speed with the optimized rotor setup. The annual energy production with the optimized rotor decreases by 0.44 % compared to that with the reference rotor. The main effect is observed on the right side with the considerable reduction (about 9.4 %) of the thrust force due to the optimized rotor from about 1600 kN with the reference rotor to about 1450 kN.

4.4.2 Change of Fatigue Loads at the Tower Bottom

The positive effect of the optimized rotor on the rotor thrust suggests the reduction of fatigue loads at the tower bottom. The damage equivalent loads (forces and moments) are computed according to Equation 4.9 at the interface between the tower bottom and the transition piece. The relative change in fatigue damage equivalent load from the reference rotor setup to a optimized one is obtained by $\Delta(L_{eq}) = -1 + L_{eq}^{opt}/L_{eq}^{ref}$.

$$L_{eq} = \int_{V_{in}}^{V_{out}} p(V) \int_{\Delta L_a}^{\Delta L_b} \left(\frac{n(\Delta L|V)\Delta L^m}{N_{eq}} \right)^{(1/m)} \mathrm{d}\Delta L \, \mathrm{d}V \tag{4.9}$$

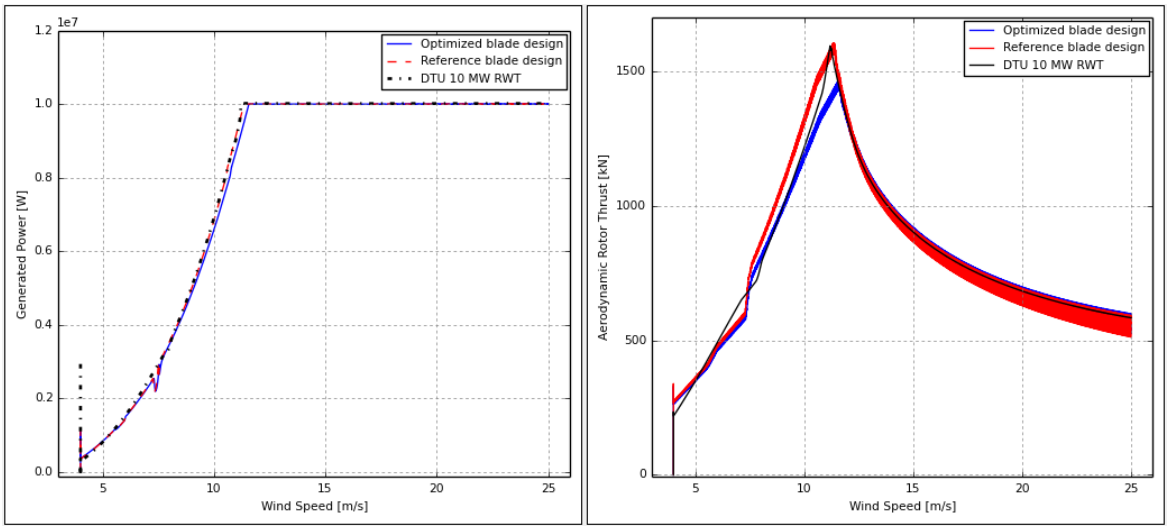

Figure 4.23: Characteristic curves for each of the three setups. (Left) power curve. (Right) aerodynamic rotor thrust.

where:

V :	mean wind speed;
V_{in}, V_{out} :	mean wind speed bounds;
$p(V)$:	probability of occurrence of the mean wind speed V;
m :	Wöhler exponent. $m = 4$;
N_{eq} :	equivalent number of cycles during the structure lifetime. $N_{eq} = 10^7$; and
$n(\Delta L\|V)$:	number of the load ranges ΔL given V, obtained after rainflow counting.

As results, Figure 4.24 shows a decrease of all fatigue loads with the optimized rotor setup in comparison to those of the reference rotor setup. In general, the reductions range from 1.4 % to 8.4 %, which suggests fatigue lifetime improvement of the jacket substructure. Especially, the largest reduction is obtained for the fatigue damage equivalent fore-aft moment, which reduces from 97,482 kNm to 89,269 kNm.

4.4.3 Fatigue Lifetime Improvement for the Jacket Components

The reduction of tower-bottom fatigue loads should reflect on the jacket component fatigue loads and thus minimum fatigue lifetime. Indeed, several hotspots are selected on the INNWIND 10 MW Jacket. Ref [13] indicates that the critical hotspot is one of the lowest K-joints. All the K-joints of the same level are investigated. The relevant nomenclature is illustrated by Figure 4.25. The four jacket sides are named with capital letters A, B, P, and Q. Given a jacket side, the K-joint are labelled with letters u and v. The overall designation of a typical K-joint is made of combination of the two tags: it can be Au or Pv, for example.

The minimum fatigue lifetime of the height selected hotspots are estimated for the reference rotor setup and the optimized rotor setup, respectively. Results are shown in Figure 4.26. Overall, the minimum lifetime of the INNWIND 10 MW Jacket has improved from four years to seven years. Hotspot by hotspot, the changes ($\Delta(L_f) = -1 + L_f^{opt}/L_f^{ref}$) range from 33 % to 125 %, approximately. This means that, due to the optimized rotor, the minimum fatigue lifetime can be increased at the critical hotspots, and steel material can be saved at other hotspots that were already satisfying the fatigue limit state. Thus, it results a combination of material saving and lifetime improvement.

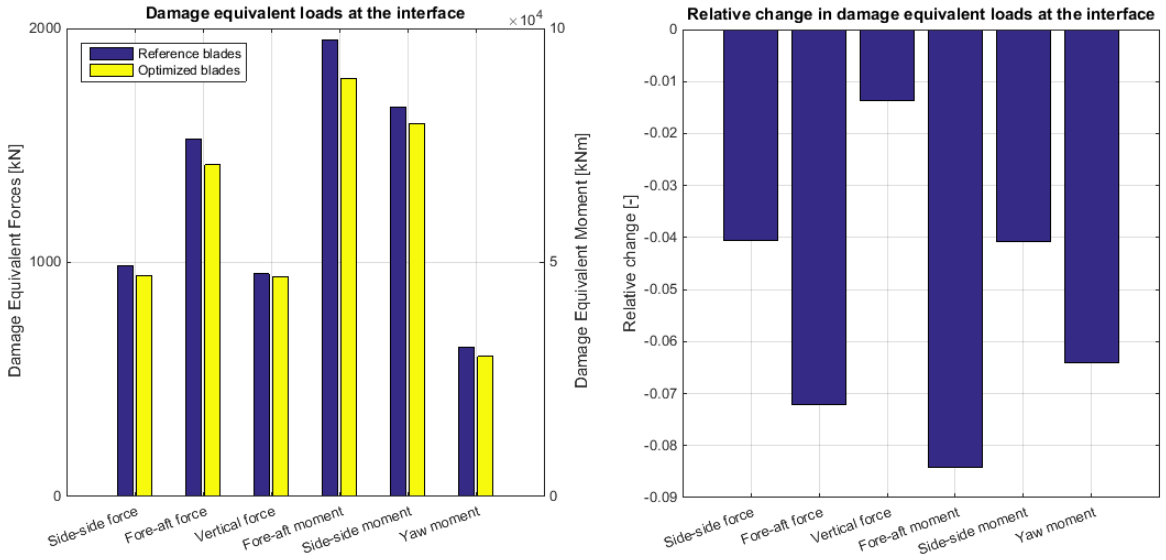

Figure 4.24: Effect of the rotor optimization on the fatigue damage equivalent loads at the interface. Due to blade optimization, all fatigue loads are reduced (right) with a relative change varying from 1.4 % to 8.4 % (left).

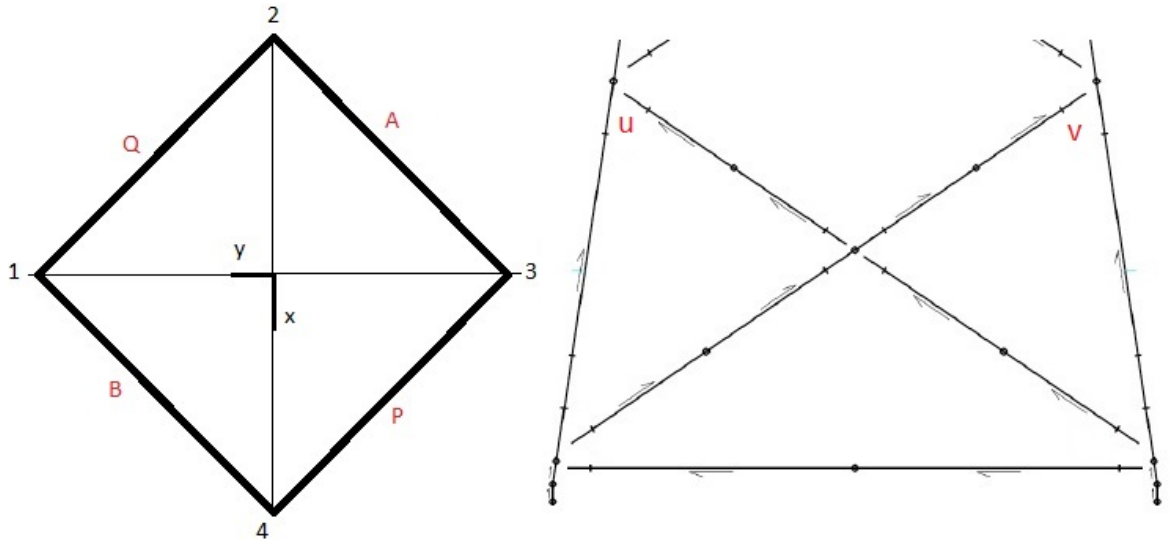

Figure 4.25: Selected hotspots for the INNWIND 10 MW Jacket substructure. (Left) plan view with sides' names: A, B, P, and Q. (Right) Label of the selected hotspots on a given jacket's side: u and v. A typical joint's name is made of the side's name and the joint's position. For example, joint's names can be Au or Pv.

4.5 Concluding Remarks

The present chapter addresses methods for fatigue lifetime improvement of jacket substructures supporting 10 MW or 20 MW wind turbines placed at 50 m water depth. After having presented the procedure to evaluate the fatigue lifetime of critical joints of jackets, three methods of fatigue lifetime improvement have been introduced. Each of these methods focuses on different levels of the structure including the joint level, the brace level, and the support-structure level.

The method acting on the joint level is based on SCF reduction strategy. Various joint types are

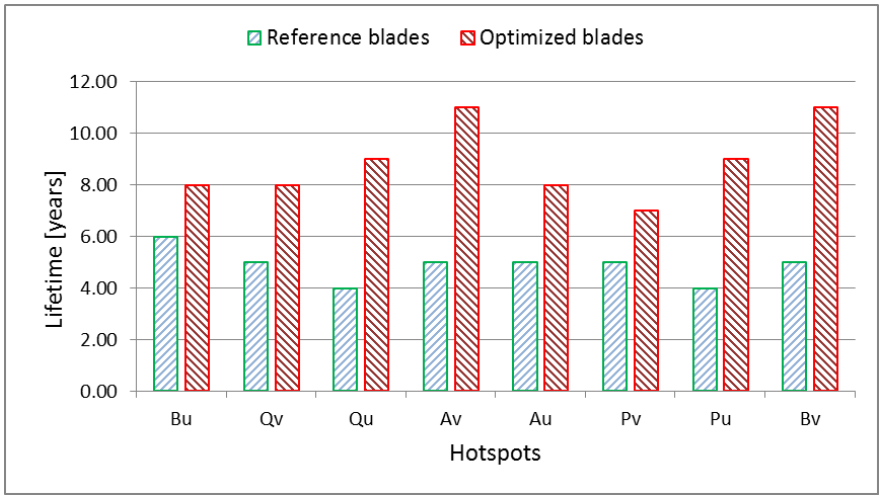

Figure 4.26: Improvement in minimum fatigue lifetime at all selected hotspots.

considered: Y- and X-joints, gap and overlap K-joints. Pearson, Spearman, and Kendall correlation coefficients of all influential parameters on SCFs are computed as sensitivity measures using the experimental design method. As a result, clear guidance rules have been stated for re-design of each joint type so as to extend their fatigue lifetimes. The rules guide the designer on how to set the joint geometrical dimensions (diameters, wall thickness, slenderness, shell rigidity, incidence angle, gap slenderness) in order to reduce the SCFs and thereby lessen the hotspot stresses.

Additional methods based on fabrication improvement are proposed as a supplement of the SCF reduction technique: post-weld heat treatment, grinding, TIG dressing, and hammer/ultrasonic peening, are mentioned. In case techniques involving SCF reduction and fabrication improvement are not sufficient to increase the fatigue resistance, the members can be supplemented by dampers of magneto-rheological type, for example.

The other fatigue lifetime improvement method, which focuses on brace level, consists of the insertion inside the brace of an assemblage of MR damper with the aim of alleviating the vibration of the brace and thereby to reduce the fatigue demand on a jacket for a 20 MW wind turbine. The proposed technique resolves some of the problems encountered with passive tuned vibration absorbers and passive tuned mass dampers for the DTU 10 MW reference wind turbine namely (i) the width of the operational frequency range; (ii) the size of the device especially for larger structures; and (iii) the interaction between multiple devices.

The study reveals the potential of MR dampers to alleviate fatigue damage. Up to 83 % of fatigue damage reduction at a critical joint can be obtained. The low energy amount needed for one damper (about 78 W) opens the possibility to have multiple devices on the same jacket. Whereas a unique damper inserted to a brace is proven not effective enough to alleviate the vibration, an assemblage of two dampers is efficient to mitigate the damage for the brace it is mounted in. However, the stress redistribution have increased fatigue damage at other connections. To circumvent this issue, damper devices were placed at several location in the structure under different configurations. Results show the necessity of selecting appropriate configurations in order to maximize the benefits of the fatigue reduction strategy at specific links, without causing any increased damage at other sections.

Further studies may be required to propose a procedure of smart distribution of the devices around the jacket. The robustness of the system with respect to external actions and manufacturing tolerances may also be investigated, as well as the effect of the additional mass on the equipped brace. The MR damper used in this study is developed for civil engineering applications; it is encouraged to design dedicated MR devices for jacket. The latter may be of smaller diameter, longer, and of large nominal capacity. As the excitation actions in jacket are of small ranges (in the order of 1 - 2 mm for the

displacement for example), the dedicated MR dampers for jacket application may be more sensitive.

While waiting for more effective dampers, the shortcomings of the currently developed damper devices can be compensated for by a global reduction of fatigue demand on the support structure. This can be done through tailoring of the rotor such that the fatigue loads generated by the aerodynamics are minimized.

An aero-elastically tailored rotor design that reduces the fore-aft fatigue moment at the tower base is used. The aim is to prolong the fatigue lifetime of the jacket substructure. Using the DTU 10 MW RWT, the optimization was carried out based on standard onshore site conditions, and the resulting blade design was mounted on a jacket supported turbine placed at specific offshore site conditions. The study has revealed three main inferences:

- It can be computationally expensive to carry out the optimization process on an offshore wind system under site specific metocean conditions. In order to reduce the computation cost, the optimization can be conducted on an onshore wind turbine under standard wind conditions, and the resulting optimized rotor will be effective on the offshore version.
- The optimized rotor effectively reduces all fatigue load components at the tower base with an insignificant loss of power production (0.44 %). This load reduction has been reflected both on nacelle components and on the jacket substructure, which results in fatigue lifetime improvement.
- It is expected that material savings can be achieved with this method at structures whose designs were already satisfactory with the reference rotor.

In general, these methods for fatigue lifetime improvement for jackets provided successful results by either the improvement of existing methods (efficient joint design and aero-elastic rotor optimization) or the adaptation of technologies from other industries (MR damper borrowed from automotive or civil engineering). Extending the innovation, disruptive substructure system that are more adapted for multi-megawatt wind turbines at deep waters can be proposed. An emerging example is the development of semi-floater substructure.

5

Paper I: Development and design of a semi-floater substructure for multi-megawatt wind turbines at 50+ m water depths

Ocean Engineering 125 (2016) 226–237

Contents lists available at ScienceDirect

Ocean Engineering

journal homepage: www.elsevier.com/locate/oceaneng

Development and design of a semi-floater substructure for multi-megawatt wind turbines at 50+ m water depths

Wilfried Njomo Wandji *, Anand Natarajan, Nikolay Dimitrov

DTU Wind Energy, Technical University of Denmark, Frederiksborgvej 399, DK-4000 Roskilde, Denmark

ARTICLE INFO

Article history:
Received 9 March 2016
Received in revised form
24 May 2016
Accepted 11 July 2016
Available online 27 August 2016

Keywords:
Large wind turbine
Moderate water depth
Articulated joint
Semi-floater
Reliability analysis

ABSTRACT

A semi-floater concept as a substructure for multi-megawatt wind turbines is developed herein for installation at 50+ m water depths. The semi-floater concept is a hybrid between a fixed monopile type support structure and a floating spar buoy. The configuration of the substructure is composed of a floating system, a mooring system, and an articulated joint. A case study is carried out under specific design conditions and constraints. The detailed designs of the mooring system and of the articulated joint are iteratively carried out using a hydro-servo-elastic analysis tool for structure response, HAWC2, coupled with dedicated in-house software packages for structural design analysis, and Abaqus. A reliability analysis and fatigue load calculations are made to ensure a desired life expectancy of the structure. The semi-floater concept is shown to maintain acceptable fatigue load levels for all turbine components, and to exhibit low platform displacement at the mean sea level. Finally, the overall performance of the structure related to energy production is similar to that of a reference wind turbine situated on land.

1. Introduction

The development of offshore wind energy in high wind potential locations at moderately deeper waters of 50 m compared to present day installations requires newer support structure concepts that allow cost-effective construction and withstand marine loads and generated fatigue during its lifetime.

On one hand, Kallehave et al. (2015) summarised some typical fixed-bottom concepts used in wind energy industry, which include gravity-based, monopile, multi-pile, and jacket sub structures. Traditionally jacket type fixed support structures have been proposed at 50 m water depth, but such fixed support structures are subjected to high fatigue loads; and their design can be challenging, Von Borstel (2013). In addition, their manufacturing process (in the case of jacket for example) or their installation (for instance large diameter monopile or suction bucket) can be daunting.

On the other hand, Wang et al. (2010) categorized floating wind turbines into four main types: (i) spar-buoy type; (ii) tension-leg platform type; (iii) semi-submersible type; and (iv) pontoon type. Floating structures are attractive for increasing water depths (100+ m), but they may prove to be highly capital intensive at moderate water depths near 50 m.

Therefore, as a merger of different current design practices, this study presents a semi-floater concept developed as a hybrid between the fixed support types and the floating ones, with the objective to achieve a cost effective solution with low fatigue damage and maintain targeted displacements at mean water level. This concept has been proven in the oil and gas industry by Sedillot and Stevenson (1983) and was conceptually adapted to 5 MW wind turbines at 100+ m water depths by Sanz et al. (2013), where a conceptual model, which has modelled the articulated joint as a flexible beam, has been used to assess loads. Herein the detailed structural design of the components of a semi floater are developed and verified to required reliability levels as used in the wind turbine industry. The loads for the design process are generated based on specific design conditions and constraints for a typical installation site. The performance of the resulting design is assessed following an iterative design scheme with structural analysis of resulting stresses on the foundation and ensuring reliability and fatigue endurance.

2. Architecture of the proposed support

2.1. Description and mode of functioning

The proposed semi-floater concept is a combination of a classic monopile sub structure and a traditional spar-buoy floater. It is illustrated in Fig. 1 and consists of three main systems: an articulated joint, a mooring system, and a floating system. The

* Corresponding author.
E-mail addresses: wilw@dtu.dk (W. Njomo Wandji), anat@dtu.dk (A. Natarajan), nkdi@dtu.dk (N. Dimitrov).

http://dx.doi.org/10.1016/j.oceaneng.2016.07.021
0029-8018/

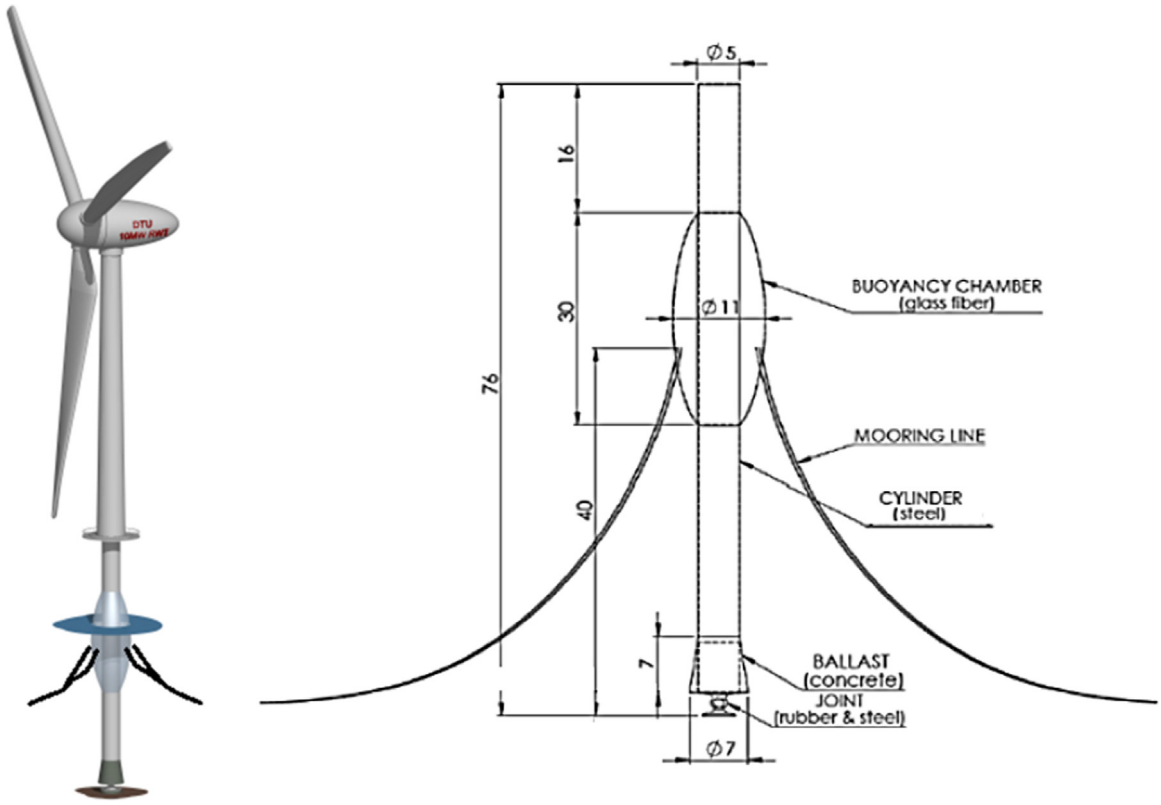

Fig. 1. Schematic of the Semi-floater concept.

floating system is made of a buoyant chamber and a main cylindrical sub structure. The buoyant chamber was developed as an ellipsoid of 30.0 m height and 11.0 m diameter cast out of glass fibre, details of which can be found in Sanz et al. (2013). The net buoyant force for platform stability is provided by the buoyant chamber placed near the sea level and from additional buoyant force generated by the cylinder. The latter is a steel rolled shell of 5.0 m diameter and 40 mm wall thickness. A concrete ballast is attached to its foot in order to lower its centre of gravity, and the weight of the ballast is calibrated to ensure that the net steady-state vertical force is in equilibrium. The ballast is a cone frustum of 7.0 m height and 7.0 m/5.0 m base diameters.

The substructure is connected to the seabed using an articulated (or universal) joint embedded into a reinforced concrete base. The universal joint is forged out of a steel shell and it is described in details in the next sections. The reinforced concrete base is a short cylinder whose upper face has a hemispherical cavity. The reinforced concrete base works like a gravity based foundation providing fixity to the platform. The other contact points to the soil are the mooring line anchors. The mooring lines are connected to the substructure with delta connections, which have their fairleads attached to the buoyant chamber. The delta connection aims at providing resistance to counter the turbine yaw moment. The six lines, which run till the seabed, define a catenary shape. They also contribute to limit the pitch motions of the platform.

2.2. The universal joint and its torque free mechanism

Adapted from Wang et al. (2010), the universal joint is roughly made of three main parts: a spherical ball, a coating of elastomeric pads and a socket. Each of these main parts can be exploded into

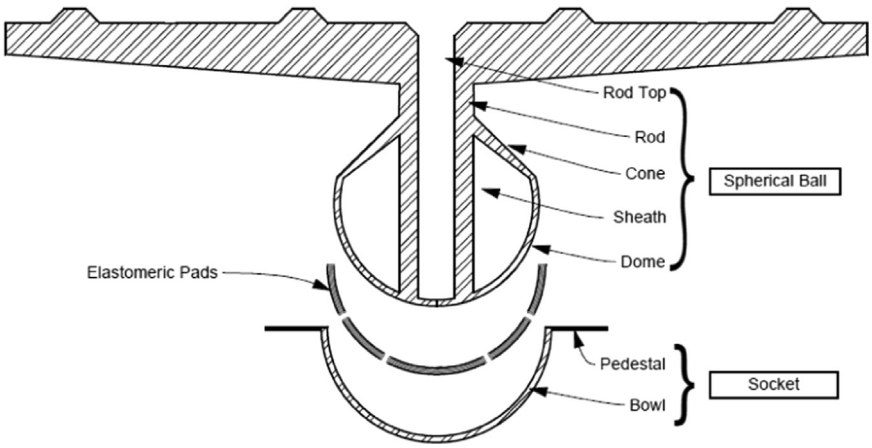

Fig. 2. Schematic of the universal joint parts.

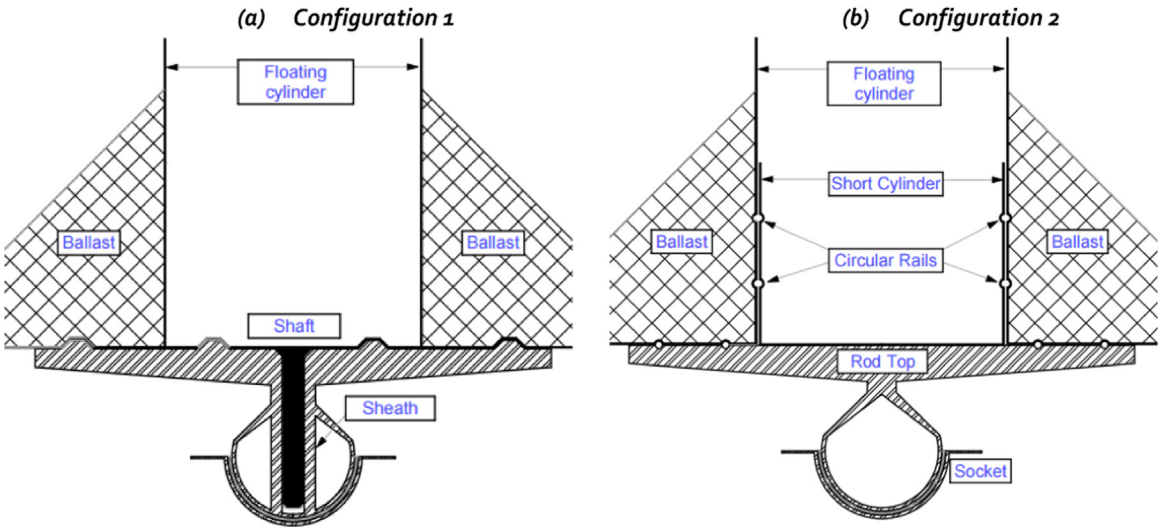

Fig. 3. Illustration of the two types of Torque-free mechanisms.

subparts as annotated in Fig. 2. The spherical ball and the socket are fabricated using a steel shell.

The elastomeric pads are made of laminated rubber placed between two external steel plates, which are securely bolted to the dome and to the bowl. During roll and pitch motions of the platform, the joint rotations induce shear deformations within the rubber layers. The universal joint is also able to withstand forces from the three principal directions but no torque is resisted by it. In order to achieve a torque-free mechanism, a passive connection is required between the cylinder and the joint for which two configurations were outlined (Fig. 3): (i) Configuration 1 with a shaft going from the cylinder into the spherical ball; and (ii) Configuration 2 with a short cylinder originating from the joint platform plugged into the floater cylinder. Configuration 1 has been found to out-perform Configuration 2 based on the following criteria:

1. *Construction:* the construction of Configuration 2 requires detailed manufacturing of circular rails, which is a feature absent in Configuration 1.
2. *Installation*: in case of non-automatic installation, plugging the shaft of Configuration 1 into the spherical ball is easier than adjusting the floating cylinder around the short cylinder of Configuration 2. The difficulty is increased due to the lateral rails, which prevent the cylinder to smoothly slide into the socket.
3. *Stress distribution*: with Configuration 2, all five directional load components are applied to the joint through the rod top, which can cause excessive stresses at its connection with the conical part. However, in Configuration 1, the bending moments are transmitted as pressure applied to the shaft sheath and resulting stresses are distributed to the whole ball.

2.3. Installation process

The installation process can be summarised in terms of six steps as depicted in Fig. 4.

(1) *Seabed preparation and cutting*. The first step consists of the removal of marine biota followed by excavation.
(2) *Foundation placement.* The universal joint mounted on the reinforced concrete base is prefabricated and assembled ex-situ, following which it is settled inside the excavation.
(3) *Backfill and scour protection.* The remaining spaces around the reinforced concrete are backfilled, and scour protection is provided.
(4) *Floating system sink.* The floating system constituted by the cylinder and the buoyant chamber is transported above the base. Its shaft is plugged into the joint sheath.
(5) *Ballast addition*. Ballast is added at the cylinder foot. This step can also be done during Step (d) to help sinking the floating system.
(6) *Mooring system.* The mooring lines are added and anchored to the seabed.

Finally, the turbine (tower plus rotor and nacelle assembly) can be mounted on the semi-floater structure using the classical run-through.

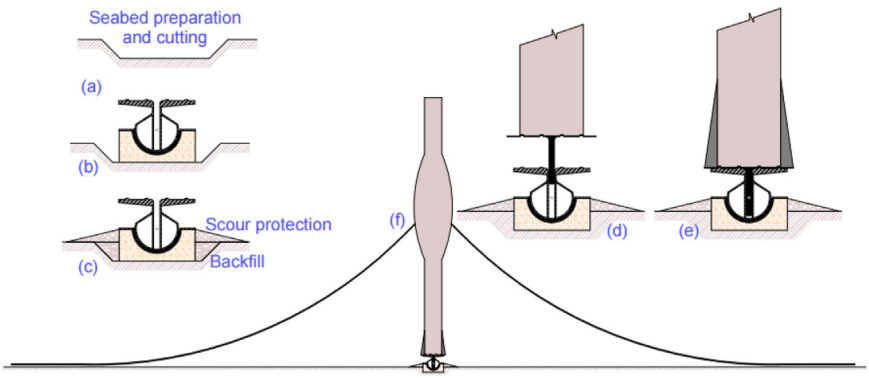

Fig. 4. Stages in the installation process.

3. Site conditions, structure, and design constraints

3.1. Wind conditions and sea states

In this study, the site conditions are adopted from the description in Von Borstel (2013). The soil consists of superimposed sand layers whose submerged weight varies between 9.00 kN/m^3 and 11.00 kN/m^3; and the characteristic angle of internal friction is equal to 35.0°. The complete description of the soil properties can be found in Von Borstel (2013).

The operational wind range is divided into 11 mean wind speed bins, based on which load simulations are carried out under normal and extreme turbulence conditions. Each mean wind speed bin is linked to a particular sea state characterised by an expected significant wave height and a peak spectral period. The wave height is modelled based on either Pierson–Moskowitz or JONSWAP spectrum at the expected value of the sea state characteristics conditional on the mean wind speed. Table 1 details the metocean conditions used in the site specific design of the configuration, and Table 2 shows the atmospheric conditions for the extreme turbulence case.

3.2. Turbine description

The DTU 10 MW reference wind turbine (DTU 10 MW RWT) (Bak et al., 2013) is considered mounted on the semi-floater substructure. The DTU 10 MW RWT is a state of the art variable speed pitch controlled conceptual offshore wind turbine, whose design parameters are summarised in Table 3. The same control system is used for the turbine mounted on the semi-floater mounted structure with no further adjustment.

Based on the rotor speed range, the corresponding Campbell diagram is shown in Fig. 5. This figure shows that multiples of the rotor speed (P); 1 P, 3 P, and 6 P ranges are respectively in hertz [0.10, 0.16], [0.30, 0.48], and [0.60, 0.96]. The first support structure is designed so that its natural frequencies are outside these frequency bands in order to avoid the risk of resonance related to rotor speed harmonics.

3.3. Design constraints

Considering the exclusion zones shown in Fig. 5, the first two tower natural frequencies should be within the soft-soft frequency range, [0.00 Hz, 0.10 Hz] or in the soft-stiff range [0.16 Hz, 0.30 Hz]. Since they should also be away from the wave peak frequency neighbourhood, the domain between [0.10 Hz 0.20 Hz], which represents a significant part of the wave spectrum, should also be avoided. In addition, the electrical production is to be ensured by keeping the power curve similar to that of the reference turbine. The aerodynamic thrust curve should also be comparable to reference turbine to ensure a similar design load level for the turbine components. For the semi-floater this implies that the design would possess a fundamental natural frequency less than 0.1 Hz.

At the serviceability limit state, the representative radial offset of the interface between the tower bottom and the substructure is limited to 2.62 m, i.e. maximum tower tilt angle of 2.00° in order to minimise the misalignment between the shaft axis and the horizontal-like wind direction, which can produce high shaft bending moments and lower the productivity. Furthermore, the yaw angle of the cylinder at the joint top should be less than 15°. Besides, the mooring lines should keep a catenary shape throughout its lifetime, i.e. at least a portion of the lines close to the anchor should lie on the seabed. Based on its ultimate limit state, the reliability index of wind turbine structures including the universal joint should not be less than 3.3 as recommended by Abdallah et al. (2015).

Table 1
Metocean conditions (Kallehave et al., 2015).

Mean wind speed [m/s]	Normal turbulence intensity [%]	Significant wave height, Hs [m]	Peak period, Tp [s]	Expected annual frequency [h/yr]
5	18.95	1.140	5.820	933.75
7	16.75	1.245	5.715	1087.30
9	15.60	1.395	5.705	1129.05
11	14.90	1.590	5.810	1106.75
13	14.40	1.805	5.975	1006.40
15	14.05	2.050	6.220	820.15
17	13.75	2.330	6.540	633.00
19	13.50	2.615	6.850	418.65
21	13.35	2.925	7.195	312.70
23	13.20	3.255	7.600	209.90
25	13.00	3.600	7.950	148.96
42.73 (storm)		9.400	13.700	

4. Fully coupled aero-hydro-servo-elastic analysis

To ensure that all ambient interactions are adequately considered, a fully coupled design load computation was carried out using the aero-hydro-servo-elastic software package HAWC2 (Larsen and Hansen, 2015). The structural design of the universal joint was carried out on the Abaqus platform (Abaqus, 2012).

HAWC2 utilises a multibody formulation, which couples different elastic bodies together using Timoshenko beam finite elements (Ankit et al., 2016) whereby their stiffness, mass and damping are assembled into the governing equations of motion coupled to aerodynamic forces, whose time domain solution is obtained using the Newmark-β method (Montasir et al., 2015). The damping coefficients are specified using Rayleigh coefficients (Navik et al., 2016) to obtain desired damping ratios for the global structure. The blade element momentum theory supplemented with Leishman–Beddoes dynamic stall model and dynamic inflow is employed to represent the rotor unsteady aerodynamics (Manwell et al., 2009). The turbulent wind field in the aeroelastic simulations is defined using the Mann model (Mann, 1994). Random Gaussian 10-minute turbulent wind realisations are used as input to simulate normal operation over the 11 mean wind speed bins and storm conditions.

The irregular wave height is modelled using either a JONSWAP or a Pierson–Moskovitz spectrum depending on the load case conditions at the expected value of significant wave height and spectral peak period at each mean wind speed. In fact, the Pierson–Moskowitz type is used for fatigue load case because of its spread spectral, which allows a better energy distribution, while the JONSWAP type is suitable for ultimate load case due to its peaked spectral shape. Random wave kinematics are computed according to the linear Airy model with Wheeler stretching (Chakrabarti, 2005). The hydrodynamic forces are calculated based on the Morison's equation (Chakrabarti, 2005) evaluated for a unit length of cylinder: $F=0.5\rho_w C_D(u_w+u_c-u_s)|u_w+u_c-u_s|+0.25\rho_w C_M\pi D^2(\dot{u}_w-\dot{u}_s)$, where D [m] is the outer diameter, u_c [m/s] is the current speed, u_w [m/s] is the wave particle speed normal to the tube axis, u_s [m/s] is the moving tube velocity, $\dot{u}_w$ [m/s^2] is the wave particle acceleration normal to the tube axis, and $\dot{u}_s$ [m/s^2] is the moving tube acceleration. ρ_w=1025 kg/m^3 is the water mass density and C_D=0.85 is the drag coefficient related to the tube cross section. The diffraction phenomenon is taken into account by correcting the inertia coefficient, C_M according to MacCamy and Fuchs (1954):

Table 2
Atmospheric conditions for extreme turbulence (Kallehave et al., 2015).

Mean wind speed [m/s]	5	7	9	11	13	15	17	19	21	23	25	42.73
Extreme turbulence intensity [%]	43.85	33.30	27.43	23.70	21.12	19.23	17.78	16.63	15.71	14.94	14.30	11.00

Table 3
Key parameters of the DTU 10 MW RWT (Bak et al., 2013).

Parameters	Values
Wind regime	(see Tables 1 and 2)
Rotor type, orientation	3 bladed - Clockwise rotation – Upwind
Control	Variable speed – Collective pitch
Cut-in, rated, cut-out wind speed	4 m/s, 11.4 m/s, 25 m/s
Rated power	10 MW
Rotor, hub diameter	178.3 m, 5.6 m
Hub height	119.0 m
Drivetrain	Medium speed, Multiple-stage gearbox
Minimum, maximum rotor speed	6.0 rpm, 9.6 rpm
Maximum generator speed	480.0 rpm
Gearbox ratio	50
Maximum tip speed	90.0 m/s
Hub overhang	7.1 m
Shaft tilt, coning angle	5.0°, −2.5°
Blade prebend	3.3 m
Rotor mass including hub	227,962 kg
Nacelle mass	446,036 kg
Tower mass	628,442 kg

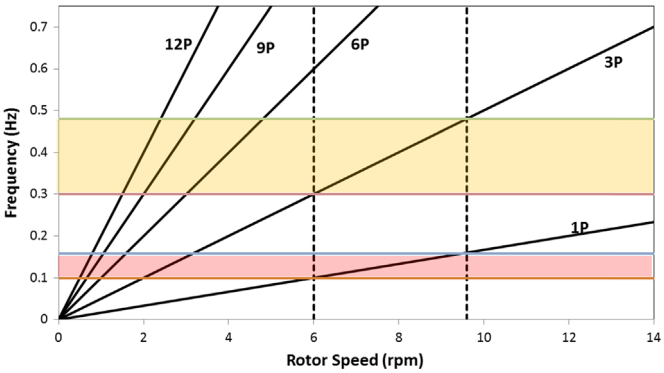

Fig. 5. Campbell diagram for the DTU 10 MW RWT.

$C_M = 16/\left(\pi k^2 D^2 \sqrt{\left[J_1'(kD/2)\right]^2 + \left[Y_1'(kD/2)\right]^2}\right)$, where k is the wave number defined as $4\pi^2 = T_p^2 gk \tanh(kh)$, and h [m] is the water depth. Below the seabed, the structure is assumed to be embedded (all degrees of freedom are fully restrained) into the soil through the reinforced concrete base. The soil-structure interaction is evaluated for three failure modes: bearing, sliding, and overturning as detailed by DNV-OS-J101 (Det Norske Veritas, 2014). Besides, the punching effect of the socket into the reinforced concrete base is considered as an additional failure mode.

Three design load cases (DLC) are considered herein as defined by IEC 61400-3 (The international Electrotechnical Commission, 2009): DLC 1.2 for fatigue limit state, DLC 1.3 and DLC 6.2a for ultimate limit state. DLC 1.2 is the load case under normal operation to account for fatigue damage over the turbine lifetime. A total of 11 wind speed bins (from 5 m/s to 25 m/s with 2 m/s step) with six wind turbulence seeds each are considered, with yaw errors of 0° and ±10° from the normal to the rotor plane. The Pierson–Moskowitz type waves are taken with misalignments relative to the wind direction of 0° or ±10°. This set of conditions provides $11 \times 6 \times 3 \times 3 = 594$ scenarios.

DLC 1.3 is the ultimate loading resulting from extreme turbulence conditions with normal sea states. Six wind seeds for each of 11 wind speed bins are simulated, all of them without yaw error. The waves of JONSWAP type are aligned along the wind direction. That provides $11 \times 6 = 66$ scenarios. DLC 6.2a is the ultimate loading resulting from the turbulent extreme wind model with extreme sea states, coupled with loss of electrical power. A mean wind speed of 42.73 m/s is applied along 24 directions: from 0° to 345° with 15° bin size. A JONSWAP wave is directed along wind direction with ±30° yaw error. With no active controller, the blades are pitched to an angle of 90° with no dynamic induction. This leads to a total of $24 \times 3 = 72$ scenarios.

5. Design process

5.1. Design workflow and material properties

It is important to capture the coupled interactions between all the structural components and with the environment during the dynamic load simulations. Since the final design of the semi-floater components is not known at the initial point of the simulation, an iterative design approach is adopted. The design of the universal joint is made as illustrated by Fig. 6. In parallel, tensile loads at the fairlead have been collected for the design of the mooring lines. The present study proposes a preliminary design algorithm for mooring lines. The algorithm has three main steps as presented in Appendix A.

The steel used for the joint shell is of type NV-620 (Extra high strength steel-EHS) as designated by DNV-OS-J101 (Det Norske Veritas, 2014). Cremer and Heckl (1988) have recommended other steel properties. The elastomeric pads consist of layers of steel shims sandwiched between rubber layers. The shim steel has the same properties as those of the one used for the shells. The rubber's properties have been given by Sedillot and Stevenson (1983). South (2001) performed a series of test on many rubber specimens with variable specifications, compositions and at different temperatures, from which he obtained characteristic shear strengths. CEB-FIP Model Code (Comite Euro-International du Beton, 1993) proposes some properties for concrete. Some soil properties are extracted from Von Borstel (2013) and others from Thonier (1992). IEC 61400-3 (The international Electrotechnical Commission, 2009) recommends a roughness parameter smaller than 1.0; it is taken as 0.9 since the reinforced concrete block is embedded deeply enough into the soil. All these material properties are presented in Table 4. In addition, the mooring lines are taken as stud link R5 chain type whose properties are given in Table 5.

5.2. Predictor design

As given in Sanz et al. (2013), the equation of static deflection of the structure connected to the articulated joint is modelled as:

$$\frac{EI}{L} = \frac{4\alpha}{3} G \frac{R_i^3 R_e}{n\,t} \tag{1}$$

where R_i and R_e are respectively the internal and external radii of the ball joint; EI is the modulus of bending rigidity of an equivalent cantilever beam model of length L; G is the shear modulus of rubber; α is the angular spread of the articulation; n is the number of rubber layers; and t is the thickness of each rubber layer.

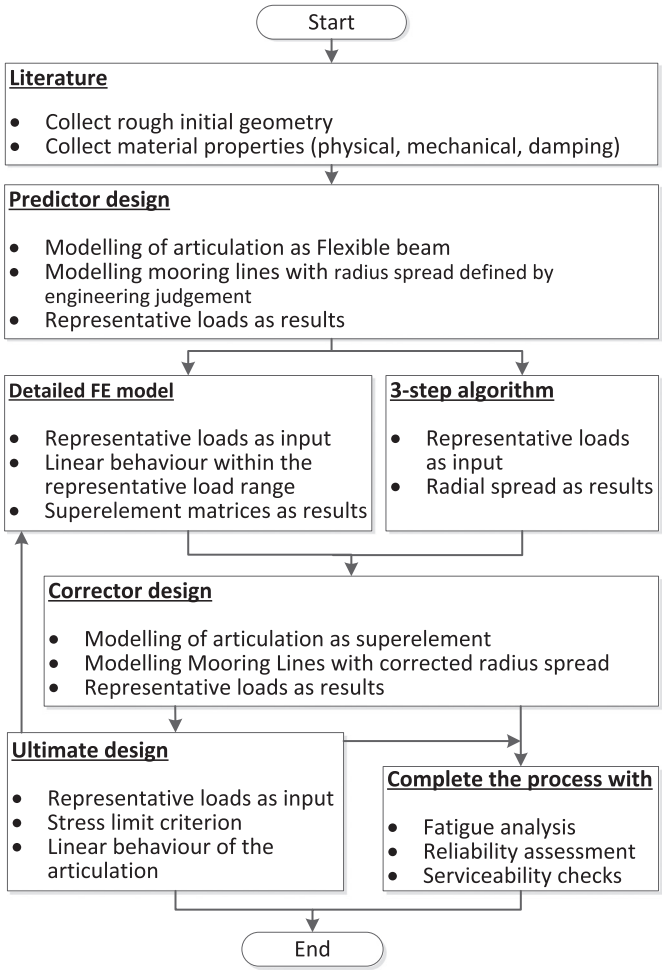

Fig. 6. Iterative design process of the universal joint.

The geometrical and mechanical properties of the beam can be defined from Eq. (1) given universal joint parameters. The resulting beam is incorporated into the model together with the initial design of the mooring lines whose radial spread is taken as 500.0 m as an initial estimate that needs to be refined in the design process. The simulation of this preliminary design results in preliminary loads, which are used to correct the parameter values of the initial design.

5.3. Corrector design

The predicted loads at the articulation and at the fairleads are collected to refine the geometrical parameters of the corresponding structural components. For the mooring lines, the preliminary tensile force at the fairlead is used as an input to the three-phase algorithm, which results in a radial spread of 325.0 m. For the articulated joint, the characteristic bending moment is used as the design driver. Considering a given pitch angle of the tower, γ from Eq. (1) it can be deduced that:

$$\frac{R_i^3 R_e}{nt} \geq \frac{3M_{driving}}{4\gamma G\alpha} \tag{2}$$

After the predictor design results, Eq. (2) is evaluated at $R_i^3R_e/(nt) \geq 165\ \text{m}^3$. A possible solution of this inequality is R_e=1.840 m, R_i=1.715 m, n = 3 *rubber layers*, t = 15.0 mm, which results in $R_i^3R_e/(nt)$=206.252 m^3. AASHTO Specifications (American Association of State Highway and Transportation, 2012) recommend that the reinforcement shims should have at service limit state a total thickness of: $hs \geq \max(1.6\ \text{mm}; 3t\sigma_s/f_s)$, where σ_s is the axial stress on a pad and f_s is the steel yield stress. Assuming the extreme case where the whole axial load is only supported by the central pad: σ_s=2. 145 MPa. Therefore, $hs \geq \max(1.6\ \text{mm}; 0.2\ \text{mm})$. Two shim layers of 5.0 mm each are selected for hs = 10.0 mm. It is worthy to note that these parameters values guarantee a good design of the elastomeric pads, but not that of the steel shell forming the ball. In other words, stress analysis will lead to the actual ball radii and thicknesses.

The universal joint is modelled in Abaqus as depicted in Fig. 3 (a) and (b). The model uses shell elements for the spherical ball and the socket, and solid elements for the elastomeric pads. The outer face of the socket is restrained in all six degrees of freedom. The elastomeric coating is modelled as a homogeneous material with equivalent properties in shear deformation mode. It is discretized with solid element C3D20H (20-node quadratic brick, hybrid with linear pressure). The ball is implemented as shell with 4-node quadrilateral element S4. The socket is input as shell of type S8R which accounts for thick shell problem since its thickness is much larger than the distance between supports. Further details can be found in Abaqus (2012).

In the model, a master node is created at the sheath top centre. Only the vertical force is applied at the master node. A shaft is introduced into the sheath, and the horizontal forces are applied as distributed pressures. The bending moments are modelled as a couple generated by two antagonist distributed pressures applied on the shaft. After elastic analyses in Abaqus, a 6×6 equivalent

Table 4
Material properties of the universal joint.

Material	Properties	References	Values
Steel	Steel type	DNV-OS-J101 (Det Norske Veritas, 2014)	NV-620
	Minimum yield stress [MPa]	DNV-OS-J101 (Det Norske Veritas, 2014)	620
	Mass density [kg/m^3]	Cremer and Heckl (1988)	7800
	Effective Elastic Modulus [GPa]	Cremer and Heckl (1988)	210
	Poisson's ratio [–]	Cremer and Heckl (1988)	0.3
Elastomer	Mass density [kg/m^3]	Sedillot and Stevenson (1983)	1250
	Bulk modulus [MPa]	Sedillot and Stevenson (1983)	1500
	Poisson's ratio [–]		0.47
	Shear strength [MPa]	South (2001)	30
Concrete	Mass density [kg/m^3]	CEB-FIP Model Code (Comite Euro-International du Beton, 1993)	2400 (2500)
	Poisson's ratio [–]	CEB-FIP Model Code (Comite Euro-International du Beton, 1993)	0.2
	Compressive yield stress [MPa]	CEB-FIP Model Code (Comite Euro-International du Beton, 1993)	18
Foundation grade	Internal friction angle [°]	Von Borstel (2013)	35
	Submerged unit weight [kN/m^3]	Von Borstel (2013)	9
	Soil cohesion strength [kPa]	Thonier (1992)	25
	Roughness parameter [–]	IEC 61400-3 (The international Electrotechnical Commission, 2009)	0.9

Table 5
Chain properties (Stud Link R5).

Properties	References	General values	Actual values
Effective Elastic Modulus [N/m^2]	DNV OS E301, 2013 (Det Norske Veritas, 2013)	$E_{eff} > 5.6 \times 10^{10}$	5.6×10^{10}
Nominal Diameter [mm]	DNV OS E302, 2008 (Det Norske Veritas, 2013)	$74 < d < 210$	124
Density in air [kg/m]	DNV OS E302, 2008 (Det Norske Veritas, 2013)	$m_a = 0.0219\ d^2$	336.7344
Density in water [kg/m]	Benassai et al. (2014)	$m_w = 0.87\ m_a$	292.9589
Breaking load [kN]	DNV OS E302, 2008 (Det Norske Veritas, 2013)	$Q = 0.032(44 - 0.08d)\ d^2$	16768.45
Drag Coefficient [–]	Brown (2005)	$C_d = 2.6$	2.6

stiffness matrix relative to the sheath top centre is obtained.

5.4. Final design and results

In the HAWC2 model, the mooring system is updated with the corrector design. The articulated joint is modelled as a super-element characterised by the obtained equivalent stiffness matrix and by a Rayleigh damping matrix calibrated to comply with the finding of Kim et al. (2014) about damping ratio in pitch mode (about 1.5%). A free-torque mechanism is inserted between the superelement and the cylinder. Hydro-aero-servo-elastic simulations are carried out based on the three design load cases described above. The resulting loads are used to check the components at ultimate limit state.

Considering a Class 2 mooring system, Det Norske Veritas (2013) recommends 1.40 and 2.10 for mean and dynamic load factors, respectively. The characteristic line strength is taken as 95% of the nominal breaking load (Benassai et al., 2014). Therefore the utilisation factor, u is calculated:

$$u = \frac{1.40T_{mean} + 2.10T_{dyn}}{0.95Q} \tag{3}$$

The representative mean, T_{mean} and dynamic loads, T_{dyn} are found on the critical line to be 2671.3 kN and 476.1 kN, respectively. The utilisation factor is therefore calculated from Eq. (3): $u = 0.2975 \leq 1$. The final layout of the mooring system is illustrated by Fig. 8.

For the universal joint, the stress distribution of the spherical ball is shown by Fig. (7c) for a loading situation where the highest stress ranges occur. It shows that the vulnerable zones are at the dome bottom, the connection between the dome and the cone, and the connection between the cone and the rod. The representative equivalent von Mises stresses are calculated in the articulated joint from the average of absolute maximum loads from DLC1.3 or DLC6.2a, separately. In other words, given a DLC, the constitutive scenarios each yield respective maximum stresses, which are all averaged over the DLC to get the representative

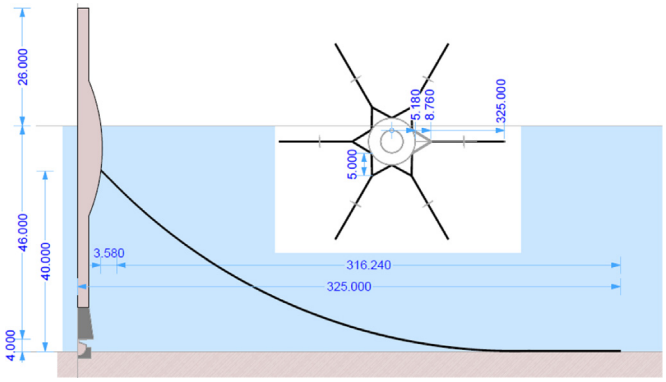

Fig. 8. Illustration of mooring system layout.

equivalent von Mises stress. The representative equivalent von Mises stress is obtained in the connection between the cone and the rod. Its characteristic value is 314.0 MPa, and is obtained through DLC 6.2a. Considering a component class 3 for consequences of failure (The international Electrotechnical Commission, 2005), the utilisation factor is determined as 79.66%. Under the same loading conditions, the rubber layer has a maximal characteristic strain of 0.026, which leads to a utilisation factor of 12.16%. This factor confirms the high durability found by Sedillot and Stevenson (1983). The final design of the universal joint is shown by Fig. 9.

In order to design the reinforced concrete base, several scenarios are selected: they correspond to the situations where respective extrema (maxima and minima) of load components occur at the joint top. Actual loads propagated to the reinforced concrete base are obtained as the reactions developed under the joint socket. Four failure modes are considered to justify the design of the base: overturning of the structure due to excessive moments, bearing capacity of the soil-structure interface, sliding on the seabed and punching of the universal joint into the reinforced concrete base. Det Norske Veritas (2014) is used to assess bearing

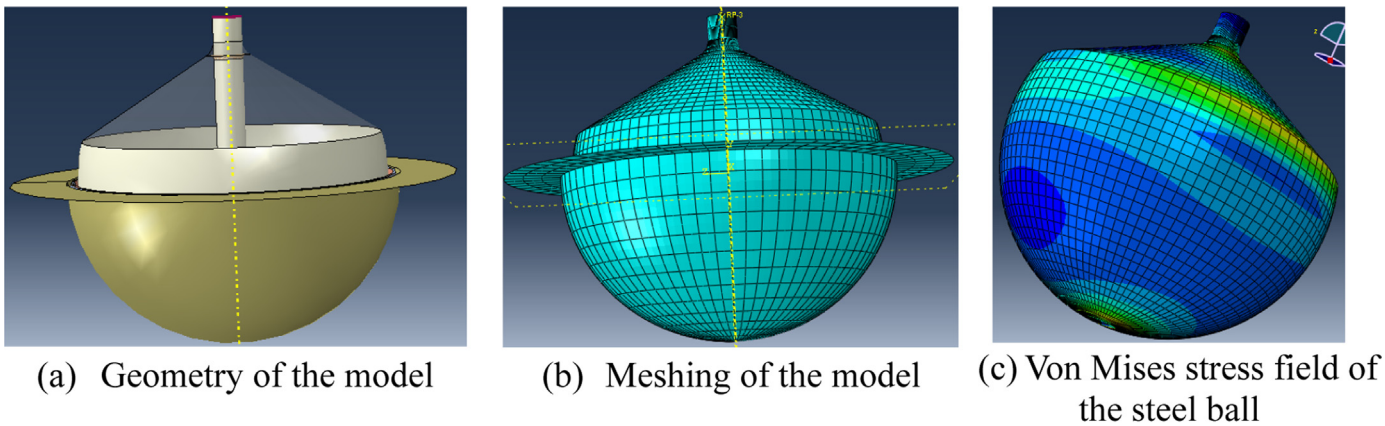

Fig. 7. Finite element model of the universal joint.

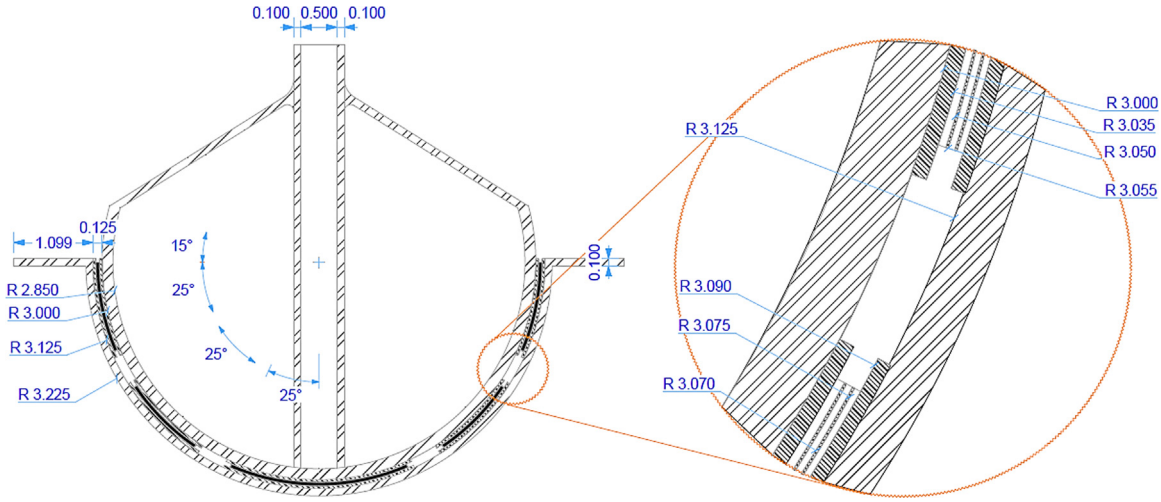

Fig. 9. Illustration of Universal joint dimensions.

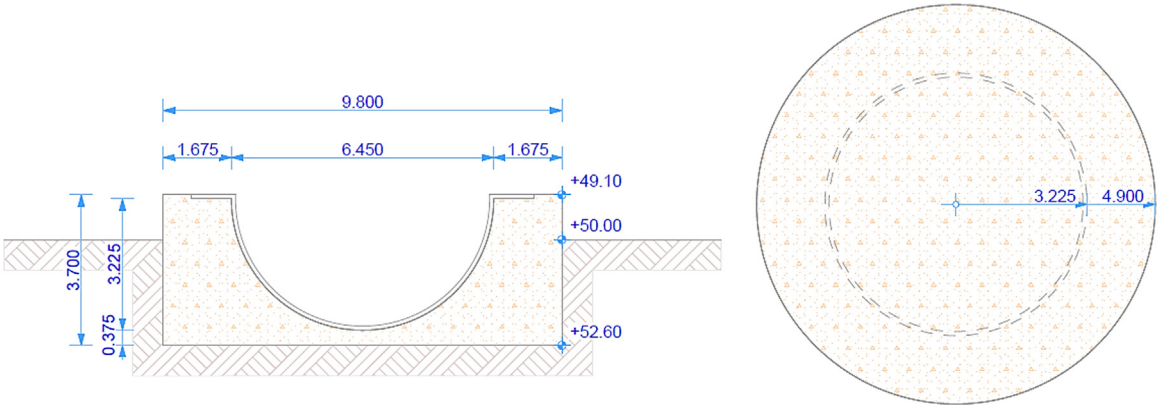

Fig. 10. Reinforced concrete base.

Table 6
Results of the reinforced base design.

	Overturning (*X*-Direct.) [MNm]	Overturning (*Y*-Direct.) [MNm]	Bearing [kPa]	Sliding [MN]	Punching [kPa]
Critical scenario	Max F_y	Min F_x	Max Fres	Max Fres	Max F_z
Resisting	91.82	86.92	277.58	9.70	5586.21
Driving	32.88	28.88	239.05	7.79	5213.33
Safety factor	2.83	5.54	1.16	1.25	1.07

capacity and sliding, while Thonier (1992) is considered for punching, assuming that the punching effect only originates from the lower elastomeric pad. A cylinder of diameter 9.80 m and 3.70 m height, as depicted in Fig. 10, is found to satisfy all the requirements. Table 6 presents the overview of these analysis results for the critical scenarios.

6. System performance

In order to investigate the performance of the structure at the system level, three criteria are considered: modal frequencies, global motion of the platform, and operational curves (power curve, thrust force curve, rotor rotational speed curve and blade pitch angle curve). Table 7 shows the natural frequencies and the logarithm decrement of the whole structure. The two first support

Table 7
Natural frequencies of the whole turbine.

Mode	Natural frequency [Hz]	Logarithmic damping [%]
1st side–side mode	0.09427	11.19
1st for-aft mode	0.09457	11.14
1st fix-free mode	0.11137	0.006
1st yaw mode	0.14918	0.009

structure modes have their natural frequencies at approximately 0.094 Hz which is just outside the 1P excitation range, [0.10 Hz, 0.16 Hz] and at the lower tail of the wave spectrum (about 14% of the wave energy during production phase is contained in frequencies below the first support structure mode).

In addition, Fig. 11 illustrates the chosen characteristic curves of the control system used for the semi-floater structure. By comparing to those of the DTU 10 MW RWT, it is found that the new system supported by the innovative semi-floater globally performs as good as the reference. Indeed, the intrinsic performance of the semi-floater design is comparable to that of the reference turbine. Since the comparison criteria used are not dependent on any metocean conditions, it can be said that the value of that statement can be generalised for other sites. However, it should be noted that the rotor rotational speed allows a slight slope once the rated rotor speed is reached. Detailed discussion of tuning of the controller is out of the scope of the present study.

The global motion of the platform is investigated under normal power production conditions, and in a storm situation. The yaw

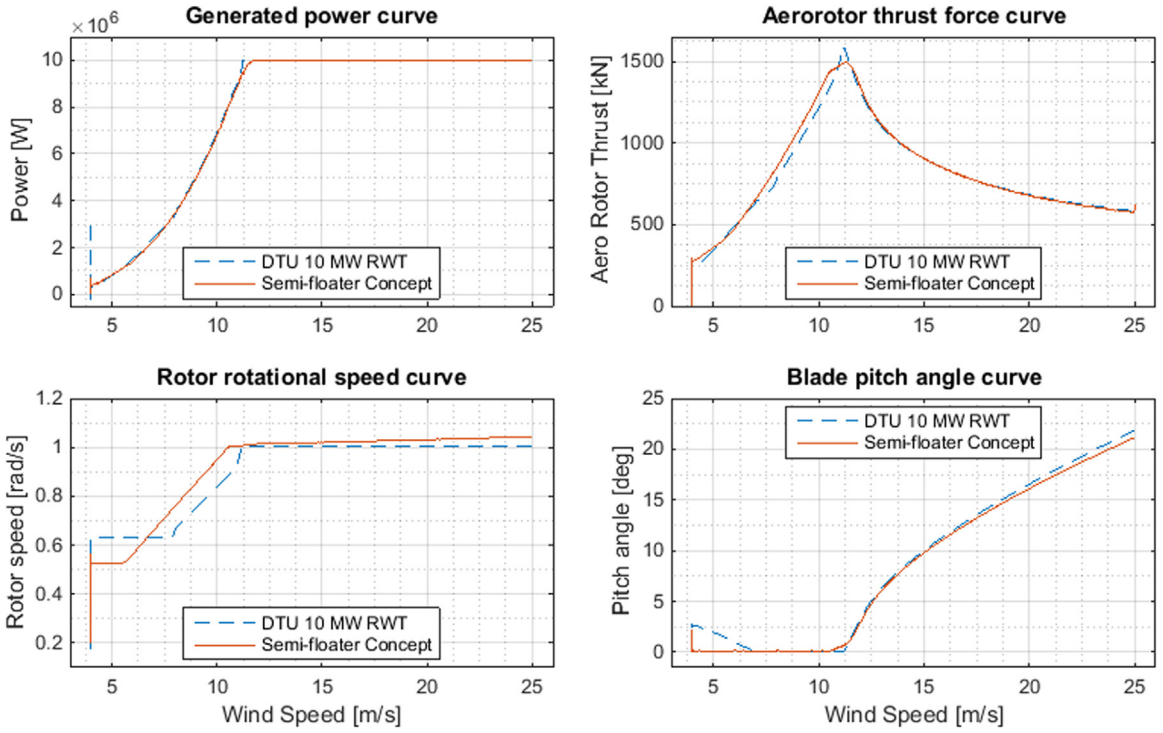

Fig. 11. Characteristic performance Curves.

Table 8
Displacement parameters of the cylinder.

Displacement parameters	Storm situation		Production situation	
	mean	max	mean	max
Interface offset [m]	1.03	2.17	0.81	1.52
Tilt angle [°]	0.78	1.66	0.62	1.16
Yaw angle [°]	0.00	3.75	−0.08	11.05

angle and the tilt angle of the cylinder are chosen as displacement parameters, as well as the radial offset of the interface between the cylinder and the tower. Table 8 shows the averages of the means and the averages of the maxima for each displacement parameter. It is observed that the cylinder tilts at maximum by 1.66° during storm situation, and yaws between ± 11.05° during production phase. These displacement parameters are lower than the design constraints.

7. Reliability and fatigue analyses

7.1. Reliability analysis

For the universal joint and the mooring lines, reliability analysis has been carried out at ultimate limit state, i.e. based on DLC 1.3 and DLC 6.2a results. For the mooring lines, the line with the highest utilisation factor is selected as the representative line. The failure limit state function for both DLCs can be expressed by: $g = Q - X_{dyn}X_{exp}X_{aero}X_{st}X_{sim}T$, where X's are uncertainty variables defined in Table 8, Q is the random variable modelling the line breaking load, and T is the stochastic variable modelling the tensile force at the fairlead. Table 9 lists the probability distribution function and the statistics (mean and coefficient of variation, COV) of each of the uncertainty variables (Abdallah et al., 2015), while the remaining random variables are described in Table 10, where the dispersion parameters are obtained after engineering assumptions.

Table 9
Uncertainty variables.

Variable	Definition	Distribution	Mean	COV
X_{dyn}	Dynamic response	Lognormal	1.00	0.05
X_{exp}	Exposure (landscape)	Lognormal	1.00	0.10
X_{aero}	Aerodynamic parameters	Gumbel	1.00	0.10
X_{st}	Climate statistics	Lognormal	1.00	0.05
X_{str}	Computation of the load effect	Lognormal	1.00	0.03
X_{sim}	Simulation statistics	Normal	1.00	0.05
X_{lin}	Stress linearization	Normal	1.00	0.005
X_w	Vertical load variation	Normal	1.00	0.03

Table 10
Random variables. The dispersion parameters are based on engineering assumptions.

Variable	Distribution	Mean/COV (DLC 1.3)	Mean/COV (DLC 6.2a)
Q	Lognormal	18.23 MN/0.05	18.23 MN/0.05
T	Weibull	2575.6 kN/0.04	2430.3 kN/0.06

For the universal joint, the reliability analysis is carried out at a stress hotspot, defined as the mesh element that has the maximum von Mises stress at ultimate limit state. Therefore, for simplicity, the reliability analysis of the universal joint is reduced to the analysis of the hotspot. The failure limit function can be written as: $f = F_s - \Sigma_v$, where F_s is a random variable related to the steel yield limit and Σ_v is a stochastic variable related to the equivalent von Mises stress at the hotspot. From theory of elasticity and under plane stress conditions, the von Mises stress can be expressed as: $\sigma_v = \sqrt{\sigma_{11}^2 - \sigma_{11}\sigma_{22} + \sigma_{22}^2 + 3\sigma_{12}^2}$. Since the structure behaves elastically under the range of loads at hand, each of the stress components, σ_{ij} $(ij = \{11,22,12\})$ can be expressed as a linear combination of the load components applied to the universal joint: $\sigma_{ij} = C_{1,ij}f_x + C_{2,ij}f_y + C_{3,ij}f_z + C_{4,ij}m_x + C_{5,ij}m_y$. Let us recall that

Table 11
Random variables. The dispersion parameters are based on engineering assumptions.

Variable	Definition	Distribution	Mean/COV (DLC 1.3)	Mean/COV (DLC 6.2a)
F_s	Steel yield limit	Lognormal	673.94 MPa/0.05	673.94 MPa/0.05
F_x	Side–side force	Weibull	47.1 kN/8.28	0.2 kN/8264.70
F_y	For-aft force	Weibull	166.5 kN/4.95	47.0 kN/29.92
F_z	Vertical load	Normal	14.1 MN/0.02	14.1 MN/0.11
M_x	For-aft moment	Weibull	127.8 MNm/0.46	5467.5 kN m/19.52
M_y	Side–side moment	Normal	13.8 MNm/1.69	−27.5 kN m/6049.3

the yaw moment, m_z, is ignored here because the universal joint does not receive any torque from adjacent structures. The deterministic coefficients $C_{k,ij}(k = 1 \text{ to } 5,\ ij=\{11,22,12\})$ are obtained from the numerical model using unit-load cases where load is applied in a single degree of freedom whilst the loads in all other degrees of freedom are set to zero.

The failure limit function expands to: $f=F_s - \sqrt{\Sigma_{11}^2 - \Sigma_{11}\Sigma_{22} + \Sigma_{22}^2+3\Sigma_{12}^2}$, where $\Sigma_{ij}(ij=\{11,22,12\})$ is the stochastic variable related to the stress component σ_{ij} $(ij=\{11,22,12\})$, respectively. With the linearization, $\Sigma_{ij} = X_{dyn}X_{exp}X_{aero}X_{st}X_{str}X_{sim}X_{lin}\left(C_{1,ij}F_x + C_{2,ij}F_y + C_{4,ij}M_x + C_{5,ij}M_y\right)$, $+ X_wX_{str}X_{lin}C_{3,ij}F_z$

where the uncertainty variables X are as defined in Table 9. The other random variables are defined and described in Table 11, where the dispersion parameters are obtained after engineering assumptions.

Monte Carlo simulations with a total of N_{MC}=1,000,000 samples were carried out in order to calculate the probability of failure for the two systems (mooring lines and universal joint). As a result, (i) the mooring system has failure probability smaller than approximately $1/N_{MC}$ for DLC 1.3 and DLC 6.2a; (ii) the probability of failure of the universal joint is less than $1/N_{MC}$ for DLC 1.3 and 4.80×10^{-4} ($\beta = 3.302$) for DLC 6.2a, which demonstrates a sufficiently reliable design compared to the minimum reliability index ($\beta = 3.3$) specified in the design constraints section.

The reason of no mooring line failure is that the mooring lines have been designed to keep a catenary shape: the limiting criterion was the total lift of the line above the seabed close to the anchorage. With a permanent catenary shape, the tensile load along the lines will practically always be smaller than the breaking load.

7.2. Fatigue analysis

Based on the results from load simulations with DLC 1.2, the damage equivalent loads (DEL) for 25 years of lifetime are calculated using Eq. (4). They are evaluated at the top of the articulated joint and at the interface between the tower bottom and the floating cylinder.

$$L_{eq} = \left(\frac{\sum_i t_i \sum_j n_{ij}L_{ij}^m}{N_{eq}T_s}\right)^{1/m} \tag{4}$$

where

$m = 4$ is the Wöhler slope for steel structures;
$N_{eq} = 10^7$ is the equivalent number of cycles during lifetime;
T_s=10 min=600 s is the simulation duration;
t_i: is a weight factor proportional to the probability of occurrence of a scenario, i, over 25 years;
L_{ij}: is the load range j for scenario i as obtained from rainflow counting;
n_{ij}: is the number of cycles of stress range bin j for scenario i.

The resulting damage equivalent loads are listed in Table 11, where the x-axis is directed along the side–side direction, the y-axis is aligned to the fore-aft direction, and the z-axis is vertical. For comparison, the substructure made of the jacket described in Von Borstel (2013) is taken as a reference. The DEL at the tower base for the two support structures are compared. Table 12 shows that, compared to a jacket design, the semi-floater concept successfully decreases the damage equivalent loads at the interface, except for the vertical force.

More importantly, the side–side DEL are reduced due to the additional hydrodynamic damping, which is uniformly spread in all directions by the mooring system. Similarly the yaw damage equivalent moment has been decreased by 28.07% thanks to the mooring system, which provides both additional damping and torque resistance through its delta connections.

8. Cost analysis

A detailed cost analysis is proposed to estimate the cost of the semi-floater concept. Table 13 breaks down the cumulative cost into a material portion, which includes the manufacturing cost, and an installation portion. Thus, the total cost is estimated at approximately 4.2 million euros and the material cost at about 3.9 million euros. As well, Von Borstel (2013) proposes a jacket solution, which weighs 2120 t, as substructure under the same conditions. With the assumption of 5000 € per kilogram of manufactured steel for jacket, a material cost of 10.6 million euros can be deduced, which is more than the double of the cost of the semi-floater concept.

9. Recommendations for further studies

Some aspects of the concept can benefit from further developments. On one hand, an important advancement can be the adaptation of this concept for different water depth ranges or for turbines with capacities up to 20 MW. To achieve this upscaling, the present results can serve as an initial estimate. Then, the

Table 12
Damage equivalent loads.

	F_x [kN]	F_y [kN]	F_z [kN]	M_x [kN m]	M_y [kN m]	M_z [kN m]
Interface						
Semi-floater	770.3	1587.1	908.7	105,970	58,671	20,833
Jacket	1064.6	1586.6	552.6	111,000	97,723	28,961
Rel. Diff.	−27.64%	+0.03%	+64.44%	−4.53%	−39.96%	−28.07%
Joint top						
Semi-floater	1784.0	4155.4	1969.8	174,920	95,113	–

Table 13
Total cost including manufacturing and installation.

Designation	Quantity	Unit cost [€]	Total cost [€]	Reference for unit cost
Floating cylinder [kg]	401,420	3	1,204,260	
Ballast [kg]	99,600	0.07	6972	
Buoyant chamber [kg]	41,363	6.00	248,178	Shah et al. (2013)
Mooring lines [m]	3070	250	767,500	Wayman et al. (2006)
Anchors+connector [U]	6	125,000	750,000	Wayman et al. (2006)
Joint shell [kg]	40	4	160	
Laminated rubber [m^3]	10	76,900	769,000	MHD (Massachussets Departement of Transport, Highway Division, 2005)
RC Base [kg]	525,000	0.25	131,250	
Material cost (including manufacturing)			**3 877 320**	
Instal. in shipyard [turbine]	1	6860	6860	Wayman et al. (2006)
Instal. at sea [turbine]	1	256,350	256,350	Wayman et al. (2006)
Anchor instal. [U]	6	9471	56,826	Wayman et al. (2006)
Total cost (including installation)			**4,197,356**	

algorithms as presented here can be used for preliminary design of the mooring system and the universal joint.

On the other hand, a stronger emphasis can be given to the joint design in other to tackle local problems such as: (i) connections – e.g. welds, bolts - between shell parts; (ii) local buckling and possible internal frame; (iii) more realistic boundary conditions and load transmissions. Similar improvement can also be done on other structural components. For example, the mooring system can be revised such as to support larger axial forces. Also, an optimised design can be pursued for the floating system regarding its shapes, its dimensions, and the structural skeleton of the buoyancy chamber.

10. Conclusion

In this paper, a semi-floater concept for a moderate water depth offshore wind turbine support structure was developed. It is a combination of a spar buoy type floater anchored to the soil with a universal joint and supported with mooring lines. Its architecture was described as an assembly of easy-to-manufacture parts and the design process was described as a step-by-step case study. The concept showed acceptable fatigue load levels and low pitch deflections at mean water level. The reliability of the universal joint was found to satisfy the ultimate design safety requirements. A possible approach to the installation process was also proposed in the paper, which can aid practical implementation of the concept. Compared to traditional fixed support structure types such as monopiles or jackets, the semi-floater design can be potentially cheaper at moderate water depths because it uses less material, and its installation process requires less effort and has fewer constraints (silent process and moderate size equipment). Furthermore, it may be more competitive than floating structures at water depths in the range 50–100 m, where monopile and jacket designs become highly challenging. In summary, the semi-floater design was shown to fulfil the necessary design requirements for supporting large wind turbines and it possesses features which make it an attractive choice as a future offshore wind turbine support structure.

Acknowledgements

The research leading to these results has received funding from the European Community's 7th Framework Programme FP7-ENERGY-2012-1-2STAGE project INNWIND. EU under grant agreement No. 308974. The financial support is greatly appreciated. In addition, we would like to acknowledge the contributions of Maria Sanz Martinez, in the preliminary phase of development of this concept.

Appendix A. Preliminary design of catenary lines

A mooring line of catenary type with uniformly distributed weight, w, hung at a vertical height, h above the seabed is depicted in Fig. A.1. It is anchored at a radial distance, Rad, away from the fairlead. Its total length, L, can be decomposed into a suspended part of length s and a straight part laying on the seabed of length B. Before or after deformations, s and B respectively take the values s_1 and s_2, B_1 and B_2. A minimal ratio $\theta=B_2/s_2$ is assumed to

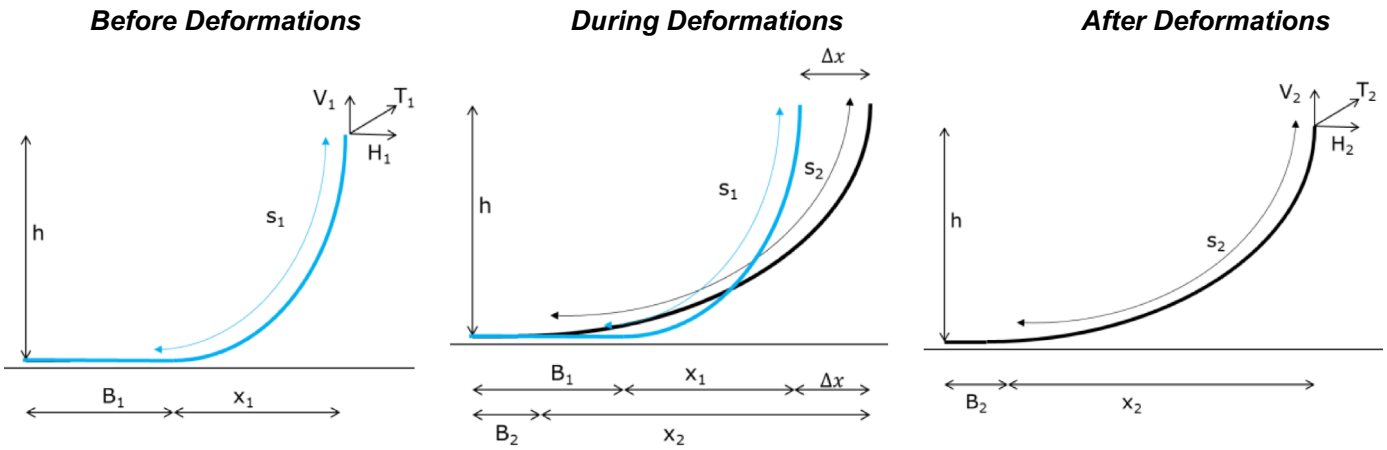

Fig. A.1. Steps of the preliminary design algorithm.

ensure that the line will not completely leave the seabed, thus it will not be completely taut. The horizontal projections of the catenary part are x_1 and x_2, corresponding to the states before and after deformations, respectively.

The deformations consist of a horizontal displacement, Δx of the fairlead. At the fairlead, the tensile force Thas a vertical component, V, and a horizontal one, H. Each of these forces has two states, 1 and 2, for before and after deformations, respectively. The aim of the present algorithm is to determine the initial geometry given parameters w, h and Δx.

After deformations, the line supports a tension T_2. Its suspended length can be calculated by

$$s_2 = \sqrt{\frac{2hT_2}{w} - h^2} \tag{A.1}$$

Then, a system of two nonlinear equations with two unknowns, H_2 and x_2, is set based on the results from Eq. (A.1) and simultaneously solved:

$$\begin{cases} s_2 = \dfrac{H_2}{w}\sinh\left(\dfrac{wx_2}{H_2}\right) \\ h = \dfrac{H_2}{w}\left[\cosh\left(\dfrac{wx_2}{H_2}\right) - 1\right] \end{cases} \tag{A.2}$$

During deformations, the total length conservation is assumed: $B_1 + s_1 = B_2 + s_2$. Horizontally along the seabed, it can be written $B_1 + x_1 + \Delta x = B_2 + x_2$. Both equations combine to $s_1 - x_1 = s_2 - x_2 + \Delta x$.

Before deformations, a system of equations similar to Eq. (A.2) is also set:

$$\begin{cases} s_1 - x_1 = s_2 - x_2 + \Delta x = \dfrac{H_1}{w}\sinh\left(\dfrac{wx_1}{H_1}\right) - x_1 \\ h = \dfrac{H_1}{w}\left[\cosh\left(\dfrac{wx_1}{H_1}\right) - 1\right] \end{cases} \tag{A.3}$$

Eq. (A.3) can be simultaneously solved for H_1 and for x_1. Therefore, the radial distance from the fairlead to the anchorage can be obtained by $\mathrm{Rad} = B_1 + x_1 = x_1 - s_1 + (1 + \theta)s_2$; and the total length $a = 2\sqrt{2}\, l_{\mathrm{Fe-As}} \sin(\theta/2) b = ac = l_{\perp \mathrm{As-As}} + 2l_{\mathrm{Fe-As}} \cos(\theta/2)$.

References

Abaqus, 2012. Keywords Reference Manual. Dassault Systèmes.

Abdallah, I., Natarajan, A., Sørensen, J.D., 2015. Impact of uncertainty in airfoil characteristics on wind turbine extreme loads. Renew. Energy 75, 283–300.

American Association of State Highway and Transportation, 2012. AASHTO LRFD Bridge Design Specifications. Ed. 6.

Ankit, A., Datta, N., Kannamwar, A.N., 2016. Free transverse vibration of mono-piled ocean tower. Ocean Eng. 116, 117–128.

Bak, C., Zahle, F., Bitsche, R., Kim, T., Yde, A., Henriksen, L.C., Andersen, P.B., Natarajan, A., Hansen, M.H., 2013. INNWIND.EU Deliverable 1.2.1 – Description of the DTU 10 MW Reference Wind Turbine. ⟨http://www.innwind.eu/-/media/Sites/innwind/Publications/Deliverables/DeliverableD1,-d-,21%20Aerodynamic_StructuralValidation_INNWIND,-d-,EU.ashx?la=da⟩.

Benassai, G., Campanile, A., Piscopo, V., Scamardella, A., 2014. Ultimate and accidental limit state design for mooring systems of floating offshore wind turbines. Ocean Eng. 92, 64–74.

Brown, D.T., 2005. Mooring systems. In: Chakrabarti, S. (Ed.), Handbook of Offshore Engineering. Elsevier, Oxford, Great Britain, pp. 663–708.

Chakrabarti, S., 2005. Handbook of Offshore Engineering. Elsevier, Oxford, Great Britain.

Comite Euro-International du Beton, 1993. CEB-FIP Model Code 1990, Design Code. Thomas Telford Services Ltd., London.

Cremer, L., Heckl, M., 1988. Structure-Borne Sound. Springer-Verlag, New York.

Det Norske Veritas, 2013. Offshore mooring chain, Offshore Standard DNV-OS-E302.

Det Norske Veritas, 2013. Position mooring, Offshore Standard. DNV-OS-E301.

Det Norske Veritas, 2014. Design of Offshore Wind Turbine Structures – Offshore Standard. DNV-OS-J101.

Kallehave, D., Byrne, B.W., LeBlanc Thilsted, C., Mikkelsen, K.K., 2015. Optimization of monopiles for offshore wind turbines. Philos. Trans. R. Soc. A 373, 1–15.

Kim, J.H., Hong, S.Y., Kim, H.J., 2014. The shape design and analysis of floating offshore wind turbine structures with damper structure and shallow draft. Ocean Wind Energy 1 (3), 170–176.

Larsen, T.J., Hansen, A.M., 2015. How 2 HAWC2, the user's manual DTU Risoe-R-1597. ⟨http://www.hawc2.dk/-/media/Sites/hawc2/HAWC2%20Download/HAWC2%20manual/manual_version_4-6.ashx⟩.

MacCamy, R.C., Fuchs, R.A., 1954. Waves Forces on Piles: A Diffraction Theory. Corps of Engineers, Washington, DC, US, pp. 1–17.

Mann, J., 1994. The spatial structure of neutral atmospheric surface-layer turbulence. J. Fluid Mech. 273, 141–168.

Manwell, J.F., McGowan, J.G., Rogers, A.L., 2009. Wind Energy Explained: Theory, Design and Application, 2nd ed. John Wiley and Sons, Ltd..

Massachussets Departement of Transport, Highway Division, 2005. 2005 MHD bridge section weighted average unit prices – guidelines for the use of the weighted average unit price tabulation sheets. Massachussets Departement of Transport, Highway Division, Massachussets.

Montasir, O.A., Yenduri, A., Kurian, V.J., 2015. Effect of mooring line configurations on the dynamic responses of truss spar platforms. Ocean Eng. 96, 161–172.

Navik, P., Ronnquist, A., Stichel, S., 2016. Identification of system damping in railway catenary wire systems from full-scale measurements. Eng. Struct. 113, 71–78.

Sanz, M., Natarajan, A., Henriksen, L.C., 2013. Feasibility study of a semi floating spar buoy wind turbine anchored with a spherical joint to the sea floor. EWEA Offshore.

Sedillot, F., Stevenson, A., 1983. Laminated rubber articulated joint for the deep water gravity tower. Trans. ASME 105, 480–486.

Shah, D.U., Schubel, P.J., Clifford, M.J., 2013. Can flax replace E-glass in structural composites? A small wind turbine blade case study. Compos. Part B 52, 172–181.

South, J.T., 2001. Mechanical Properties and Durability of Natural Rubber Compound and Composites. Virginia Polytechnic Institute, Blacksburg, Virginia, US.

The international Electrotechnical Commission, 2005. Wind Turbines – Part 1: Design requirements, IEC 61400-1 Ed 3.

The international Electrotechnical Commission, 2009. Wind Turbines – Part 3: Design requirements for offshore wind turbines, IEC 61400-3 Ed 1.

Thonier, H., 1992. Conception Et Calcul Des Structures De Batiment. Ponts et chaussees, Paris, France.

Von Borstel, T., 2013. INNWIND.EU Deliverable 4.3.1 – Design report – Reference Jacket. ⟨http://www.innwind.eu/-/media/Sites/innwind/Publications/DeliverableD4,-d-,31_20131030_INNWIND,-d-,EU.ashx?la=da⟩.

Wang, C.M., Utsunomiya, T., Wee, S.C., Choo, Y.S., 2010. Research on floating wind turbines: a literature survey. IES J. Part A: Civil. Struct. Eng. 3 (4), 267–277.

Wayman, E.N., Sclavounous, P.D., Butterfield, S., Jonkman J., Musial, W., 2006. Coupled Dynamic Modeling of Floating Wind Turbine Systems. Offshore Technology Conference, Houston, Texas.

6

Paper II: Influence of Model Parameters on the Design of Large Diameter Monopiles for Multi-megawatt Offshore Wind Turbines at 50 m Water Depths

Influence of model parameters on the design of large diameter monopiles for multi-megawatt offshore wind turbines at 50 m water depths

NJOMO WANDJI Wilfried, Anand NATARAJAN, Nikolay DIMITROV
Department of Wind Energy, Technical University of Denmark, Risoe campus, Roskilde Denmark

Abstract

Relevant modelling approaches towards the design of a large diameter monopile for 10 MW offshore wind turbines at 50 m water depths are considered to evaluate their respective impacts on the structural integrity. The analysed models or model parameters include soil-structure interaction, construction errors, and damping. The study is conducted on a reference structure verified with respect to fatigue, ultimate (strength, stability, and soil capacity), and serviceability limit states after fully-coupled load simulations. Models and their parameters are carefully obtained in line with the case in hand. Perturbation analysis is used to assess the impact of the soil model, the geometric imperfections, and the damping on the structure safety and robustness. Results show that all of them significantly influence the fatigue lifetime, the geometric imperfections and the soil model impact the ultimate stresses, and the soil model affects the deformations of the final design, from which guidance on the optimal selection of these parameters leading to material savings is made.

1 Introduction

The growing offshore wind industry continues to extensively use monopile substructures for offshore wind turbines installations. As offshore wind turbines get larger and installed in increasingly deeper sea waters, they require substructures that are both cost effective and reliable. Amongst the fixed bottom types used in offshore environments, Kallehave *et al.* [1] have listed monopile (74 %), gravity based foundation (16 %), multiple foundation (5 %) and jacket foundation (5 %) as common concepts. Whereas the gravity based foundation is suitable for shallow waters, jackets can be proven extremely challenging to ensure durability for 25 years with respect to their fatigue limit state (FLS) for 10 MW wind turbines at 50 m waters [2]. Thus, monopile stands as a potential candidate for a 10 MW wind turbine at 50 m water depth, if such a design can be proven feasible.

Few investigations have been made on monopile foundations for multi-megawatt wind turbines at greater water depths (25 m to 40 m). Sharff and Siems (2013a) [3] proposed a monopile design based on parameter study for 6 MW wind turbine at water depths between 20 m and 40 m. In this study, the buckling state of the pile shell was not explicitly discussed. Later, Sharff and Siems (2013b) [4] presented a new design methodology where the buckling limit state was studied using a 3D numerical shell model. Furthermore, Arany *et al.* (2015) [5] have mentioned the necessity to assess the soil limit states in case of large diameter monopile, as the soil can fail before the structure.

However, the soil models or their parameters used in these studies are generally derived and appropriate for small diameter monopiles and may not be optimal for large ones. Indeed, the recommended nonlinear soil stiffness values based on the Murchison and O'Neil's work [6] and firstly incorporated in API-RP2A-WSD [7] were developed for monopile diameter smaller than 1.00 m. It has been since shown that this method, although widely used, was improper for large diameter monopiles, e.g. [8]. Actually, Thieken *et al.* [8] have underlined that the standard method tends to underestimate the soil stiffness for small displacements, which is the operational domain of large monopiles, and overestimate the soil capacity. In addition, it does not account for the soil medium continuity and proposes similar behaviour at the pile head, partway, or tip, which leads to erroneous pile deflection shape. Therefore, an adequate soil-structure interaction model, developed by Thieken *et al.* [8], is employed for the design process in this study.

In other situations, the design values of the parameters may present a large deviation in comparison to their actual values. For instance, typical design values for overall structural logarithmic decrement damping are about 6.00 % [1]. Koukoura *et al.* [9] measured a stand-still support-structure damping of approximately 12 % for a multi-megawatt wind turbine supported by monopile substructure. The study concludes that significant savings could be achieved if appropriate damping value was used in the design phase for stress calculations. These stresses are usually amplified at the welded connections mainly due to geometric imperfections as suggested by standards [10]. However, it is challenging to estimate the level of imperfections that will be actually present once the structure will be commissioned. The selection of a given geometric imperfection level with respect to the fabrication tolerance significantly impacts the result and may affect the design integrity if the construction does not ensure that the hypothesised level is respected.

The aim of this study is not to offer an optimal or ready-to-build design but to propose a feasible reference design obtained out of the suggested design procedure. The subsequent sections investigate the impact of the primary modelling choices on the design of the reference large diameter monopile. They explore models and model parameters related to soil-structure interaction, construction errors, and damping. Based on fully coupled load simulations of a conceptual 10 MW wind turbine located at 50 m water depth, several limit states are analysed -

fatigue, ultimate (strength, stability, and soil capacity), and serviceability – and the effects of modelling choices are discussed.

2 Site conditions, structure, and design constraints

2.1 Metocean conditions

Throughout this study, site specific metocean conditions, taken from [1], are considered. The operational mean wind speed range varying from 4 m/s to 25 m/s is divided into 11 bins of 2 m/s width. An additional mean wind speed of 42.73 m/s accounts for extreme storms. The distribution of the wind direction is shown on Figure 1 [11].

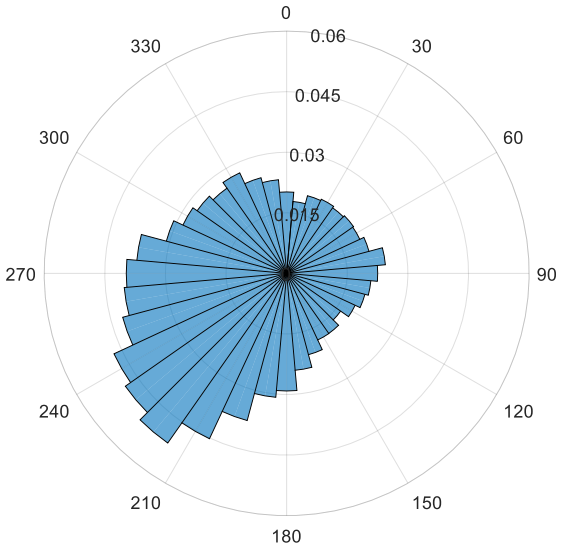

Figure 1. Distribution of the wind direction [11]

Each mean wind speed bin is associated with expected sea states, i.e. significant wave height (Hs) and peak spectral period (Tp), and an expected annual frequency as shown in Table 1. Table 2 gives the respective characteristic turbulence intensities observed for each wind speed bin during normal turbulence and extreme turbulence together with the turbulence associated with the storm wind speed. The wave height is modelled based on either the JONSWAP spectrum (under extreme turbulence conditions or extreme wind conditions) or the Pierson-Moskowitz spectrum (under normal turbulence) at the expected value of the sea state characteristics conditional on the mean wind speed. The Pierson-Moskowitz type is used for fatigue load case simulations because of its wide-band energy distribution, while the JONSWAP type is suitable for ultimate load cases due to its peaked shape which can promote resonance if the peak coincides with the natural frequencies of the structure.

Marine growth is present from the mean sea level to the seabed with a thickness of 100 mm in accordance with API-RP2A-WSD [7]. The submerged density of the marine growth is taken as 373 kg/m^3.

Table 1: Sea state characteristics conditional on the mean wind speed.

Wind speed [m/s]	Expected Significant height, Hs [m]	Peak period, Tp [s]	Expected annual frequency [%]
5	1.140	5.820	10.65
7	1.245	5.715	12.40
9	1.395	5.705	12.88
11	1.590	5.810	12.63
13	1.805	5.975	11.48
15	2.050	6.220	9.36
17	2.330	6.540	7.22
19	2.615	6.850	4.78
21	2.925	7.195	3.57
23	3.255	7.600	2.39
25	3.600	7.950	1.70
42.73 (Storm)	9.400	13.700	

Table 2: Atmospheric turbulence for normal or extreme model.

Wind speed [m/s]	5	7	9	11	13	15	17	19	21	23	25	42.73
Normal Turbulence Intensity [%]	18.95	16.75	15.60	14.90	14.40	14.05	13.75	13.50	13.35	13.20	13.00	11.00
Extreme Turbulence Intensity [%]	43.85	33.30	27.43	23.70	21.12	19.23	17.78	16.63	15.71	14.94	14.30	11.00

2.2 Soil properties

The soil properties used in [1] will be employed herein. It is composed of superimposed sandy layers of medium to high density. The complete description of the relevant soil properties is presented in Table 3.

Table 3: Soil properties.

Depth range [m]	0.0 – 15.0	15.0 – 20.0	20.0 – 22.5	22.5 – 90.0
Angle of internal friction [°]	35.0	37.5	40.0	40.0
Poisson's ratio [-]	0.250	0.225	0.200	0.200
Void ratio [-]	0.69	0.65	0.60	0.57
Submerged unit weight [kN/m^3]	9.76	10.0	10.5	11.0

2.3 Structure as case study

A conceptual 10 MW wind turbine is chosen as the structure to be mounted on the monopile whose design is sought. The DTU 10 MW reference wind turbine (DTU 10 MW RWT) is a variable-

speed, pitch-controlled, direct drive machine, and its design is described in detail in Bak *et al.* (2013) [12]. Its key design parameters are presented in Table 4.

Table 4: Key parameters of the DTU 10 MW RWT.

Parameters	Values
Wind regime	(see Table 1 and Table 2)
Rotor type, orientation	3 bladed - Clockwise rotation – Upwind
Control	Variable speed – Collective pitch
Cut-in, rated, cut-out wind speed	4 m/s, 11.4 m/s, 25 m/s
Rated power	10 MW
Rotor, hub diameter	178.3 m, 5.6 m
Hub height	119.0 m
Drivetrain	Medium speed, Multiple-stage Gearbox
Minimum, maximum rotor speed	6.0 rpm, 9.6 rpm
Maximum generator speed	480.0 rpm
Gearbox ratio	50
Maximum tip speed	90.0 m/s
Hub overhang	7.1 m
Shaft tilt, coning angle	5.0°, -2.5°
Blade prebend	3.3 m
Rotor mass including hub	227,962 kg
Nacelle mass	446,036 kg
Tower mass	628,442 kg

The DTU 10 MW RWT has a rotor speed varying between 6.0 rpm and 9.6 rpm. With the help of a Campbell diagram, the allowable support-structure soft-soft natural frequency domain is found to range within [0.00 Hz 0.10 Hz], the soft-stiff domain ranges within [0.16 Hz 0.30 Hz], and the stiff-stiff domain within [0.48 Hz 0.60 Hz].

The appurtenances [13] consist of boat-landing of 772 mm equivalent diameter running from 6.0 m above the mean sea level till 2.0 m below and J-tube of 324 mm running from 26.0 m above the mean sea level till the mudline. Figure 2 presents a view of the substructure and its secondary structures. Four homogeneous portions can be distinguished where the hydrodynamic coefficients are constant. Portion 1 contains the plain monopile and the J-tube, Portion 2 comprises the monopile, the J-tube and the boat-landing equipment, Portion 3 differs to Portion 2 by marine growth, and Portion 4 adds marine growth to Portion 1.

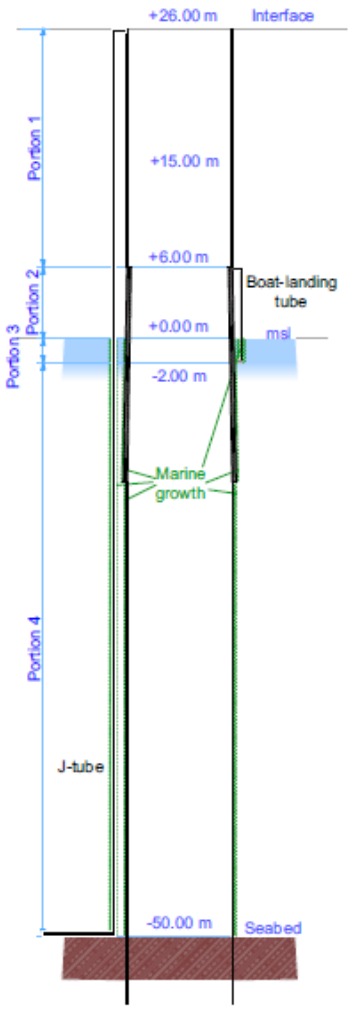

Figure 2. View of the substructure with the appurtenances and marine growth.

2.4 Design constraints

The design of the monopile must satisfy several constraints related to resonance avoidance, elastic/plastic operational behaviour of the system, hammering induced stresses, and global performance.

- Resonance should be avoided by setting the dominant natural frequencies of the support-structure away from the above-mentioned rotor harmonics and the dominant wave frequencies, whose significant energy (95 % of the area under the wave spectrum curve) is contained up to approximately 0.23 Hz. Thus, the first natural frequencies of the support-structure may lie within [0.23 Hz 0.30 Hz] and [0.48 Hz 0.60 Hz].
- The whole structural system should operate within its elastic range throughout the turbine's lifetime (assumed to be 25 years) in order to apply linear summation (Miner rule for example) throughout the years.
- The monopile is assumed to be driven into the soil by hammering, whose induced extreme stresses are assumed to be lower than those developed during the operations. API-RP2A-WSD

[7] recommends a minimum thickness $t_{min}[mm] = 6.35 + D[mm]/100$ to ensure the endurance during the hammering phase. However, Scharff and Siems [4] noted that this recommendation applied for diameters up to 3000 mm and should not be taken as a strict limitation for large monopile. Therefore, 10 % of the intended service lifetime is provided as equivalent endured fatigue during the construction phase [14].

3 Load assessment

3.1 Damping

The net damping, which is generally defined with respect to the first bending mode of the structure, is difficult to quantify since it is composed of structural, hydrodynamic, soil, and aerodynamic parts. Arany *et al.* [5] recommend a total logarithmic decrement damping of 18.86 %. As the aerodynamic damping is inherent to aeroelastic interactions handled by the load simulation code, only the remaining constituents are prescribed during the load simulation. Kallehave *et al.* [1] report an overall structural logarithmic decrement damping lying between 5.66 % and 7.54 %. Tarp-Johansen *et al.* [15] propose a decomposition of the overall structural logarithmic decrement damping: about 3.00 % to 5.00 % for the visco-elastic behaviour of the soil; about 1.50 % for only the hydrodynamic radiation; and about 1.20 % for the steel tower and pile disregarding the grout. These quantities sum up to 5.70 % to 7.70 %, which agree well with the report of Kallehave *et al.* [1]. The reference value in this study of the logarithmic decrement damping will be taken as 6.70 %, which decomposes as: about 4.00 % from the soil; about 1.50 % for the sea; and about 1.20 % for the structure.

3.2 Sea-structure interactions

Random wave kinematics is computed according to the linear Airy model with Wheeler stretching [16]. The hydrodynamic forces are calculated based on the Morison's equation [16]. For a unit length monopile, the hydrodynamic force normal to monopile axis is calculated as:

$$F = \frac{1}{2}\rho_w\, D\, C_D(u_w + u_c - u_s)|u_w + u_c - u_s| + \rho_w C_a \frac{\pi D^2}{4}(\dot{u}_w - \dot{u}_s) + \rho_w \frac{\pi D^2}{4}\dot{u}_w \qquad (1)$$

Where

D [m]:	monopile's outer diameter;
u_c [m/s]:	current speed;
u_w [m/s]:	wave particle speed normal to the monopile axis;
u_s [m/s]:	moving monopile velocity;
$\dot{u}_w$ [m/s^2]:	wave particle acceleration normal to the monopile axis;
$\dot{u}_s$ [m/s^2];	moving monopile acceleration; and
$\rho_w = 1025\ kg/m^3$:	water mass density.

To account for the effect of appurtenances, diffraction, and marine growth, the equivalent drag coefficient C_D and the equivalent inertia coefficient $C_M = 1 + C_a$ are estimated as in IEC 61400-3 [17]:

$$C_D = \frac{D'}{D} C_{DS}(e)\ \varphi(C_{DS}, K_C) + \sum_{i=1}^{N} \left[\frac{d_i'}{D} C_{DS,i}(e)\ \varphi\left(C_{DS,i}, K_{C,i}\right) IF_D\left(\theta_i, K_{C,i}\right) \right] \tag{2}$$

$$C_M = \left(\frac{D'}{D}\right)^2 C_{M,D} + \sum_{i=1}^{N} \left\{ \left(\frac{d_i'}{D}\right)^2 \left[1 + \left(\left(C_{M,i}\left(C_{DS,i}, K_{C,i}\right) - 1 \right) IF_M\left(\theta_i, K_{C,i}\right) \right) \right] \right\} \tag{3}$$

Where

$$R = \frac{U_m D'}{\nu};\ R_i = \frac{U_m d_i'}{\nu};\ K_C = \frac{U_m T_p}{D'};\ K_{C,i} = \frac{U_m T_p}{d_i'};\ e = \frac{k}{D'};$$

$$D' = D + 2t_{MG};\ d_i' = d_i + 2t_{MG};\ U_m = u_w + u_c$$

The symbols used denote:

t_{MG} : marine growth thickness;

d_i : appurtenance diameter;

θ_i : appurtenance orientation on monopile relative to wave and current direction;

D : monopile outer diameter;

k : surface roughness;

ν : kinematic viscosity of the water;

$\varphi(C_{DS}, K_C), \varphi\left(C_{DS,i}, K_{C,i}\right)$: sea wake amplification factors, whose values depend on Keulegan–Carpenter number and current/wave velocity ratio [18] and vary around 1.0. For simplicity, they have been set to 1.0 [13].

$IF_D\left(\theta_i, K_{C,i}\right), IF_M\left(\theta_i, K_{C,i}\right)$: Interference factors expressing the variation in hydrodynamic coefficients for the appurtenance i due to the presence of the monopile. For large monopiles, this interference is negligible: $IF_D\left(\theta_i, K_{C,i}\right) = 1.00;\ IF_M\left(\theta_i, K_{C,i}\right) = 1.00;$

$C_{DS}(e), C_{DS,i}(e)$: drag coefficients for steady state;

$C_{M,i}\left(C_{DS,i}, K_{C,i}\right)$: inertia coefficient related to the appurtenance i.

$C_{M,D}$: inertia coefficient related to the monopile, which accounts for the diffraction.

DNV-OS-J101 [19] gives for steady-state flow the value of the drag coefficient:

$$C_{DS}(e) = \begin{cases} 0.65, & for\ e < 10^{-4}\ (smooth) \\ \dfrac{29 + 4\log_{10}(e)}{20}, & for\ 10^{-4} < e < 10^{-2} \\ 1.05, & for\ e > 10^{-2}\ (rough) \end{cases} \tag{4}$$

New uncoated steel and painted steel can be assumed to be smooth. For marine growth, $k = 0.005\ m\ to\ 0.05\ m$ can be assumed. $C_{DS,i}(e)$ is computed in the similar fashion. For the inertia coefficient, DNV-OS-J101 [19] recommends:

$$C_{M,i}(C_{DS,i}, K_{C,i}) = \begin{cases} 2.0, & K_{C,i} < 3 \\ max\{2.0 - 0.044(K_{C,i} - 3); 1.6 - (C_{DS,i} - 0.65)\}, & K_{C,i} \geq 3 \end{cases} \quad (5)$$

For large structures whose characteristic length, i.e. outer diameter, is greater than one fifth of the wave length, the diffraction phenomenon becomes important. This is accounted for in the coefficient of inertia as [20]:

$$C_{M,D} = \frac{4}{\pi^3 \lambda^{-2} D'^2 \sqrt{[J_1'(\pi D'/\lambda)]^2 + [Y_1'(\pi D'/\lambda)]^2}} \quad (6)$$

J_1' and Y_1' are derivatives of Bessel function of first and second kinds, respectively. λ is the wave length defined as $2\pi\lambda = T_p^2 g \tanh(2\pi h/\lambda)$, where g [m/s^2] is the gravity acceleration and h [m] is the water depth.

Based on this algorithm and the design conditions presented in Section 2, equivalent drag and inertia coefficients are computed and given in Table 5.

Table 5: Hydrodynamic coefficients.

		Plain monopile	Portion 1	Portion 2	Portion 3	Portion 4
C_D		0.65	0.67	0.72	1.18	1.09
C_M	Operational range	2.00	2.00	2.01	2.10	2.09
	Storm	1.93	1.93	1.94	2.03	2.01

3.3 Soil-structure interactions

Conventionally, the interactions between the pile and the surrounding soil are described based on the models introduced by API-RP2A-WSD [7] and recommended by DNV-OS-J101 [19] or ISO 19902:2007 [18]. The model is based on Winkler elastic beam, which assumes that the soil acts as a series of vertical and lateral nonlinear springs distributed along the pile axis (see Figure 3). It is also assumed that the stiffness of the soil in yaw is large enough so that the pile does not undergo significant yaw rotation. The other rotational DOFs and all the translational DOFs are free at both the pile toe and at the mudline.

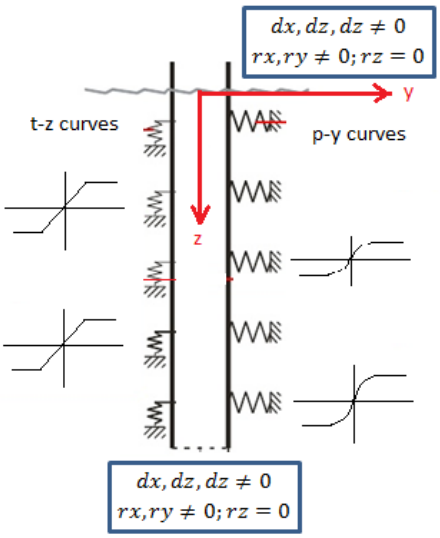

Figure 3. Soil-pile interactions – Boundary conditions – Coordinates system.

The model recommended by the present offshore guidelines ([7], [18], [19]) is based on Murchison and O'Neil (1984) work [6], where the lateral force-displacement relationship is expressed as:

with

$$p(y) = Ap_u \tanh\left(\frac{kz}{Ap_u}y\right)$$
$$p_u = min\{(C_1 z + C_2 D)\gamma' z\ ;\ C_3 D\gamma' z\} \quad (7)$$

The initial modulus of subgrade reaction, k is given as function of the internal friction angle in the guidelines ([7], [18], [19]). Similarly, the coefficients C_1, C_2, and C_3 are dependent on the angle of internal friction and can be found in guidelines. The factor accounting for the cyclic loading mode $A = 0.9$. z is the depth below the mudline, D is the pile outer diameter, and γ' is the submerged unit weight.

However, as presented in the introduction, the above-mentioned model is not as accurate as the approach proposed by Thieken *et al.* (2015) [8], which has been calibrated for piles with arbitrary dimensions in sand. This approach proposes piece-wise p-y curves composed of four intervals as expressed by the equations in Table 6 and Table 7.

Table 6: Subdivision of the curve in intervals and corresponding parameters.

	0		A		B		C	
y	0	$0 \le y \le y_A$	y_A	$y_A \le y \le y_B$	y_B	$y_B \le y \le y_C$	y_C	$y_C \le y$
n	n_0	n_{0A}	n_A	$n_{AB} = n_A$				
p	0	$p(y) = p_{0A}$	p_A	$p(y) = p_{AB}$	p_B	$p(y) = p_{BC}$	p_C	$p(y) = p_C$

Table 7: Values of the model parameters.

$\sigma_m = \frac{p_0'}{3}(3 - 2\sin\varphi')$	$SF_{py,bend} = \begin{cases} 0.3 + 2.3\frac{y}{y_{max}}, & z \le z_{y_0} \\ 0.3 + 1.2\frac{y}{y_{min}}, & z_{y_0} < z \le z_{y_{min}} \\ \max\left(1.0, 0.3 + 1.2\frac{y}{y_{min}}\right), & z > z_{y_{min}} \end{cases}$	$G_0 = 220\frac{(2.17 - e)^2}{1 + e}\sigma_m^{0.5}$
$SF_{py} = SF_{py,bend} + SF_{py,tip}$	$SF_{py,tip} = \begin{cases} 0, & z < L - 2D \\ 5\left(\frac{z - L}{2D} + 1\right)^5, & L - 2D \le z < L - 0.1D \\ 5\left(\frac{z - L}{2D} + 1\right)^5 + 3, & z \ge L - 0.1D \end{cases}$	$E_{py}^0 = G_0\frac{2(1 - \nu^2)}{1 - \nu - 2\nu^2}SF_{py}$
$\delta_p = -\frac{2}{3}\varphi'$	$K_{pgh} = \sqrt{\frac{\left[\frac{1 + \sin\varphi'}{1 - \sin\varphi'}\left(1 - 0.53\delta_p\right)^{0.26 + 5.96\varphi'}\right]^2}{1 + \left(\tan\delta_p\right)^2}}$	$p_C^{Basic} = \frac{11}{16}\gamma' z^{1.5}K_{pgh}(1 + 2\tan\varphi')\sqrt{D}$
$y_C = 4\frac{p_C}{E_{py}^0}$	$p_C^0 = \max\left(p_C^{Basic}, p_C^{Basic}\left[3 - 2\left(\frac{z}{2.5D}\right)^{0.25}\right]\right)$	$p_C = \frac{0.9}{\max(0.9,\ 3.0 - 0.8z/D)}p_C^0$
$y_A = 0.005D\frac{p_C}{E_{py}^0}$	$y_B = \frac{p_C}{E_{py}^0}$	$n_{0A} = n_0 + (n_A - n_0)\left(\frac{y}{y_A}\right)^{0.25}$
$n_0 = \frac{\log(10^{-5}D/y_B)}{\log(E_{py}^0 10^{-5}D/p_B)}$	$n_A = 2.4 - 0.08(\varphi' - 30°)$	$p_{0A} = \min\left(E_{py}^0, p_B\left(\frac{y}{y_B}\right)^{1/n_{0A}}\right)$
$p_{AB} = \min\left(E_{py}^0, p_B\left(\frac{y}{y_B}\right)^{1/n_A}\right)$	$p_B = p_C\max\left(0.35, 0.63 - 0.33\left(\frac{z/D}{7.5}\right)^{0.5}\right)$	$p_{BC} = p_B + \left(\frac{p_C - p_B}{y_C - y_B}\right)(y - y_B)$

Where:

γ': submerged unit weight [MN/m^3]
φ': angle of internal friction [°]
ν: Poisson's ratio [-]
D: outer diameter [m]
z_{y_0}: depth of the rotation point [m]
$z_{y_{min}}$: depth of the minimum deflection y_{min} [m]
z: distance below the seabed [m]
e: void ratio [-]
L: embedded pile depth [m]
y: lateral displacement of the pile [m]
y_{max}: maximum pile deflection [m]
y_{min}: minimum deflection on the rear side of the pile [m]

The new model is prepared for static cases. A simplified adaptation of this model, in line with that done in the standard model, is implemented to extend it to cyclic loading conditions. Actually, the model for dynamic situations is obtained in the standards by modifying the lateral resistance, keeping the initial stiffness unchanged. This is consistent with the statement of Thieken *et al.* [8], who reported that dynamic loading has marginal influence on the initial stiffness. In the standards, the dynamic lateral resistance, p_d, is related to the static resistance, p_s, as expressed by Equation (8). Similar relationship is used to convert the Thieken *et al.*'s static model to dynamic model.

$$p_d = \frac{0.9}{\max(0.9, 3.0 - 0.8z/D)}p_s \tag{8}$$

Whether lateral model is used, the vertical force-displacement relationship is modelled by a bilinear curve, which increases linearly from the neutral state (zero deformation and zero force) to the pile vertical capacity, t_{max}, which corresponds to a settlement of 2.5 mm. After the knee point, the unit skin friction stays constant. The pile vertical capacity is given as $t_{max} =$

$min\{Kp_0' \tan\delta \; ; \; f_1\}$. f_1 is the limiting unit skin friction; δ is the friction angle between the pile wall and the soil. f_1 and δ are given in API-RP2A-WSD in dependence of soil relative density. Because the pile is open-ended, $K = 0.8$. p_0' is the effective overburden pressure at the point of interest.

Figure 4 compares the nonlinear stiffness of the springs in the novel approach with those in the approach recommended by the guidelines for a pile of 60 m embedded depth, 9500 m outer diameter, and 102 mm wall thickness. It can be seen that the initial stiffness is higher in the novel approach while the resistance is smaller.

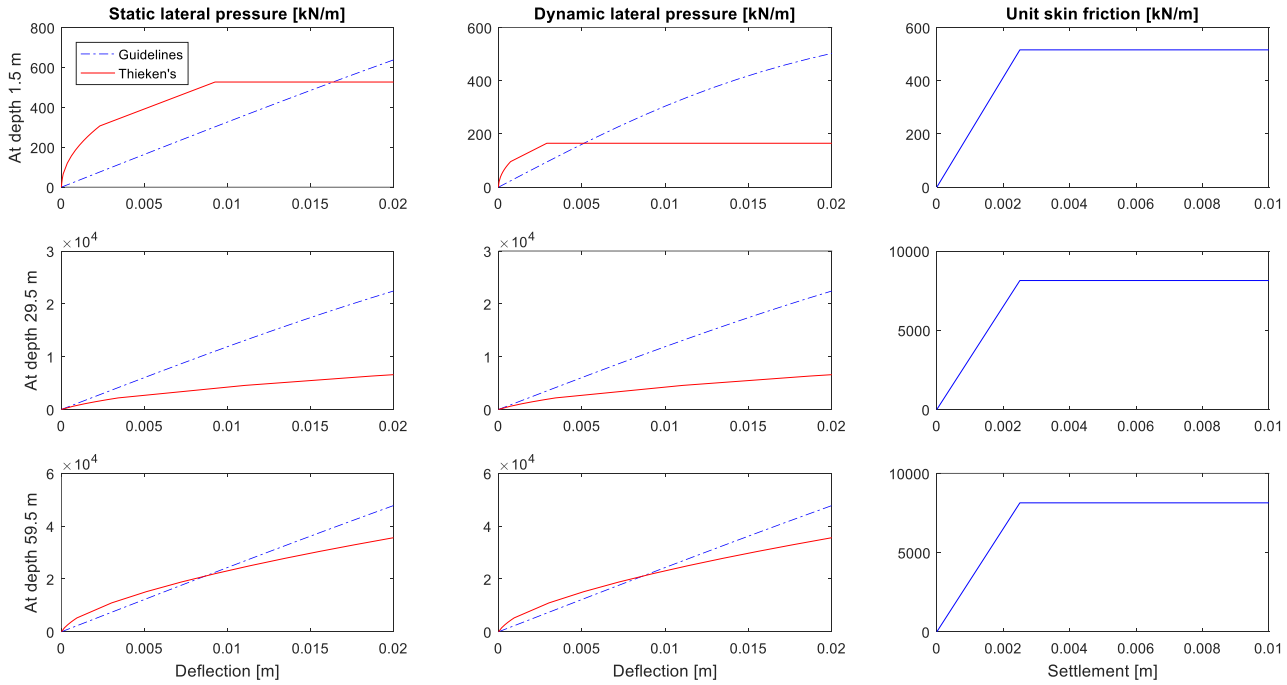

Figure 4. P-y and t-z curves representing both models for various depths and for static and dynamic loadings. The monopile used has L=60 m, D=9500 mm, t=102 mm.

4 Limit states

The dynamic analyses for load assessment of the turbine mounted on the monopile are carried out with the aero-hydro-servo-elastic tool HAWC2 [21]. HAWC2 is a time domain solver which utilizes a multibody elastic formulation which couples the structure with rotor aerodynamics, turbine control and hydrodynamics, maintaining dynamic equilibrium.

4.1 Estimation of stress concentration factors

The hotspot stresses are evaluated using stress concentration factors (SCFs) at the weld connections. The weld connections of the appurtenances to the main steel are not studied here. For butt connections with same nominal diameter and thickness, DNV RP C203 [22] recommends estimating SCFs as in Equation (9):

$$SCF = 1 + \frac{3\,\delta_m}{t} e^{-\sqrt{t/D}} \tag{9}$$

where D and t are respectively the outer diameter and the wall thickness, $\delta_m = \sqrt{\delta_t^2 + \delta_r^2}$ is the resultant geometric imperfection measure, whose components are due to out-of-roundness or eccentricity. The actual imperfection measure is project dependent and brings uncertainties to the design procedure as it cannot accurately be predicted in advance. In any case, it is comprised between zero (perfect manufacturing and handling) and the admissible tolerance as recommended by DNV OS C401 [10] for example. Imperfection levels, λ, can be defined as the ratios between the resultant geometric imperfection measure, δ_m, and the admissible tolerance. For a 9500 mm diameter, Figure 5a illustrates the variation of SCF values in dependence of wall thickness and for various levels of imperfection. It is obvious that SCF equal one in case of no imperfection. It can be seen that, for small thicknesses, SCF values are very dispersed depending on the imperfection level. The dispersion reduces for large thicknesses. For a typical thickness of 100 mm, the SCFs vary between 1.0 and 1.8. In this study, a reference imperfection level of 0.50 is considered.

At butt welds where thicknesses change from a larger thickness T to a smaller thickness t, SCFs are calculated from Equation (10) [22]:

$$SCF = 1 + \frac{6\,(0.5(T-t) + \delta_m - \delta_0)}{t\left(1 + \left(\frac{T}{t}\right)^{\beta}\right)} e^{-\alpha} \tag{10}$$

where $\alpha = \frac{1.82L}{\sqrt{Dt}} \frac{1}{1 + (\frac{T}{t})^{\beta}}$; $\beta = 1.5 - \frac{1.0}{\mathrm{Log}\left(\frac{D}{t}\right)} + \frac{3.0}{\left[\mathrm{Log}\left(\frac{D}{t}\right)\right]^2}$; $\delta_0 = 0.1t$

As per Figure 5b, SCF values related to thickness change vary by a factor of about 1.8 from zero imperfection till full allowable imperfection. For a given imperfection level, a large difference between the connected thicknesses will give a large SCF, which increases further if the thicknesses are small.

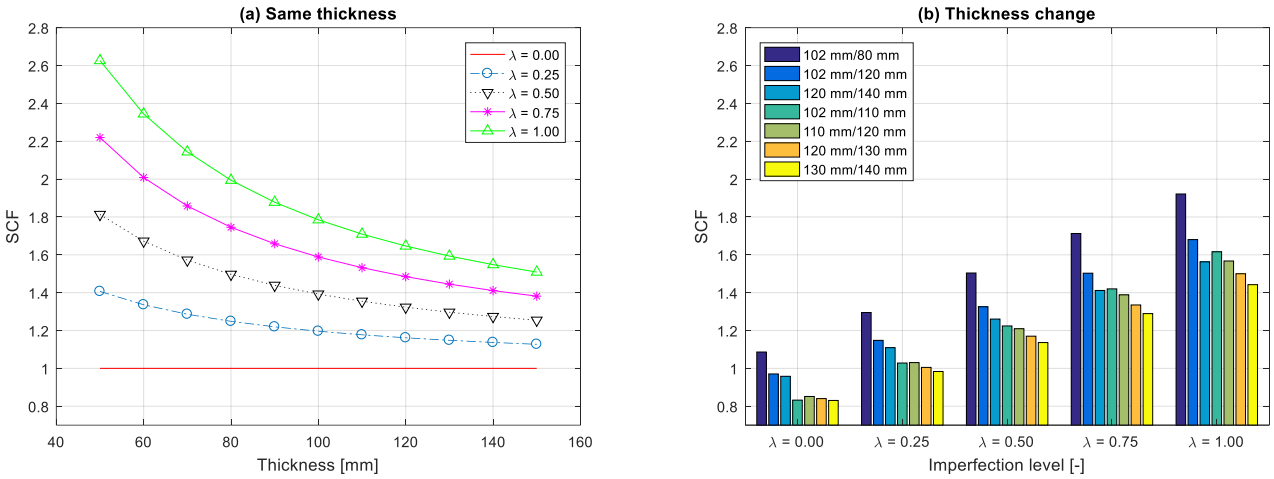

Figure 5. Effect of the geometry imperfection on stress concentration factors for OD = 9500 mm. (a) Case of butt welds with same thickness. (b) Case of butt welds with change of thickness.

4.2 Serviceability limit state

The monopile substructure is considered to have failed if its accumulated deformations (displacement and rotation) at the mudline exceed the allowable limits. Arany *et al.* (2015) [5] reported that these limits could be 20 cm for the displacement and 0.5° for the rotation at the pile head. Due to verticality error of driven pile, the maximum allowable permanent rotation is reduced to 0.25°. Achmus *et al.* (2005) [23] pointed the difficulty to estimate the accumulated deformations for monopile structures where loadings are omnidirectional and of levels that depend on the extremely changing environmental conditions. However, the accumulated deformations w_a can be approximated from the instantaneous deformations w_i that occur in the main loading direction based on:

$$w_a = w_{i,1}\left[1 + t\ \ln\left(N_1 + \sum_k N_k^*(V)\right)\right] \tag{11}$$

where $$N_k^*(V) = \exp\left\{\frac{1}{t}\left[\frac{w_{i,k}}{w_{i,1}}\left(1 + t\ \ln\left(p(V)\,N_k(V)\right)\right) - 1\right]\right\}$$

$w_{i,1}$ is taken as the maximum instantaneous deformation and occurs N_1 cycles. N_k^* is the equivalent number of cycles that is required by the instantaneous deformation $w_{i,k}$ to produce the same accumulated deformation than that produced by $w_{i,1}$ in N_1 cycles. $N_k(V)$ is the number of cycles associated to $w_{i,k}$ produced by mean wind speed V whose probability of occurrence is $p(V)$. $t = 0.032\beta\xi\varphi\min(5, L/T)$ is the degradation variable. The soil type parameter $\beta = 1.00$ for dense soil. The installation method parameter $\xi = 1.00$ for driven pile. The cyclic load method parameter φ is given in dependence of the cyclic load ratio $R_H = H_{min}/H_{max}$ in [24]. $\frac{L}{T}$ is the ratio between the pile depth and the pile-soil relative stiffness ratio; $T = \sqrt[5]{EI/n_h}$ where E is the steel modulus of elasticity; I is the pile moment of inertia; and n_h is the coefficient of soil reaction.

For wind turbine applications where the loading direction, thereby the deflection direction, is changing over time the method implementation is challenging. Conservatively, loadings are assumed to be oriented in its dominant direction during the whole turbine lifetime, i.e. 25 years. Under this assumption, the pile does not oscillate around its neutral position but around a deflected position as shown in Figure 6. Consequently, instead of accumulating the total displacement measured from the unloaded structure position, the accumulation is done over the deflection amplitudes measured from the average deflection. The accumulated amplitude is then added to the average deflection to obtain the total permanent deflection line, whose derivative corresponds to the accumulated rotation (see Figure 9).

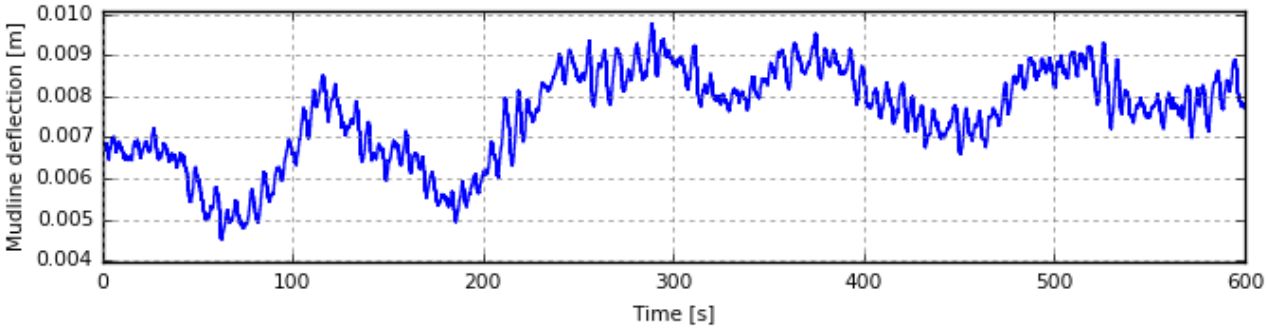

Figure 6. Deflection time series of the pile at the mudline for operational conditions under 11 m/s wind speed. Oscillations are around a mean displacement of 7.5 mm.

4.3 Ultimate limit state

The ultimate limit state (ULS) encompasses three conditions: the steel strength, the pile stability, and the soil-pile capacity.

4.3.1 Strength limit state

The steel strength and the pile stability are dependent on steel material properties, which are given in Table 8.

Table 8: Steel properties of the monopile's material.

Properties	References	Values
Steel type	DNV-OS-J101 [19]	High strength steel (HS) / NV-32
Minimum yield stress [MPa]	DNV-OS-J101 [19]	315
Mass density [kg/m^3]	Cremer and Heckl [25]	7850
Effective Elastic Modulus [GPa]	Cremer and Heckl [25]	210
Poisson's ratio [-]	Cremer and Heckl [25]	0.3

The ovalization of the monopile due to hydrodynamic effects is negligible. The main stress components are the longitudinal membrane stress, the shear stress, and the circumferential membrane stress (see Figure 7).

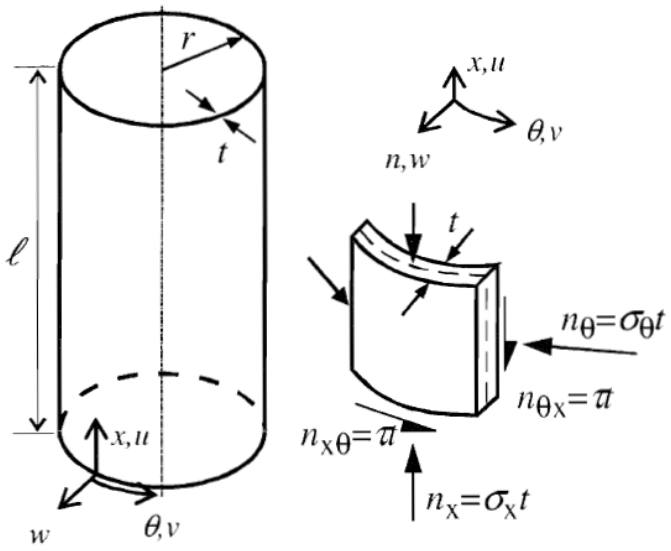

Figure 7. Primary resulting stresses applied on a monopile shell [26].

The longitudinal membrane stress and the shear stress are given by Equations (12) and (13) [27], respectively:

$$\sigma_x = \frac{N}{A} + \frac{M_1}{I/R}\sin\theta - \frac{M_2}{I/R}\cos\theta \tag{12}$$

$$\tau = \left|\frac{T}{2\pi t R^2} - \frac{2Q_1}{A}\sin\theta + \frac{2Q_2}{A}\cos\theta\right| \tag{13}$$

The circumferential membrane stress is expressed as:

$$\sigma_\alpha = \frac{p(y)}{4\pi t}[4 - (\pi - 2\alpha)\sin\alpha] \tag{14}$$

where

N : axial force
M_1, M_2 : bending moments about axis 1 and 2, respectively
T : torsional moment
Q_1, Q_2 : shear forces along axis 1 and 2, respectively
$p(y)$: lateral force due to soil resistance
A : section's area
I : section's second moment of area
R : outer radius
t : wall thickness
θ : circumferential co-ordinate, measured from axis 1
α : circumferential co-ordinate, measured from the resultant horizontal force.

The yield failure of the monopile steel occurs when the design stress exceeds the design yield limit, i.e. the design is safe when the utilization ratio (UR) associated with the strength limit state is less than one: $u_{ULS,1} \leq 1$, where $u_{ULS,1} = \gamma_m \gamma_c \gamma_l \, \sigma_v / f_y$. The partial safety factors are taken from [28] and from IEC 61400-1 ed.3 [29]: $\gamma_m = 1.30$, $\gamma_c = 1.10$, and $\gamma_l = 1.35 \; or \; 1.1$ are associated to the material properties, to the component's consequence of failure, and to the loads in normal or abnormal cases, respectively. f_y is the steel yield limit and $\sigma_v = \sqrt{(SCF\sigma_x)^2 - SCF\sigma_x\sigma_\theta + \sigma_\theta^2 + 3\tau^2}$ is the equivalent von Mises stress.

4.3.2 Stability limit state

Furthermore, situations of instability should also be avoided, which means the monopile should resist both local and global buckling modes whose respective URs should be less than one. Under the column buckling mode, it is considered that only the pile part above the seabed can be subjected to column buckling. The corresponding utilisation factor is given as [27]:

$$u_{ULS,2} = \frac{\sigma_{a0}}{f_{kcd}} + \frac{1}{f_{akd}} \left[\left(\frac{\sigma_{m1}}{1 - \frac{\sigma_{a0}}{f_{E1}}} \right)^2 + \left(\frac{\sigma_{m2}}{1 - \frac{\sigma_{a0}}{f_{E2}}} \right)^2 \right]^{0.5} \tag{15}$$

where

σ_{a0} : design axial stress due to axial forces. Its value is taken as positive if compression or zero if tension

σ_{m1}, σ_{m2} : maximum design bending moments about axis 1 and 2, respectively.

f_{E1}, f_{E2} : Euler buckling strength about axis 1 and 2, respectively. See DNV RP C202 [27].

f_{akd} : design local buckling strength. See DNV RP C202 [27].

f_{kcd} : design column buckling strength. See DNV RP C202 [27].

For the local buckling mode the UR, $u_{ULS,3} = \gamma_l \sigma_v / f_{ksd}$, where f_{ksd} is the design buckling strength, as defined by DNV RP C202 [27].

4.3.3 Soil capacity limit state

The load equilibrium of the pile-soil system [30] should be ensured by verifying that the lateral loads over the pile are lower than the fully mobilised passive earth pressure. This translates for the horizontal force into $u_{ULS,4} = \gamma_m \gamma_c \gamma_l Q_{res} / \sum_z p_c$ where Q_{res} is the resulting acting horizontal force, and for the bending moment into $u_{ULS,5} = \gamma_m \gamma_c \gamma_l M_{res} / \sum_z z p_c$ where M_{res} is the resulting acting bending moment at the zero-crossing point and z is the distance from that point. $\gamma_m = 1.25$ as per DNV-OS-J101 [19].

4.4 Fatigue limit state

The accumulated fatigue damage due to hotspot stresses during the turbine's lifetime should be less than one: $D_{lifetime} \leq 1$. From the nominal stresses, the hotspot stresses are obtained as $\sigma_i =$

$SCF\ \sigma_x$. The stress ranges are obtained from the rainflow counting method applied on the design stress time series. The number of cycles, $N(\Delta\sigma)$, corresponding to full damage induced by a given stress range, $\Delta\sigma$, is obtained by the design S-N curve corresponding to the detail of type C1 for seawater with cathodic protection [22], [31] which is described as:

$$\log N = \log \bar{a} - m \log \left[\Delta\sigma \left(\frac{t}{t_{ref}} \right)^k \right] \tag{16}$$

where

m and $\log \bar{a}$ = respectively the negative inverse slope of the S-N curve and the intercept of the logN axis. For S-N curves in seawater with cathodic protection, ($m = 3, \log \bar{a} = 12.049$) for $N < 10^6$, and ($m = 5, \log \bar{a} = 16.081$) for $N > 10^6$;

t_{ref}= reference thickness equal to 25 mm;

t = thickness through which the crack will most likely grow; $t = t_{ref}$ if $t < t_{ref}$;

k = thickness exponent on fatigue strength. $k = 0.15$

Then, Palmgren Miner's rule [32] is applied to quantify the accumulated damage. Over one year, the accumulated damage is expressed as [29]:

$$D_1 = \gamma_{DF} \sum_{DLC} \frac{T_1(DLC)}{T} \int_{V_{in}}^{V_{out}} \int_{\Delta\sigma_A}^{\Delta\sigma_B} \frac{n(\Delta\sigma|V,T)}{N(\Delta\sigma)} p(V)\, \mathrm{d}\Delta\sigma\, \mathrm{d}V \tag{17}$$

where $\gamma_{DF} = 3.0$ is the fatigue reserve factor associated to the no-inspection situations, $T_1(DLC)$ is the number of seconds in one year corresponding to the occurrence of a given design load case, $n(\Delta\sigma|V,\ T)$ is the actual number of cycles corresponding to the stress range $\Delta\sigma$, given a wind speed V and a simulation duration $T = 600\ s$, and $p(V)$ is the probability of occurrence of the wind speed V.

The service lifetime of the offshore structure is typically set to 25 years. Considering the 10 % corresponding to the fatigue damage related to the construction, the total equivalent fatigue lifetime of the structure sums up to 28 years. Based on the one year accumulated fatigue damage, the damage accumulated during the lifetime of the structure is $D_{lifetime} = 28D_1$ and the fatigue lifetime in years is obtained by $L = D_1^{-1}$.

5 Reference design

5.1 Selected design load cases

Six design load cases (DLCs) are chosen from IEC 61400-3 Ed 1 [17] to check the design in various limit states: DLC 1.2 and DLC 7.2 are selected for fatigue; and DLC 1.3, DLC 1.4, DLC 1.5, and 6.2a are taken for ultimate analysis. DLC 1.2 is associated with wind speeds in the operational range with normal turbulence model and normal sea states, while DLC 7.2 simulates the situation of parked turbine with locked rotor and mean wind speed of 21 m/s for 11 % turbulence intensity.

DLC 1.3 considers normal operation with extreme turbulence but normal sea states. DLCs 1.4 and 1.5 are associated to extreme coherent gust with wind direction change and extreme wind shear, respectively. DLC 6.2a results from turbulent extreme wind under storm conditions (42.73 m/s) with extreme sea states, coupled with loss of electrical power.

5.2 Final design - Geometry

Given the environmental data and the structure properties, the design process starts with an initial substructure design with outer diameter, wall thickness, and penetration depth upscaled from previous designs. The initial design should satisfy the design constraints. Thus, satisfactory natural frequencies are obtained with an initial value of 9500 mm for the outer diameter of the monopile. In order to simplify the manufacturing, to ease the installation process, and to provide a working pile whose surrounding soil has been less disturbed, the diameter will be kept constant throughout its length.

However, the wall thickness could vary along the monopile axis in order to maximize the axially varying URs. The initial estimate of the wall thickness is taken close to the minimal recommendation of API-RP2A-WSD [7], i.e. about 102 mm for the monopile and for the transition piece, which is not subjected to hammering induced stresses, the wall thickness is initialised to 80 mm. The pile capacity is primarily provided by its embedded length, which should be long enough to ensure no soil failure and acceptable translational and rotational displacement. Common values of the embedded length are approximately equal to the water depth: the first estimate is taken as 50 m.

Then, the initial design is checked against the limit states. The outer diameter and the wall thickness distribution are iteratively adjusted to comply with the limit state requirements. The reference modelling choices are taken as: (1) overall structural damping logarithmic decrement of 6.70 %; (2) soil model as derived by Thieken *et al.* [8]; and (3) SCF values corresponding to an imperfection level of 50 %. Analyses led to a reference design with outer diameter of 9500 mm, a penetration depth of 60 m, i.e., a total length under the interface of 136.0 m, and variable wall thickness along the length as tabulated in Table 9. The total mass of the primary substructure is about 2715 t. This reference design presents 0.243 Hz and 0.247 Hz as natural frequencies for the first support-structure bending modes.

Table 9: Distribution of the pile wall thickness.

	Upper part	Around the mudline	Lower part
Depth below the interface [m]	0.00 – 56.5	56.5 – 100.5	100.5 - 136
Wall thickness [mm]	80	112	60

5.3 Verification at the limit states

The accumulated deflection at the seabed over the turbine lifetime is estimated to be 1.42 cm, and the accumulated rotation is computed to be 0.06° approximately. These permanent deformations are all lower than the limits, 20 cm for the deflection and 0.25° for the rotation at the seabed. Figure 8 below depicts the short-term deflection shape plotted together with the permanent one.

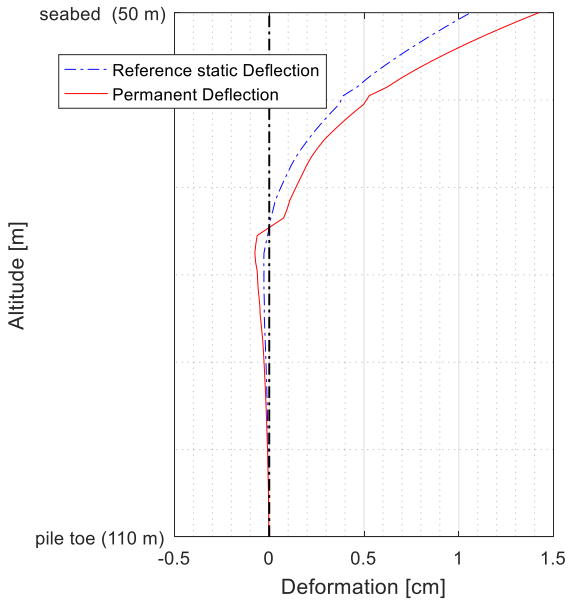

Figure 8. Permanent deflection of the monopile over its lifetime

The URs for the ULS are shown in Figure 9 and are all lower than one as required for survival. Global buckling is analysed only in the part above the mudline as it cannot occur below. DLC 1.5 is consistently milder than DLC 6.2a, which globally governs the design for every buckling limit state. Close to the interface (transition piece), the local maximum URs result from DLCs other than DLC 6.2a. Therefore, it is important to investigate as many as possible DLCs for the structural check of various parts of the structure.

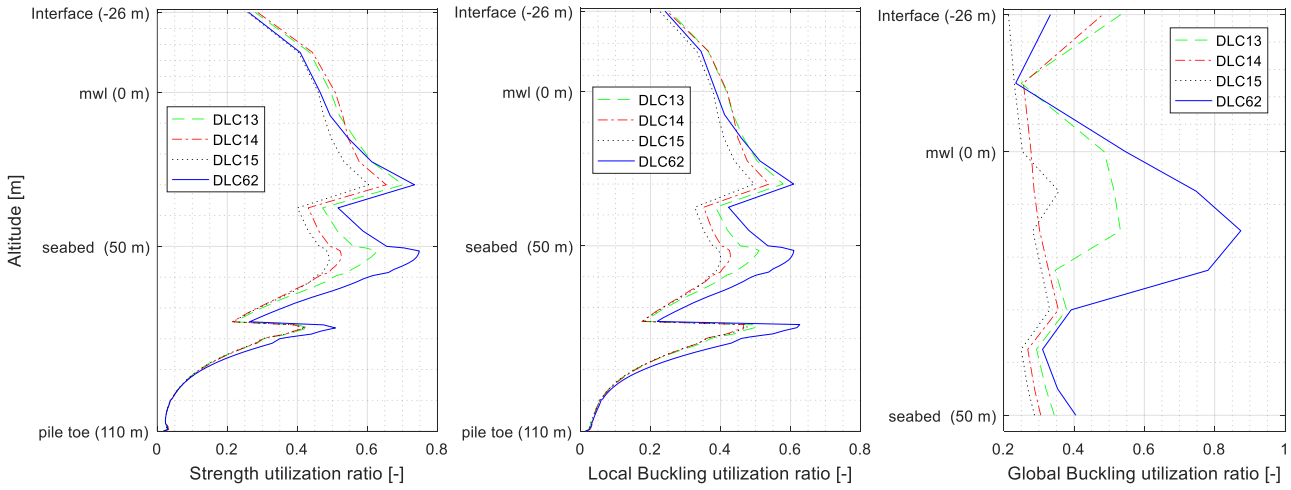

Figure 9. Strength, local buckling, and global buckling URs

The URs related to the soil capacity evaluated for the horizontal force and for the bending moments are presented in Table 10. With a UR of 29.6 ‰, the critical scenario is obtained with DLC 6.2a under the bending failure mode.

Table 10: Utilisation ratios related to the soil capacity.

	DLC 1.3	DLC 1.4	DLC 1.5	DLC 6.2a
Horizontal failure mode	5.5 ‰	2.5 ‰	3.0 ‰	7.3 ‰
Bending failure mode	21.5 ‰	14.6 ‰	14.0 ‰	29.6 ‰

The minimum fatigue lifetime computed in conjunction with DLC 1.2 and DLC 7.2 is about 28.67 years, which indicates that the design will survive the endured fatigue damage through the intended 25-year lifetime plus three construction-equivalent years. This fatigue lifetime corresponds to an accumulated damage of 97.67 %. The distribution of the fatigue damage and lifetime along the substructure axis are shown on Figure 10.

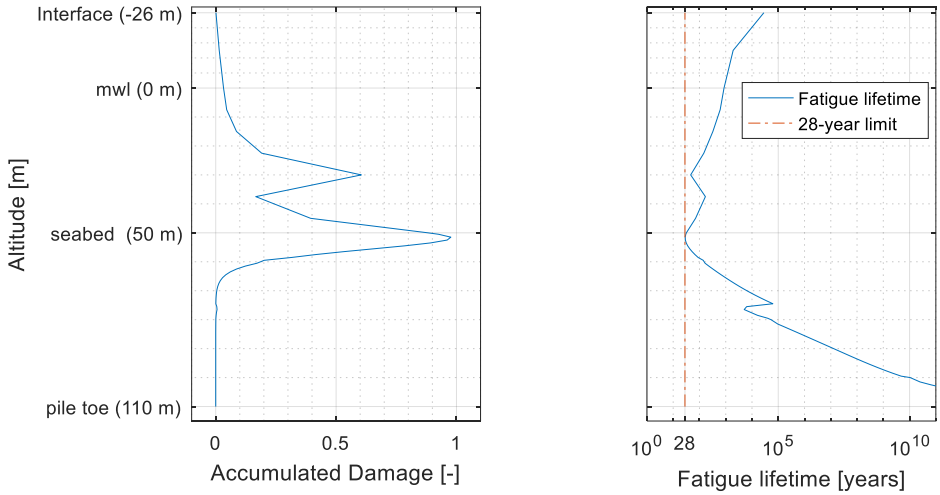

Figure 10. Fatigue Assessment. Left: fatigue damage over the lifetime. Right: fatigue lifetime

6 Influences of the main modelling choices

6.1 Discussion on the driving limit states

Figure 11 compares the URs from different limit states. It can be seen that the FLS is the overall design driver, but its influence area is restricted to a location just below the mudline. Compared to the fatigue damage, the other limit states are preponderant elsewhere. In the majority of hotspots DLC 6.2a dominates DLC 1.4. Except at the portion towards the pile toe where the wall thickness is reduced, the local buckling limit state utilizes less material that the strength limit state. Despite the global domination of the global buckling, the strength limit state will be used due to the fact

that it can be estimated along the whole structure, together with the fatigue damage, for the assessment of the influence of the modelling choices.

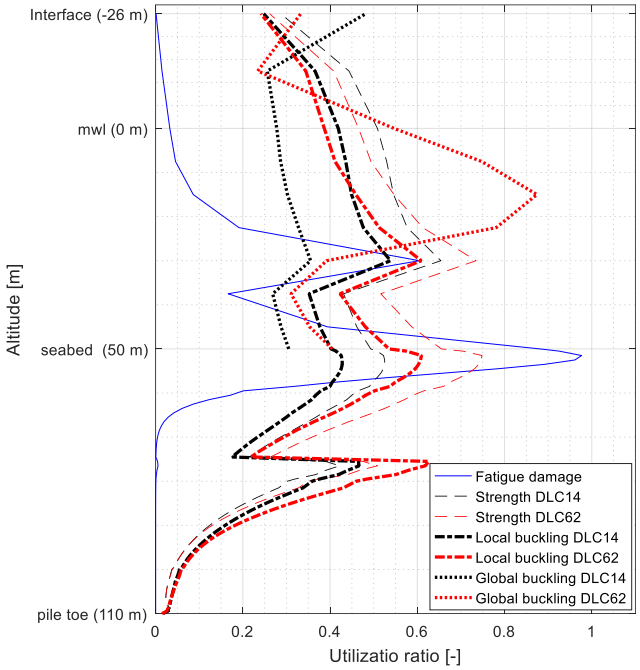

Figure 11. Comparison of the utilization ratios from different limit states

6.2 Influence of the damping

The reference logarithmic decrement damping value of the 6.70 % has been obtained ignoring effects such as elasto-plastic behaviour of the soil at seabed and toe, the hydrodynamic dissipation due to drag, and Coulomb friction between the structural parts [15]. Moreover, the damping due to tower-top damper is not included. All these effects can lead to a logarithmic decrement damping value of 12 % as measured by Koukoura *et al.* [9]; another value of 30 % has also been set in the model. Figure 12 presents the variation of the fatigue lifetime from one damping case to the other. The maximum fatigue damage changes from 97.67 % (28.67 years) for 6.70 % damping to 62.02 % (45.15 years) for 12 % damping and to 36.13 % (77.50 years) for 30 % damping. An increase of about 40 % of the minimum fatigue lifetime is gained with the value 12 %. This shows that with the inclusion of all relevant damping sources and a more realistic estimation of each damping component values, savings can be achieved.

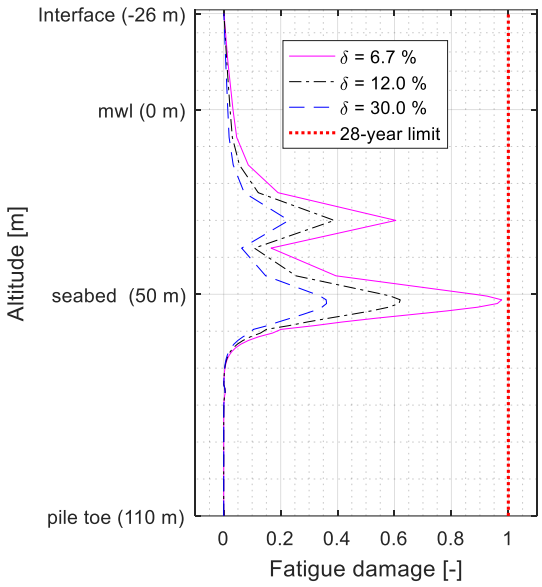

Figure 12. Influence of the damping on the fatigue lifetime.

6.3 Influence of the geometric imperfections

The level of geometric imperfections impacts the stress concentration factors at the welded connections, henceforth the fatigue lifetime of the structure. Figure 13 (left) shows that for a carefully manufactured product, i.e. without imperfections, the lifetime extends to about 127 years; whereas it reduces to about nine years if the fabrication is carried out just at the tolerance limits. For imperfection level of 25 % and 75 % of the tolerance, the fatigue lifetime corresponds to approximatively 57 years and 15 years, respectively. This shows an approximately log-linear dependence of fatigue lifetime, L, to the imperfection level, λ: $\ln(L) \cong 4.751 - 2.652\lambda$. On figure 14 (right), the change of the strength URs in dependence of the geometric imperfections is also significant. The maximum strength URs vary between about 58 % ($\lambda = 0\ \%$) and 92 % ($\lambda = 100\ \%$).

On the one hand, these results indicate possible failures in case of geometric imperfection level greater than what was set as design hypothesis. On the other hand, this suggests that material can be saved by setting lower geometric imperfection level as the design hypothesis provided that necessary precaution is taken during the construction phase. The large variation range of the structural performance reveals the higher sensitivity of the structure reliability with respect to the construction errors.

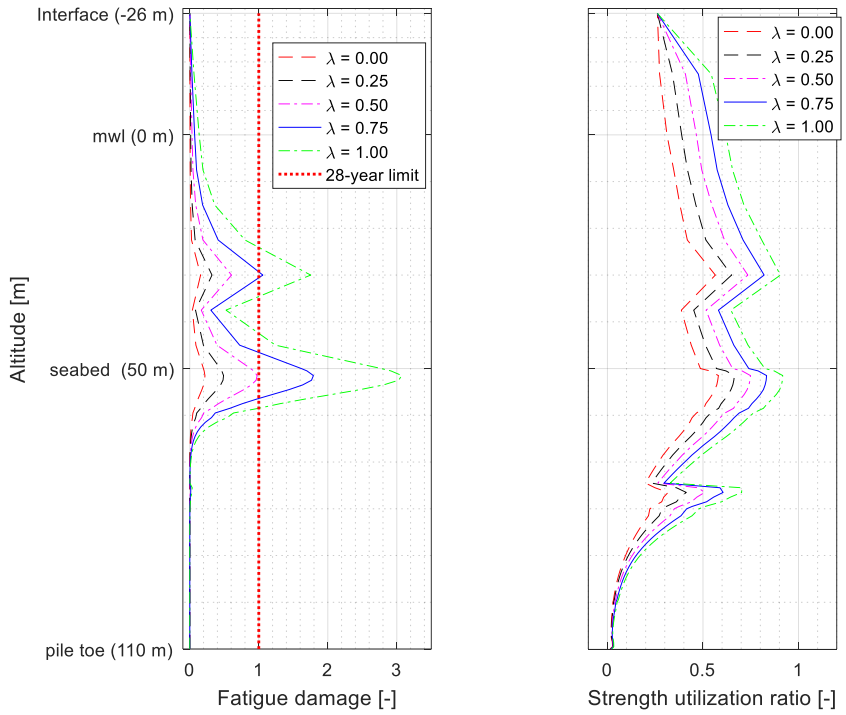

Figure 13. Influences of the geometric imperfections (a) on the fatigue lifetime and (b) on the strength limit state.

6.4 Influence of the soil-structure interaction models

Figure 14 assesses the influence of the soil model on the fatigue response of the monopile. The comparison in the variation in fatigue damage along the monopile when using Thieken *et al.*'s soil model to the guidelines' model, shows a larger portion of significantly mobilized soil in the latter, due to lower soil rigidity. However, the nominal minimum fatigue lifetime at the respective critical hotspots of the structure is not significantly altered. Figure 14a depicts the responses with the reference design, where a wall thickness change lies at 74.5 m below the seabed. As a relatively higher damage level is present at the point of thickness variation where the stresses concentrate, the fatigue damage is seen to be further amplified when using the guidelines' soil model.

In order to evaluate the interaction between stress concentration and soil model, two other design geometries are chosen. The first pile geometry is taken with constant wall thickness till its toe. It is seen in Figure 14b, that the amplification in fatigue damage disappears due to the absence of wall thickness change. In another variant of the design, the wall thickness change lies at 66.5 m below the seabed where fatigue level is significant. Figure 14c shows the fatigue damage with the new position of thickness change, wherein using the guidelines soil model aggravates the fatigue damage amplification further and leads to a minimum lifetime of about two years. However, it is expected that the amplification reduces if logarithmic decrement damping of 10 % to 30 % magnitude is considered (see Figure 12).

This study shows that even if a soil model reveals a suitable soil capacity, its effect on the fatigue damage distribution along the foundation interacts with the steel structure design and may lead to failure. This calls for greater accuracy in choosing the the soil model to ensure the integrity of the monopile design.

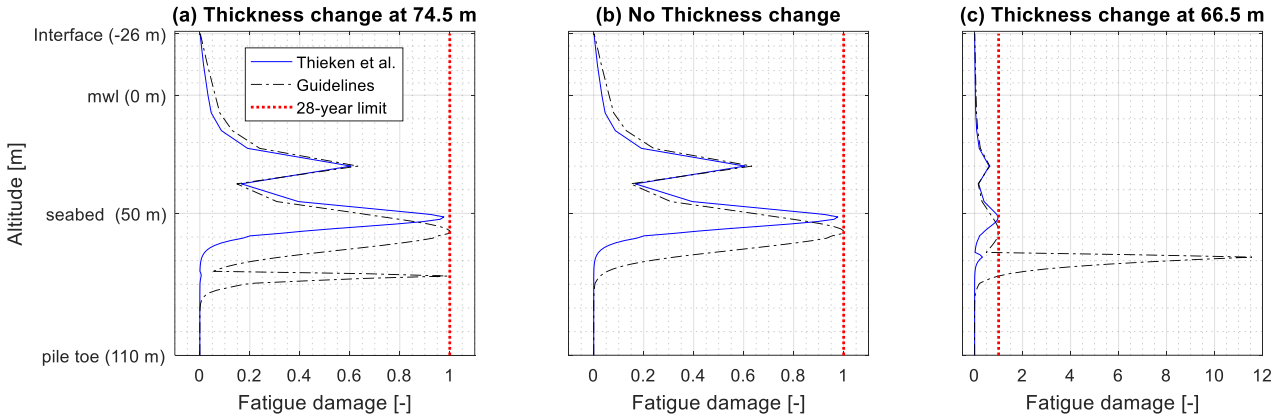

Figure 14. Influence of the soil model on fatigue lifetime.

From Figure 15, it is seen that when using the guidelines, the maximum strength UR is increased by about 14 percentage points and the permanent deflection is significantly amplified by about 67.0 %, resulting in an increase in permanent rotation of 47.0 %. However, due to the overestimation of the soil capacity, the soil URs decrease by about 40.0 % for horizontal mode and by about 42.0 % for the bending mode. The first two natural frequencies of the support-structure in bending mode are 0.231 Hz and 0.234 Hz, which are off the reference design's values by about 5%.

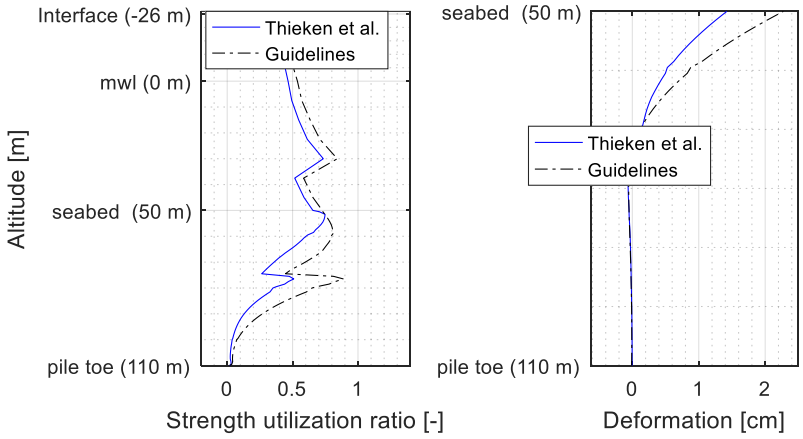

Figure 15. Influence of the soil model on (left) strength utilization ratio and (right) permanent deflection.

7 Conclusion and recommendations

The present study focuses on the detailed investigation of the primary design modelling choices made for large diameter monopile. The influences of the damping values, geometric imperfections, and soil model on structural integrity are investigated based on fatigue lifetime, ULS (strength, local buckling, global buckling, and soil capacity), and permanent deformations of the structure. All the model parameters have been varied within realistic values, yet the structural performance shows a significant variability. For example, the fatigue lifetime can be affected by a factor of 3 to 7 at the most critical hotspot. At least five major conclusions can be drawn from this study:

1) It is feasible to design a large monopile at 50 m water depth for 10 MW wind turbines based on specific models consistent with the current design standards and that can be installed with present technology. In addition, a design process with tractable relationships, which allows the development of a unified numerical design tool, can be integrated into procedures for reliability analysis and optimization.
2) The FLS drives the design. While DLC 6.2a is a decisive loadcase for ULS, other DLCs can drive some of the structural sections. Therefore none of the DLCs should be overlooked.
3) The construction phase should be carried out with the necessary care in order to ensure that the design hypotheses regarding geometric imperfection levels are kept intact at the commissioning moment.
4) Proper design modelling choices can help reducing the structure cost. Indeed more realistic damping value, necessary care to lower geometric imperfection levels, and adequate soil model have shown potential of better use of steel material.
5) The large variation of structural response in terms of fatigue lifetime and strength UR with respect to all these parameters shows that the integrity of the structure is very sensitive to the design choices. Thus, the design procedure requires an appropriate probabilistic approach to guarantee robust designs.

The soil-structure interaction model proves to be very essential in the design process. Whether loading term is considered, the deflection line of the foundation is changed from one soil model to the other. This induces a change in distribution of the related structural responses, which can lead to fatigue amplification by interacting with stress concentrations. Therefore, designs should be carried out with accurate as possible soil model, which should be proven suitable enough for with large monopile substructures. Henceforth, further attention should be given to the validation of soil models for large diameter monopiles with on-site measurements under dynamic loadings.

Acknowledgments

The research leading to these results has received funding from the European Community's 7th Framework Programme FP7-ENERGY-2012-1-2 STAGE project INNWIND.EU under grant agreement No. 308974. The financial support is greatly appreciated. The contributions of Thomas Buhl at the initiation of this study are gratefully acknowledged.

References

[1] Kallehave D, Byrne BW, LeBlanc Thilsted C, Mikkelsen KK. Optimization of monopiles for offshore wind turbines. Phil. Trans. R. Soc. A 373. 1-15; 2015

[2] Von Borstel T. INNWIND.EU Deliverable 4.3.1 – Design report – Reference Jacket. 2013. http://www.innwind.eu/-/media/Sites/innwind/Publications/Deliverables/DeliverableD4,-d-,31_20131030_INNWIND,-d-,EU.ashx?la=da.

[3] Scharff R, Siems M. Monopile foundations for offshore wind turbines – solutions for greater water depths. Steel Construction 6 No 1; 2013a.

[4] Scharff R, Siems M. Pushing the limits – mega monopile foundations for offshore wind turbines. Steel Construction 6 No 3; 2013b.

[5] Arany L, Bhattacharya S, Macdonald JHG, Hogan SJ. A critical review of serviceability limit state requirements for monopile foundations of offshore wind turbines. Offshore Technology Conference, 2015.

[6] Murchison JM, O'Neil MW. Evaluation of p-y relationship in cohesionless soils, analysis and design of the pile foundation. ASCE, 1984, 174-191.

[7] American Petroleum Institute. Recommended practice for planning, designing and constructing fixed offshore platforms—Working stress design. API RP2A WSD; 2005

[8] Thieken K, Achmus M, Lemke K. A new static p-y approach for piles with arbitrary dimensions in sand. Geotechnik 38 No 4, 2015, 267-288

[9] Koukoura C, Brown C, Natarajan A, Vesth A. Cross-wind fatigue analysis of a full scale offshore wind turbine in the case of wind–wave misalignment. Engineering Structures 120 (2016) 147–157.

[10] Det Norske Veritas. Fabrication and testing of offshore structures - Offshore Standard. DNV-OS-C401; 2010

[11] de Vries W. UpWind WP4 D4.2.8 Final Report WP4.2: Support structure concepts for deep water, 2011.

[12] Bak C, Zahle F, Bitsche R, Kim T, Yde A, Henriksen LC, Andersen PB, Natarajan A, Hansen MH. INNWIND.EU Deliverable 1.2.1 – Description of the DTU 10 MW Reference Wind Turbine. 2013. http://www.innwind.eu/-

/media/Sites/innwind/Publications/Deliverables/DeliverableD1,-d-,21%20Aerodynamic_StructuralValidation_INNWIND,-d-,EU.ashx?la=da

[13] Segeren MLA. Influence of boatlanding and J-tubes on wave loads and wall thickness of the monopile support structure design. 2011.

[14] Stolpe M, Njomo Wandji W, Natarajan A, Shirzadeh R, Kuhn M, Kaufer D. Innovative design of a 10 MW steel-type jacket. INNWIND.EU Deliverable 4.34. 2016. http://www.innwind.eu/-/media/Sites/innwind/Publications/Deliverables/230117/DeliverableD434_Innovative-Design-of-a-10MW_steel-jacket_Rev10_FINAL.ashx?la=da

[15] Tarp-Johansen NJ, Morch C, Andersen L, Christensen E, Frandsen S, Kallesoe. Comparing sources of damping of cross-wind motion. Dong Energy

[16] Chakrabarti S. Handbook of Offshore Engineering. Elsevier; 2005.

[17] The international Electrotechnical Commission: Wind Turbines – Part 3: Design requirements for offshore wind turbines, IEC 61400-3 Ed 1. 2009.

[18] International Organization for Standardization. Petroleum and natural gas industries - Fixed steel offshore structures. ISO 19902:2007.

[19] Det Norske Veritas. Design of offshore wind turbine structures - Offshore Standard. DNV-OS-J101; 2007

[20] MacCamy RC, Fuchs RA. Waves forces on piles: A diffraction theory. Corps of Engineers 1954; 1-17.

[21] Larsen TJ, Hansen AM. How 2 HAWC2, the user's manual. DTU Risoe-R-1597; 2015. http://www.hawc2.dk/-/media/Sites/hawc2/HAWC2%20Download/HAWC2%20manual/manual_version_4-6.ashx.

[22] Det Norske Veritas. Fatigue Design of Offshore Steel Structures – Recommended Practice. DNV-RP-C203; 2011.

[23] Achmus M, Abdel-Rahman K, Peralta P. On the design of monopile foundations with respect to static and quasi-static cyclic loading. Copenhagen Offshore Wind 2005.

[24] Lin SS, Liao JC. Permanent strains of piles in sand due to cyclic lateral loads. Journal of geotechnical and geoenvironmental engineering 125 No 9, 1999, 798-802.

[25] Cremer L, Heckl M. "*Structure-Borne Sound*". Springer-Verlag, New York (1988).

[26] European committee for standardization. Eurocode 3 – Design of steel structures – Part 1-6: Strength and stability of shell structures. EN 1993-1-6; 2007.

[27] Det Norske Veritas. Buckling strength of shells – Recommended Practice. DNV-RP-C202; 2013

[28] Sorensen JD, Toft HS. Safety Factors. DTU Wind Energy– E – Report - 0066 (EN); 2014.

[29] The international Electrotechnical Commission. Wind Turbines – Part 1: Design requirements. IEC 61400-1 Ed 3; 2009.

[30] Thieken K, Achmus M, Schmoor KA. On the ultimate limit state design proof for laterally loaded piles. Geotecnik 37 No 1, 2014, 19-31.

[31] Arany L, Bhattacharya S, Macdonald J, Hogan SJ. Design of monopiles for offshore wind turbines in 10 steps. Soil Dynamics and Earthquake Engineering 92 (2017) 126-152.
[32] Miner AM. Cumulative damage in fatigue. *Journal of Applied Mechanics Vol. 12*, 1945, A159-A164

7

Paper III: Probabilistic Structural Assessment of Conical Grouted Joint using Numerical Modelling

Probabilistic structural assessment of conical grouted joint using numerical modelling

NJOMO WANDJI Wilfried[a], Anand NATARAJAN[b], Nikolay DIMITROV[c]

[a,b,c]DTU Wind Energy, Technical University of Denmark,
Frederiksborgvej 399, DK-4000 Roskilde, Denmark
[a]wilw@dtu.dk, tel.: +45 9351 1501 (corresponding author);
[b]anat@dtu.dk; [c]nkdi@dtu.dk;

Abstract

Conical grouted joints have been proposed as a solution for the relative settlement observed between the sleeve and the pile on monopiles for wind turbines. In this paper, the influence of the design parameters such as steel wall thicknesses and conical angle on the failure modes associated to continual loadings are assessed based on finite element analysis. It is found that both the sleeve's and pile's wall thicknesses have a significant impact on the grouted joint health. Namely, the larger are the wall thicknesses, the more vulnerable the grout is with respect to fatigue and material degradation but the more limited the progressive settlement is, and inversely. This implies that the appropriate wall thicknesses should be chosen by designers having in mind that neither extreme is conservative. Based on statistical modeling, the grout length is found to be the most influential parameter of the settlement caused by extreme loadings: longer grout significantly contributes to the reduction of extreme settlement. To ensure that the inevitable settlement does not jeopardize the joint's structural integrity, a probability-based method has been developed to estimate the minimal gap between the pile top and the brackets required to achieve a targeted annual reliability index (of 3.3).

Keywords*: Multi-megawatt wind turbines; Conical grouted joint; Progressive settlement; Finite element; Reliability analysis.*

1. Introduction

In order to support the wind turbines placed at seas, monopile substructures are the most frequently employed types in commercial wind farms [1]. Relying on experience from the Oil and Gas industry, the connections between the transition piece and the monopile for wind turbine support structures are made by the means of grouted joints. Classically, the grouted joints for monopile substructures are built from the overlap of two cylindrical tubes: a transition piece and a pile, and the resulting annular gap is filled with a high strength concrete. The grouted joints are efficient as they are easily constructible and they serve to correct the pile misalignment due to driving errors [2] as presented in Figure 1.

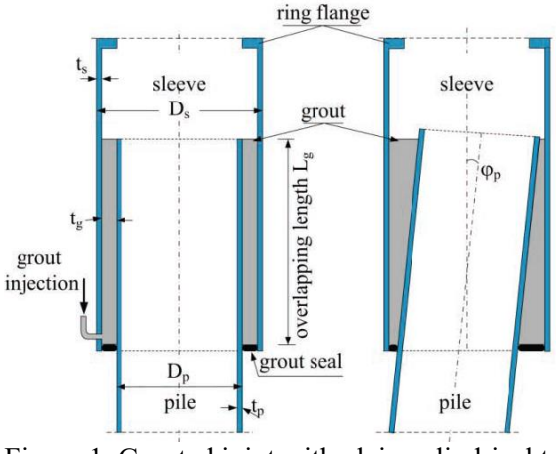

Figure 1. Grouted joint with plain cylindrical tubes [2].

A typical construction process follows few steps: (1) the transition piece is jacked up at the pile top edge using jacking brackets; (2) the concrete is poured in the annulus and left for curing; and (3) after the concrete has hardened, the jack-ups are removed and the transition piece holds due to the passive friction resistance at the contact faces between the layers. The passive friction resistance is made of two contributions, which are the chemical adhesive bond between the concrete and the steel and the mechanical interlock between the rough concrete surface and the undulations on the steel surfaces. An additional contribution, Coulomb friction, is generated during the loading operations by the normal-to-the-interface components of the loads transferred from the transition piece to the pile.

After few cycles, gaps open between the grout and the steel walls at the connection top and bottom; the adhesive bond deteriorates and cannot recover. Furthermore, the friction abrades the geometrical imperfections at the adjacent surfaces over the whole connection length. At very early age of the structure, the two initial contributions depreciate and only the coulomb friction persists, which is only effective when the normal pressure is present. In case of insignificant normal pressure, the shear resistance may not support the weight of the structure anymore and the transition piece will progressively slide downwards until the jacking brackets touch the pile top edge: the connection fails.

This failure mode has been observed in some commercial wind farms [3]. In order to constantly keep the shear resistance, two principal solutions were proposed [4], [5]: the conical grouted joint and the shear-keyed grouted joints. Figure 2 illustrated both proposed solutions.

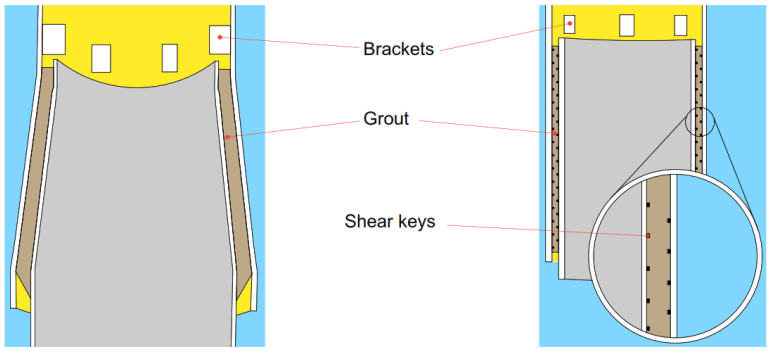

Figure 2. Conical grouted joint (left) and shear-keyed cylindrical grouted joint.

The conical grouted joint is derived from the convention grouted joint by imposing a small conical angle (1° to 3°) to the overlapping tubes. With the conical angle, the effect of the structure weight on the connection decomposes into a shear component along the contact faces and a normal component to the contact faces. The latter component generates a permanent coulomb friction resistance, which prevents the failure described above. The alternative solution adds shear keys to the inner faces of the steel walls close to the connection middle in order to enhance the mechanical interlock: the resulting friction resistance is said active. It is not advisable to put shear keys close to the connection edges as the gap openings will nullify their effect. In either solution, as the passive mechanical interlock and the adhesive bond are ephemeral, it is realistic to carry out analysis without accounting for their respective contributions [6]. As many studies devoted attention to the shear-keyed grouted joints, e.g. [2], [3], [7], [8], [9], [10], this work will focus on the conical solution, which is also addressed in [8], [11] for example. Whereas Lotsberg *et al*. (2012) [8] have introduced the concept of conical grouted joints as a solution to limit settlements, Lee *et al*. (2014) [11] have presented a reliability-based design optimization method for conical grouted joints. They have considered various limit states except the grout degradation and the progressive settlement, which has been proven crucial for grouted joints.

This article aims at investigating the behavior under continual loadings of the conical grouted joint based on detailed finite element analysis. Over years, in addition to fatigue, the grout material will progressively lose its elastic modulus [6], [12], which might impact the support structure stiffness. The influence of the design parameter such as pile's wall thickness, transition piece's wall thickness, and conical angle on the grouted joint performance under continual loadings will be assessed.

Although the conical shape of grouted joints will reduce the progressive settlement of the transition piece, its vertical displacement cannot completely be precluded as materials have finite

elastic moduli. Even if appropriate designs lead to acceptable progressive settlement at the end of their lifetime under normal conditions, higher vertical displacement can be expected after extreme events. Therefore, provisions should be given such that extreme settlements do not close the gap between the brackets and the pile top. Otherwise, loads will not follow the same path or be transferred anymore as intended. Hence, a procedure to estimate the minimum gap between the brackets and the pile top required to achieve a targeted annual reliability index (of 3.3) is established. This problem formulation is preferred to counterpart that consists in designing the grouted joint in such way that the vertical settlement lies below a certain threshold. In fact, as long as the settlement is not excessive, the size of the gap will not strongly influence the remaining design features.

2. Site conditions, structure, and design constraints

2.1 Metocean conditions

The selected site is located in the North Sea at 53°13’04.0" N and 3°13’13.0" E and its metocean conditions are given by [13]. The operational wind range goes from 4 m/s to 25 m/s and is binned into 11 intervals whose centres are 2 m/s apart. Each mean wind speed bin is associated with a turbulence level as presented in Table 1. The expected values of the sea states are conditional on each mean wind speed. Pierson-Moskowitz or JONSWAP spectra are used to model the wave height in case of normal operations or extreme cases, respectively. The mean sea level (msl) is 26.0 m above the seabed. The verification of the grouted joint structure is done under loading cases corresponding to the wind turbine operations. For the continual loadings, the design load case DLC 1.2 [14] is considered and for the extreme loading (design load case that drives the ultimate limit state), DLC 1.3 [14] is used as it has been shown by [15] to be critical at the grouted joint level. DLC 1.2 is characterized by the wind normal turbulence and DLC 1.3 by the wind extreme turbulence.

Table 1:
Metocean conditions [13]. The expected annual frequency only applies to the normal conditions.

Mean wind speed [m/s]	Normal turbulence intensity [%]	Extreme turbulence intensity [%]	Significant wave height, Hs [m]	Peak period, Tp [s]	Expected annual frequency [hrs/yr.]
5	18.95	43.85	1.140	5.820	933.75
7	16.75	33.30	1.245	5.715	1087.30
9	15.60	27.43	1.395	5.705	1129.05
11	14.90	23.70	1.590	5.810	1106.75
13	14.40	21.12	1.805	5.975	1006.40
15	14.05	19.23	2.050	6.220	820.15
17	13.75	17.78	2.330	6.540	633.00
19	13.50	16.63	2.615	6.850	418.65
21	13.35	15.71	2.925	7.195	312.70
23	13.20	14.94	3.255	7.600	209.90
25	13.00	14.30	3.600	7.950	148.96

The wind direction distribution is depicted by Figure 3 as indicated by Ref [16]. From the metocean conditions of the selected site, a statistical model describing the extreme loading case is prepared as tabulated in Table 2. A probabilistic study is carried out only for the ultimate limit state whereas the limit case associated to the continual loadings will be studied based on load-resistance-factor-design method. The extreme turbulence intensity is computed based on the formula recommended by IEC 61400-1 Ed 3 [14] and polynomials have been used to fit the relationship between the significant wave height, and the wave peak period from Table 1 and the mean wind speed. During the sampling from this statistical model, each mean wind speed will be associated to a unique seed.

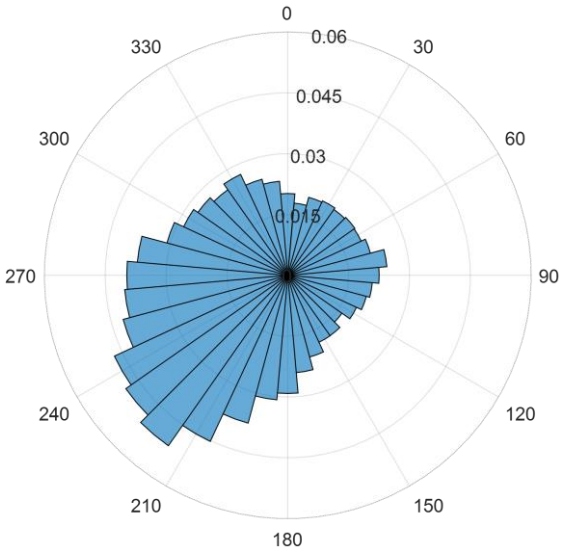

Figure 3. Wind direction on the site [16].

Table 2:
Statistical metocean conditions for the extreme loading. V is the wind speed variable in m/s.

Parameters	Value
Wind speed $\boldsymbol{V}$ [m/s]	Rayleigh (9.25)
Turbulence intensity [-]	$0.06912 + 1.84704/V$
Wind shear	0.14
Wave significant height [m]	$(3.16V^2 + 30.31V + 885.99) \times 10^{-3}$
Wave peak period [s]	$(6.63V^2 - 83.80V + 5989.80) \times 10^{-3}$
Wind-wave misalignment [°]	0

2.2 Soil properties

The soil conditions are the same as those used in [15]. The top 90.0 m are made of four layers of medium to highly dense sand. The soil data presented in Table 3 are assumed deterministic.

Table 3:
Soil properties [15]

Depth range [m]	0.0 – 15.0	15.0 – 20.0	20.0 – 22.5	22.5 – 90.0
Angle of internal friction [°]	35.0	37.5	40.0	40.0
Poisson's ratio [-]	0.250	0.225	0.200	0.200
Void ratio [-]	0.69	0.65	0.60	0.57
Submerged unit weight [kN/m^3]	9.76	10.0	10.5	11.0

2.3 Wind turbine for case study

The DTU 10 MW reference wind turbine (DTU 10 MW RWT) [17] is selected for the case study as a relevant turbine that depicts future large offshore installations. It is a variable speed pitch controlled conceptual offshore wind turbine with 10 MW rated power. Its other key design properties are tabulated in Table 4. The operational rotor speed range intersects the three first rotor harmonics (1P, 2P, and 3P) within the ranges [0.10 Hz, 0.16 Hz], [0.30 Hz, 0.48 Hz], and [0.60 Hz, 0.96 Hz], respectively. The wind turbine parameters are deterministic in this study.

Table 4:
Key design properties of the DTU 10 MW RWT [17]

Parameters	Values
Wind regime	(see Table 1)
Rotor type, orientation	3 bladed - Clockwise rotation – Upwind
Control	Variable speed – Collective pitch
Cut-in, rated, cut-out wind speed	4 m/s, 11.4 m/s, 25 m/s
Rated power	10 MW
Rotor, hub diameter	178.3 m, 5.6 m
Hub height	119.0 m
Drivetrain	Medium speed, Multiple-stage Gearbox
Minimum, maximum rotor speed	6.0 rpm, 9.6 rpm
Maximum generator speed	480.0 rpm
Gearbox ratio	50
Maximum tip speed	90.0 m/s
Hub overhang	7.1 m
Shaft tilt, coning angle	5.0°, -2.5°
Blade prebend	3.3 m
Rotor mass including hub	227,962 kg
Nacelle mass	446,036 kg
Tower mass	628,442 kg

3. Descriptive parameters of the grouted joint

3.1 Grouted joint topology and dimensions

The conical grouted joint is made of double co-axial frusto-conical tubes overlapping each other whose annulus is filled with a concrete grout. The outer frustum is the transition piece (or sleeve) and the inner frustum is the pile. Figure 4 presents the topology and the dimension labels of a typical conical grouted joint; the nomenclature is given in Table 5. The relative position of the connection top with respect to the mean water level can also be considered as a design parameter.

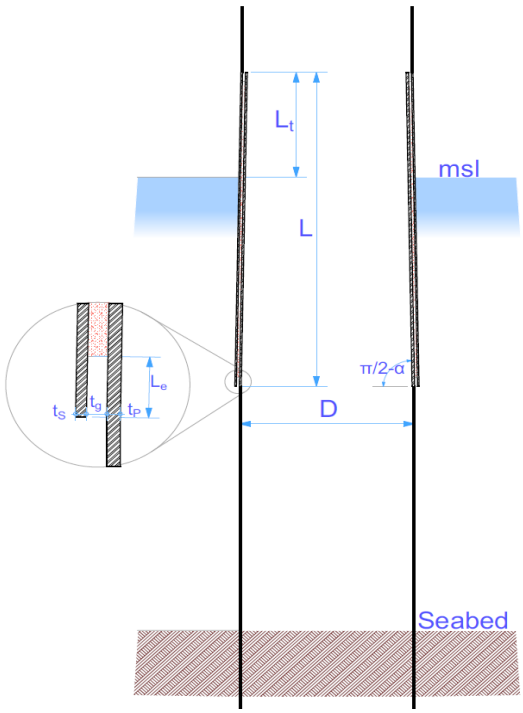

Figure 4. Topology and dimension labels of a typical conical grouted joint.

Table 5:
Geometric design parameters of a typical conical grouted joint

Symbol	Description
$\boldsymbol{D}$	Outer diameter of the cylindrical monopile [m]
$\boldsymbol{\alpha}$	Angle of the connection [°]
$\boldsymbol{t_p}$	Wall thickness of the pile in the connection [m]
$\boldsymbol{t_s}$	Wall thickness of the transition piece (sleeve) in the connection [m]
$\boldsymbol{t_g}$	Grout thickness [m]
$\boldsymbol{L}$	Length of the connection [m]
$\boldsymbol{L_e}$	Length of the pile/sleeve edges [m]
$\boldsymbol{L_t}$	Length of the connection above the mean sea level [m]

For the reliability analysis, the geometry is considered deterministic. However, it has been varied within realistic bounds for the sensitivity analysis presented in subsequent sections. Table 6 tabulated the bounds used for the sensitivity analysis.

Table 6:
Bounds for the geometric parameters

Parameters	Lower bounds	Nominal values	Upper bounds
Pile wall thickness, $\boldsymbol{t_p}$ [m]	0.03	0.07	0.12
Transition wall thickness, $\boldsymbol{t_s}$ [m]	0.03	0.06	0.12
Grout thickness, $\boldsymbol{t_g}$ [m]	0.05	0.15	0.25
Length, $\boldsymbol{L}$ [m]	9.00	18.00	25.00
Conical angle, $\boldsymbol{\alpha}$ [deg]	0.10	3.00	5.00
Length of wall ends, $\boldsymbol{L_e}$ [m]	0.10	0.50	1.00
Length of the connection above the msl, $\boldsymbol{L_t}$ [m]	0.00	6.00	25.00

3.2 Materials: Constitutive behaviour and parameter values

The grouted joint is made of two principal materials (steel and concrete) and one interface (steel-concrete contact). The steel material is assumed elastic transitioning into perfectly-plastic. The characteristic values of its properties are indicated by Cremer and Heckl (1988) [18] and DNV-0S-J101 [19]. The Joint Committee on Structural Safety (JCSS) [20] gives the statistical properties of the steel material as summarised in Table 7.

Table 7:
Statistical description of the steel material

Parameters	Characteristic value	Bias		
		Mean	Cov	Distribution
Density, $\boldsymbol{\rho_s}$ [kN/m^3]	7850	Deterministic		
Yield strength (compr. and tension), $\boldsymbol{f_y}$ [Pa]	315 x 10^6	1.045	0.07	Lognormal
Modulus of elasticity, $\boldsymbol{E}$ [Pa]	210 x 10^9	1.000	0.03	Lognormal
Poisson's ratio, $\boldsymbol{\nu_s}$ [-]	0.30	1.000	0.03	Lognormal

The grout is a high strength concrete of grade C120 [12]. Nielsen (2007) [6] proposed three candidates as constitutive formulation of the response for the grout. The most sophisticated and most

adapted alternative is the damaged plasticity model [6], [12], [21], [22]. This formulation models strain hardening and softening, and thereby also cracking and crushing. Moreover, it captures the material degradation along the loading cycles by altering the material stiffness, as well as it accounts for material recovery. Figure 5 depicts the said formulation for the uniaxial load cycle path with the extreme cases of stiffness recovery factors, while the yield surfaces are illustrated in Figure 6. The basic relationships between the uniaxial parameters can be found in Model Code 2010 [12]. The parameters of this model and their values are taken or adapted from Tyau (2009) [22], and are given in Table 8 and Table 9 together with their statistical distributions. For the compressive strength, the distribution is given by JCSS [20], the mean by Model Code 2010 [12], and the coefficient of variation is obtained from [23], [24], [25], which indicate as appropriate values about 11 % for samples from random producer and approximately 5 % for samples within the same batch. For the Poisson's ratio, Model Code 2010 [12] sets the range between 0.14 and 0.26; the distribution type and the coefficient of variation are assumed based on engineering judgement. The strain-degradation relationships and some concrete properties in Table 8 are set deterministic mainly due to lack of information. The concrete intrinsic parameters (density, characteristic strength, and Poisson's ratio) are given by Model Code 2010 [12].

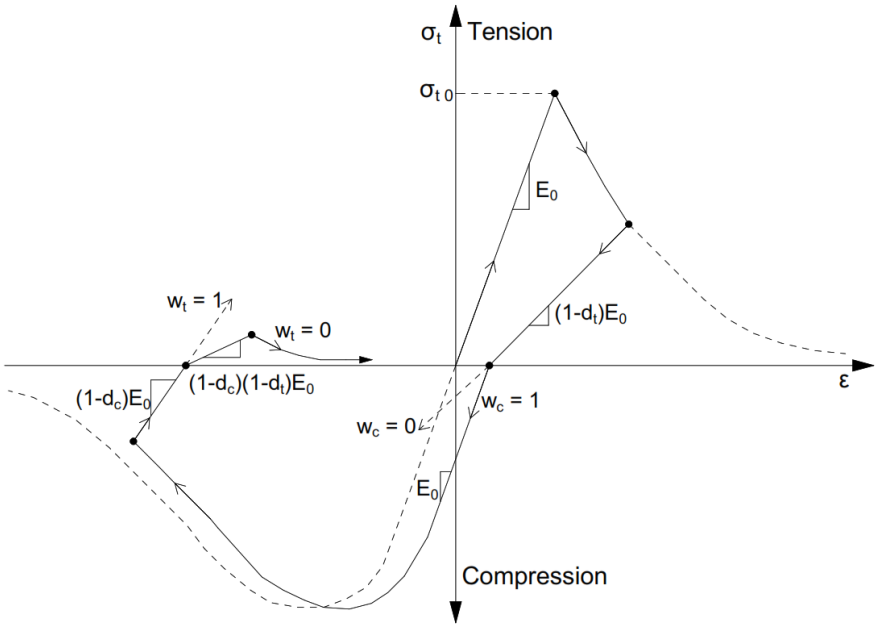

Figure 5. Uniaxial load cycle (tension-compression-tension).

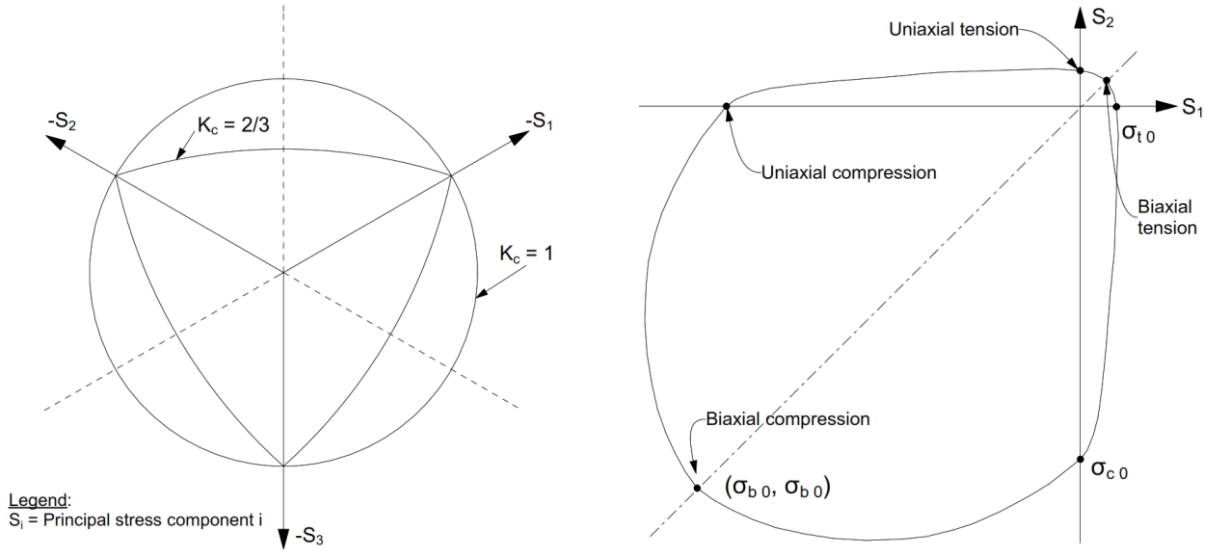

Figure 6. Yield surfaces. Left: deviatoric plane. Right: plane stress.

Table 8:
Statistical description of the concrete material. N ([a, b]) corresponds to a Gaussian distribution truncated with bounds a and b, a < b.

Parameters	Characteristic value	Bias		
		Mean	Cov	Distribution
Density, $\boldsymbol{\rho_c}$ [kN/m^3]	2500	Deterministic		
Compressive strength, $\boldsymbol{f_c}$ [Pa]	120 x 10^6	1.067	0.12	Lognormal
Poisson's ratio, $\boldsymbol{\nu_c}$ [-]	0.20	1.000	0.05	N ([0.14, 0.26])
Dilatation angle, $\boldsymbol{\psi}$ [^{0}]	31	Deterministic		
Flow potential eccentricity, $\boldsymbol{m}$ [-]	0.1	Deterministic		
Initial biaxial/uniaxial ratio, $\boldsymbol{\sigma_{bo}/\sigma_{co}}$ [-]	1.16	Deterministic		
Shape parameter, $\boldsymbol{K_c}$ [-]	2/3	Deterministic		
Viscosity parameter, $\boldsymbol{\mu_c}$ [-]	0	Deterministic		
Compression recovery factor, $\boldsymbol{w_c}$ [-]	0.95	Deterministic		
Tension recovery factor, $\boldsymbol{w_t}$ [-]	0.05	Deterministic		

Table 9:
Strain-degradation relationships for compression and tension (adapted from Tyau (2009) [22])

Compression											
Inelastic strain	0.0007	0.0014	0.0020	0.0054	0.0088	0.0122	0.0155	0.0189	0.0223	0.0257	0.0290
Degradation	0.0000	0.0500	0.1000	0.1954	0.3500	0.4800	0.5964	0.7000	0.8000	0.8949	0.9500
Tension											
Inelastic strain	0.0000	0.0000	0.0001	0.0004	0.0007	0.0010	0.0013	0.0017	0.0020	0.0023	0.0026
Degradation	0.0000	0.0000	0.0000	0.4064	0.6964	0.8100	0.8800	0.9204	0.9400	0.9600	0.9801

The contacts between the steel walls and the grout surfaces are modelled according to the classic hard contact theory [21]. This formulation assumes that the sticking contributions from geometric imperfections and chemical adhesion are negligible [6]. Therefore, only the Coulomb friction contributes to the stress transfer between the various parts. With the absence of chemical adhesion (and geometric imperfections), the sliding parts can translate with respect to each other in the direction normal to the contact surface. For a given normal pressure, the shear strength is proportional to the Coulomb friction coefficient, i.e. the shear resistance is equal to the product between the normal pressure and the Coulomb friction coefficient but does not exceed the shear strength, in which case sliding occurs after the sticking phase. The Coulomb friction coefficient and the shear strength are respectively obtained from the experiments carried out by Baltay and Gjelsvik (1990) [26] and Rabbat and Russel (1985) [27]. Table 10 presents the statistical properties of the contact used in this study.

Table 10:
Statistical description of the contact

Parameters	Characteristic value	Bias		
		Mean	Cov	Distribution
Coulomb friction coefficient, $\boldsymbol{\mu}$ [-]	0.47	1.00	0.15	N
Shear strength, $\boldsymbol{\tau}$ [Pa]	105 x 10^3	1.00	0.05	N

4. Reference monopile substructure

4.1.Boundary conditions and load assessment

Loads are assessed with the help of the aero-hydro-servo-elastic software package HAWC2 [28]. It utilizes a multibody formulation, which couples different elastic bodies together using Timoshenko

beam finite elements [29], [30] whereby their stiffness, mass, and damping are assembled into the governing equations of motion coupled to aerodynamic forces, whose time domain solution is obtained using the Newmark-β method [30], [31]. The damping coefficients are specified using Rayleigh coefficients [30] to obtain desired damping ratios for the global structure. Tarp-Johansen *et al.* [32] recommended 6.70 % as overall structural logarithm decrement damping.

Based on IEC 61400-3 Ed 1 [33], two design load cases (DLCs) have been selected: DLC 1.2 for the continual (fatigue) loading and DLC 1.3 for the extreme loading. DLC 1.2 models the operational case associated to normal turbulence. Each mean wind speed is considered with six wind turbulence seeds, no yaw error and no wave misalignment. This set of conditions provides 11 × 6 = 66 scenarios of 10–minute simulation durations. DLC 1.3 considers normal operations with extreme turbulence but normal sea states. Six wind turbulence seeds for each of the 11 wind speed bins are simulated, all assuming zero yaw error. Sea waves of JONSWAP type are aligned along the wind direction.

The loads resulting from sea-structure interaction are computed based on the Morison's equation [34] evaluated for a unit length of cylinder:

$$F = 0.5\rho_w D C_D(u_w + u_c - u_s)|u_w + u_c - u_s| + 0.25\rho_w C_a \pi D^2(\dot{u}_w - \dot{u}_s) + 0.25\rho_w \pi D^2 \dot{u}_w \qquad (1)$$

where D [m] is the outer diameter, u_c [m/s] is the current speed, u_w [m/s] is the wave particle speed normal to the tube axis, u_s [m/s] is the moving tube velocity, $\dot{u}_w$ [m/s^2] is the wave particle acceleration normal to the tube axis, and $\dot{u}_s$ [m/s^2] is the moving tube acceleration. $\rho_w = 1025\, kg/m^3$ is the water mass density. The drag coefficient $C_D = 0.65$ and the added mass coefficient $C_a = 1.00$. Verifications have been done that the diffraction phenomenon is insignificant [35].

The soil-structure interactions are modelled as a Winkler elastic beam on continuous support. Horizontal and vertical springs with nonlinear stiffness are distributed along the embedded pile. API-RP2A-WSD (2005) [36] recommends a hyperbolic force-displacement relationship along the lateral direction as given by Eq. (2):

$$p(y) = Ap_u \tanh\left(\frac{kz}{Ap_u} y\right) \qquad (2)$$

with $p_u = min\{(C_1 z + C_2 D)\gamma' z\,;\, C_3 D\gamma' z\}$ is the soil capacity. The initial modulus of subgrade reaction, k is given as function of the internal friction angle in the standard [36]. The coefficients C_1, C_2, and C_3 are given in the standard [36] in dependence on the angle of internal friction. The factor accounting for the cyclic loading mode $A = 0.9$. z is the depth below the mudline, D [m] is the pile outer diameter, and γ' [N/m^3] is the submerged unit weight.

4.2.Limit states for the monopile design

Ultimate, fatigue, and serviceability limit states are selected to check the monopile substructure. The ultimate limit state (ULS) encompasses the strength limit state, the stability limit state, and the soil capacity limit state. The strength limit state ensures that there is no yield of the steel material. The utilization ratio $u_{ULS,1} = \gamma_m \gamma_c \gamma_l\, \sigma_v / f_y$ should be lower than one. σ_v is the hotspot von Mises stresses obtained with hotspot stress components. The partial safety factors are taken from [37] and from IEC 61400-1 ed.3 [14]: $\gamma_m = 1.30$, $\gamma_c = 1.10$, and $\gamma_l = 1.35$ (for extreme loads only) are associated to the material properties, to the component's consequence of failure, and to the extreme loads, respectively.

The stability limit state addresses the global and local buckling of the monopile. For the global buckling, the utilization factor $u_{ULS,2}$ is computed as the combination of the respective ratios of the axial forces and bending moments applied at the column ends over their capacities. Reference is made to DNV-RP-C202 [38]. The utilization ratio of the local buckling is computed as $u_{ULS,3} = \gamma_l \sigma_v / f_{ksd}$, where f_{ksd} is the design buckling strength, as defined by DNV RP C202 [38]. Both utilization ratios should be lower than one for structural safety.

The soil capacity limit state is checked by verifying that the equilibrium of the soil-pile is not violated. This means that, for each failure mode, the ratio of the load over the capacity should stay below one. For the translation failure mode, $u_{ULS,4} = \gamma_m \gamma_c \gamma_l Q_{res} / \sum_z p_u$ where Q_{res} is the resulting

acting horizontal force; and for the rotation failure mode, $u_{ULS,5} = \gamma_m \gamma_c \gamma_l M_{res} / \sum_z z p_u$ where M_{res} is the resulting acting bending moment at the zero-crossing point and z is the distance from that point. $\gamma_m = 1.25$ as per DNV-OS-J101 [19].

In addition, the accumulated fatigue damage during the structure lifetime, assumed to be 25 years augmented by three equivalent years corresponding to the construction induced fatigue [39], should be smaller than one. The fatigue damage is aggregated using the Palmgren Miner's rule [40] where the number of stress cycles are obtained by the rainflow counting method and the number of cycles to failure are computed with the design S-N curve corresponding to the detail of type C1 for seawater with cathodic protection [41]. It is assumed that the cathodic protection is sufficient for the entire structure lifetime or can be renewed such that the protection against corrosion is always ensured

Over years, the deformations of the pile-soil system accumulate. Arany *et al.* (2015) [42] reported that the permanent displacement limits could be 20 cm and the permanent rotation limit 0.5^0 at the pile head. Due to verticality error of driven pile, the maximum allowable permanent rotation is reduced to 0.25^0. Lin and Liao (1999) [43] proposed an experiment-based method to evaluated the permanent strains of piles in sand due to cyclic lateral loads. As also employed by Achmus *et al.* (2005) [44], this method will be used in this study. Reference is made to [15], [43], and [44] for the details.

4.3.Reference design and verifications

The design of the monopile consists of the determination of its dimensions (outer diameter, wall thickness, and penetration depth) such that the limit states are satisfied. This study aims at the determination of a feasible reference substructure, not an optimal or a ready to build design [15]. The determination process is iterative. The initial and the retained reference values are given in Table 11.

Table 11:
Dimensions of the reference monopile substructure design

Structural parts	Parameters	Initial values	Reference values
Transition piece	Outer diameter [mm]	8500	8500
	Wall thickness [mm]	80	60
Pile	Outer diameter [mm]	9000	9000
	Wall thickness [mm]	100	60 - 80
	Penetration depth [m]	26.00	30.00

Figure 7 depicts the distribution of the utilization ratios corresponding to each limit states. On the left, the maximum utilization ratio for the ULS, 0.81, is obtained with the global buckling limit state and is lower than one.

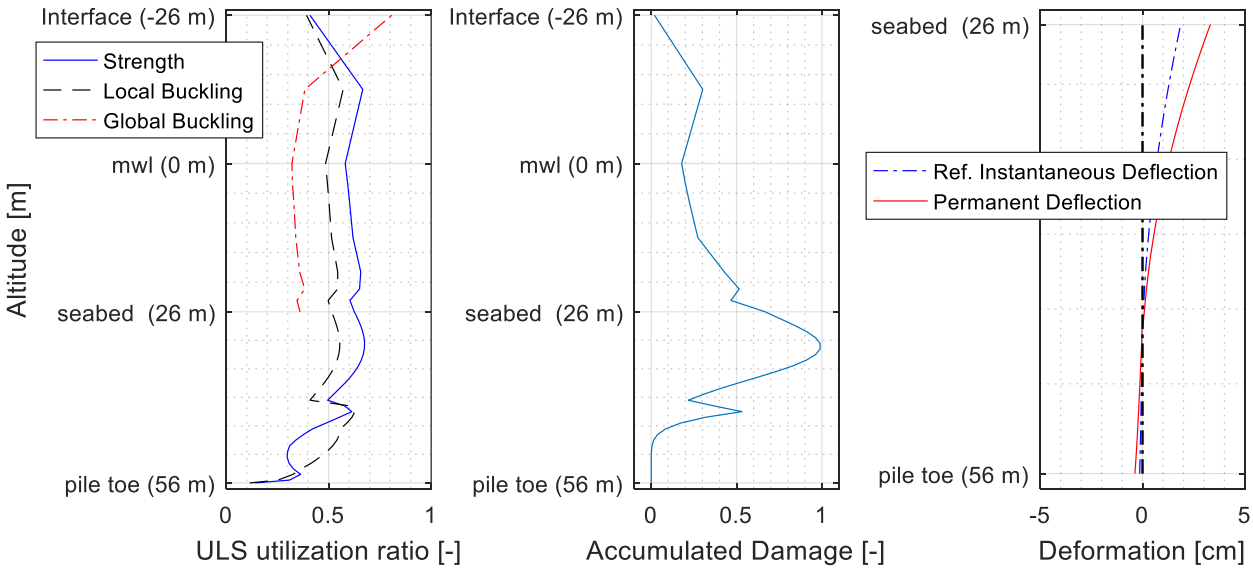

Figure 7. Distribution of the utilization ratios along the axis. ULS (left), FLS (center), and SLS (right).

The soil capacity is utilized at up to 1.69 % for the translational failure mode and up to 23.47 % for the bending failure mode. On the center, the maximum fatigue damage accumulated over 28 years is 0.99, which is smaller than one. On the right, the permanent displacement at the pile head is 3.32 cm, which is lower than the allowable 20 cm, and the permanent rotation is 0.15º, which is lower than the 0.25º limit. Satisfying all the limit states with moderate reserve and feasible dimensions, the reference design stands as a good candidate for this study.

5. Finite element model

5.1 Substructure modelling and loading strategy

For the detailed analysis of the grouted joint, a finite element model (FEM) is prepared on the Abaqus platform [21]. In order to effectively couple the aero-hydro-servo elastic simulations with detailed soil boundary conditions, the FEM of the whole substructure could be prepared as presented on the center of Figure 8. However, the model would have been very expensive with no additional benefit. Bush and Manuel (2009) [45] have shown that the foundation models of apparent-fixity type and of coupled-spring type lead to similar fatigue behavior at the tower bottom than that of distributed-spring type. That is why the distributed-spring foundation has been replaced by its equivalent apparent fixity model such that the mass, the damping, and the natural frequencies of the whole support structure is preserved. This modelling strategy does not only result in a computationally moderate effort but also allows a high-fidelity model, which minimizes boundary effects.

The tower bottom loads are applied at the transition piece top. The distributed loads along the transition piece (aerodrag) and the monopile (sea loads) have been modelled as nodal loads at 10 locations spread along the axis above the seafloor. The loads have been applied in two steps. First, the self-load of the structure is applied. The transition piece settles onto the grout. Second, the operational loads are then applied to the structure.

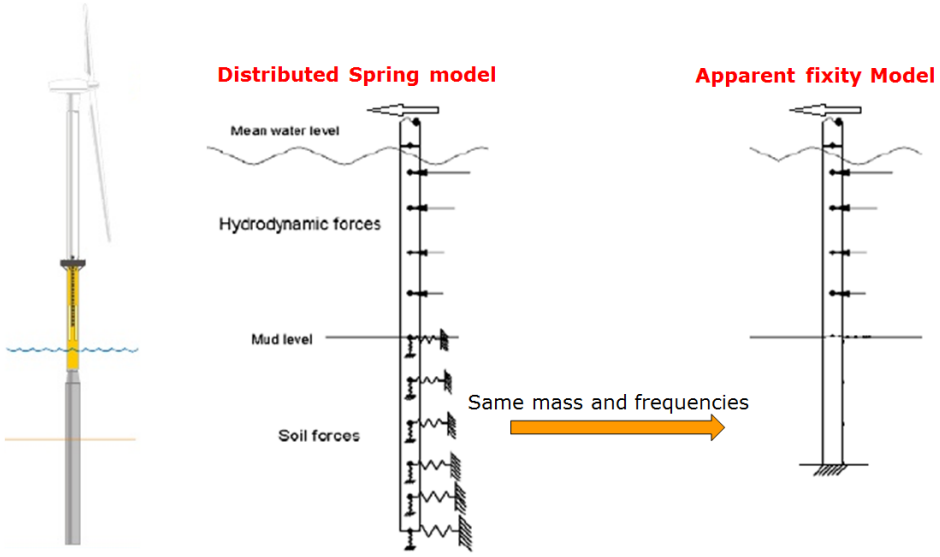

Figure 8. Substructure modelling. Left: full structure. Center: Substructure model in HAWC2. Right: Substructure model in Abaqus.

5.2 Finite elements: element types and meshing size

DNVGL-RP-0419 [5] recommends to use 1st order shell elements for a steel wall in conjunction with 1st order solid elements for the grout. This recommendation has been adopted for the finite element model prepared in this study. An aspect ratio equal to one has been used for all elements. For the steel wall, elements of type S4RS have been selected, which corresponds to 4-node doubly curved shell, reduced integration, hourglass control, small membrane strains. For the grout, elements of type

C3D8R are selected, which corresponds to 8-node linear brick, reduced integration, hourglass control. The relax stiffness method is used to control hourglass [31] for the shell element and the pure stiffness method is used for that of the solid element. For details of these methods, reference is made to [21].

With the setup described above, a convergence analysis was conducted in order to find out the appropriate size of a typical mesh element. Across the grout thickness, three finite elements are used in accordance to DNVGL-RP-0419 [5]. Various analyses have been conducted with different meshing arrangements. Several structural responses have been monitored at some selected hotspots; the results at one of them are shown in Figure 9. It can be seen that above 46500 mesh elements for the grout part, the structural strain converges; this corresponds to a mesh size of 20 cm x 20 cm for the connection (both grout and steel wall).

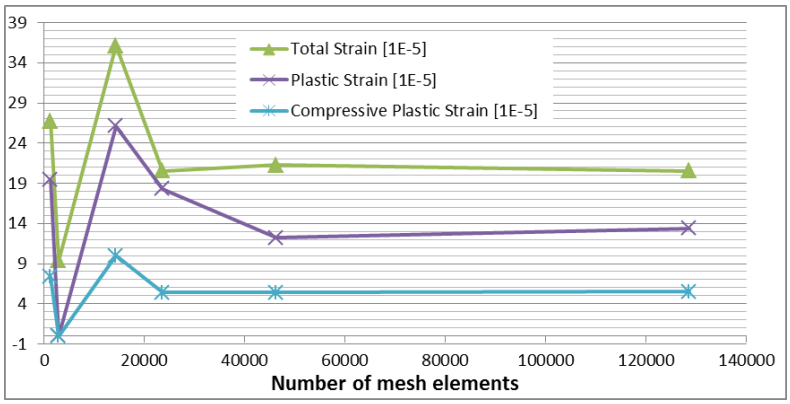

Figure 9. Convergence analysis for meshing size.

6. Limit states for the conical grouted joint design

The design of the monopile substructure has ensured the safety of the steel components of the grouted joint. This section will not address their limit states anymore; rather it will focus on the grout material and the contact. Nielsen (2007) [6] pointed out the almost-inevitable appearance of the hairline cracks due to primary hoop stresses. Dallyn *et al.* (2015) [3] recognized the effect of these cracks in the reduction of bending stiffness, but stating that the influence is limited (about 5%) as long as the lateral stresses are still transferred. Therefore, the assumption made by Lee *et al.* (2014) [11] is considered here: the grout material does not support significant tensile stress in the hoop direction; the grout is primarily in charge of transferring the pressure between the transition piece and the pile through shear friction, thus limiting the slide of the transition piece. The crack growths and their propagations are assumed sufficiently small such that their influences are limited. These phenomena will not be considered in the subsequent analyses.

6.1. Limit states related to extreme events

In the case of extreme loading, three failure modes can be distinguished for the grouted connection: failure of the steel-grout contacts, failure of the grout due to compressive stresses, and excessive vertical displacement of the transition piece relative to the pile. The shear stress, τ, due to the friction between the steel wall and the grout surfaces should be lower than the shear strength, τ_{max}, of the interface to prevent excessive relative motion between the transition piece and the pile (Eq. (3a)). This limit state is evaluated for both sides of the grout. The Tresca stress, σ_{Tresca}, generated in the grout material should be kept lower than the concrete strength, f_c, as specified by Eq. (3b). Moreover, the relative settlement, Δ, of the transition piece with respect to the pile under extreme loading should be moderate and is limited to a vertical settlement h (See Eq. (4)).

$$g_1 = \tau_{max} - \tau \tag{3a}$$

$$g_2 = f_c - \sigma_{Tresca} \tag{3b}$$

$$g_3 = h - \Delta \quad (4)$$

6.2.Limit states related to continual loadings

Over the structure lifetime, failures associated to continual loadings can occur. They include the wear of the grout surfaces in contact with steel walls, the reduction of the grout elastic modulus due to material degradation, the fatigue of the grout material, and the progressive vertical displacement of the transition piece relative to the pile as observed in some commercial wind systems. The friction at the contact faces abrades the grout surfaces. The wear rate is function of shear stress, which is proportional to the normal pressure exerted from one layer to another. In this paper, the wear phenomenon is not investigated as a more sophisticated finite element model is required for an accurate prediction of the phenomenon.

Two types of deterioration are engendered by continual loadings on grout material, fatigue damage and degradation, which are evaluated independently one to the other. The concrete degradation corresponds to a variation (diminution) of elastic modulus with the possibility of material recovery. As the word 'grade' is generally used to characterize grout material strength, the term 'degradation' refers to the loss of its elastic modulus. For the fatigue damage, the S-N curves have been calibrated based on samples that have been subjected to loadings till fatigue failure. During the experiments, the sample materials have been deteriorated continually and no full healing has been periodically assumed. So the extrapolation of the fatigue damage includes the progressive degradation of the grout material. Therefore, fatigue analyses do not require the monitoring of the damage parameters related to the degradation. However, it is relevant to monitor the appearance of cracks in the grout based on the damage parameters.

The reduction of the grout stiffness will be monitored based on the evolution of the material degradation parameters. It is important to keep the severely affected areas marginal in the grout in order to preserve the bending stiffness of the substructure. A change of the substructure bending stiffness can be noticed by following the lateral displacement of the interface for example. Subjected to cyclic loadings, the connection engenders cyclic stresses that induce fatigue in the materials. The accumulated fatigue, D_{25}, in the grout during the intended lifetime, calculated according to the Palmgren-Miner assumption should be lower than one (See Eq. (5)). The rate of progression of the long term vertical settlement, δ, of the transition along the pile should be close to zero so that over time, the initial gap, g, between the pile top edge and the brackets (See Eq. (6)) does not completely close.

$$g_4 = 1.00 - D_{25} \quad (5)$$

$$g_5 = g - \delta_h \quad (6)$$

7. Behavior of the grouted joint under continual loadings

7.1. Fatigue loads and resulting stresses

Fatigue loads result from DLC 1.2 simulations. Some load samples at the interface resulting from 13 m/s mean wind speed are presented in Figure 10.

Dynamic finite element analyses carried out with this loading set result in stresses in the grout material. For fatigue assessment, the influence of multiaxial stress states is generally accepted insignificant. Therefore the focus is on principal stresses as illustrated for few selected hotspots (Figure 11) in Figure 12 and during a turbulent wind with mean speed of 13 m/s. Whereas the structural responses of the grouted joint are computed over the whole mesh domain, the hotspots are selected only to collect the stress and material degradation time series. In Figure 12 the positive sign refers to tension. The minimum principal stresses are mainly of compressive type, whereas the maximum principal stresses are of tensile type.

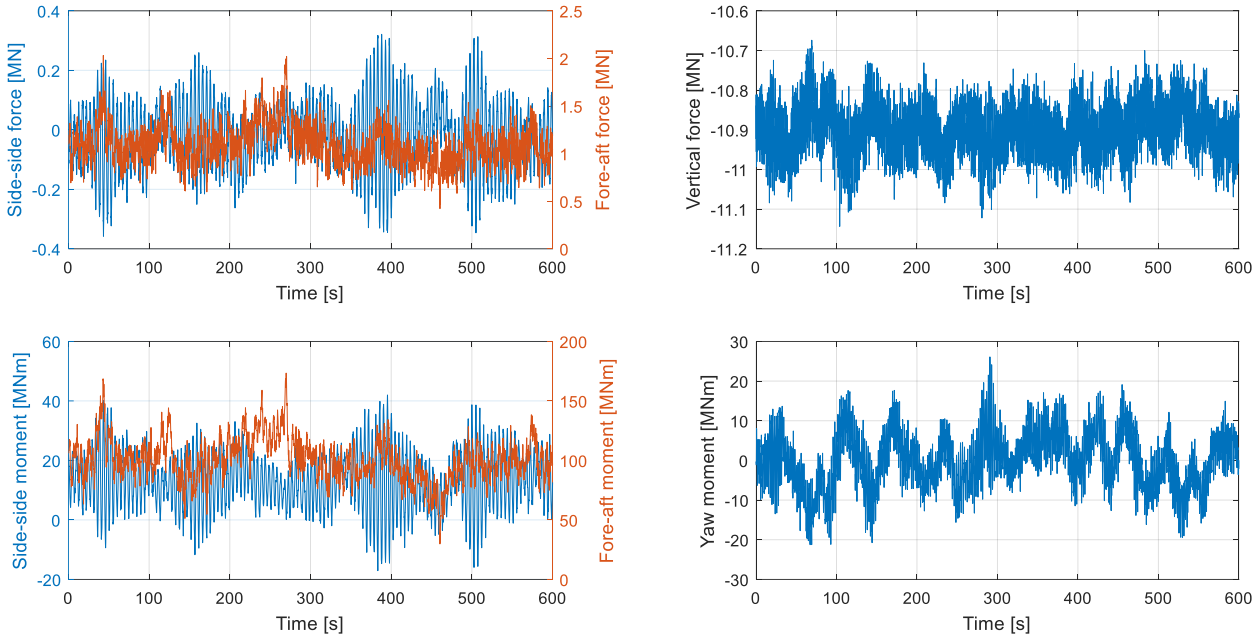

Figure 10. Load time series at the interface for 13 m/s mean wind speed.

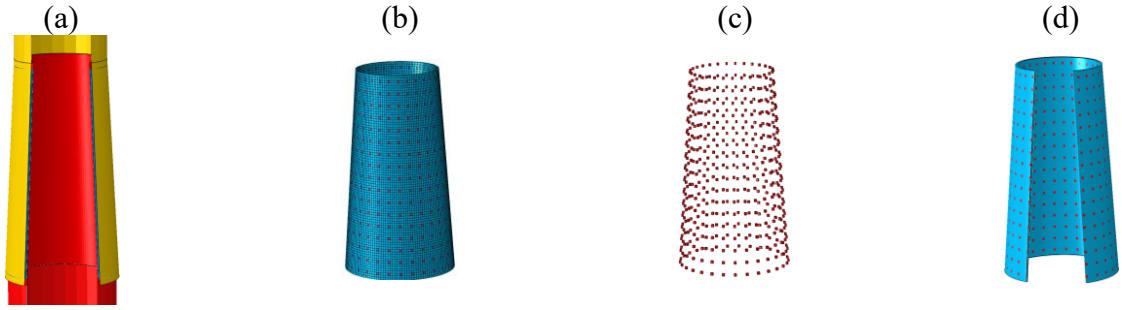

Figure 11. Selected hotspots on the grout. They are systematically picked at the center of squares of dimension 5 mesh elements x 5 mesh elements on the envelope. There are three hotspots across the grout thickness. (a) General view of the grouted connection. (b) Distribution of the hotspots. (c) Exploded view of the hotspots. (d) Hotspots across the grout thickness.

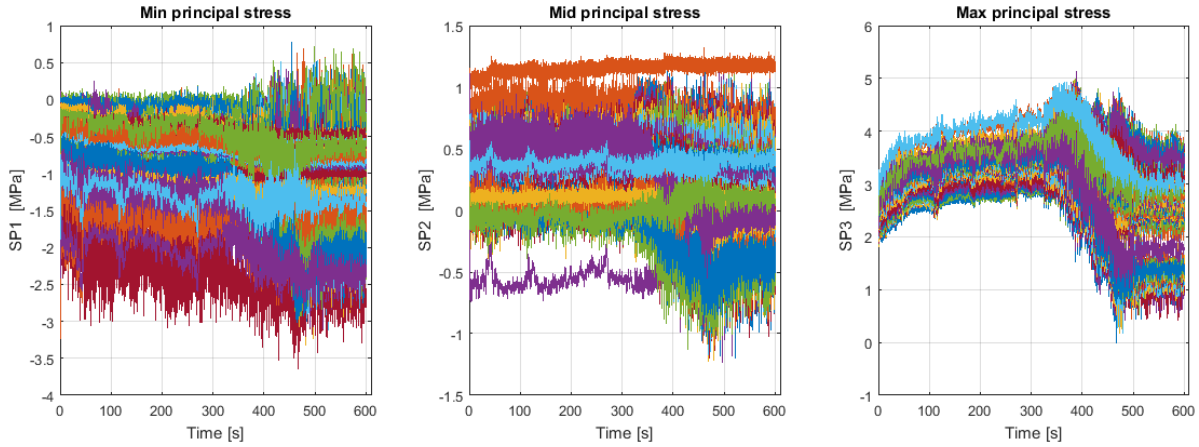

Figure 12. Principal stress time series for 13 m/s mean wind speed for the reference grouted joint collected as the hotspots presented in Figure 11.

7.2.Degradation of the concrete

Following the concrete damaged plasticity model [21], the occurrences of plastic strain generate the tridimensional degradation either of compressive (d_c) or of tensile (d_t) types in the grout material. The equivalent degradation (d), which combines the effect of the compressive and of the tensile

degradation, alters the elastic stiffness of the concrete: $\mathbf{D}^{el}|_{t+\Delta t} = (1 - d|_{t+\Delta t})\mathbf{D}^{el}|_t$, where $\mathbf{D}^{el}$ is the material stiffness matrix. The scalar degradation variable, d, is computed based on the tensile and compressive degradation variables: $(1 - d) = (1 - s_t d_c)(1 - s_c d_t)$. d_c and d_t are taken as the maxima between their respective previous state values and the present state values obtained by interpolation in Table 9. $s_t = 1 - w_t r(\widehat{\boldsymbol{\sigma}})$ and $s_c = 1 - w_c(1 - r(\widehat{\boldsymbol{\sigma}}))$. w_t and w_c are the recovery factor indicated in Table 8. $r(\widehat{\boldsymbol{\sigma}}) = \sum_{i=1}^{3}\langle\hat{\sigma}_i\rangle / \sum_{i=1}^{3}|\hat{\sigma}_i|$ is a stress weight factor, equal to one if all principal stress components $\hat{\sigma}_i, (i = 1, 2, 3)$ are positive, or zero if they are negative. $\langle\cdot\rangle$ is the Macaulay bracket.

Figure 13 presents the evolution at various hotspots of the material degradation over 600 s with 13 m/s mean wind speed and normal turbulence. On the left, the history data of the compressive degradation at the selected hotspots are shown. Similar data are shown for the tensile degradation on the center of the figure. These two quantities monotonically increase over time. On the right, the time series of equivalent degradation variable is presented. Due to the material recovery phenomenon, the degradation variable can reduce. The plots show that the tensile degradation mainly contributes to the degradation variable compared to the compressive degradation. This was expected as the plastic tensile stresses reach relatively higher levels compared to those from compressive ones for comparable magnitudes of strain.

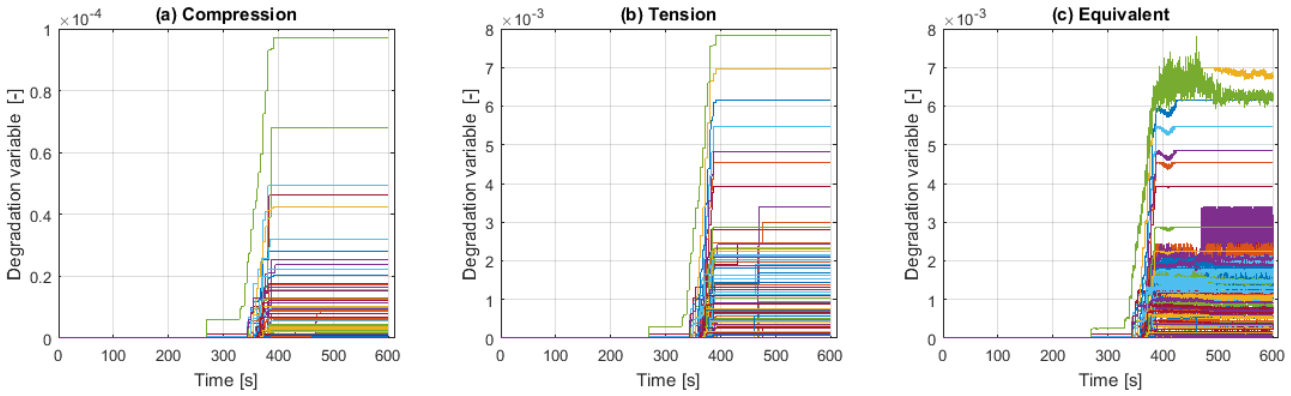

Figure 13. Evolution of the material degradation at various hotspots over 600 s for 13 m/s mean wind speed.

In Table 12, the visual history of the degradation variable is illustrated. It shows that significant tensile degradation initiates before the compressive one. The locus of degradation indicates a future appearance of hairline cracks in the meridional direction and concrete crushes at the grout edges. These observations are in line with previous experimental or numerical studies presented by Lee *et al.* (2014) [11], Nielsen (2007) [6], and Dallyn *et al.* (2015) [3]. The hairline cracks are due to the hoop stresses generated by the grout ovalization whereas the concrete crushes are the consequence of the compression of the transition piece towards the pile during operational oscillations of the support structure. During the 600 s simulation, the severely affected areas are marginal: it can be expected that the joint preserves its connection bending stiffness as it will be seen later.

7.1.Fatigue of the concrete

Fatigue damage accumulates over lifetime due to cyclic stresses such as presented above. DNVGL-ST-0126 (2016) [4] proposes an algorithm to estimate the total damage. The characteristic number of cycles to failure is calculated from:

$$\log N = \begin{cases} \mathrm{Y}, & \mathrm{Y} < \mathrm{X} \\ \mathrm{Y}\big(1 + 0.2(Y - X)\big), & \mathrm{Y} \geq \mathrm{X} \end{cases} \tag{7}$$

with $Y = C_1\left(1 - \frac{\sigma_{max}}{0.8 f_{cn}/\gamma_m}\right) / \left(1 - \frac{\sigma_{min}}{0.8 f_{cn}/\gamma_m}\right)$; $X = C_1 / \left(1 - \frac{\sigma_{min}}{\frac{0.8 f_{cn}}{\gamma_m}} + 0.1 C_1\right)$; $f_{cn} = f_{ck}\left(1 - \frac{f_{ck}}{600}\right)$

where

σ_{max}, σ_{min} = are respectively the largest value of the maximum principal compressive stress during a stress cycle within the stress block and the smallest compressive stress in the same direction during this stress cycle. They are to be individually set to zero if they belong to the tensile range;

γ_m= 1.5 is the safety factor associated to the grout material;

f_{ck} is the characteristic grout cylinder strength measured in MPa;

C_1 = calibration factor. For structures in water, $C_1 = 10.0$ for compression-compression range and $C_1 = 8.0$ for compression-tension range.

Table 12:
Visual history of the compressive, tensile, and equivalent degradation variables

Time [s]	0 - 300	375	600	Legend
Compressive degradation			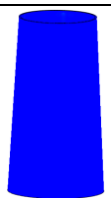	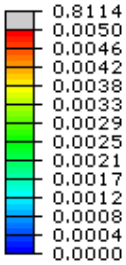
Tensile degradation				
Degradation variable				

The damage accumulated over one year is linearly aggregated using Eq. (8); and the lifetime is calculated as $L_f = D_1^{-1}$ and $D_{25} = 25D_1$.

$$D_1 = \gamma_{FF} \sum_i \frac{n_i(\Delta\sigma)\ t_i(\Delta\sigma)}{N_i(\Delta\sigma)} \tag{8}$$

where $\gamma_{FF} = 3.0$ is the fatigue reserve factor and $t_i(\Delta\sigma)$ is the occurrence frequency in one year of stress range $\Delta\sigma$, which is counted $n_i(\Delta\sigma)$ times in the simulation time.

Figure 14 presents the spatial distribution of the fatigue damage accumulated over 25 years on an unrolled grout accounting for the full directionality of the loads. As the grout has been meshed in three layers across its thickness, the respective fatigue damage levels of the different layers are shown. The cumulative fatigue damage level at the critical hotspot is lower than one. The alignment of the peaks of fatigue damage on the surfaces suggests the nascence of the hairline cracks as indicated by the previous observations. It can also be noticed that fatigue affects the top edge of the grout on the transition face. This was expected as the highest compressive stresses are transferred from the transition piece to the pile through the grout top edge.

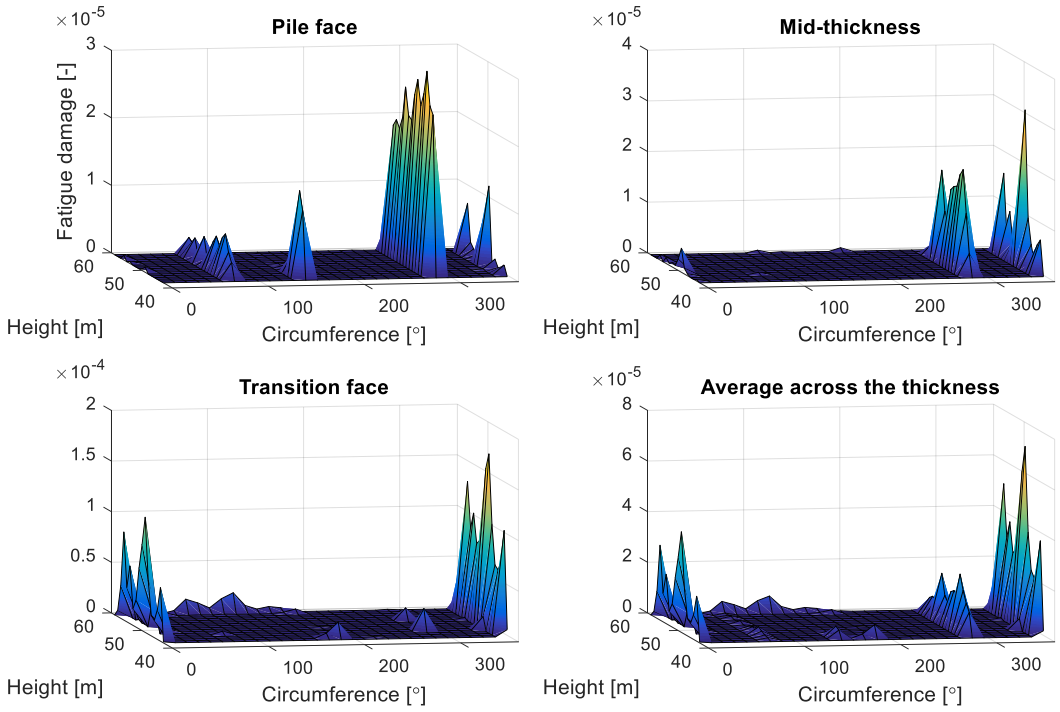

Figure 14. Fatigue damage on unrolled grout over the lifetime for the reference grouted joint.

The fatigue damage magnitudes indicate that the proposed design is not optimal with respect to the fatigue limit state. Carrying out a deterministic optimization design, Lee *et al*. [11] have shown that decreasing the grouted joint mass contributes to the increase of fatigue lifetime of the structure. The sensitivities of the design parameters have been evaluated based on a design of experiment and using analysis of variance. They have found that the wall thicknesses of the steel components were the variables that had the most influence on the fatigue lifetime. Indeed, the wall thickness of the transition piece has a sensitivity of 46 % whereas the wall thickness of the pile has a sensitivity of 35 %. The other variables were: length of the grout, 10 %; conical angle, 3 %; pile's radius, 1 %; grout's elastic modulus, 1 %; steel's elastic modulus, 1 %; and loads (axial force, torsional moment, maximum bending moment, and minimum bending moment), 1%; grout's thickness, 0 %; contact friction, 0 %.

In order to investigate the influence of the wall thickness of the steel components, a design with the other dimensions unchanged has been prepared with transition piece's wall thickness changed from 60 mm to 80 mm and pile's wall thickness changed from 70 mm to 100 mm. Load assessment has been done and the monopile substructure has been proven sufficient for the serviceability, fatigue, and ultimate limit states as per the reference monopile. The results are not shown here for readability. The evaluation of fatigue damage for this modified structure over the lifetime is depicted in Figure 15. The mid-layer and the outer layer show fatigue damage levels lower that one at all points, whereas a minimal region of the inner layer has a damage level of 1.12. The hairline cracks and the vulnerability of the top edge can still be observed. It is noticeable that the loci of high fatigue damage are at the top edge and along the meridian at 0°, where loads are primarily transferred.

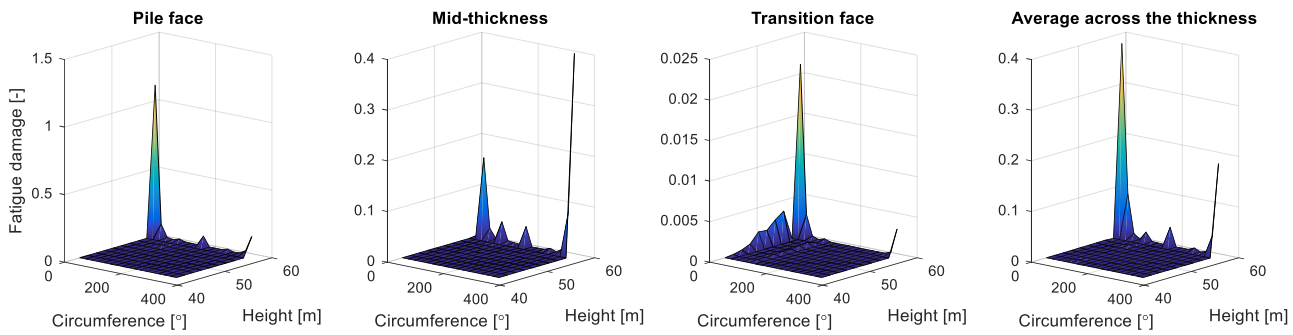

Figure 15. Fatigue damage on unrolled grout over the lifetime for the modified grouted joint.

The variation of the fatigue lifetime between both designs can be explained by the compressive stresses generated in the grout. With thick steel walls, the structural system is more rigid and the transition piece squeezes the grout more during load transfer. Thus, higher compressive stress levels are generated within the grout material as shown by Figure 16, where the compressive stresses are up to 9 MPa whereas they were up to 3.5 MPa with thinner walls (see Figure 12).

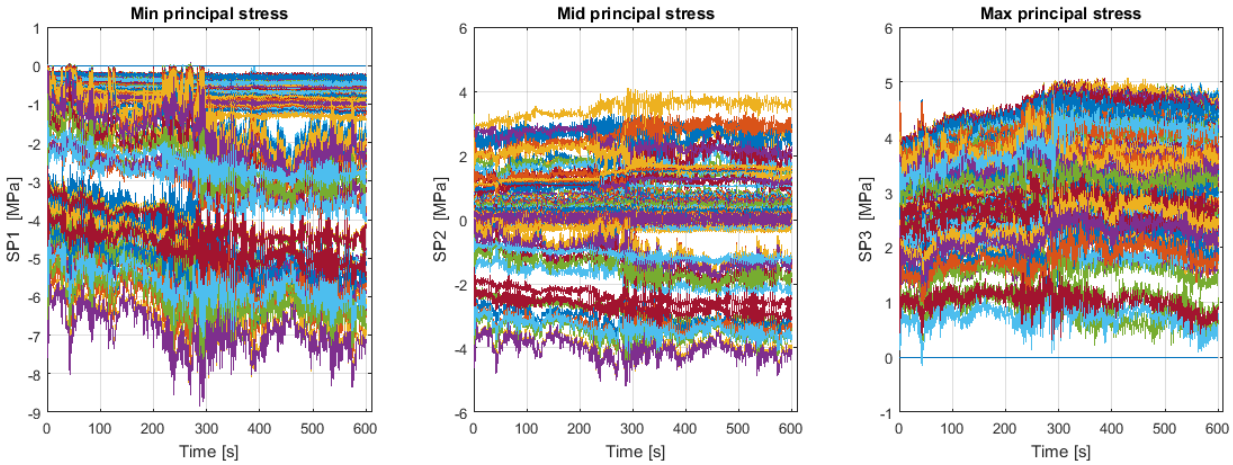

Figure 16. Principal stress time series for 13 m/s mean wind speed for the modified grouted joint.

7.2.Vertical settlement

With the progressive degradation of the grout, the conical grouted joint could exhibit a gradual failure like the continuous settlement of the transition piece. Schaumann *et al.* [2] observed a continuous settlement of the transition piece on a cylindrical connection without shear keys where the passive shear resistance was due to coulomb friction and chemical adhesion. They have explained that the vertical displacement is caused by the reduction of coulomb friction when the transition piece approaches its neutral position, where the operational loads are small.

For the case (in presence) of conical grouted connection with the initial settlement already being undergone and under the assumption that the shear resistance is only due to coulomb friction, a large amount of shear resistance is permanently due to the structural weight. Therefore, it is expected that with a sufficient conical angle, the settlement due to loss of coulomb friction is significantly reduced. With a conical angle of 3°, simulation results depicted in Figure 17 show (i) an initial vertical settlement due to the application of the dead load; (ii) a slight gradual settlement due to the deformation of components (steel and grout) and grout degradation.

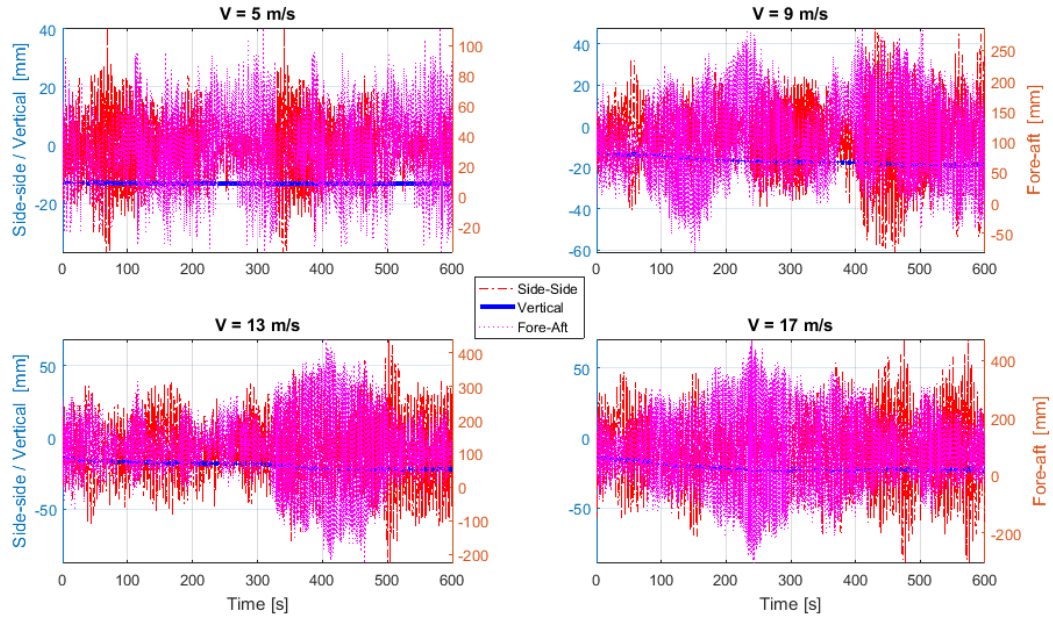

Figure 17. Displacement history of the interface central node at several mean wind speeds.

For simulation of 600 s duration, the relationship between the grout degradation and the increase in vertical settlement can be observed in Figure 15 for 13 m/s mean wind speed. As the degradation onsets in the grout at about 300 s, the vertical settlement increases at that instant but tends to stabilize notwithstanding the apparition of cracks. Furthermore, no trend change is observed during the 600 s simulation on the fore-aft and the side-side displacements, suggesting no significant loss of the support structure global bending stiffness during the simulation period. In case of bending stiffness reduction, the amplitudes of the side-side displacements would have increased and the means of the fore-aft displacements would have shifted.

These observations are in line with the assumption that the hairline cracks do not significantly deter load transfer and also do not significantly elongate. However, it can be argued that 600 s simulations are not long enough to really capture a long term behavior of the connection. Therefore 1800 s simulations at 11 m/s mean wind speed has been carried out. Figure 18 shows that the rate of vertical settlement of the interface central node continuously decreases even after 1800 s.

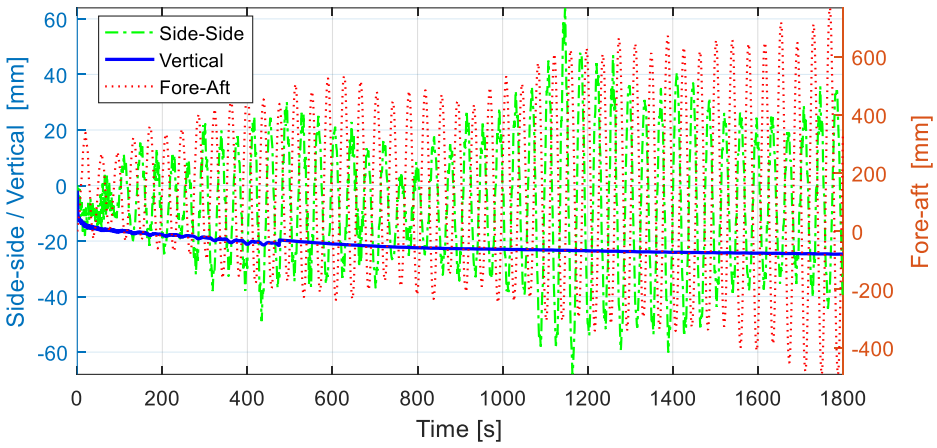

Figure 18. Displacement history of the interface central node at 11 m/s mean wind speed during 1800 s.

7.3.Effect of the conical angle

In particular, the influence of the conical angle on the vertical displacement of the interface is studied. The structure dimensions are set as their nominal values (see Table 6) but the conical angle is varied from 1^0 to 4^0. The loading set corresponding to 11 m/s mean wind speed is applied on the structure during 600 s and the displacement of the interface is monitored. Depicted in Figure 19, the results show that both the initial settlement and the settlement rate reduce as the conical angle increases. For small conical angles, the settlement fails to stabilize during the 600 s, suggesting a continuous vertical displacement till failure. This indicates the necessity to choose a conical angle large enough to guarantee the grouted joint stability.

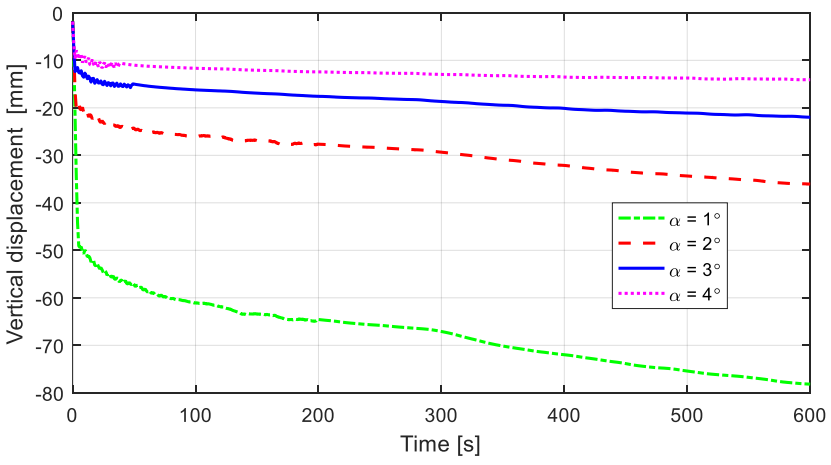

Figure 19. Influence of the conical angle on the vertical displacement of the interface for the reference grouted joint.

For the structure with thicker pile's and transition piece's wall, the evolution of the interface vertical displacement is show in Figure 20 for 1° and 3° conical angle. It shows that with thicker steel wall the vertical displacement stabilizes quicker than with the reference design. This is partly due to the high shear friction resistance generated due to the high compressive stresses exerted on the contact faces.

However, with 1° angle a two-step phenomenon occurs. The first step is the initial displacement due to the self-weight, which is larger for the thin wall case due to high steel flexibility and the lower shear friction resistance at the contact faces. Then, the second step is the progressive settlement due to the operational loadings, which is about 30 mm for the thin wall case and 70 mm for the thick wall case. The greater vertical displacement in the case of thick walls can mainly be explained by the degradation of the grout material (at about 100 s). Indeed, during the first 100 s where both structures are intact, the vertical displacement of the thin wall case is similar to that of the thick wall. It is recalled that grout between thick steel walls is prone to rapid degradation due to high stresses generated by the compression it undergoes.

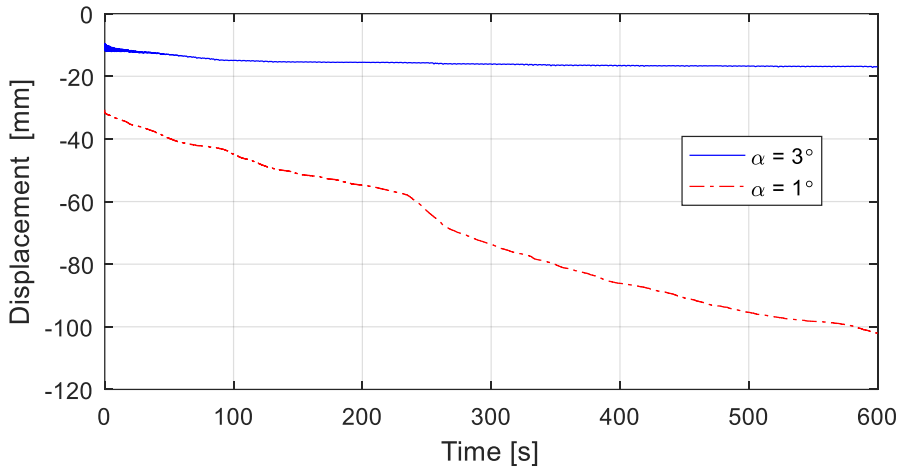

Figure 20. Influence of the conical angle on the vertical displacement of the interface for the modified grouted joint.

In short, the comparison of the designs with different wall thickness ranges has shown that the wall thicknesses of the pile and transition piece impact the behavior of the grouted joint in a nonlinear manner. Thick walls negatively affect fatigue and grout degradation, however the progressive settlement is reduced provided that grout degradation is minimal. The opposite observation is done with the thin walls as summarized in Table 13. In both cases, high conical angle limits the vertical displacement of the transition piece. However, as mentioned before, critical settlements can be due to the occurrence of extreme values of the load components and requirements to accommodate such deformation levels should be evaluated.

Table 13:
Effect of the wall thicknesses on the behavior of the grouted joint under continual loadings

Limit states	Thick wall	Thin wall
Fatigue	Negative effect	Positive effect
Grout material degradation	Negative effect	Positive effect
Progressive settlement	Positive effect*	Negative effect

*Thick walls yield to lower progressive settlement provided that the grout material is not severely degraded.

8. Structural responses under extreme loadings (ULS)

The selected structural responses under extreme loadings are the Tresca stress in the concrete, the shear stress at the contact faces, and the vertical settlement. Investigations are carried out over the design space to determine their respective distributions and their sensitivities with respect to the

design variables. The design space consists of load variables, geometry variables, and material variables. In this study, the geometry variables are assumed deterministic but are varied within bounds to cover various possible designs of the grouted joint. The probability density functions (PDFs) of the material variables are given in Section 3. The PDFs of the extreme load variables are sought based on Monte Carlo simulations with N points. For each point, the load values that yield to extreme structural responses should be identified. An approximate method for this identification is introduced. As the 66 load variables are generated for one structural system by the same environmental conditions, high correlations between the variables are expected. The load set will then be reduced retaining only some variables taken as insufficiently-correlated. From the characterization of the reduced load set, the PDFs of the whole set can be calculated.

8.1.Extreme loadings

Load assessment carried out in HAWC2 under metocean conditions described by Table 2 results in load time series collected at the 11 locations as described above. The locations are numbered from 1 to 11 from bottom to top (interface). For each location, six load time series are obtained corresponding to each degree of freedom. Ideally, the ultimate structural responses should be obtained as the "maximum" of the structural response time series generated in the structure subjected to a set of load time series. This requires that the finite element analysis is done for 600 s for a given set of load time series, which is extremely computationally expensive.

In order to reduce the computational cost, it is assumed that the ultimate structural responses occur when horizontal force, vertical force, bending moment, or torsional moment measured at the center of the grouted joint is extreme. This corresponds to four load criteria as depicted in Figure 21. Given a load criterion, the time instant at which its extreme is attained is identified and the other load components corresponding to this instant are collected to form the set of contemporaneous extreme nodal loads resulting from the load scenarios. A load scenario is understood here as an aero-hydro-servo-elastic simulation with a given mean wind speed.

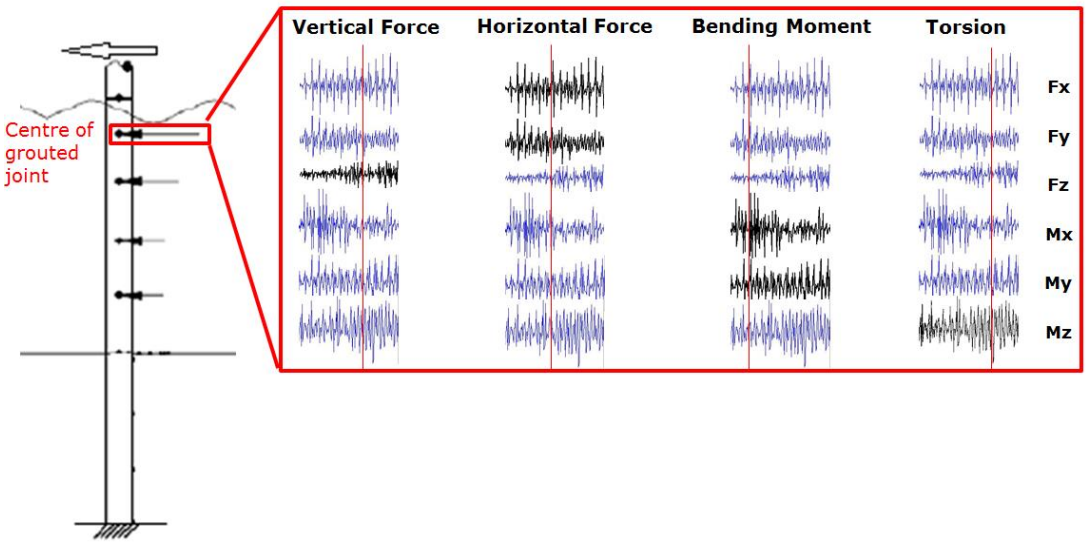

Figure 21. Selection of nodal loads for finite element analysis.

Let take as an example the load criterion horizontal force. The resultant horizontal force is obtained as the Euclidian summation of the forces in x- direction and y-direction. At the time t_m when the extreme resultant horizontal force at the grouted joint center is attained, the load vector $\langle F_x(t_m), F_y(t_m), F_z(t_m), M_x(t_m), M_y(t_m), M_z(t_m)\rangle$ is constructed for each of the 11 locations, which gives 66 nodal loads. This operation is repeated for the other three load criteria such that, to every load scenario, are related four sets of 66 nodal loads.

It can be noted that the nodal loads of interest are not necessarily the extreme values of their time series, but the values that maximize the load criterion. Moreover, as results from HAWC2 are the internal loads at selected hotspots, the distributed external loads at the 10 locations (the interface is exempted) are estimated as the difference between two consecutive hotspots.

8.2.Load randomness: Dimensionality reduction and parametrization

For the probabilistic study of the grouted joint, 500 data samples have been drawn from Table 2 and the corresponding nodal loads are obtained from them. Given a load criterion, each of the 66 nodal loads is established as a random variable numbered from 1 to 66: the first 6 variables are associated to location 1, the second 6 variables to location 2, and so forth. Figure 22 illustrates for the vertical force criterion the marginal distributions of the random variables numbered $\{1 + 6i, i = 0, \dots, 10\}$, which correspond to F_x at the eleven locations, together with the one-by-one dependence structure between them as an example.

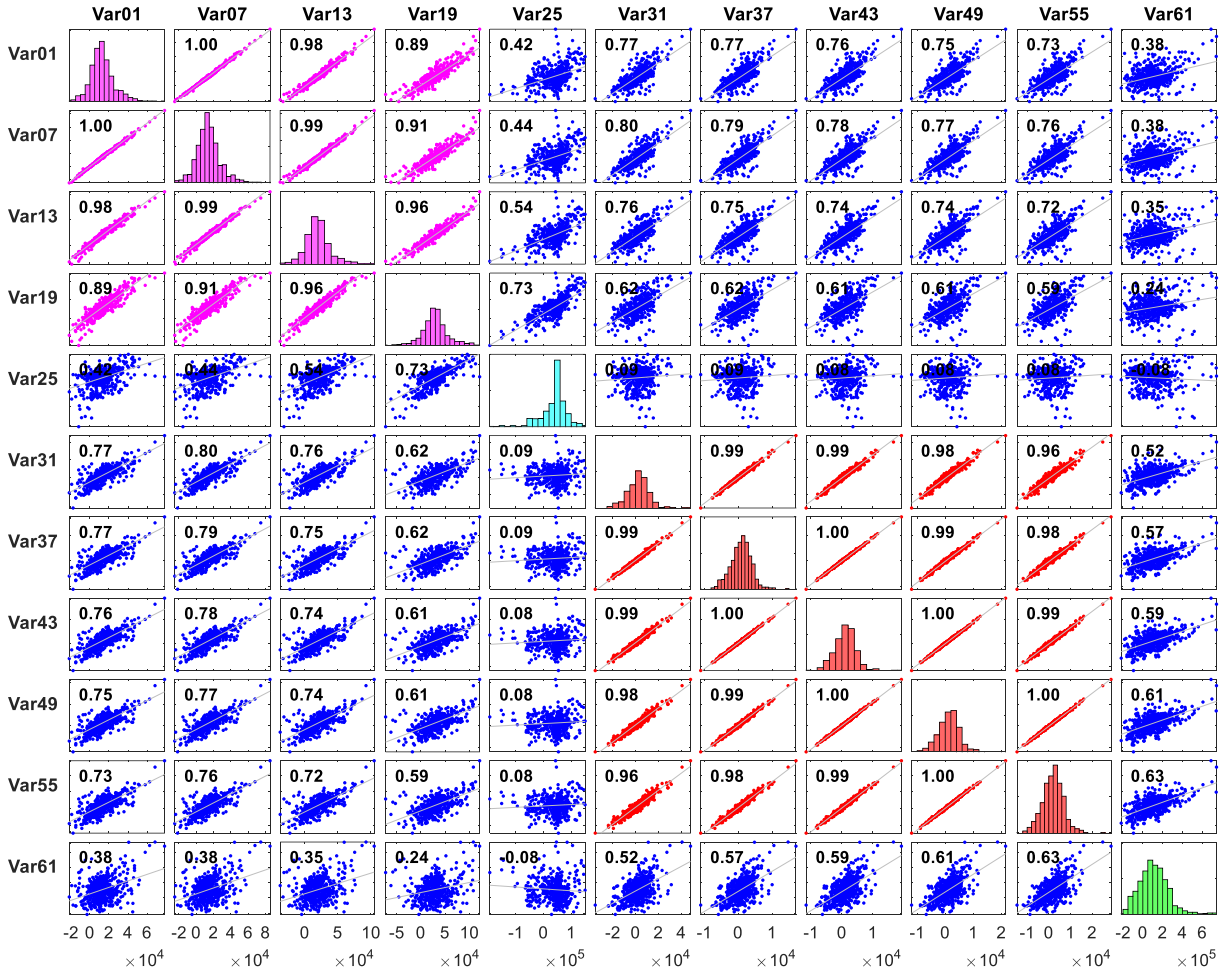

Figure 22. Cross-correlation of the observed random variables F_x for the vertical force criterion. Pearson's correlation coefficients are indicated for each scatter plot. Units: Newton. Variables within blocks of same color are considered correlated.

As it could be expected, some variables are highly correlated as grouped with color in Figure 20. Physically, the magenta-colored variables mainly represent the hydrodynamic loads, the cyan-colored variable is the monopile section at the sea surface, the red-colored variables are primarily associated to the aerodynamic loads transmitted from the rotor, and the green-colored variable is the interface force in the side-side direction. This suggests that each group can be represented by one variable selected as insufficiently-correlated, and the other variables within the group are expressed as a function of it. This reduces the set of 11 variables to four variables. The same operation is carried out for all degrees of freedom resulting in the dimension reduction from $m = 66$ to $n = 17$ variables for the case of horizontal force criterion and to $n = 15$ variables for the other criteria.

If $\mathbf{Z}$ denotes the insufficiently-correlated variables, the dependent variables, $\mathbf{X}$ can be obtained by:

$$\mathbf{X}_{m\times 1} = \boldsymbol{\alpha}_{m\times n}\mathbf{Z}_{n\times 1} + \boldsymbol{\beta}_{m\times 1} \tag{9}$$

where $\boldsymbol{\alpha}$ is the matrix of the scale factors obtained as the ratio of $\mathbf{X}$'s standard deviation over $\mathbf{Z}$'s standard deviation; and $\boldsymbol{\beta}$ is the vector of the shifts obtained as the difference between the $\mathbf{X}$'s average and the $\boldsymbol{\alpha}\mathbf{Z}$'s average.

The marginals of the insufficiently-correlated variables are modeled with parametric probability density functions (PDFs). Three standard probability distributions: Gaussian [46], Gumbel [47], and Logistic [47] have been selected on the basis of their ability to represent the physical phenomena of interest here. The Gaussian is appropriate to accommodate the natural randomness contained in the environmental data. The Gumbel distribution is suitable for extreme values. The difference of two Gumbel distributed variables follows a Logistic distribution. As nodal loads are obtained as the difference of loads possibly Gumbel-distributed, the Logistic distribution is applicable. Each insufficiently-correlated variable is tested against every selected probability distribution using Kolmogorov-Smirnov test [48] with 0.05 significance level and the relevant PDF is identified as the probability distribution with the highest p-values. The null hypothesis poses that the insufficiently-correlated-variable data are from the assumed distribution. Figure 23 illustrates the marginals of the insufficiently-correlated variables for the torsional moment criterion where the identified PDF and the corresponding p-value are indicated.

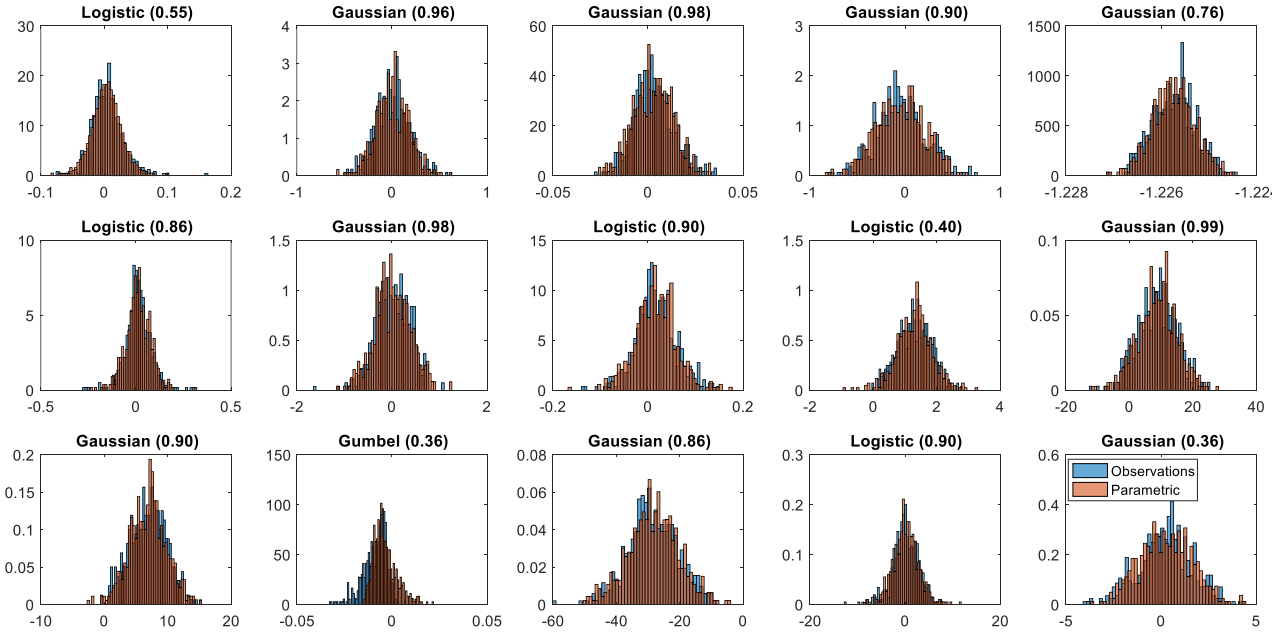

Figure 23. Marginal distributions of the insufficiently-correlated random variables for the torsional moment criterion. P-values greater than 0.05 is assumed sufficient for the suitability.

The dependence structure within the sets of insufficiently-correlated variables, $\mathbf{Z}$, is captured using Gaussian copula [49], which results in the joint probability distribution of the set of the insufficiently-correlated random variables. Given the correlation matrix $\mathbf{R}$ of $\mathbf{Z}$, the Gaussian copula is defined as $c(u_1, \cdots, u_n) = \boldsymbol{\Phi}_{\mathbf{R}}\left(\boldsymbol{\Phi}^{-1}(u_1), \cdots, \boldsymbol{\Phi}^{-1}(u_n)\right)$, where $u_i = F_i(Z_i)$; F_i cumulative distribution function (CDF) of the insufficiently-correlated variable Z_i; $\boldsymbol{\Phi}_{\mathbf{R}}(\cdot)$ is the joint cumulative distribution function of a n-dimension multivariate normal distribution with mean vector zero and covariance matrix equal to $\mathbf{R}$; and $\boldsymbol{\Phi}^{-1}(\cdot)$ is the inverse cumulative distribution function of a standard normal. The accuracy of the constructed dependence structure has been evaluated by comparing the correlation matrix from the observed data versus that of synthetic data generated from the constructed joint probability distribution. The root-mean-square deviations (RMSD) between the correlation matrices of the two data sets are 1.12 %, 0.85 %, 0.83 %, 0.60 % for the horizontal force, the vertical force, the bending moment, and the torsional moment criteria, respectively.

8.3.Design space exploration

In order to explore the design space, uniformly distributed loads have been sampled within the bounds of the marginals, defined as values corresponding to 10^{-7} cumulative and survival

probabilities, respectively. The survival function is defined as the complementary cumulative distribution function. Figure 24 shows for the vertical force criterion as an example that the sampled loads cover well the tails of the variables, suggesting a good representativeness of the edges of the design space.

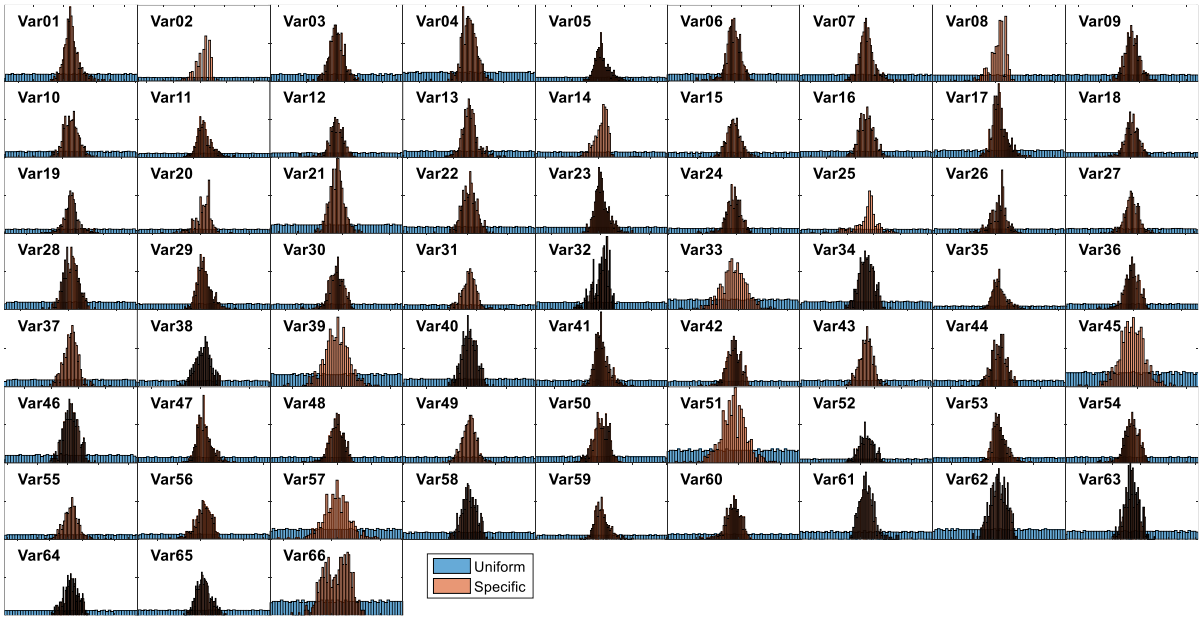

Figure 24. Uniformly sampled load to cover the design space for the vertical force criterion.

The bounds have been defined similarly for the other load criteria. They have been superimposed in order to find the global bounds and generate a unique uniform sampling for the four load criteria. The results are depicted in Figure 25.

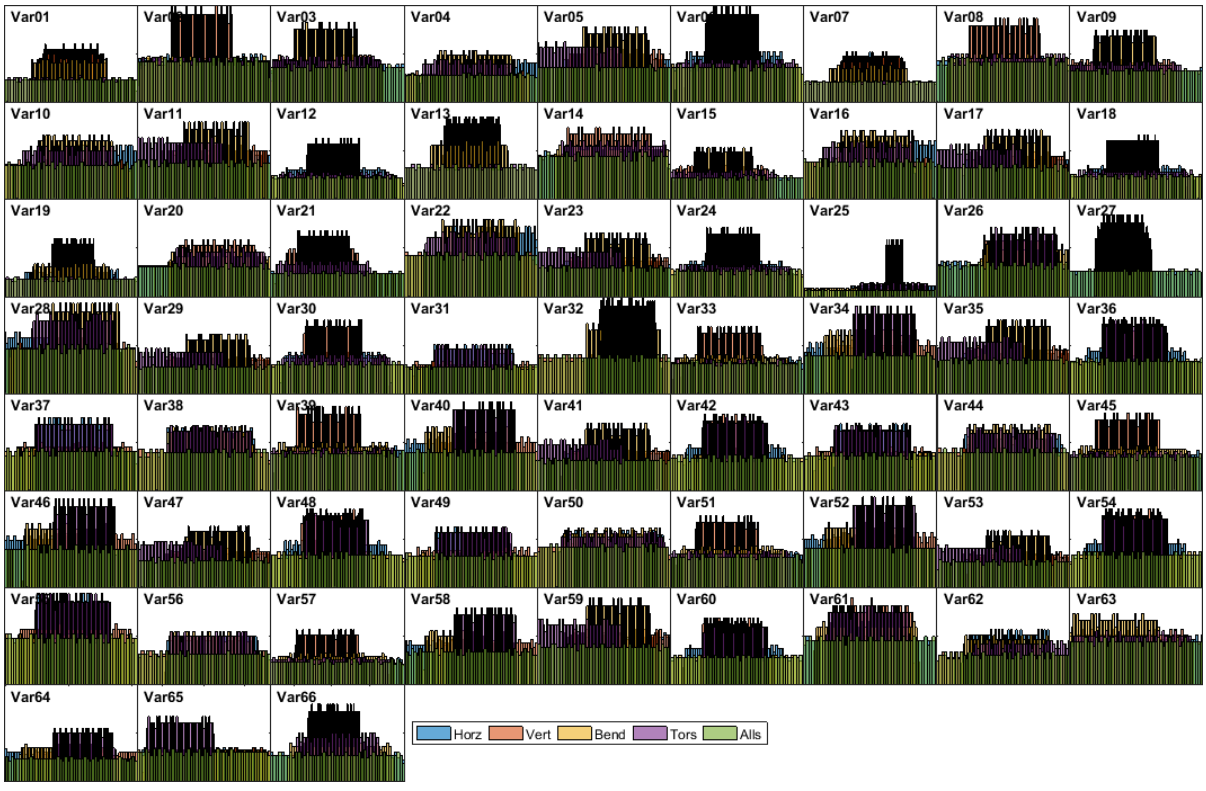

Figure 25. Uniformly sampled loads to cover the design space for all the load criteria.

In addition, the variables related to the material properties have been independently and uniformly sampled between the bounds found as per the load case. The geometry-related variables are also independently and uniformly sampled between the bounds as indicated in Table 6.

With the 500 uniformly sample variables describing loads, material, and geometry, a batch of finite element simulations has been run in Abaqus. The absolute maxima of the structural responses pertaining to extreme loading, which are the settlement of the transition piece relative to the pile, the Tresca equivalent stress in the concrete, the shear forces at both sides of the contact grout-steel, have been collected. Figure 26 depicts the normalized safety margins for each structural response when the variables map the whole design space. The safety margins are computed as the difference between the resistance parameters (see Eqs. 3 and 4) and the structural responses, respectively. In preparing Figure 26, the variable h in Eq. (4) has been set to 100 mm. The difference is then divided by the respective characteristic values of the resistance parameters (see Tables 8 and 10) to obtain the normalized safety margins. Except for the settlement, it can be noted that the safety margins of the other structural responses are all greater than zero, indicating that failure will not arise from these failure modes. Therefore, the reliability analysis will only focus on the failure mode respective to vertical displacement.

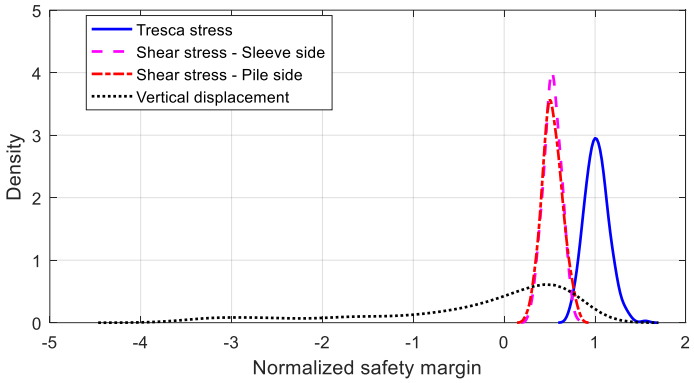

Figure 26. Normalized safety margins of the structural responses over the design space.

8.4.Sensitivity of the extreme vertical displacement with respect to the design parameters

In order to assess the influence of the design parameters - which are mainly the geometry and material types - on the extreme vertical displacement, a sensitivity analysis based on correlation between the design parameters and the structural responses has been carried out. The sensitivity measures are computed as correlation coefficients between each design parameters and the structural response. The correlation coefficients are calculated both as of Pearson's or linear type [49] and of Spearman's or rank type [49].

Figure 27 presents the resulting indices, where the grout length demarcates from the rest of the parameters. Its index indicates that longer grouted connections generate lower relative displacements of the transition piece, which can be explained by the fact larger surfaces offer larger shear resistance. Other parameters like the conical angle, the position of the grouted joint with respect to the mean sea level, and the transition piece's wall thickness show lesser influence on the extreme vertical displacement than that of the grout length.

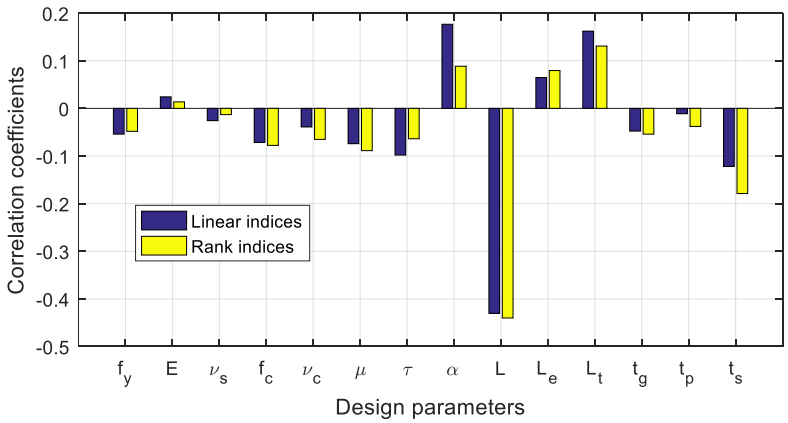

Figure 27. Sensitivity coefficients of the vertical displacement with respect to the geometry and material variables.

This sensitivity analysis suggests that the set of variables of the system can be reduced further as only the connection length emerged as the key design variables of conical grouted joints. During a design process, whereas the material properties are generally known in advance, the structural dimensions are primarily the sought variables. Thus, from the set of material and geometry properties, only the grout length is retained for further parametric study.

9. Prediction of the extreme settlement

9.1. Problem formulation

From each point of the simulation batch of size N described in Section 8, the maximum vertical displacements $\Delta_i, i = 1, \dots, N$ are collected. Each can be seen as the peak of the time series of vertical displacement related to a given mean wind speed. In this sense, they are reasonably assumed to be independent and identically distributed random variables. With this assumption, the extreme value theory applies and the random variable Δ_i follows the cumulative distribution function (CDF):

$$F_{\mathrm{s}}(x|\mu,\sigma,\varepsilon) = \exp[-z(x|\mu,\sigma,\varepsilon)] \tag{10}$$

μ, σ, ε are the parameters of the CDF F_{s}, and z is a function of the random variable x. For the traditional extreme value families (Gumbel, Frechet, and Weibull) [50],

$$z(x|\mu,\sigma,\varepsilon) = \left(1 + \varepsilon\frac{x-\mu}{\sigma}\right)^{-1/\varepsilon} \text{ with } x \in \begin{cases} [\mu - \frac{\sigma}{\varepsilon} \quad +\infty), & \varepsilon > 0 \\ (-\infty \quad +\infty), & \varepsilon \to 0 \\ (-\infty \quad \mu - \frac{\sigma}{\varepsilon}], & \varepsilon < 0 \end{cases} \tag{11}$$

As a substitute of Eq. (11), several studies [51], [52] have proposed a quadratic shape for z such that

$$z(x|\mu,\sigma,\varepsilon) = \mu\, x^2 + \sigma\, x + \varepsilon \text{ with } x \in (-\infty \quad +\infty) \tag{12}$$

and have shown its appropriateness and its robustness for fitting extreme structural responses of various wind turbine structures.

Furthermore, the empirical CDF [53] is generally constructed by sorting the random variables Δ_i in ascending order so that each is associated to a rank d_i. The following expression of the empirical CDF can be written:

$$F_{\mathrm{e}}(\Delta) = \frac{d}{N+1} \tag{13}$$

Equating Eq. (10) and Eq. (13), the parameters μ, σ, ε can be obtained by regression. Hence the probability of exceeding a given vertical displacement is calculated as $G(\Delta) = 1 - F_{\mathrm{s}}(\Delta)$. As per modern standards, the targeted reliability index is about $\beta_0 = 3.3$, which corresponds to a targeted failure probability $Pf_0 = 4.93 \times 10^{-4}$. This means that in order to be safe, the grouted joint should be able to undergo a vertical displacement up to $\Delta_0 = G^{-1}(Pf_0)$ without any consequence on its structural integrity. With an allowable settlement $h \leq \Delta_0$ (see Eq. (4)) failure is not prevented; the design should provide an allowable settlement greater than or equal to Δ_0.

9.2. Provisions for a safe extreme settlement

The reliability index is determined for a given design, with given material and geometry properties. In order to evaluate the survival distribution function (SDF), G, the grouted joint design with similar properties have been binned with respect to grout length, which is the primary influencing parameter. Four bins of equal width are constructed over the length range [9 m, 25 m] and the corresponding

SDFs are fitted as illustrated in Figure 28. For each bin, the settlement threshold required to achieve the targeted annual reliability index is obtained by graphical projection.

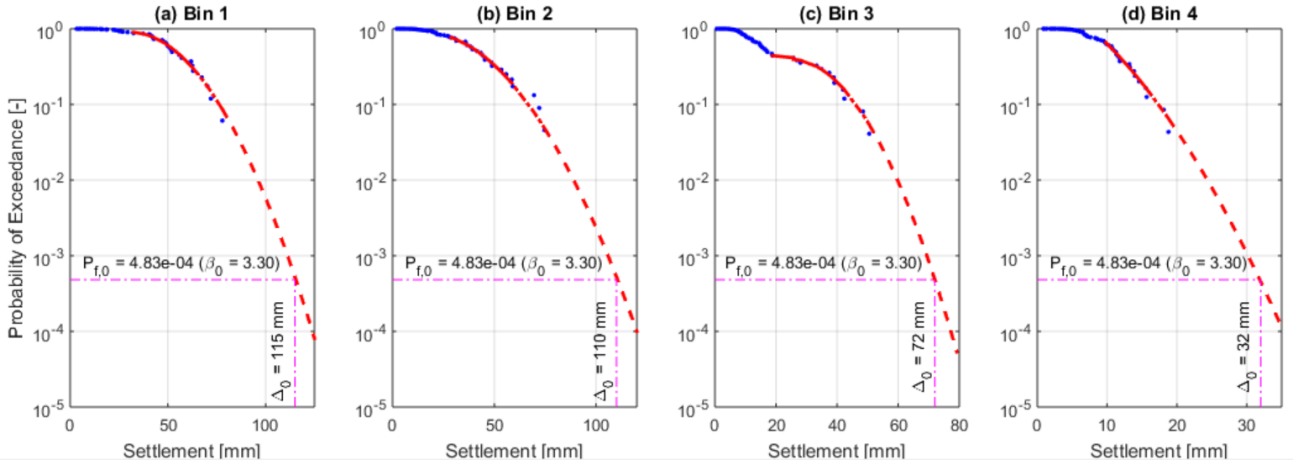

Figure 28. Sensitivity coefficients of the structural responses with respect to the geometry and material variables. The fitted curves are in red and the data point are in blue.

For each bin range, Table 14 gives the settlement thresholds. It shows that for the reference grouted joint, which has 18 m grout length, provisions for 72 mm of vertical displacement should be afforded. For example, the gap between the pile top edge and the jacking brackets should be at least 72 mm to ensure that with sufficient reliability, the settlement of the transition piece does not create any consequence on the structural integrity. Within the framework of this study, allowing a settlement of 72 mm is possible as the other failure modes associated to extreme events are proven improbably realizable. In general, in case high settlement cannot be afforded, long grout should be used to achieve the required reliability.

Table 14:
Settlement thresholds for each grout length bin

Bin No	Bin 1	Bin 2	Bin 3	Bin 4
Bin range	[9 m, 13 m)	[13 m, 17 m)	[17 m, 21 m)	[21 m, 25 m]
Settlement threshold	115 mm	110 mm	72 mm	32 mm

10. Conclusion and recommendations for further studies

In this paper, the behavior of conical grouted joints under continual loadings is investigated based on short term numerical simulations. Three failure modes are considered: the reduction of the grout elastic modulus due to successive yielding phenomena, the fatigue of the grout material due to numerous repeated loading cycles, and the progressive vertical displacement of the transition piece relative to the pile. It is found that the transition piece's wall thickness and the pile's wall thickness have a significant impact on the realization of these failure modes. The larger are the wall thicknesses, the more vulnerable the grout is with respect to fatigue and material degradation but the more limited the progressive settlement is, and inversely. This implies that the appropriate wall thicknesses should be chosen by designers having in mind that neither extreme is conservative.

The reduction of support structure bending stiffness was not observed during short term simulations although the grout material degradation reveals the nascence of hairline cracks along grout meridians and concrete crushes at the grout edges. However, rate increases of progressive settlement coincide with the increase of grout degradation level. The conical angle has been proven determinant to reduce the progressive settlement: conical angle of up to 4^0 can be required for grouted joint on large diameter monopiles in order to nullify the progressive settlement rate. In practice, a typical design process can start with relatively thin steel walls and a conical angle of 3^0. Then, verifications with respect to the progressive settlement can require the increase of the wall thicknesses or of the conical angle. Verifications can be done by ensuring that the settlement rate is within a certain threshold after a specified simulation time.

However, more severe vertical displacement can occur during extreme events and may lead to failure. The grout length is found to be the most influential design parameter for the settlement due to extreme loadings. Longer grout enhances the structural performance of the grouted joint in this respect. In order to ensure that the inevitable vertical displacement does not jeopardize the structural integrity, a probability based method has been developed to estimate the minimal gap between the pile top and the brackets required to achieve a targeted annual reliability index (of 3.3).

This probability based method employs the maximum values of load time series, which is uncertain. Indeed, the highest values of time series of same mean wind speeds should be averaged in order to achieve comparable probability level of each load point. Further studies can incorporate this modification in the algorithm. Furthermore, the vertical displacement values used for extreme value models were not generated based on the actual distributions of the input parameters but on the corresponding uniform distributions. Upcoming investigations can solve this issue, for example, by fitting surrogate models that will be used to generate vertical displacement values that are based on actual input distributions. For this solution, larger simulation batch will be required. Finally, the study of the wear of the grout surfaces in contact with steels, which has not been investigated in this paper, can be considered in other works.

Acknowledgements

The research leading to these results has received funding from the European Union Seventh Framework Programme - project IRPWIND - under the grant agreement 609795. The financial support is greatly appreciated.

References

[1] Kallehave, D., Byrne, B.W., LeBlanc Thilsted, C., Mikkelsen, K.K., 2015. Optimization of monopiles for offshore wind turbines. Phil. Trans. R. Soc. A 373, 1-15.

[2] Schaumann, P., Lochte-Holtgreven, S., Eichstadt, R., 2013. Numerical investigation on local degradation and vertical misalignment of grouted joint in monopile foundations. ISOPE 2013, Anchorage, Alaska, USA.

[3] Dallyn, P., El-Hamalawi, A., Palmeri, A., Knight, R., 2015. Experimental testing of grouted connections for offshore substructures: A critical review. Structures 3 90-108.

[4] DNVGL AS, 2016. Support structures for wind turbines – Standard. DNVGL-ST-0126.

[5] DNVGL AS, 2016. Analysis of grouted connections using the finite element method – Recommended Practice. DNVGL-RP-0419.

[6] Nielsen, L.P., 2007. Finite element analysis of large diameter grouted connections. OMAE2007. San Diego, California, USA.

[7] Lotsberg, I., 2013. Structural mechanics for design of grouted connections in monopile wind turbine structures. Marine Structures, 32:113–135.

[8] Lotsberg, I., Serednicki, A., Bertnes, H., Lervik, A., 2012. Design of grouted connections for monopile offshore structures. Stahlbau, 81:695–704.

[9] Schaumann, P., Raba, A., 2015. Systematic testing of the fatigue performance of submerged small-scale grouted joints. International Conference on Ocean, Offshore and Artic Engineering (OMAE2015). St. John's, Newfoundland, Canada

[10] Schaumann, P., Raba, A., Bechtel, A., 2014. Experimental fatigue tests on axially loaded grouted joints. International Wind Engineering Conference (IWEC2014).

[11] Lee, Y.-S., Choi, B.-L., Lee, J.H., Kim, S.Y., Han, S., 2014. Reliability-based design

optimisation of monopile transition piece for offshore wind turbine system. Renewable Energy 71 729-741.

[12] The International Federation for Structural Concrete, 2010. Fib Model Code for concrete structures. Lausanne, Switzerland.

[13] Von Borstel, T., 2013. INNWIND.EU Deliverable 4.3.1 – Design report – Reference Jacket. http://www.innwind.eu/-/media/Sites/innwind/Publications/Deliverables/DeliverableD4,-d-,31_20131030_INNWIND,-d-,EU.ashx?la=da

[14] The international Electrotechnical Commission, 2005. Wind Turbines – Part 1: Design requirements, IEC 61400-1 Ed 3.

[15] Njomo Wandji, W., Natarajan, A., Dimitrov, N., 2017. Influence of model parameters on the design of large diameter monopiles for multi-megawatt offshore wind turbines at 50 m water depths. Submitted to Wind Energy.

[16] de Vries, W., 2011. UpWind WP4 D4.2.8 Final Report WP4.2: Support structure concepts for deep water.

[17] Bak, C., Zahle, F., Bitsche, R., Kim, T., Yde, A., Henriksen, L.C., Andersen, P.B., Natarajan, A., Hansen, M.H., 2013. INNWIND.EU Deliverable 1.2.1 – Description of the DTU 10 MW Reference Wind Turbine. http://www.innwind.eu/-/media/Sites/innwind/Publications/Deliverables/DeliverableD1,-d-,21%20Aerodynamic_StructuralValidation_INNWIND,-d-,EU.ashx?la=da

[18] Cremer, L., Heckl, M., 1988. Structure-Borne Sound. Springer-Verlag, New York.

[19] Det Norske Veritas, 2014. Design of Offshore Wind Turbine Structures - Offshore Standard. DNV-OS-J101.

[20] Joint Committee on Structural Safety, 2001. Probabilistic model code. JCSS-OSTL/DIA/VROU-10-11-2000. http://www.jcss.byg.dtu.dk/Publications/Probabilistic_Model_Code

[21] ABAQUS, 2011. ABAQUS Documentation, Dassault Systèmes, Providence, RI, USA.

[22] Tyau, J.S., 2009. Finite element modeling of reinforced concrete using 3-dimensional solid elements with discrete rebar. Master thesis, Brigham Young University.

[23] Aitcin, P.-C., 2004. High-Performance Concrete. Taylor & Francis, London.

[24] Cauberg, N., Tronci, C., Pierard, J., van Itterbeeck, P., van der Zee, P., 2013, Case study ultra-high performance concrete: Tests on two UHPC I-girders and analysis of flexural behavior. RILEM-fib-AFGC Int. symposium on ultra-high performance fibre-reinforced concrete. Marseille, France.

[25] Nowak, A.S., Rakoczy, A.M., Reliability-based calibration of design code for concrete structures (ACI 318). University of Nebraska-Lincoln.

[26] Baltay, P., Gjelsvik, A., 1990. Coefficient of friction for steel on concrete at high normal stress. Journal of Materials in Civil Engineering 2-1, 46-49.

[27] Rabbat, B.G., Russell, H.G., 1985. Friction coefficient of steel on concrete or grout. Journal of structural engineering 111 No 3, 505-515

[28] Larsen, T.J, Hansen, A.M., 2015. How 2 HAWC2, the user's manual. DTU Risoe-R-1597. http://www.hawc2.dk/-

/media/Sites/hawc2/HAWC2%20Download/HAWC2%20manual/manual_version_4-6.ashx

[29] Ankit, A., Datta, N., Kannamwar, A.N., 2016. Free transverse vibration of mono-piled ocean tower. Ocean Engineering Vol 116, 117-28.

[30] Chopra, A.K., 1995. Dynamics of Structures – Theory and Applications to Earthquake Engineering. Prentice Hall, Englewood Cliffs, New Jersey.

[31] Cook, R.D., Malkus, D.S., Plesha, M.E., 1989. Concepts and Applications of Finite Element Analysis. John Wiley & Sons, Inc.

[32] Tarp-Johansen, N.J., Morch, C., Andersen, L., Christensen, E.D, Frandsen, S.T., 2009. Comparing sources of damping of cross-wind motion. European Offshore Wind 2009: Conference & Exhibition. The European Wind Energy Association.

[33] The international Electrotechnical Commission, 2009. Wind Turbines – Part 3: Design requirements for offshore wind turbines, IEC 61400-3 Ed 1.

[34] Chakrabarti, S., 2005. Handbook of Offshore Engineering. Elsevier.

[35] MacCamy, R.C, Fuchs, R.A., 1954. Waves forces on piles: A diffraction theory. Corps of Engineers 1-17

[36] American Petroleum Institute, 2005. Recommended practice for planning, designing and construction fixed offshore platforms – Working stress design. API-RP2A-WSD.

[37] Sorensen, J.D., Toft, H.S., 2014. Safety Factors. DTU Wind Energy– E – Report - 0066 (EN).

[38] Det Norske Veritas, 2013. Buckling strength of shells, Recommended practice DNV-RP-C202.

[39] Stolpe, M., Njomo Wandji, W., Natarajan, A., Shirzadeh, R., Kühn, M., Kaufer, D., 2016. INNWIND.EU Deliverable 4.3.4 – Innovative design of a 10 MW steel-type jacket. https://share.dtu.dk/sites/INNWIND_28450/_layouts/15/WopiFrame.aspx?sourcedoc=/sites/INNWIND_28450/Work%20package%204/Task%204.3/D4.34%20-%20Innovative%20design%20of%20a%2010MW%20steel%20type%20jacket/DeliverableD434_Innovative%20Design%20of%20a%2010MW_steel%20jacket_Rev00.pdf&action=default.

[40] Miner, A.M., 1945. Cumulative damage in fatigue. Journal of Applied Mechanics Vol. 12, A159-A164

[41] Det Norske Veritas, 2011. Fatigue Design of Offshore Steel Structures, Recommended practice DNV-RP-C203.

[42] Arany, L., Bhattacharya, S., Macdonald, J.H.G., Hogan, S.J., 2015. A critical review of serviceability limit state requirements for monopile foundations of offshore wind turbines. Offshore Technology Conference.

[43] Lin, S.S., Liao, J.C., 1999. Permanent strains of piles in sand due to cyclic lateral loads. Journal of geotechnical and geoenvironmental engineering 125 No 9, 798-802.

[44] Achmus, M., Abdel-Rahman, K., Peralta, P., 2005. On the design of monopile foundations with respect to static and quasi-static cyclic loading. Copenhagen Offshore Wind 2005.

[45] Bush, E., Manual, L., 2009. The influence of foundation modelling assumptions on long-term load prediction for offshore wind turbines. OMAE2009, Honolulu, Hawaii.

[46] Johnson N.L., Kotz, S., Balakrishnan, N., 1994. Continuous Univariate Distributions, Vol. 1. Wiley.

[47] Johnson N.L., Kotz, S., Balakrishnan, N., 1995. Continuous Univariate Distributions, Vol. 2. Wiley.

[48] MATLAB 2016b, The MathWorks, Natick, 2016.

[49] Abdallah, I., 2015. Assessment of extreme design loads for modern turbines using the probabilistic approach. PhD Thesis, DTU Wind energy, Roskilde, Denmark.

[50] Singh, V.P., 1998. Generalized Extreme Value Distribution. In: Entropy-Based Parameter Estimation in Hydrology. Water Science and Technology Library, Vol. 30. Springer, Dordrecht.

[51] Natarajan, A., Holley, W.E., 2008. Statistical extreme load extrapolation with quadratic distortions for wind turbines. Journal of solar Energy Engineering 130, (031017) 1-7.

[52] Natarajan, A., Verelst, D.R., 2011. Outlier robustness for wind turbine extrapolated extreme loads. Wind Energy 497, doi:10.1002.

[53] Dimitrov, N., 2015. Comparative analysis of methods for modelling the short-term probability distribution of extreme wind turbine loads. Wind Energy 1861, doi:10.1002.

8

Comparative Analysis Between the Three Substructures (Jacket, Semi-floater, and Monopile)

> The differences between a tart, a pie and a quiche are a blur.
>
> *Yotam Ottolenghi*

The previous chapters studied three substructure types for multi-megawatt wind turbines placed at 50 m water depth. Jackets, semi-floaters, and monopiles present some common aspects and some dissimilarities that are worthy to sort out to help designers for better decision at the early phase of projects. This chapter carries out a comparative analysis between the said substructure types based on various criteria. Its objective is not to be exhaustive, but to provide with some basics in line with the previous chapters of this thesis.

8.1 Description of the Concepts

8.1.1 Technology Readiness Level

The European commission defined different levels for technology readiness, which are shown in Figure 8.1. Jackets and monopiles have already been employed in many commercial wind farms [4], proving their efficacy in operational environments. Thus, they can be classified as TRL 9. However, the semi-floater concept as presented here has not been experimentally proven, hence it is ranked as TRL 2.

8.1.2 Range of Application

Traditionally, jacket and monopile substructures are known to be economically competitive at water depths ranging from 20 m to 40+ m [64], [65] and up to 30+ m [65], respectively. However, recent studies (such as [13], [18], [36]) including the present thesis have shown that their limitation can be over 50+ m water depths.

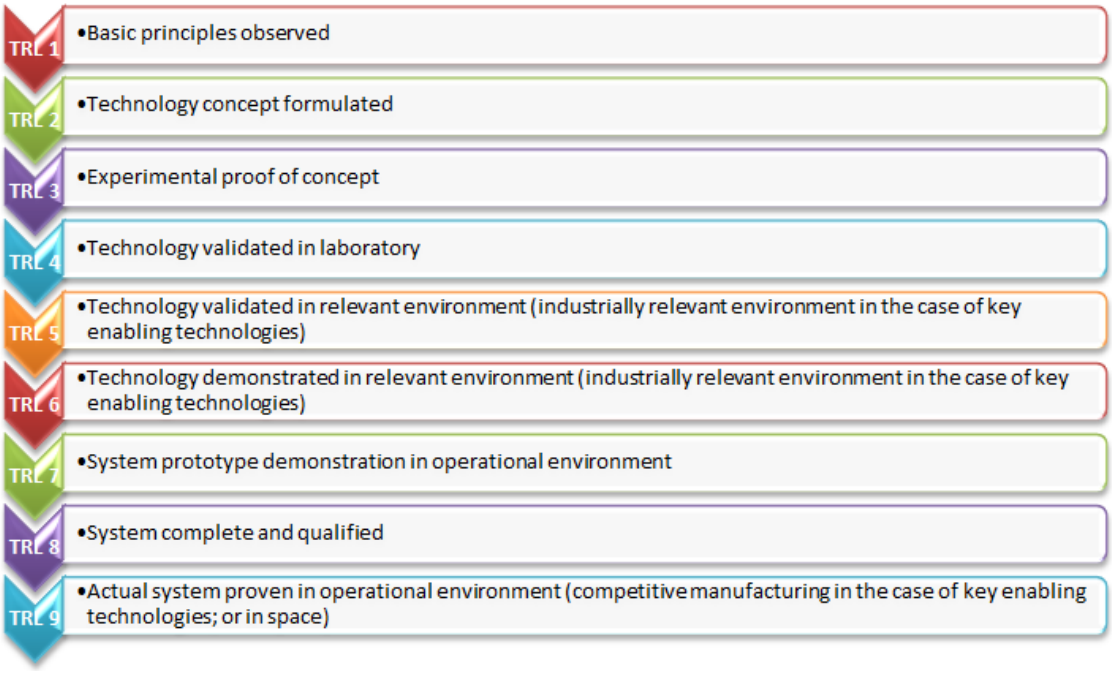

Figure 8.1: Technology readiness levels as defined by the European Commission.

For the semi-floater, the encouraging results in this study suggest the feasibility at waters deeper than 50+ m. This is in conformity with the results of Sanz *et al.* [21] who investigated its feasibility at 100+ m water depth. Contrary to the other substructures which can be technically used at any water depth, a minimum water depth is required for the semi-floater.

8.1.3 Post-design to Decommissioning

The challenges faced after the design phase are specific for each substructure. The fabrication process of the jackets including their transition pieces are complex and expensive, which can hinder the mass production. For monopiles, the fabrication process is relatively easy and eases the serial manufacturing. The fabrication of semi-floaters can substantially benefit from the monopile experience due to their resemblance.

Monopile substructures can be very heavy and require special equipment for transportation and installation. Although voluminous, jackets are light-weight structures, which offer less burden for transportation and installation. Semi-floater substructures are also light but require many on-site trips for mooring line anchorage.

In addition to the mooring line anchorage to the seabed, some earthworks may be required for the reinforced concrete footing of semi-floater. Much earthworks may be required for jackets, whereas virtually no earthworks are needed for monopiles.

At the end of the service, the decommissioning of monopiles are extremely challenging whereas it is less difficult for the jacket substructures, especially if the foundation is not made of piles. The decommissioning of the semi-floater is a relatively easy task as there is no active connection with its foundation. The removal of the reinforced concrete footing, when necessary, is not demanding either as it can be hoisted up and taken ex-situ.

8.2 Structural Design Considerations

In general, wind turbine substructures realize their higher structural utilization ratios under long-term limit states that include fatigue, progressive material degradation, progressive surface wear, or accumulated deformation.

For jacket substructures, the critical hotspots are in most of the cases at the welded connection between the members. For the monopile, the grouted joint has been proven very fragile. For the semi-floater, further analyses need to be carried out, but the universal joint at the bottom required great attention.

In case of failure of the joints present in these substructures, monopiles and semi-floaters (for the main floating system) do not offer any redundancy, whereas jackets have some extent of redundancy which can prevent the ultimate collapse of the structure in case of a failure of a member and can waive the necessity of repair. Techniques to repair the monopiles' grouted joint have been developed, but those related to the semi-floaters' universal joints are still to be proposed.

8.3 Robustness with respect to External Conditions

A robust substructure design is one whose engineering performance is insignificantly influenced by a reasonable significant change of external conditions. The robustness is a sought property for these offshore structures, which are subjected to extremely changing conditions.

8.3.1 Sensitivity to Ambient Frequencies

The ambient frequencies that exist around the substructures are the rotor harmonics, the wave frequencies, and the wind turbulence frequencies. Their respective typical ranges are shown in Figure 8.2.

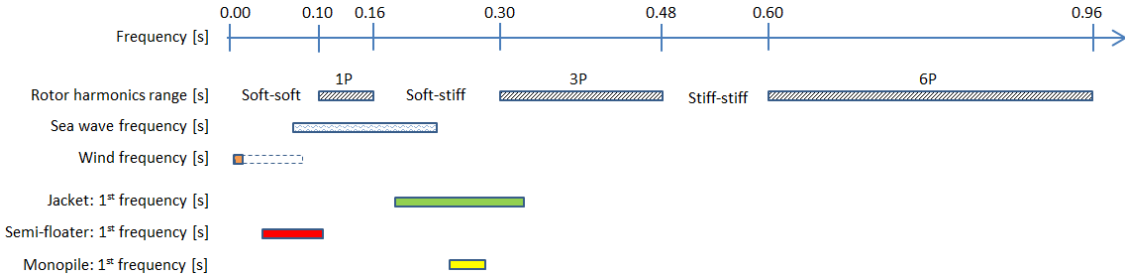

Figure 8.2: Typical ranges for ambient frequencies and natural frequencies related to the various substructures. The rotor harmonics are specific to the DTU 10 MW RWT.

In order to avoid resonance, the support structure's natural frequencies (amongst other components' natural frequencies) should be away from the ambient frequencies. Figure 8.2 depicts the typical ranges of the first support-structure system's natural frequencies associated to each substructure type. The expression 'support-structure system' denotes the support structure with the mass at the tower top. It can be seen that some jacket substructures can have their first natural frequencies coinciding with the 3P rotor harmonics. Proper design [17] can avoid this coincidence or dedicated control strategy (exclusion zone) can limit its influence. Moreover, as a jacket substructure is made of various members, a member can resonate without the whole support structure being excited. This

can be due to the interaction with another component, including the rotor, or with the sea waves. In general, it is advisable to target the soft-stiff regime for the jacket substructure during the design.

The semi-floater is a very compliant substructure which allows low support structure frequencies in the soft-soft regime. Whereas the rotor harmonics can be easily avoided, the effect of the wave frequency should be regarded with some attention. For the monopile, designers are generally successful at avoiding all the ambient frequencies by placing the design within the soft-stiff range.

8.3.2 Sensitivity to Sea

Substructures are to be designed so that they do not have resonant interactions with the sea. Whereas jackets are more transparent to sea loads than monopiles are, the former may be more sensitive to marine growth or corrosion in reason of the smaller size of their members (small diameter and wall thickness). Moreover, attention should be given to the development of diffraction phenomenon with large diameter monopiles.

The situation of semi-floater is more similar to that of large diameter monopiles than it is to the jackets' one. Due to its compliance and to its buoyant systems, the semi-floater will generate less net sea loads. The use of glass fibre material makes the semi-floater better resistant to corrosion.

Depending on the foundation type, the sea-structure-soil interactions can cause seabed scour of various severity levels if adequate protection is not provided.

8.3.3 Sensitivity to Soil and Foundation

The proposed foundation of the semi-floater is a reinforced concrete footing. The foundation for monopile is obviously a pile in continuity to the substructure portion. Jacket substructure can be founded on various foundation types: piles, common or separate suction buckets, common or separate footings.

As the displacements of footings and suction buckets are relatively small, the substructures anchored by them to the seabed are generally less sensitive to the soil-structure interactions. Yet, the designs of these foundation types significantly depend on the soil properties. Some earthworks can be necessary before their installation.

The piles are very sensitive to the soil properties in term of loads, deformations, or damping. Henceforth, their designs should be carefully done with adequate models and suitable modelling parameters. They required less soil preparation for their installation.

8.4 Dashboard

Table 8.1 summarises the key points presented and discussed in this chapter. The comparison does not involve any cost-benefit analysis but only technical criteria.

Table 8.1: Comparison between jacket, semi-floater, and monopile substructures

Criterion	Jacket	Semi-floater	Monopile
Technology readiness	TRL 9	TRL 2	TRL 9
Water depth	Up to 50+ m	Up to 100+ m, with a lower bound that is design specific	Up to 50+ m
Fabrication	Complex process, complicated transition piece	Relatively light process, can benefit from monopile experience	Light process
Transport/Installation	Large volume, light equipment	Light equipment	Moderate volume, heavy equipment
Seabed preparation	Much seabed preparation	Limited seabed preparation	Virtually no seabed preparation
Decommissioning	Relative easy removal, especially with foundations other than piles	Easy removal	Difficult removal
Hotspot	Welded joints	Universal joint	Grouted joint
Limit state	Fatigue	To be determined	Sleeve settlement
Redundancy	Redundant	The floating system has no redundancy, but the multiple mooring lines bring a level of redundancy depending on the failure mode	Not redundant
Natural frequencies	Soft-stiff but can coincide with 3P	Soft-soft	Soft-stiff
Sea loads	Sensitive	Less sensitive	Very sensitive
Marine growth	Very sensitive	Sensitive	Sensitive
Corrosion	Very sensitive	Less Sensitive	Sensitive
Scour	Sensitive	Less sensitive	Very sensitive
Foundation type	Pile, suction bucket, or footing.	Reinforced concrete footing	Pile
Soil type	Less sensitive	Less sensitive	Very sensitive
Soil modelling	Less sensitive	Less sensitive	Very sensitive

9 Conclusion and Recommendations

Even in the busiest kitchen, there's always a point at the end of the day when you go home.

Yotam Ottolenghi

9.1 Summary

The present work aims at the probabilistic design of wind turbine structures. It aims at providing methods for the design of robust multi-megawatt wind turbine structures that are structurally safe and cost-efficient, placed at medium to deep waters. Offshore wind industry faces several challenges. In particular, this work addresses the cost reduction, the problems related to large turbines, the necessary robustness of the structures, and the better insight of the structures' mechanisms. These challenges have been organised in three research areas (reduction of conservatism, fatigue lifetime improvement, and innovative systems) and dealt with based on various structures: shaft, jacket, semi-floater, monopile, grouted joint.

The different analyses and design processes were carried out based on specific environmental conditions and reference structures taken from literature. The environmental conditions covered atmospheric data, sea states conditional to mean wind speed, and soil properties. The reference structures included the INNWIND 10 MW Jacket, the DTU 10 MW Jacket, the DTU 20 MW Jacket, the INNWIND 20 MW RWT, and the DTU 10 MW RWT, which was successively associated to a reference and to an optimized rotor. The second rotor was optimized with the objective to minimize the force-aft fatigue bending damage equivalent bending moments at the tower bottom while limiting the amplitude of the side-side moments. The responses to the research questions posed as objectives of the thesis have been given in the different chapters of this thesis.

9.1.1 Shaft: Extreme and Fatigue Loads

In the first chapter, the shaft of the DTU 10 MW RWT was chosen as the representative of nacelle components. A post-processing method of extreme loads that are to be exchanged between the participants of a design process with better accuracy and lower conservatism level has been introduced. The promoted method is based on the stress-based design format and is in conformity with the selection of extreme loads as the highest average of the peaks as recommended by standards. As a result, this method could reduce by up to about 8 % the extreme loads compared to the traditional load preparation method.

Investigations have been carried out to check how the replacement of a structure can impact the structural integrity of the other structures of the wind turbine. For this, ultimate and fatigue loads have been evaluated with the reference rotor and the optimised rotor, successively mounted on the shaft. Results show that extreme loads are more sensitive to the change of the rotor than fatigue loads. All loads have globally decreased when replacing the reference rotor by the optimized one. Thus, optimizing the rotor can be considered as a technique for fatigue lifetime improvement.

9.1.2 Jacket Substructure: Fatigue Lifetime Improvement

The second chapter introduces or assesses three methods for fatigue lifetime improvement acting on different levels of jacket substructures. The first method consists in reducing stress concentration factors (SCFs) at the welded joints. Based on experimental design, the sensitivities of the SCFs with respect to the geometrical properties of the joints have been computed. Clear guideline rules are established to support designers during the preliminary design phase, the main design phase, or the design updating.

Another method acts at the brace level and involves the use of magneto-rheological (MR) dampers to alleviate the vibrations undergone by the member in which it is a mounted. An installation process is proposed consisting of inserting the damper device in the brace hollow and attaching the MR damper ends to the member joints. Analyses reveal that the MR damper primary alleviates the axial vibrations of the member at an extent that depends to the number of devices and their configurations. Whereas a unique damper was proven inefficient for the DTU 20 MW jacket, a pair of devices mounted in a parallel assemblage is satisfactory for the equipped member but detrimental for the other joints. Therefore, various configurations were designed to mitigate the detriment caused at the other joints. This solution was found successful in general as up to 83 % of fatigue damage could be reduced.

The optimized rotor, which has an impact on the whole structure, is used for fatigue alleviation on the support structure level. The fatigue load reduction at the tower bottom translates to fatigue lifetime improvement at jacket's critical hotspots, where up to 125 % of fatigue lifetime increase can be observed point-wise. Overall, the fatigue lifetime of the jacket extends from 4 years to 7 years.

9.1.3 Semi-floater Substructure: Innovative Substructure System

To circumvent the challenges posed in ensuring a sufficient design fatigue lifetime for jackets, an innovative concept, referred to as semi-floater, is proposed. It is an adaptation of a spar buoy type floater anchored to the soil with a universal joint and supported with mooring lines. Its architecture is described as an assembly of easy-to-manufacture parts and the design process is described as a step-by-step case study. The concept has shown acceptable fatigue load levels and low pitch deflections at mean water level. The reliability of the universal joint is found to satisfy the ultimate design safety requirements.

A possible installation process is also proposed, which can aid practical implementation of the concept. Compared to the two other traditional substructure types, the semi-floater design can be potentially cheaper at moderate water depths because it uses less material, and its installation process requires less effort and has fewer constraints (silent process and moderate size equipment). Furthermore, it may be more competitive than floating structures at water depths in the range 50 m - 100 m, where monopile and jacket designs become highly challenging.

9.1.4 Monopile Substructure: Influences of Model Parameters

On a monopile substructure supporting the DTU 10 MW RWT at 50 m water depth, the influences of model parameters on the engineering performance of monopile design were investigated. Three model parameters were studied: the damping parameter, the geometric imperfections, and the soil stiffness. Varying the design values for overall structural logarithmic decrement damping between its typical values and more likely values has shown that substantial material savings can be realized if more appropriate damping values are used.

As the geometric imperfections increases the SCFs at the welded connections and thereby increases the hotspot stresses, analyses demonstrate that a careful fabrication would result in material savings and careless fabrication can be detrimental to the structural integrity of the design. It is concluded that mass reduction can be achieved by setting tight manufacturing tolerances and attention should be given during the fabrication to respect the manufacturing tolerances set as design hypotheses.

A soil-structure interaction model devised for arbitrary monopile dimensions is compared against the model recommended by the standards. It is seen that the standard model is very conservative, thus the usage of the advanced model facilitates mass reduction. However, it is underlined that the monopile design should be robust enough to handle the interactions between the soil-structure interaction and the welded connections. By selecting an inappropriate soil model, the fatigue demand could be exacerbated at misplaced hotspots.

9.1.5 Conical Grouted Joint: Insight of Structural Mechanism

The grouted joint, a monopile sensitive structure, has been studied in detail using the finite element method. The grouted joint of conical shape has been investigated under normal conditions and under extreme events. It is found that the wall thicknesses of both the transition piece and the pile have a significant impact on the grout degradation, on the grout fatigue, and on the progressive settlement. Namely, the larger are the wall thicknesses, the more vulnerable the grout is with respect to fatigue and material degradation, but the more limited the progressive settlement is, and vice versa. This implies that the appropriate wall thicknesses should be chosen by designers having in mind that neither extreme is conservative. The grout length is found to be the most influential parameter of the settlement caused by extreme loadings: longer grout significantly contributes to the reduction of extreme settlement. In order to ensure that the inevitable vertical displacement does not jeopardize the structural integrity of the grouted joint, a probability based method has been developed to estimate the minimal gap between the pile top and the brackets required to achieve a targeted annual reliability index of 3.3.

9.1.6 Comparative Analysis: Jacket versus Semi-floater versus Monopile

A comparative analysis between the three different substructures studied in this thesis is carried out. After a technological description of the substructure concepts, the comparison is made in terms of

structural design considerations and robustness with respect to external conditions. A table summarising the comparison is drawn as a dashboard to guide designers at the preliminary phase of projects.

9.2 Contributions

At the end of this study, the principal contributions can be listed as follows.

Format for load exchange. A preparative method of loads to be exchanged between the different stakeholders of a complex design process is introduced. This method aims at reducing the level of conservatism and follows the stress calculation while being in line with standards' recommendations.

Improvement of fatigue lifetime. Three methods for fatigue lifetime improvement have been developed for jacket substructures. The first focuses on the joint design methodology. Clear guideline rules have been established to help designers to reduce SCFs at joints. They are intended to be utilized to initialize designs for advanced design procedure like optimization, to carry out designs by the traditional trial-and-error techniques, or to update unsatisfactory designs generated by an advanced design procedure. The second intends to reduce the vibration of braces based on the application of magneto-rheological dampers. Modelling methods and effectiveness are presented together with installation steps. The third employs an aeroelastically tailored rotor to alleviate fatigue loads on the support structure. The effectiveness of this technique has been shown for the jacket substructures. Whereas the rotor optimization process was not done within the present study, its effect on the substructure is one of this work's results.

Semi-floater: Design methods. The semi-floater concept has been introduced by previous studies. In this work, the detailed design of the universal joint has been proposed together with the installation process of the substructure. A design process of such substructure type has been presented along side with an algorithm to design mooring line at the preliminary phase.

Monopile: Influence of model parameters. The individual influences of some key model parameters (damping, construction errors, soil) and their interaction have been quantified in a comparative manner. It has been established for example that the soil-structure interactions can interact with the construction errors to amplify the fatigue demand at some hotspots of the monopile.

Grouted joint: Mechanism and role of the geometric parameters. The steel wall thickness has been proven determinant for the grout degradation and fatigue, and thereby for the progressive settlement of the transition piece. It has been established that there is non-monotonic dependence between the wall thickness and the joint performance. The advantage of higher conical angles on the progressive settlement of the transition piece has also been clearly shown. It has been found that longer grouts prevent higher extreme vertical displacement of the transition piece. A probabilistic design approach based on finite element model has been developed. In order to reduce the expensive analysis of the joint, a method based on load criteria is proposed and the adapted reliability analysis process is explained.

9.3 Recommendations for future developments

Notwithstanding the sound results, there are some aspects of the thesis' topic that requires further attention.

Effect of rotor change. By replacing the reference rotor by the tailored one, the shaft, selected as the representative of the nacelle components, has been proven less loaded. This is not guaranteed for the other components. For example, bearings or gearboxes can suffer from the additional weight of the tailored rotor, which induces a constant force and moment. To fully establish the safeness of the new rotor further verifications are needed.

Interaction between SCFs and the nominal stresses. Guidelines to reduce the SCFs at welded tubular joints are established as geometrical modification rules of the design. The modifications may also impact the nominal stresses, unless joint corrections are solely made on the chord. In case the nominal stresses will be altered, further investigations will be required to determine how the interaction between SCF reduction and the change of the nominal stresses influences the hotspot stresses.

Improved modelling of MR dampers. The MR damper mainly acts by exerting resisting force at the brace ends. The model developed during this application only accounts for this primary contribution. However, the mass of the damper significantly changes the local mass of the jacket. In addition, it can be expected that construction errors, for example, may alter the efficiency of the MR damper. It is necessary to develop a higher fidelity model that accounts for the mass change of the brace and the robustness of the MR damper. Moreover, as the efficiency of MR dampers is related to some extent to the configurations they are mounted in, systematic methods to select smart configurations can be developed.

Superposition of the fatigue mitigation techniques. Three fatigue alleviation techniques applicable at various levels of the structure have been studied, each with different efficiencies. The said techniques can readily be applied on the same structure. It will be interesting to investigate how efficient the superposition of their effect will be.

Advanced design of the semi-floater. The semi-floater concept is still at its early development phase. Detailed studies on the structural design of the glass fibre buoyancy chamber and steel cylinder can be carried out. The manufacturing of the buoyancy chamber and its connection procedure to the cylinder can be considered. It is probable that there is a great potential of conservatism reduction by selecting a better pattern of mooring lines for example.

Larger design load basis. During the investigations carried out on the structures, an excerpt of the design load basis has been used to demonstrate the methods. However, it is not excluded that some critical events will rise up under the design load cases not considered. Therefore, further attention can be given to the better cover of the design load basis as recommended by standards [66], [39].

Quantification of the gain. Several solutions for conservatism reduction have been investigated here. The gain in term of mass saved has not been clearly evaluated. This could be devoted to a future study. In particular, the mass reduction of monopile substructures can be assessed under a set of parameter values that reduce the conservatism. For example, the effect of the combination of measured damping values, careful manufacturing, and adequate soil model can be checked.

Grouted joint. The long-term behaviour of the conical grouted joint under normal conditions has been verified under *deterministic* considerations. As already done for fatigue analysis of shear-keyed cylindrical grouted joints [67], other investigations can focus on the probabilistic assessment of these limit states of conical grouted joint. Similarly, corrosion assessment can also be investigated for conical joints as already studied for shear-keyed cylindrical grouted joints [67]. Finally, what could be the effect of shear keys on a conical grouted joint?

APPENDICES

Appendix A: Superelement Representing the INNWIND 10 MW Jacket Substructure

The matrices are derived for the connection between the tower and the transition piece at 26 m above the mean sea level. There are taken from the reference [A.1]. The coordinates system is such that:

- the x-axis faces the wind stream, say the North;
- the y-axis points to the West; and
- the z-axis is directed upwards.

!Mass matrix (units kg, kgm, kgm2)

Deflection X	Deflection Y	Deflection Z	Rotation X	Rotation Y	Rotation Z
1.35E+06	-2.92E+00	-7.99E+02	1.36E+04	-1.58E+07	-2.51E+04
-2.92E+00	1.35E+06	-5.50E+02	1.58E+07	1.37E+04	3.75E+04
-7.99E+02	-5.50E+02	9.86E+05	7.68E+03	-1.39E+04	-2.41E+04
1.36E+04	1.58E+07	7.68E+03	2.38E+08	1.02E+03	5.18E+05
-1.58E+07	1.37E+04	-1.39E+04	1.02E+03	2.38E+08	3.83E+05
-2.51E+04	3.75E+04	-2.41E+04	5.18E+05	3.83E+05	8.34E+07

!Stiffness matrix (units N/m, N, Nm)

Deflection X	Deflection Y	Deflection Z	Rotation X	Rotation Y	Rotation Z
1.05E+08	-1.12E-01	-2.75E-02	8.53E+05	-1.83E+09	-1.18E-02
-1.12E-01	1.05E+08	-1.06E-03	1.83E+09	8.53E+05	1.01E+01
-2.75E-02	-1.06E-03	1.74E+09	-2.13E-02	6.74E-01	-3.48E+06
8.53E+05	1.83E+09	-2.13E-02	1.95E+11	1.09E+01	1.98E+02
-1.83E+09	8.53E+05	6.74E-01	1.09E+01	1.95E+11	3.71E-01
-1.18E-02	1.01E+01	-3.48E+06	1.98E+02	3.71E-01	3.20E+10

!Damping matrix (units kg/s, kgm/s, kgm2/s)

Deflection X	Deflection Y	Deflection Z	Rotation X	Rotation Y	Rotation Z
1.39E+05	-4.16E-02	-1.14E+01	1.17E+03	-2.32E+06	-3.57E+02
-4.16E-02	1.39E+05	-7.82E+00	2.32E+06	1.17E+03	5.34E+02
-1.14E+01	-7.82E+00	2.00E+06	1.09E+02	-1.97E+02	-4.31E+03
1.17E+03	2.32E+06	1.09E+02	2.26E+08	1.45E+01	7.37E+03
-2.32E+06	1.17E+03	-1.97E+02	1.45E+01	2.26E+08	5.45E+03
-3.57E+02	5.34E+02	-4.31E+03	7.37E+03	5.45E+03	3.76E+07

Bibliography:

[A.1] T. von Borstel. Design Report - Reference Jacket (INNWIND.EU Deliverable 4.3.1). Technical report, Ramboll, 2013. http://www.innwind.eu/-/media/Sites/innwind/Publications/Deliverables/DeliverableD4-31_20131030_INNWIND-EU.ashx?la=da.

Appendix B: Pile Ovalization and Resulting Stress Determination

Let us consider a unit length pile of outer diameter D and wall thickness t, undergoing a lateral displacement y. The surrounding soil exerts on the pile a horizontal force $p(y)$ collinear to the displacement but in the opposite direction (Figure B.1a). At a cross sectional level, the pile shell is subjected to a distributed force whose resultant is equivalent to the force $p(y)$, as Figure B.1b illustrates.

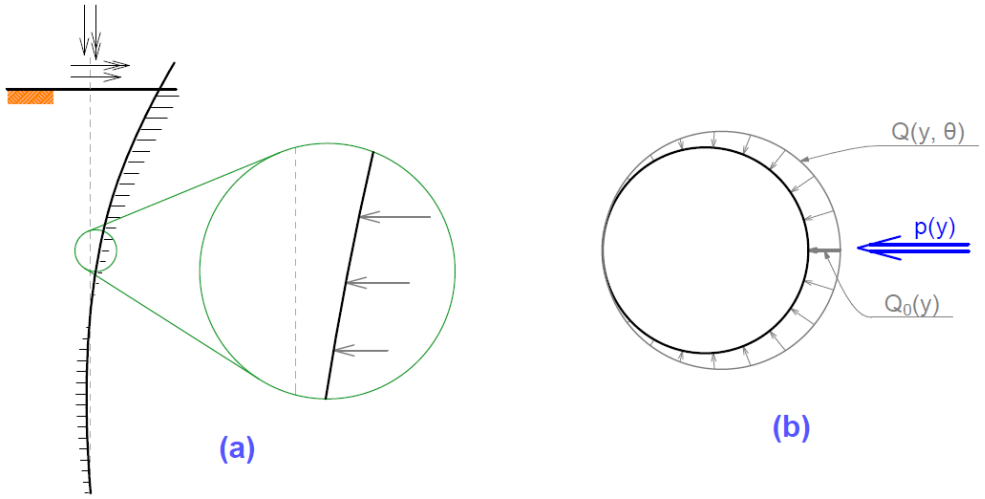

Figure B.1. Soil lateral force on the pile. (a) Distributed force along the pile axis. (b) Distributed force around the pile circumference.

The following expressions can be written as geometrical description of the pile section (Figure B.2):

Outer diameter [m]	D	Wall thickness [m]	t
Outer radius [m]	$R = D/2$	Mid-layer radius [m]	$\rho = R - t/2$
Inner diameter [m]	$d = D - 2t$	Inner radius [m]	$r = d/2$

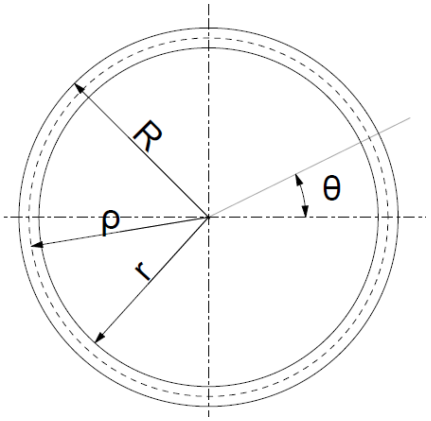

Figure B.2. Section geometry.

$p(y=0)=0$ means that there is no force exerted on the shell by the soil when the pile is at the initial position. For a given displacement y, the surrounding soil resists at the pile front with maximum amplitude, and no soil force is applied at the trail: the distributed force gradually decreases from a maximum at the pile front to zero at pile trail. Scharff et Siems [B.1] has indicated that the soil force distribution follows a [co]sine shape. Therefore, the distributed force around the shell can be expressed as:

$$Q(y,\theta)=Q_0(y)\frac{1+\cos\theta}{2} \tag{B.1}$$

where θ is the position of a point on the shell measured from the displacement axis such that $\theta=0$ is the pile front (Figure B.2). The equivalence between the distributed force around the shell and the total lateral force is expressed as:

$$\begin{aligned}\int_0^{2\pi} Q(y,\theta)\cos\theta\, Rd\theta &= \frac{Q_0(y)}{2}R\int_0^{2\pi}(1+\cos\theta)\cos\theta\, d\theta = p(y)\\ \int_0^{2\pi} Q(y,\theta)\sin\theta\, Rd\theta &= \frac{Q_0(y)}{2}R\int_0^{2\pi}(1+\cos\theta)\sin\theta\, d\theta = 0\end{aligned} \tag{B.2}$$

which gives $Q_0(y)=2p(y)/(\pi R)$

Under thin shell assumption, the shell stresses consist of hoop stress and radial stress. Due to symmetry about the displacement axis, only one half of the shell will be considered later on.

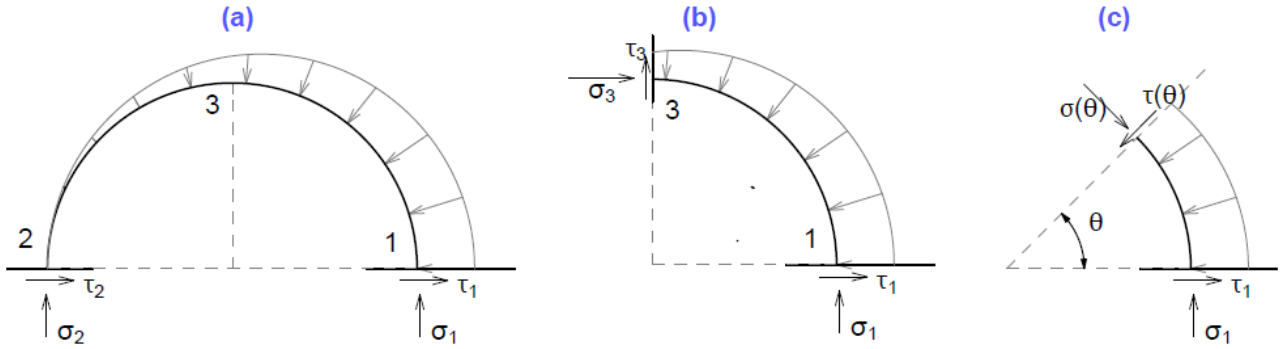

Figure B.3. Induced stresses in pile shell due to surrounding soil.

The equilibrium of the half section (Figure B.3a) requires:

$$\begin{aligned}\sigma_1 t+\sigma_2 t &= R\int_0^{\pi} Q(y,\theta)\sin\theta\, d\theta\\ \tau_1 t+\tau_2 t &= \frac{p(y)}{2}\\ 2\rho\sigma_1 t &= R\rho\int_0^{\pi} Q(y,\theta)\sin\theta\, d\theta\end{aligned} \tag{B.3}$$

And the equilibrium of the quarter section (Figure B.3b) needs:

$$\rho\sigma_1 t + \rho\tau_1 t = R\rho \int_0^{\pi/2} Q(y,\theta)\cos\theta \, d\theta \tag{B.4}$$

The simultaneous solution of Equations (B.3) and (B.4) for the circumferential stresses σ_1 and σ_2 and the radial stresses τ_1 and τ_1 at the section axis gives: $\sigma_1 = \sigma_2 = p(y)/(\pi t)$ and $\tau_1 = \tau_2 = p(y)/(4t)$.

From Figure B.3c, the circumferential compressive stress and the radial shear stress around the shell is determined as:

$$\sigma'(\theta) = \frac{p(y)}{4\pi t}[4 - (\pi - 2\theta)sin\theta]$$
$$\tau'(\theta) = \frac{p(y)}{4\pi t}[(\pi - 2\theta)cos\theta - 2sin\theta] \tag{B.5}$$

The plot of the stresses can be seen on Figure B.4. The shear stress distribution gives an idea of the shell ovalization. Indeed, Figure B.4b shows an inward shear stress in the vicinity of the front-trail line, which denotes a flattening, and an outward shear stress at Point 3, which denotes a bump shape.

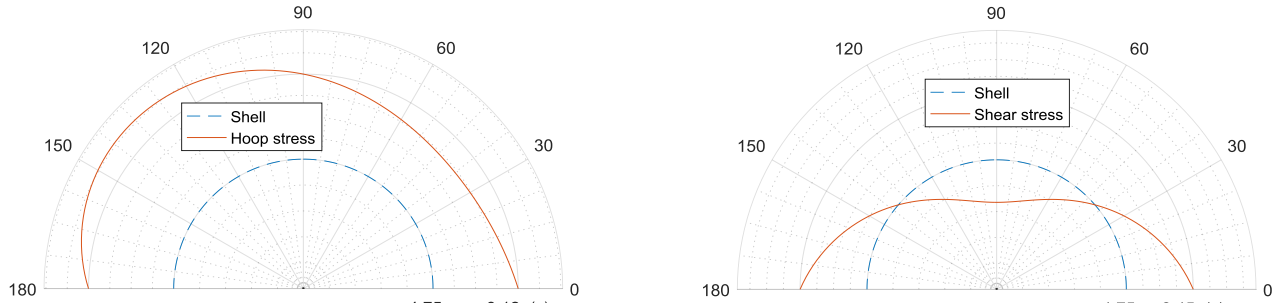

Figure B.4. Shell stresses due to soil external pressure. (a) Compressive hoop stress. (b) Radial shear stress.

Bibliography:

[B.1] Scharff R, Siems M. Pushing the limits – mega monopile foundations for offshore wind turbines. Steel Construction 6 No 3; 2013b.

Appendix C: Stress Concentration Factors for Simple Tubular Joints

Based on Efthymiou's equations [C.1], DNV-RP-C203 [C.2] recommends a series of expressions for the estimation of the stress concentration factors (SCFs) for simple tubular joints used in fatigue analysis.

i. Joint parameterization

The said expressions have been derived for geometrically non-dimensional joints in order to be generalised. However, their usage is restricted within the valid ranges of the non-dimensional geometrical parameters defined in Figures C.1 and C.2. The valid ranges are:

$$0.2 \le \beta \le 1.0 \qquad 0.2 \le \tau \le 1.0 \qquad 8.0 \le \gamma \le 32.0$$

$$4.0 \le \alpha \le 40.0 \qquad 20.0° \le \theta \le 90.0° \qquad -0.6\beta/\sin\theta \le \zeta \le 1.0$$

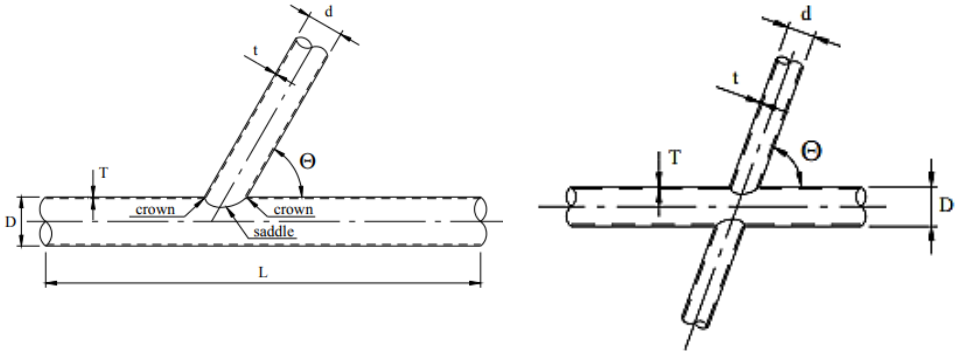

$$\beta = \frac{d}{D}$$

$$\tau = \frac{t}{T}$$

$$\gamma = \frac{D}{2T}$$

$$\alpha = \frac{2L}{D}$$

Figure C.1. Definition of geometrical parameters forY- and X-joints [C.2].

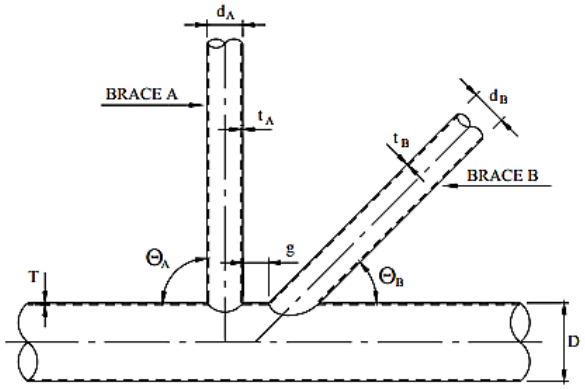

$$\beta_A = \frac{d_A}{D} \qquad \beta_B = \frac{d_B}{D}$$

$$\tau_A = \frac{t_A}{T} \qquad \tau_B = \frac{t_B}{T}$$

$$\gamma = \frac{D}{2T} \qquad \zeta = \frac{g}{D}$$

$$\alpha = \frac{2L}{D}$$

Figure C.2. Definition of geometrical parameters for K-joints [C.2].

ii. Stress Concentration Factors for K-Joints[C.2]

Load type and fixity conditions	*Expressions*	*No.*
Balanced axial loads 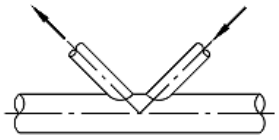	***Chord*** $$\tau^{0.9}\gamma^{0.5}(0.67-\beta^2+1.16\beta)\sin\theta\left(\frac{\sin\theta_{max}}{\sin\theta_{min}}\right)^{0.30}\left(\frac{\beta_{max}}{\beta_{min}}\right)^{0.30}\times\left(1.64+0.29\beta^{-0.38}\tan^{-1}(8\zeta)\right)$$ ***Brace*** $$1+(1.97-1.57\beta^{0.25})\tau^{-0.14}(\sin\theta)^{0.7}(\text{Eqn. }09)+\sin^{1.8}(\theta_{max}+\theta_{min})\left(0.131-0.084\tan^{-1}(14\zeta+4.2\beta)\right)C\beta^{1.5}\gamma^{0.5}\tau^{-1.22}$$ Where: C = 0.0 for gap joints C = 1.0 for the through brace C = 0.5 for the overlapping brace Note that τ, β, θ, and the nominal stress relate to the brace under consideration. $\tan^{-1}(\cdot)$ is arctangent evaluated in radians.	(01) (02)
Unbalanced in-plane bending 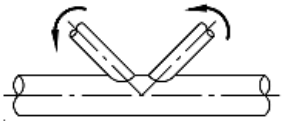	***Chord crown*** $$1.45\beta\tau^{0.85}\gamma^{(1-0.68\beta)}(\sin\theta)^{0.7}$$ (for overlaps exceeding 30% of contact length use 1.2 (Eqn. 03)) ***Gap joint brace crown*** $$1+0.65\beta\tau^{0.4}\gamma^{(1.09-0.77\beta)}(\sin\theta)^{(0.06\gamma-1.16)}$$ (for overlaps, use $(0.9+0.4\beta)(\text{Eqn. }04)$)	(03) (04)
Unbalanced out-of-plane bending 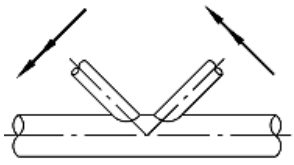	$$\gamma\tau\beta(1.7-1.05\beta^3)(\sin\theta)^{1.6}$$ ***Chord saddle SCF adjacent to brace A*** $$(\text{Eqn. }05)_A(1-0.08(\beta_B\gamma)^{0.5}\exp(-0.8x))+$$ $$+(\text{Eqn. }05)_B(1-0.08(\beta_A\gamma)^{0.5}\exp(-0.8x))(2.05\beta_{max}^{0.5}\exp(-1.3x))$$ Where $$x=1+\frac{\zeta\sin\theta_A}{\beta_A}$$ ***Brace A saddle SCF*** $$\tau^{-0.54}\gamma^{-0.05}(0.99-0.47\beta+0.08\beta^4)(\text{Eqn. }06)$$ For short chord, Eqn. 06 and Eqn. 07 are corrected with the factor $F1$ $$F1=1-1.07\beta^{1.88}\exp(-0.16\gamma^{-1.06}\alpha^{2.4})$$ $(\text{Eqn. }05)_A$ is the chord SCF adjacent to brace A as estimated from $(\text{Eqn. }05)$. Note that the designation of braces A and B is not geometry dependent. It is nominated by the user.	(05) (06) (07)

iii. Stress Concentration Factors for X-Joints[C.2]

Load type and fixity conditions	*Expressions*	*No.*
Axial load (balanced) 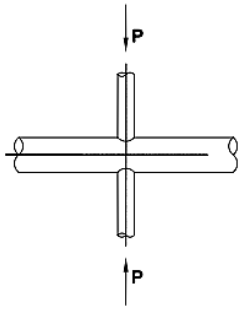 	***Chord saddle*** $3.87\gamma\tau\beta(1.10-\beta^{1.8})(\sin\theta)^{1.7}$ ***Chord crown*** $\gamma^{0.2}\tau\,(2.65+5\,(\beta-0.65)^2)-3\tau\beta\sin\theta$ ***Brace saddle*** $1+1.9\gamma\tau^{0.5}\beta^{0.9}(1.09-\beta^{1.7})(\sin\theta)^{2.5}$ ***Brace crown*** $3+\gamma^{1.2}(0.12\exp(-4\beta)+0.011\beta^2-0.045)$ In joints with short chords ($\alpha<12$), the saddle SCF can be reduced by the factor $F2$ (fixed chord ends) or $F3$ (pinned chord ends) where: $F2=1-(0.83\beta-0.56\beta^2-0.02)\gamma^{0.23}\exp(-0.21\gamma^{-1.16}\alpha^{2.5})$ $F3=1-(1.43\beta-0.97\beta^2-0.03)\gamma^{0.04}\exp(-0.71\gamma^{-1.38}\alpha^{2.5})$	(08) (09) (10) (11)
In-plane bending 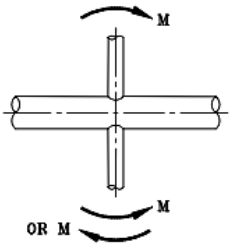 	***Chord crown*** $1.4\beta\tau^{0.85}\gamma^{(1-0.68\beta)}(\sin\theta)^{0.7}$ ***Brace crown*** $1+0.65\beta\tau^{0.64}\gamma^{(1.09-0.77\beta)}(\sin\theta)^{(0.06\gamma-1.16)}$	(12) (13)
Out-of-plane bending (balanced) 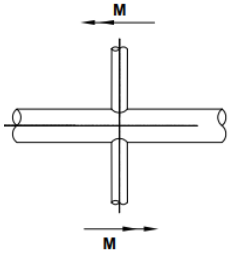 	***Chord saddle*** $\gamma\tau\beta(1.56-1.34\beta^4)(\sin\theta)^{1.6}$ ***Brace saddle*** $\tau^{-0.54}\gamma^{-0.05}(0.99-0.47\beta+0.08\beta^4)(\text{Eqn. }14)$ In joints with short chords ($\alpha<12$), Eqns. (14) and (15) can be reduced by the factor $F4$ where: $F4=1-0.55\beta^{1.8}\gamma^{0.16}\exp(-0.49\gamma^{-0.89}\alpha^{1.8})$	(14) (15)

iv. Stress Concentration Factors for Y-Joints[C.2]

Load type and fixity conditions	*Expressions*	*No.*
Axial loads – Chord ends fixed 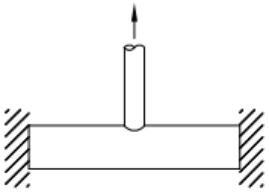	***Chord saddle*** $$\gamma\tau^{1.1}(1.11-3(\beta-0.52)^2)(\sin\theta)^{1.36}$$	(16)
	Chord crown $$\gamma^{0.2}\tau(2.65+5(\beta-0.65)^2)+\tau(0.25\alpha-3)\sin\theta$$	(17)
	Brace saddle $$1.3+\gamma\tau^{0.52}\alpha^{0.1}(0.187-1.25\beta^{1.1}(\beta-0.96))(\sin\theta)^{(2.7-0.01\alpha)}$$	(18)
	Brace crown $$3+\gamma^{1.2}\left(0.12e^{-4\beta}+0.011\beta^2-0.045\right)+\beta\tau(0.1\alpha-1.2)$$	(19)
	In joints with short chords ($\alpha<12$), the saddle SCFs should be reduced by the factor $F2$.	
Axial loads – General fixity conditions 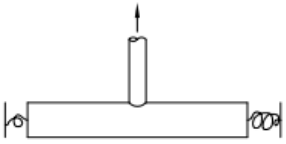	***Chord saddle*** $$(\text{Eqn. } 16)+C_1(0.8\alpha-6)\tau\beta^2(1-\beta^2)^{0.5}(\sin 2\theta)^2$$	(20)
	Chord crown $$\gamma^{0.2}\tau(2.65+5(\beta-0.65)^2)+\tau\beta(C_2\alpha-3)\sin\theta$$	(21)
	Brace saddle $$1.3+\gamma\tau^{0.52}\alpha^{0.1}(0.187-1.25\beta^{1.1}(\beta-0.96))(\sin\theta)^{(2.7-0.01\alpha)}$$	(22)
	Brace crown $$3+\gamma^{1.2}\left(0.12e^{-4\beta}+0.011\beta^2-0.045\right)+\beta\tau(C_3\alpha-1.2)$$	(23)
	In joints with short chords ($\alpha<12$), the saddle SCFs should be reduced by the factor $F3$.	
	The chord end fixity parameter: $0.5\le C\le 1.0$. Typically $C=0.7$ $C_1=2(C-0.5)$ $C_2=C/2$ $C_3=C/5$	
In-plane bending 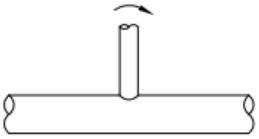	***Chord crown*** $$1.45\beta\tau^{0.85}\gamma^{(1-0.68\beta)}(\sin\theta)^{0.7}$$	(24)
	Gap joint brace crown $$1+0.65\beta\tau^{0.4}\gamma^{(1.09-0.77\beta)}(\sin\theta)^{(0.06\gamma-1.16)}$$	(25)
Out-of-plane bending 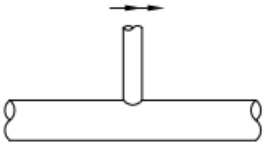	***Chord saddle*** $$\gamma\tau\beta(1.7-1.05\beta^3)(\sin\theta)^{1.6}$$	(26)
	Brace saddle $$\tau^{-0.54}\gamma^{-0.05}(0.99-0.47\beta+0.08\beta^4)(\text{Eqn. } 26)$$	(27)
	For short chord, Eqn. 26 and Eqn. 27 are corrected with the factor $F1$	

Bibliography:

[C.1] Efthymiou M. Development of SCF formulae and generalised influence functions for use in fatigue analysis. OTC'88: Proceedings of the Conference OTJ'88 on Recent Developments in Tubular Joints Technology. Surrey, UK; 1988.

[C.2] Det Norske Veritas. Fatigue design of offshore steel structures. Recommended practice DNV-RP-C203, Det Norske Veritas, 2011.

Appendix D: Authorship Statement

The aim of this appendix is to clearly distinguish between the work done by the thesis' author and the others' contributions. The distribution of the contributions is presented for each chapter of the thesis. The thesis' author is later referred to simply as 'the author'.

i. Definition of the Design Parameter Sets

The environment conditions used in this thesis are taken or adapted from Ref [D.1], which originates from Ref [D.2]. The reference wind turbine of 10 MW (DTU 10 MW RWT) is designed by Ref [D.3] and the HAWC2 digital model is available for download at Ref [D.4].

ii. Shaft: Extreme and Fatigue Loads

The tower of the HAWC2 digital model of DTU 10 MW RWT has been shortened by the author and placed on a superelement representing the support structure (See Appendix A). Based on its properties given by Ref [D.1], the superelement has been digitalized by the author using a pre-processing tool developed within the HAWC2 family. The aero-servo-elastic simulations have been carried out by the author. The technical solutions and the post-processing codes have been developed by the author.

iii. Jacket Substructure: Fatigue Lifetime Improvement

Three fatigue lifetime improvement techniques are explored in the thesis: efficient joint design, use of magneto-rheological damper, and optimization of the rotor blades. The author has written and run all the MATLAB scripts required for post-processing the simulation results.

For the first technique, the author has developed the technical solution and implemented it using MATLAB scripts written by him. This study uses a jacket that has been developed by Ref [D.5] (with minor contributions of the author), and that served as support structure of DTU 10 MW RWT [D.3]. The digital model and the aero-hydro-servo-elastic simulations have been carried out by the author.

The second technique is demonstrated on a 20 MW wind system. The 20 MW wind turbine (rotor, nacelle, and tower) has been designed by Ref [D.6]. The digital model and the controller tuning have been done by the author. The 20 MW jacket has been upscaled from the 10 MW jacket [D.5] by the author. The magneto-rheological damper has been designed by Ref [D.7] and its digital model has been built by the author. The full setups and the aero-hydro-servo-elastic simulations have been carried out by the author.

The optimized rotor blade used to demonstrate the third technique has been designed by Ref [D.8] (with minor contributions of the author) and the jacket data has been taken from Ref [D.9]. The aero-hydro-servo-elastic simulations have been carried out by the author.

iv. Semi-floater Substructure: Innovative Substructure System

Starting from an existing digital model of DTU 10 MW RWT on a semi-floater, the author has prepared the final digital model of the wind system used in this thesis. From the existing model to the final model, the universal joint model and the design of the mooring lines have been changed:

- In the existing model, the universal joint was modeled as a flexible beam. The author has designed the universal joint in detail using an ABAQUS finite element model, from which data has been extracted to prepare a superelement which has been used as universal joint model in aero-hydro-servo-elastic simulations. The final design of the universal joint has required modifications of the initial floating-cylinder and ballast designs.
- An algorithm for preliminary design of catenary lines is proposed by the author. Based on this algorithm, the author has obtained a new mooring-line design, which differs from that of the existing model.

The author has run the batch simulation and has developed & run MATLAB scripts to post-process the results.

v. Monopile Substructure: Influences of Modelling Parameters

Based on the digital model of DTU 10 MW RWT downloaded from Ref [D.4], the author has added the monopile substructure after having shortened the tower. Subsequently, the author has run the aero-hydro-servo-elastic simulations with soil boundary conditions, and developed & run MATLAB scripts for monopile structural design. The soil-structure interaction models have been taken from Ref [D.10]. The stresses resulting from pile ovalization as presented in Appendix B has been derived by the author.

vi. Conical Grouted joint: Insight of Mechanical Behavior

Based on the digital model of DTU 10 MW RWT downloaded from Ref [D.4], the author has added the monopile substructure after having shortened the tower. Subsequently, the author has run the aero-hydro-servo-elastic model, developed & run MATLAB scripts coupled with ABAQUS for finite element analyses of the grouted joint, run the batch simulations, and post-processed the results for the normal conditions and the extreme events.

vii. Comparative Analysis: Jacket versus Semi-floater versus Monopile

The comparative analysis has been done by the author.

Bibliography:

[D.1] T. von Borstel. Design Report - Reference Jacket (INNWIND.EU Deliverable 4.3.1). Technical report, Ramboll, 2013. http://www.innwind.eu/-/media/Sites/innwind/Publications/Deliverables/DeliverableD4-31_20131030_INNWIND-EU.ashx?la=da.

[D.2] T. Fisher, W. de Vries, and B. Schmidt. Upwind Design Basis (WP4: Offshore Foundations and Support Structures). Technical report, Endowed Chair of Wind Energy (SWE) at the Institute of Aircraft Design, Universität Stuttgart, 2010.

[D.3] C. Bak, F. Zahle, R. Bitsche, T. Kim, A. Yde, L. C. Henriksen, P. B. Andersen, A. Natarajan, and M. H. Hansen. Description of the DTU 10 MW reference wind turbine (INNWIND.EU Deliverable 1.2.1). Technical report, Technical University of Denmark, DTU Wind Energy, 2013.

[D.4] http://www.hawc2.dk/download/hawc2-model. Accessed on January 20, 2018.

[D.5] M. Stolpe, W. Njomo Wandji, and A. Natarajan. Modularized jacket design. In Innovative design of a 10MW steel-type jacket (INNWIND.EU Deliverable 4.3.4), pages 31 – 42. 2016.

[D.6] P. Chaviaropoulos and A. Milidis. 20 MW Reference Wind Turbine - Aeroelastic data of the onshore version (INNWIND.EU Deliverable 1.2.5(a)). Technical report, National Technical University of Athens, 2016.

[D.7] G. Yang, Jr. B. F. Spencer, H.-J. Jung, and J. D. Carlson. Dynamic Modeling of Large-Scale Magnetorheological Damper Systems for Civil Engineering Applications. Journal of Engineering Mechanics, 130 (9):1107–1114, 2004.

[D.8] W. Njomo Wandji, C. Pavese, A. Natarajan, and F. Zahle. Reduction of fatigue loads on jacket substructure through blade design optimization for multi-megawatt wind turbines at 50 m water depths. Journal of Physics: Conference Series, 753(042022), 2016.

[D.9] T. von Borstel. Design Report - Reference Jacket (INNWIND.EU Deliverable 4.3.1). Technical report, Ramboll, 2013.

[D.10] K. Thieken, M. Achmus, and K. Lemke. A new static p-y approach for piles with arbitrary dimensions in sand. Geotechnik, 38 No 4:267–288, 2015.

Bibliography

[1] U.S. Energy Information Administration. Monthly Energy Review - September 2017. Report, U.S. Department of Energy, 2017.

[2] Nordic Energy Research. Nordic Energy Technology Perspectives 2016 - Cities, flexibility and pathways to carbon-neutrality. Technical report, Nordic Energy Research, 2016.

[3] M. R. Loos, C. R. O. Loos, D. L. Feke, I. Manas-Zloczwer, U. Younes, S. Unal, P. Emrich, F. Bradish, and R. Sesco. World's first carbon nanotube reinforced polyurethane wind blades. https://engineering.case.edu/emac/news/Carbon-Nanotube-Reinforced. Accessed: 01 Nov 2017.

[4] D. Kallehave, B. W. Byrne, C. LeBlanc Thilsted, and K. K. Mikkelsen. Optimization of monopiles for offshore wind turbines. *Phil. Trans. R. Soc*, A 373:1–15, 2015.

[5] T. Chaviaropoulos. Costs models v1.02.1 mar 2016-10mw rwt. https://share.dtu.dk/sites/, 2017.

[6] International Renewable Energy Agency IRENA. Renewable energy technologies: cost analysis series - Wind power. Working paper, International Renewable Energy Agency, 2012.

[7] P. Dallyn, A. El-Hamalawi, A. Palmeri, and R. Knight. Experimental testing of grouted connections for offshore substructures: A critical review. *Structures*, 3:90–108, 2015.

[8] I. Lotsberg. Structural mechanics for design of grouted connections in monopile wind turbine structures. *Marine Structures*, 32:113–135, 2013.

[9] P. Schaumann, S. Lochte-Holtgreven, and R. Eichstadt. Numerical investigation on local degradation and vertical misalignment of grouted joint in monopile foundations. Anchorage, Alaska, USA, 2013. International Society of Offshore and Polar Engineers (ISOPE).

[10] Y.-S. Lee, B.-L. Choi, J. H. Lee, S. Y. Kim, and S. Han. Reliability-based design optimization of monopile transition piece for offshore wind turbine system. *Renewable Energy*, 71:729–741, 2014.

[11] KidWind Project (www.kidwind.org). http://slideplayer.com/slide/4329877/, 2017. Accessed: 04 Aug 2017.

[12] W. Njomo Wandji, C. Pavese, A. Natarajan, and F. Zahle. Reduction of fatigue loads on jacket substructure through blade design optimization for multi-megawatt wind turbines at 50 m water depths. *Journal of Physics: Conference Series*, 753(042022), 2016.

[13] T. von Borstel. Design Report - Reference Jacket (INNWIND.EU Deliverable 4.3.1). Technical report, Ramboll, 2013.

[14] K. Sandal. *Design optimization of jacket structures for mass production*. PhD thesis, Technical University of Denmark, 2017.

[15] J. Oest, K. Sandal, S. Schafhirt, Stieng L. E. S., and M. Muskulus. Comparison of fatigue constraints in optimal design of jacket structures for offshore wind turbines. 12th World Congress of Structural and Multidisciplinary Optimisation (WCSMO12), 2017.

[16] P. Haselbach, A. Natarajan, R. G. Jiwinangun, and K. Branner. Comparison of coupled and uncoupled load simulations on a jacket support structure. *Energy Procedia*, 35, 2013.

[17] A. Natarajan, M. Stolpe, and W. Njomo Wandji. Optimal Design of Jacket Type substructure for 10 MW Offshore Wind Turbines. *Renewable Energy*, 2017. To be submitted.

[18] N. Scholle, L. Radulović, R. Nijssen, L. B. Ibsen, M. Kohlmeier, A. Foglia, J. Thiel, B. Kuhnle, and D. Kaufer. Innovations on component level (final report)). Technical report, 2016.

[19] C. M. Wang, T. Utsunomiya, S. C. Wee, and Y. S. Choo. Research on floating wind turbines: a literature survey. *The IES Journal Part A: Civil & Structural Engineering*, 3:4:267–277, 2010.

[20] F. Sedillot and A. Stevenson. Laminated rubber articulated joint for the deep water gravity tower. *Transactions of the ASME*, 105:480–486, 1983.

[21] M. Sanz, A. Natarajan, and L. C. Henriksen. Feasibility study of a semi floating spar buoy wind turbine anchored with a spherical joint to the sea floor. EWEA Offshore 2013, 2013.

[22] N. Scholle, L. Radulović, T. Westphal, L. B. Ibsen, M. Kohlmeier, V. Fedorov, M. Sanz, J. Pollmann, B. Kuhnle, P. Brosche, and T. von Borstel. Innovations on component level (Interim report - INNWIND.EU Deliverable 4.1.2). Technical report, 2014.

[23] R. Scharff and M. Siems. Monopile foundations for offshore wind turbines - solutions for greater water depths. *Steel Construction*, 6 No 1, 2013.

[24] R. Scharff and M. Siems. Pushing the limits - mega monopile foundations for offshore wind turbines. *Steel Construction*, 6 No 3, 2013.

[25] L. Arany, S. Bhattacharya, J. H. G. Macdonald, and S. J. Hogan. A critical review of serviceability limit state requirements for monopile foundations of offshore wind turbines. Offshore Technology Conference, 2015.

[26] J. M. Murchison and M. W. O'Neil. Evaluation of p-y relationship in cohesionless soils, analysis and design of the pile foundation. *ASCE*, pages 174–191, 1984.

[27] American Petroleum Institute. Recommended practice for planning, designing and constructing fixed offshore platforms – Working stress design. Standard, American Petroleum Institute, 2005. API RP2A WSD 2005.

[28] K. Thieken, M. Achmus, and K. Lemke. A new static p-y approach for piles with arbitrary dimensions in sand. *Geotechnik*, 38 No 4:267–288, 2015.

[29] C. Koukoura, C. Brown, A. Natarajan, and A. Vesth. Cross-wind fatigue analysis of a full scale offshore wind turbine in the case of wind–wave misalignment. *Engineering Structures*, 120:147–157, 2016.

[30] Det Norske Veritas. Fabrication and testing of offshore structures. Offshore standard, Det Norske Veritas, 2010. DNV-OS-C401.

[31] I. Lotsberg. Summary report from the JIP on the capacity of grouted connections in offshore wind turbine structures. Report, Det Norske Veritas, 2010. DNV Report No. 2010-1053 Rev 05.

[32] T. Fisher, W. de Vries, and B. Schmidt. Upwind Design Basis (WP4: Offshore Foundations and Support Structures). Technical report, Endowed Chair of Wind Energy (SWE) at the Institute of Aircraft Design, Universität Stuttgart, 2010.

[33] H. F. Veldkamp. *Chances in wind energy - A probabilistic approach to wind turbine fatigue design*. PhD thesis, Technische Universiteit Delft, 2006.

[34] C. Bak, F. Zahle, R. Bitsche, T. Kim, A. Yde, L. C. Henriksen, P. B. Andersen, A. Natarajan, and M. H. Hansen. Description of the DTU 10 MW reference wind turbine (INNWIND.EU Deliverable 1.2.1). Technical report, Technical University of Denmark, DTU Wind Energy, 2013.

[35] P. Chaviaropoulos and A. Milidis. 20 MW Reference Wind Turbine - Aeroelastic data of the onshore version (INNWIND.EU Deliverable 1.2.5(a)). Technical report, National Technical University of Athens, 2016.

[36] M. Stolpe, W. Njomo Wandji, and A. Natarajan. Modularized jacket design. In *Innovative design of a 10MW steel-type jacket (INNWIND.EU Deliverable 4.3.4)*, pages 31 – 42. 2016.

[37] The International Electrotechnical Commission. Wind Turbines - Part 1: Design requirements. Standard, The International Electrotechnical Commission, 2009. IEC 61400-1 Ed. 3.

[38] Det Norske Veritas. Design of offshore wind turbine structures - Offshore standard. Standard, Det Norske Veritas, 2014. DNV-OS-J101.

[39] Germanischer Lloyd. Guideline for the Certification of Wind Turbines. Standard, Germanischer Lloyd, 2010.

[40] T. J. Larsen and A. M. Hansen. *How 2 HAWC2, the user's manual. DTU Risoe-R-1597*, 2015.

[41] J. S. Przemieniecki. *Theory of matrix structural analysis*. Dover Civil and Mechanical Engineering. Dover Publications Inc, New York, 1968.

[42] A. K. Chopra. *Dynamics of structures*. Prentice-Hall: Upper Saddle River, N.J., 2011.

[43] J. F. Manwell, J. G. McGowan, and A. L. Rogers. *Wind Energy Explained: Theory, Design and Application, 2nd Ed.* John Wiley and Sons, Ltd, 2009.

[44] J. Mann. The spatial structure of neutral atmospheric surface-layer turbulence. *Journal of Fluid Mechanics*, 273:141–168, 1994.

[45] S. Chakrabarti. *Handbook of offshore engineering*. Elsevier, 2005.

[46] DNV GL. Machinery for wind turbines. Standard, Det Norske Veritas, 2016. DNVGL-ST-0361.

[47] H. M. Rafsanjani and J. D. Sørensen. Reliability analysis of fatigue failure of cast components for wind turbines. *Energies*, 8:2908–2923, 2015.

[48] DNV GL AS. Fatigue design of offshore steel structures. Recommended practice, Det Norske Veritas, 2016. DNVGL-RP-C203.

[49] DNV GL. Loads and site conditions for wind turbines. Standard, Det Norske Veritas, 2016. DNVGL-ST-0437.

[50] M. Efthymiou. Development of SCF formulae and generalised influence functions for use in fatigue analysis. Surrey, UK, 1988. Conference OTJ'88 on Recent Developments in Tubular Joints Technology.

[51] Det Norske Veritas and Risø National Laboratory. *Guidelines for Design of Wind Turbines, 2nd Ed.* DNV/Risø, 2009.

[52] A. M. Miner. Cumulative damage in fatigue. *Journal of Applied Mechanics*, 12:A159–A164, 1945.

[53] DNV GL AS. Design of offshore steel structures, general - LRFD method. Offshore standard, Det Norske Veritas, 2015. DNVGL-OS-C101.

[54] I. Abdallah. *Assessment of extreme design loads for modern wind turbines using the probabilistic approach*. PhD thesis, Technical University of Denmark, 2015.

[55] P. Moze. ESDEP Course - Strcutural systems: offshore - Tubular Joints in Offshore Structures. http://fgg-web.fgg.uni-lj.si/ /pmoze/esdep/master/wg15a/l0700.htm, 2017. Accessed: 29 Sept 2017.

[56] M. S. Ramos, M. V. Pereira, S. H. Motta, and Carneiro M. A. Fatigue life extension in a structural steel. Sao Paulo, Brazil, 2001. X Congresso e Exposição Internacionais da Tecnologia da Mobilidade.

[57] L. L. Martinez, Z. Barsoum, and A. Paradowska. State-of-the-art: fatigue life extension of offshore installations. Rio de Janeiro, Brazil, 2012. International Conference on Ocean, Offshore and Artic Engineering (OMAE2012).

[58] INVENTUS Engineering GmbH. https://de.wikipedia.org/wiki/Datei:MRF-Effekt.gif, 2008. Accessed: 21 Aug 2017.

[59] Y. Kim, R. Langari, and S. Hurlebaus. Semi active nonlinear control of a building with a magnetorheological damper system. *Mechanical Systems and Signal Processing*, 23:300–315, 2009.

[60] G. Yang, Jr. B. F. Spencer, H.-J. Jung, and J. D. Carlson. Dynamic Modeling of Large-Scale Magnetorheological Damper Systems for Civil Engineering Applications. *Journal of Engineering Mechanics*, 130 (9):1107–1114, 2004.

[61] Y. K. Wen. Method for random vibration of hysteretic systems. *Journal of Engineering Mechanics*, 102 (2):249–263, 1976.

[62] Y. Liu, F. Gordaninejad, C. A. Evrensel, and G. Hitchcock. An Experimental Study on Fuzzy Logic Vibration Control of a Bridge Using Fail-Safe Magneto-Rheological Fluid Dampers, Smart Structures and Materials. *Smart Systems for Bridges, Structures, and Highways*, 4003:281–288, 2001.

[63] H.-S. Kang, M.-H. Kim, S. S. B. Aramanadka, and H.-Y. Kang. Semi-Active Magneto-Rheological Damper to Reduce the Dynamic Response of Top-Tension Risers. pages 837–844, Anchorage, Alaska, USA, 2013. International Society of Offshore and Polar Engineers (ISOPE).

[64] O. Yanguas Miñambres. Assessment of current offshore wind support structures concepts - Challenges and technological requirements by 2020. Master's thesis, Karlshochschule International University, 2012.

[65] R. Damiani, K. Dykes, and G. Scott. A comparison study of offshore wind support structures with monopiles and jackets for U.S. waters. *Journal of Physics: Conference Series*, 753(092003), 2016.

[66] The International Electrotechnical Commission. Wind Turbines - Part 3: Design requirements for offshore wind turbines. Standard, The International Electrotechnical Commission, 2009. IEC 61400-3 Ed. 1.

[67] N. Scholle, L. Radulović, R. Nijssen, L. B. Ibsen, M. Kohlmeier, A. Foglia, J. Thiel, B. Kuhnle, and D. Kaufer. Innovations on component level (final report)). Technical report, 2016.

Technical University of Denmark
Department of Wind Energy
Frederiksborgvej 399
Building 118
4000 Roskilde
Denmark
Telephone 46 77 50 85

info@vindenergi.dtu.dk
www.vindenergi.dtu.dk